

**BUILDING THE CONTINENTAL LITHOSPHERE:
THE HISTORY OF THE CONTIGUOUS U.S. AS PRESERVED IN
CRUST AND LITHOSPHERIC MANTLE STRUCTURES**

EMILY HOPPER

B.A. UNIVERSITY OF CAMBRIDGE, 2010
M.SCI., UNIVERSITY OF CAMBRIDGE, 2011
SC. M., BROWN UNIVERSITY, 2013

A DISSERTATION SUBMITTED IN PARTIAL FULFILLMENT OF THE REQUIREMENTS
FOR THE DEGREE OF DOCTOR OF PHILOSOPHY
IN THE DEPARTMENT OF EARTH, ENVIRONMENTAL,
AND PLANETARY SCIENCES AT BROWN UNIVERSITY

Providence, Rhode Island

May, 2016

© Copyright 2016 by Emily Hopper

This dissertation by Emily Hopper is accepted in its present form by the Department of Earth, Environmental, and Planetary Sciences as satisfying the dissertation requirements of the degree of Doctor of Philosophy.

Date

Karen M. Fischer, Brown University
Advisor

Recommended to Graduate Council

Date

Donald W. Forsyth, Brown University
Reader

Date

Greg Hirth, Brown University
Reader

Date

Stephen Parman, Brown University
Reader

Date

Lara Wagner, Carnegie Institute, Washington
Reader

Approved by the Graduate Council

Date

Peter Weber, Dean of the Graduate School

EMILY HOPPER

14 Glenwood Ave
Rumford, RI 02916

emily_hopper@brown.edu
401 572 1962

QUALIFICATIONS

Ph.D. (Seismology)	Brown University	anticipated May, 2016
M.Sc. (Seismology)	Brown University	May, 2014
M.Sci. (Earth Sciences, 1st class hons.)	University of Cambridge	May, 2011
B.A. (Natural Sciences)	University of Cambridge	May, 2010
5 A Levels	West Buckland School	May, 2007

(Chemistry [A]; Physics [A]; Maths [A]; Spanish [A]; Music [A])

RESEARCH EXPERIENCE

I have expertise in analysis of scattered seismic phases, in particular using common conversion point stacked receiver functions, forward modeling, and a wavefield migration technique (2D generalized radon transform). I use these to image lithospheric mantle and crustal structures across the United States.

The work in the southeastern U.S. uses data from a portable array in Georgia, which I helped to install, service, and demobilize in several field seasons between 2011 and 2014.

I have also mentored graduate and undergraduate students in the processing and analysis of receiver functions.

PUBLICATIONS

Hopper, E., Fischer, K. M., Wagner, L. S., & Hawman, R. B., 2016. Reimagining the end of the Appalachian Orogeny: crustal structures in the southeast U.S.

Hopper, E. & Fischer, K. M., 2015. The meaning of midlithospheric discontinuities: A case study in the northern U.S. craton. *Geochem. Geophys. Geosyst.* 16 (12), 4057-4083.

Hopper, E., Ford, H. A., Fischer, K. M., Lekić, V. & Fouch, M. J., 2014. The lithosphere-asthenosphere boundary and the tectonic and magmatic history of the northwestern United States. *Earth and Planet. Sci. Lett.* 402, 69-81. [19 citations].

PRESENTATIONS

Hopper, E., Fischer, K. M., Wagner, L. S., & Hawman, R. B., 2016 (*invited*). Reimagining the end of the Appalachian Orogeny: crustal structures in the southeast U.S. Talk at LDEO, Columbia University 10th February.

Hopper, E., Fischer, K. M., Wagner, L. S., & Hawman, R. B., 2016 (*invited*). Reimagining the end of the Appalachian Orogeny: crustal structures in the southeast U.S. Talk at Yale University 11th February.

Hopper E., K. Fischer, L. Wagner, R. Hawman & Rondenay, S., 2015, New insights on the final stages of the Appalachian orogeny in the southeast U.S.A. Abstract T11D-2929 presented at 2015 Fall Meeting, AGU, San Francisco, Calif., 14-18 Dec.

Hopper, E., Fischer, K. M., Wagner, L. S., Hawman, R. B., & Rondenay, S., 2015. Imaging accretionary structures in the crust and mantle of the southeastern U.S.A. Abstract presented at Gordon Research Seminar, Mt. Holyoke, Mass., 6 June.

Hopper, E., Fischer, K. M., Wagner, L. S., Hawman, R. B., & Rondenay, S., 2015. Imaging accretionary structures in the crust and mantle of the southeastern U.S.A. Abstract presented at Student Seismology Workshop, LDEO, Columbia University, 19 March.

Hopper, E., & Fischer, K.M., 2015. Mantle discontinuities and the origins of cratonic lithosphere in the northern U.S.A. Abstract presented at British Geophysical Association – New Advances in Geophysics 2015 Meeting, London, U.K., 5-6 Feb.

Hopper, E., Fischer, K. M., Wagner, L. S., Hawman, R. B., & Rondenay, S., 2014. Imaging accretionary structures in the crust and mantle of the southeastern U.S.A. Abstract S33D-04 presented at 2014 Fall Meeting, AGU, San Francisco, Calif., 15-19 Dec.

Hopper, E. & Fischer, K. M., 2014 (*invited*). Sp scattered wave imaging of lithospheric structure beneath Wyoming. Abstract presented at 2014 Basement Cored Uplift Workshop, Tucson, Ariz., 21-23 Feb.

Hopper, E., Fischer, K.M., Wagner, L.S., Hawman, R.B., Parker, E.H., & Howell, D.K., 2013. Crust and mantle discontinuities beneath the southern Appalachians. Abstract presented at 2013 Fall Meeting, AGU, San Francisco, Calif., 9-13 Dec.

Perry-Houts, J., Calo, M., Eddy, C.L., Guerri, M., Holt, A., **Hopper**, E., Tesoniero, A., Romanowicz, B., Becker, T., & Wagner, L.S., 2013. Deep vs. shallow expressions of continental cratons: Can cratonic roots be destroyed by subduction? Abstract T22A-06 presented at 2013 Fall Meeting, AGU, San Francisco, Calif., 9-13 Dec.

Hopper, E., Ford, H.A., Fischer, K.M., Lekić, V., & Fouch, M.J., 2013. How has magmatism in the northwest United States affected the lithosphere? Insights from Sp receiver functions. Abstract presented at 2013 CIDER Summer Program, Berkeley, Calif., 7 Jul – 2 Aug.

Hopper, E., Ford, H.A., Fischer, K.M., Lekić, V., & Fouch, M.J., 2013. How has magmatism in the northwest United States affected the lithosphere? Insights from Sp receiver functions. Abstract presented at 2013 EarthScope National Meeting, Raleigh, North Carolina, 12-14 May.

Hopper, E., Ford, H.A., Fischer, K.M., Lekić, V., & Fouch, M.J., 2012. How has magmatism in the northwest United States affected the lithosphere? Insights from Sp receiver functions. Abstract DI21A-2349 presented at 2012 Fall Meeting, AGU, San Francisco, Calif., 3-7 Dec.

TEACHING

Teaching Assistant

Modeling and Quantitative Analysis in Natural Sciences: An Introduction	Autumn, 2013
Physical Processes in Geology	Autumn, 2012

SERVICE

Student rep. to geology faculty, representing geophysics graduate students	2014 - present
----------------------------------------------------------------------------	----------------

AWARDS, HONOURS, AND SOCIETY MEMBERSHIPS

Sigma Xi	2014 – present
AGU	2012 – present
Dissertation fellowship, Brown University	2015
Research assistantship, Brown University	2011 – 2012
Girton College Instrumental Award	2007 - 2009

PREFACE

Surface observations of the continental crust provide much of our knowledge of Earth's history, from inferences of ancient crustal formation to its continued alteration today. Geophysical methods, such as seismic imaging, may only give us a snapshot of the continents as they look now – the end product of up to billions of years of history. But such three-dimensional imaging on the spatial scale of plate tectonic processes is invaluable in understanding the response of the lithosphere to current mantle conditions, at the very least. The preservation of structures within both the crust and lithospheric mantle extends the utility of seismic imaging back into deep geological time.

The lithosphere-asthenosphere boundary (LAB) defines the rheological boundary between the rigid plate and the underlying creeping asthenospheric mantle. The LAB is associated with a transition from fast to slow seismic velocities, low to high conductivity, and depleted to enriched mantle compositions. Many aspects of the LAB system remain poorly understood: its depth, the depth range over which the transition occurs, whether or not there is a compositional gradient associated with it, the control of tectonic setting and tectonic inheritance, and the processes that can alter it. Yet understanding the nature of the LAB is fundamental to our understanding of plate tectonics. It is the most common plate boundary, the contrast across which defines the rheological differences that make the lithosphere plate-like. The nature of the LAB itself has implications for mantle dynamics and the forces behind plate tectonics. Variations in the LAB may also point to important differences in the overlying lithospheric mantle, the strength of which impacts the degree of crustal deformation.

Within the lithosphere, preserved structures record the history of continental formation and alteration. Such structures have long been observed in the continental crust, but their recognition and study well below the Moho is relatively recent. When preserved structures are manifest by localized velocity gradients, they are described as mid-lithospheric discontinuities

(MLDs). MLDs are particularly prevalent within the ancient cores of the continents. Study of these structures, both in the crust and lithospheric mantle, allows us to infer tectonic processes that occurred hundreds or even thousands of millions of years ago.

In this thesis, I present the results of scattered wave imaging across the contiguous U.S. The recent deployment of EarthScope's Transportable Array, a broadband network that marched across the Lower 48 with a station spacing of 70 km, provided an incredible dataset with uniform coverage across the varied terranes of the contiguous U.S. Higher density temporary arrays, such as SESAME (the Southeastern Suture of the Appalachian Margin Experiment), allow even more detailed imaging of particular structures of interest. The use of scattered waves, in this work largely S-to-P converted phases, produces high resolution models with excellent imaging of sharp changes in properties, in contrast to the volumetric imaging of seismic tomography. In particular, these results demonstrate the dependence of lithospheric structures on current and past tectonic processes, the longevity of tectonic inheritance, the mechanisms of continent formation by lateral accretion at both crustal and lithospheric mantle depths, and the consistency of the observed lithospheric response across extremely disparate tectonic terranes.

Chapter 1 examines the structures of the Pacific Northwest, with a focus on the Yellowstone and High Lava Plains volcanism. The western U.S. is tectonically the youngest part of the country, with active extension and volcanism over broad regions. As such, the lithosphere here is relatively simple, preserving only the most recent tectonism. The observations show that in the areas of most recent Holocene volcanism, such as the youngest portion of the High Lava Plains, the LAB is strong and shallow. The high amplitude suggests a strong, localized velocity contrast, such as could be generated by ponding of partial melt at the base of the lithosphere (Figure 1). This interpretation implies that melts pond and equilibrate at the seismically observed LAB, consistent with pressure-temperature estimates for recent volcanics. The phase deepens beneath areas of less recent Neogene volcanism, consistent with a view of the lithosphere as a

thermal boundary layer that conductively thickens with time. The age of the surface volcanism records the time since extensive melt infiltration thermally eroded the lithosphere, and the change in depth is consistent with thermal modeling of a cooling geotherm, where the LAB is defined by the intersection of the geotherm with the solidus. Yellowstone, which has had very extensive recent volcanism, lacks any strong phases beneath the Moho; total thermal erosion of the lithospheric mantle by extensive infiltration of heat and melt could explain the lack of an LAB phase.

In Chapters 2-4, images of the eastern U.S. are presented. Here, two complete Wilson cycles are preserved – from the assembly of Rodinia at ~1 Ga to the mid-Mesozoic rifting of Pangea that formed the Atlantic Ocean. The youngest structures are the result of passing hot spots or lithospheric delamination [Chapter 2], characterized by low asthenospheric velocities and regionally shallow LABs. While the LAB is deeper and weaker than seen in the very recently active western U.S., its shallowing in areas of most recent mantle upwelling is analogous to that observed beneath the youngest portion of the High Lava Plains [Chapter 1] (Figure 1).

The building of the Appalachian Mountains during the final assembly of Pangea in the late Proterozoic is the focus of Chapter 3. Here, a novel application of the Sp technique, based around the new dataset recorded by the SESAME array, is applied to image crustal structures that preserve the mechanism of continental collision. An observed large, low-angle detachment dips southward over 300 km, confirming that the final stages of this collision involved significant shortening across this continental suture. These observations rule out models with primarily strike-slip motion on the suture at the final stages of the Appalachian orogeny. Instead, these observations show that the mechanisms of continental collision in this Paleozoic orogeny are similar to those imaged today in active collisional zones worldwide.

In Chapter 4, the SESAME dataset is processed using a full waveform inversion of scattered incident P waves. This provides a high resolution image of the crust with more accurate retrieval of dipping structures. This entirely independent dataset confirms the geometry and strength of the continental suture observed with Sp waves in Chapter 3. Furthermore, new images of the Moho are produced. These agree with previous Ps receiver function observations of Moho topography, and additionally identify a zone with a weakened contrast across the Moho beneath the highest surface topography. This may be related to the initial stages of lower crustal delamination, a possible factor contributing to regional topographic rejuvenation.

Older tectonic events are also preserved at mantle lithospheric depths. While we do not observe clear evidence of collisional structures as in the crust, Proterozoic rifting appears to have a strong influence [Chapter 2]. This rifting event (if not poorly preserved tectonism pre-dating it) has been cited as the controlling factor on the localization of much of the subsequent crustal deformation. At lithospheric depths, a step change in the depth of the LAB is observed and correlated with the limit of extensive crustal thinning. The LAB is observed most clearly around this topographic step, suggesting that enhanced local convection (and associated decompression melting) makes the LAB velocity gradient sharp enough to be imaged by Sp waves. Additionally, zones of weakness identified from this same rifting event are correlated with regions of very weak uppermost mantle phases, though seismic tomography still identifies these regions as having relatively thick (~100 km), seismically fast lids. The seismic transparency of the lithosphere in these regions may be related to extensive, localized deformation or even delamination of the lithosphere, disrupting or destroying any pre-existing structures. These results indicate that repeatedly exploited Proterozoic rift structure exerts significant control on the large-scale lithospheric structure observed today; that is, the importance and longevity of tectonic inheritance extends throughout the whole of the lithosphere.

In Chapter 5, the ancient continental interior is examined. This region, with its much thicker (>200 km) lithosphere, does not in general have a visible LAB using the Sp technique (Figure 1). This is expected, given the assertion that the LAB is only visible when it acts as a barrier to melt; at these greater depths, the temperature relative to the solidus is much lower. Instead, MLDs are observed. Within the core of the Wyoming Craton [Chapters 1, 5] and the undeformed Mesoproterozoic Granite-Rhyolite Province [Chapter 2], there is a laterally extensive, subhorizontal MLD at 70-100 km depth. Given its presence in both the 2.7-2.5 Ga Wyoming Craton and the 1.5-1.3 Ga Granite-Rhyolite Province, the mechanism forming this thin, shallow low velocity zone must have been relatively ubiquitous, at least before 1.3 Ga. A frozen layer of volatile-rich melt is modeled as a sufficient velocity contrast, localized in depth due to a kink in the carbonated peridotite solidus. That a clear, sub-horizontal MLD is unique to these relatively ancient terranes suggests that such a layer either formed more efficiently in the Mesoproterozoic and earlier, or that sufficient time since the last deformation event is required to accumulate enough volatile-rich material to generate a strong phase.

Chapter 5 also examines the origin of inward-dipping MLDs found at the margins of cratonic blocks. By association with eclogitic xenoliths and modeling of predicted velocity contrasts, these MLDs are interpreted to be the upper or lower boundaries of relict subducted slabs. These structures support models of craton formation by thickening of sub-arc mantle or slab imbrication, some of the proposed mechanisms to generate the extraordinarily thick, strong, buoyant, long-lived lithospheric root found only beneath cratons. The exclusive observation of such dipping structures in and around Archean cratonic blocks is compatible with these mechanisms as forming the strong Archean roots.

Having a consistent body of observations across the diverse contiguous U.S. (Figure 1) using the same methodology allows significant discoveries to be made about the formation and alteration of lithospheric structures. Across all study regions, the seismic LAB is consistent with

interpretation as a melt-mediated thermal boundary. In the youngest, volcanically active regions, the lithospheric thermal boundary layer has a layer of ponded melt trapped beneath it; with time since the volcanism, this layer conductively cools and the LAB deepens. Beneath middle-aged lithosphere, there is not typically enough melt to allow the LAB to be consistently visible; however, small-scale convection at topographic steps can enhance melt production and sharpen the LAB velocity gradient. Beneath the oldest lithosphere, the thermal boundary layer is too thick for any significant melt layer to form beneath it, and an LAB velocity gradient localized enough to produce converted waves is not typically observed.

In addition to this thermal definition, the lithosphere must be chemically isolated, allowing the preservation of tectonic structures over hundreds to thousands of millions of years. In the crust and cratonic lithospheric mantle, structures produced by lateral accretion (Figure 1) are preserved as the predominant mode of continental growth. A shallow mantle lithospheric phase observed in terranes separated by a billion years of history and thousands of kilometers of accreted terranes is compatible with a continuous process of lithospheric mantle enrichment, building up a low velocity, volatile rich layer. Additionally, where the lithosphere has been extensively deformed, and in particular where it has been weakened by tectonism, such a phase is not observed; here the chemically isolated lithosphere appears vulnerable to disruption or perhaps complete removal. A step in lithospheric thickness associated with late Proterozoic rifting implies that, even outside of the cratonic interior, relict lithospheric structures play a significant role, indicating that the LAB is not the simple product of lithospheric cooling.

Although the results from these disparate regions can be understood with a unified view of the lithosphere (Figure 1), this work also raises new questions. How are some structures preserved over hundreds of millions of years, while some changes (e.g. conductive cooling and thickening) occur on timescales of 10 Ma? What is the timescale for lithospheric recovery, e.g. after the passage of a hot spot, or extensive deformation or delamination? How does chemically

isolated lithosphere form, and what is its relationship to the thermally defined root? What is the rheological contrast across this thermally defined root, and how does that vary with inferred degree of ponded melt? This area of research is still rich with unanswered questions, awaiting further high resolution seismological imaging of structure and anisotropy within the lithosphere and asthenosphere, and its integration with geochemical and other geophysical observations and the results of geodynamic modeling.

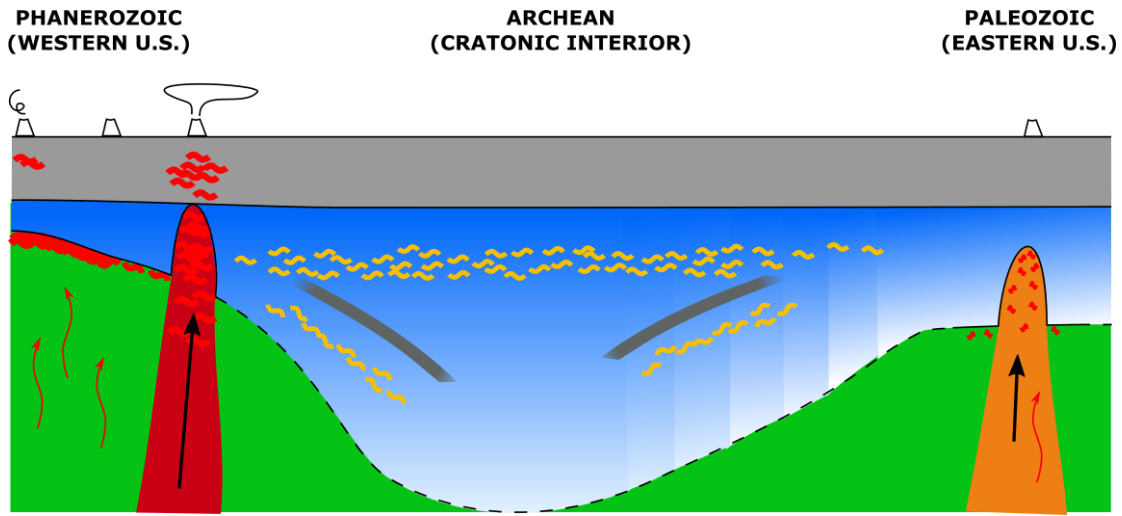


Figure 1: Schematic overview of the lithosphere-asthenosphere system in the contiguous U.S. In the tectonically active western U.S., the LAB is observed to be strong and shallow. The strong velocity contrast shown here as generated by melt pooling beneath the LAB. This ponded melt is shallowest beneath active volcanism (westernmost volcano), and deepens with time since the most recent volcanism (adjacent extinct volcano). This suggests the LAB is a melt-mitigated thermal boundary that deepens as the lithosphere conductively cools with time. Yellowstone (volcano with large ash cloud) has no observable LAB beneath it, implying the lithosphere has been totally thermally eroded by melt advection. Within the cratonic interior, an extensive, subhorizontal MLD is observed, shown here as a band of frozen volatile-rich mantle at 60-80 km depth. This MLD is only observed beneath ancient, undisturbed crust, suggesting this layer formed more efficiently before the Neoproterozoic, or that a very long time is required to accumulate sufficient frozen-in volatile-rich melt to generate a strong S_p conversion. Dipping MLDs within the cratonic root support the model of root formation by lateral accretion involving subduction; the MLDs may represent remnant oceanic crust, or a similar frozen-in volatile-rich layer within the dipping remnant oceanic lithosphere. No sub-cratonic LAB is observed (dashed black line), indicating a gradual velocity gradient compatible with a purely thermal base to the lithosphere. Beneath the eastern U.S., the lithosphere is still relatively thick (~100km), and in general a strong LAB is not observed. In old hotspot tracks, zones of delamination, or pre-existing lithospheric steps (not shown here), enhanced upwelling leads to sufficient fractions of partial melt to illuminate the LAB.

ACKNOWLEDGMENTS

To Karen, my lab sisters, my friends, my family, and the many, many others who helped me along the way – thank you so much for your guidance and support. I could not have done it (and would not have enjoyed it nearly so much!) without you. You have my deepest appreciation and my love.

TABLE OF CONTENTS

Title Page	i
Copyright Page	ii
Signature Page	iii
Curriculum Vitae	iv
Preface	vii
Acknowledgements.....	xv
Table of Contents.....	xvi

CHAPTER 1: The lithosphere-asthenosphere boundary and the tectonic and magmatic history of the northwestern United States	1
Abstract.....	2
1. Introduction.....	3
1.1. The lithosphere–asthenosphere boundary	3
1.2. Tectonic and magmatic setting and prior studies of seismological structure.....	3
2. Data and methods.....	7
2.1. Sp waveforms.....	7
2.2. Deconvolution, migration, stacking and bootstrapping	8
2.3. Discontinuity depths and uncertainties	9
3. Observed mantle discontinuities and their origin	10
3.1. Cratonic lithosphere	10
3.1.1. Cratonic vs. more recently tectonized lithosphere	10
3.1.2. The origin of layering within the cratonic lithosphere.....	12
3.2. Lithosphere to the west of the Sevier Thrust Belt.....	13
3.2.1. Columbia River flood basalts, the High Lava Plains and the northwest Basin and Range.....	13
3.2.2. Yellowstone and the Snake River Plain.....	15
3.2.3. Owyhee Plateau and Grouse Creek Block	16
3.3. The base of the low velocity zone.....	16
3.4. The origins of the LAB	17
4. Conclusions.....	21
Acknowledgements.....	22
References.....	22

Figures	33
Supplementary Materials	41
Effects of different bandpass filters	41
Bootstrap Testing	41
Supplementary References.....	44
Supplementary Figures	46

CHAPTER 2: Controls on lithospheric structures in the eastern United States:

Tectonic inheritance and asthenospheric melts.....	53
Abstract.....	54
1. Introduction.....	55
1.1. Tectonic setting.....	55
1.1.1. Tectonic inheritance in the eastern U.S.	56
1.2. The lithosphere-asthenosphere system.....	57
1.3. The impact of mantle dynamics	60
2. Data and Methods	61
2.1. Data.....	61
2.2. Processing	62
2.3. Picking and classification of NVGs.....	63
3. Observed LAB and MLD structures and their meaning	64
3.1. The lithosphere-asthenosphere boundary.....	64
3.1.1. Shallow, low velocity anomalies associated with upwellings.....	65
3.1.2. Changes across the hinge zone.....	66
3.1.3. The thick lithosphere of the continental interior	67
3.1.4. Local strengthening of the LAB.....	67
3.2. Mid-lithospheric discontinuities	70
3.3. Gaps in the NVGs	71
4. Conclusions.....	72
4.1. Tectonic inheritance.....	72
4.2. The lithosphere-asthenosphere system.....	73
4.3. The impact of mantle dynamics	74
Acknowledgements.....	74
References.....	75

Figures	86
CHAPTER 3: Reimagining the end of the Appalachian Orogeny: Crustal structures in the southeast U.S.	93
Abstract.....	94
Main Text.....	95
Acknowledgments.....	100
References.....	101
Figures	106
Supplementary Materials	109
Data.....	109
Processing	109
Bootstrapping.....	110
Forward modeling.....	110
Modeling of Sedimentary Basins.....	111
Modeling anisotropic structures at single stations	112
Supplementary References.....	112
Supplementary Figures	115
CHAPTER 4: Imaging of crustal structures in the southeast U.S. by scattered wavefield migration	123
Abstract.....	124
1. Introduction.....	125
2. Data and Methods	126
2.1. Data.....	126
2.2. Inversion of scattered waves.....	127
2.3. Suitability of the dataset.....	128
3. Observed discontinuities.....	130
3.1. Crustal structure beneath the Blue Ridge and Inner Piedmont: the D line	130
3.1.1. Moho topography and strength variations	130
3.1.2. Robustness of the Moho.....	132
3.1.3. Upper crustal structure beneath the thrust sheets.....	133
3.2. Crustal structure beneath the Coastal Plain: the W line	134
3.2.1. Moho topography.....	134

3.2.2. The Suwannee suture	134
3.3. Crustal structure beneath the Coastal Plain: the E line	136
4. Conclusions.....	136
Acknowledgements.....	137
References.....	137
Figures	143

CHAPTER 5: The meaning of midlithospheric discontinuities: A case study in the northern U.S. craton

northern U.S. craton	150
Abstract.....	151
1. Introduction.....	152
1.1. Cratonic mantle seismic velocity discontinuities	152
1.2. Tectonic, geophysical, and geochemical setting	154
2. Data and methods.....	156
2.1. Data	156
2.2. Phase processing: picking, deconvolution, migration, and stacking.....	156
2.3. Bootstrapping and uncertainties.....	157
3. Observed mantle discontinuities	158
3.1. Summary of observed mantle discontinuity types	158
3.2. Observed shallow, subhorizontal NVG	158
3.3. Dipping structures within the lithosphere	159
3.3.1. Observed dipping NVGs.....	159
3.3.2. The Cheyenne Belt.....	159
3.3.3. The Yavapai-Superior craton boundary	161
3.3.4. Other Proterozoic and Archean collision zones	161
3.4. Base of the lithosphere	162
3.5. Sporadic PVGs.....	163
4. The origin of lithospheric layering.....	163
4.1. Summary of observational constraints	163
4.2. Widespread NVG in the shallow upper mantle.....	163
4.2.1. Possible origins: chemical composition, rock fabric and deformation mechanism.....	163
4.2.2. Relationship of large-scale, shallow negative phase to lithospheric mantle seismicity	169
4.3. Dipping NVGs within the lithospheric mantle.....	171

4.3.1. Possible origins: chemical composition, rock fabric and deformation mechanism	171
4.3.2. Timing of dipping and shallowmost NVGs	173
4.4. Modeling of NVG depths and amplitudes	174
4.5. Lithosphere-asthenosphere boundary	176
4.6. Positive phases near the base of the lithosphere	177
4.7. Relationship of MLDs and LAB to cratonic mantle formation models	178
4.8. Evolution of the Wyoming lithospheric mantle	179
5. Conclusions.....	181
Acknowledgements.....	182
References.....	183
Figures	211
Supplementary Materials	224
Introduction.....	224
S1. Example of criteria for interpreting CCP stack.....	224
S2. Additional comparisons of CCP stack with tomography.....	225
S3. Sp CCP stacks from different backazimuth ranges.....	225
S4. More background information on the Wyoming and Utah lithospheric mantle earthquakes	225
S5. Receiver function modeling.....	226
Supplementary References.....	228
Supplementary Figures	229

CHAPTER 1

The lithosphere-asthenosphere boundary and the tectonic and magmatic history of the northwestern United States

Emily Hopper¹, Heather A. Ford^{1,*}, Karen M. Fischer¹, Vedran Lekić², Matthew J. Fouch³

¹Department of Earth, Environmental and Planetary Sciences, Brown University, Providence, RI, USA

²Department of Geology, University of Maryland, College Park, MD, USA

³Department of Terrestrial Magmatism, Carnegie Institution of Washington, Washington, D.C., USA

*Now at Department of Earth Sciences, University of California, Riverside, CA, USA

This chapter has been published in:

Earth and Planetary Sciences

Citation: **Hopper, E.**, Ford, H. A., Fischer, K. M., Lekić, V., and Fouch, M. J. (2014), The lithosphere-asthenosphere boundary and the tectonic and magmatic history of the northwestern United States, *Earth. Planet. Sci. Lett.*, 402, 69-81, doi:10.1016/j.epsl.2013.12.016

Abstract

This study explores the properties of the lithosphere–asthenosphere boundary (LAB) and other shallow mantle discontinuities across the diverse geologic provinces of the northwest United States. Sp phases were used to image three-dimensional discontinuity structure by common conversion point stacking with data from 804 temporary and permanent broadband stations, including 247 from EarthScope’s USArray Transportable Array. Substantial variations in mantle discontinuity structure are apparent over a variety of spatial and temporal scales. To the west of the Sevier Thrust Belt, a coherent Sp negative phase coincides with the LAB depth range inferred from tomographic models. To the east, within the stable craton, multiple negative phases typically occur in the high velocity lithospheric layer, although in places a single mid-lithospheric discontinuity is imaged. Sub-cratonic LAB phases are often absent, indicating an LAB velocity gradient that is distributed over >50 km and that is consistent with effects of temperature alone. Where weak and intermittent LAB phases appear, they suggest more vertically localized velocity gradients produced by other factors such as bulk composition, volatile content, or contrasts in grain size or melt. In the tectonically active west, a positive Sp phase at depths consistent with the base of the asthenospheric low velocity zone in tomography models is intermittently observed. Beneath magmatic provinces in the west, the LAB Sp discontinuity deepens by ~10 km from the High Lava Plains, where magmatism has occurred from 0–10.5 Ma, to the northern region of the Columbia River Basalts, which has been magmatically quiet since 15 Ma. Here we suggest a model in which the negative LAB velocity gradient is created by a layer of partial melt ponding beneath a solidus-defined boundary. This model predicts that higher temperatures associated with more recent magmatism would result in a shallowing of the intersection of the geotherm with the solidus. Beneath the Yellowstone Caldera, the absence of an LAB Sp phase suggests that the contrast in seismic velocity between the lithosphere and asthenosphere has been erased by intrusion of partial melt and heat into the lithosphere.

1. Introduction

1.1. The lithosphere–asthenosphere boundary

The lithosphere is classically defined rheologically and kinematically as the rigid plate that translates coherently with surface plate motions. In this study we probe the properties of the mantle portion of the lithosphere as defined by its seismic wavespeed, i.e. the high velocity layer above the asthenospheric low velocity zone. The primary mechanisms for the velocity decrease from lithosphere to asthenosphere are temperature, volatile content, bulk composition, partial melt, grain size, and anisotropic fabrics, all of which can be reset by tectonic and magmatic processes. Here we image the seismologically-defined lithosphere–asthenosphere boundary (LAB) and other shallow mantle discontinuities across the diverse geologic provinces of the northwest United States. Our goal is to better understand the mechanisms responsible for producing the seismically observed LAB and how the LAB and other mantle discontinuities relate to the region’s tectonic and magmatic evolution.

1.2. Tectonic and magmatic setting and prior studies of seismological structure

The tectonic and magmatic evolution of the northwestern United States is expressed over several different temporal and spatial scales. At the broadest scales, our study region is divided along the Sevier Thrust Belt into a western region that has experienced significant deformation and magmatic activity throughout the Phanerozoic, and an eastern region where deformation has been less extensive, particularly in the last 50 My (Figure 1). The Archean Wyoming Craton forms the core of the eastern region, though there are also other ancient, stable continental blocks, including the Medicine Hat Block and the Colorado Plateau [Foster et al., 2006] (Figure S3). The ancient continental blocks extending several hundreds of kilometers west of the Sevier Thrust Belt, i.e. the Paleoproterozoic Selway Terrane and Archean Grouse Creek Block, underwent greater degrees of tectonic and magmatic reworking [Foster et al., 2006]. These blocks are bounded on the west by Phanerozoic accreted terranes, a boundary often associated with

strontium isopleths, with $^{87}\text{Sr}/^{86}\text{Sr}$ decreasing westwards [Armstrong et al., 1977; Coney et al., 1980].

Phanerozoic tectonism was dominated first by subduction and orogenesis. Convergence has included the Cretaceous to Eocene Sevier and Laramide Orogenies. While the Sevier Thrust Belt marks the eastern limit of the Sevier Orogeny, Laramide deformation extended further east, building the Rocky Mountains [Dickinson, 2004; Saleeby, 2003; Tikoff and Maxson, 2001]. By the Early Miocene, part of the convergent boundary on the continental margin had converted to the San Andreas transform. Consequent Basin and Range extension is estimated to have reached values of 50% or more within the study area [Dickinson, 2004; McQuarrie and Wernicke, 2005].

One feature common to many recent tomography models is the marked transition from shallow upper mantle with low seismic velocities in regions that have experienced high degrees of tectonic reworking and magmatism to a thick, high velocity mantle layer elsewhere [e.g. Burdick et al., 2012; Darold and Humphreys, 2013; James et al., 2011; Obrebski et al., 2011; Schmandt and Humphreys, 2010; Shen et al., 2013; Sigloch, 2011; Yuan et al., 2011]. South of $\sim 45^\circ\text{N}$, this transition appears at the eastern margin of the Basin and Range and Snake River Plain, with the exception of lower velocity upper mantle beneath the High Rockies south of the Wyoming Craton. In the northern portion of our study region, the transition typically occurs further west at longitudes of $118^\circ\text{--}119^\circ\text{W}$.

The region has experienced a long and varied magmatic history. The Columbia River Flood Basalts, emplaced between 16.6 and 15.0 Ma [Camp et al., 2003; Hooper et al., 2002], outcrop in the northwest of the study region (Figure 1). Their southern lobe was overprinted by later High Lava Plains volcanism. In the High Lava Plains, a wave of silicic volcanism started at ~ 15.5 Ma and has propagated towards the northwest [e.g. Jordan et al., 2004]. Recent work extends this trend into the northwest Basin and Range to 12 Ma [Ford et al., 2013]. Along the

eastern Snake River Plain, silicic volcanics decrease in age from 12–0 Ma in the direction opposite to North American plate motion, culminating in the active volcanism beneath Yellowstone Caldera [e.g. Christiansen et al., 2002; Pierce and Morgan, 2009, 1992; Shervais and Hanan, 2008]. In both the High Lava Plains and eastern Snake River Plain, basaltic magmas have erupted since 10.5 Ma with no age-progressive trend [e.g. Christiansen et al., 2002; Jordan et al., 2004; Till et al., 2013a].

In the High Lava Plains area, low velocities are observed to shallow mantle depths, implying small lithospheric thicknesses [Wagner et al., 2010; Obrebski et al., 2011; Hanson-Hedgecock et al., 2012; Gao and Shen, 2014]. Furthermore, temperatures and pressures of basaltic melt equilibration indicate that asthenospheric conditions exist at very shallow mantle depths [Till et al., 2013a]. The upper limit on crustal extension in the High Lava Plains, constrained by paleomagnetic and crustal thickness observations, is 16–17% [Eagar et al., 2011; Wells and Heller, 1988]; some postulate advective and convective thinning instead [Long et al., 2012].

The Yellowstone–Snake River Plain volcanic trend lies above the most prominent low velocity mantle anomaly in the western United States, a low velocity channel extending to depths of ~200 km [e.g. Burdick et al., 2012; Obrebski et al., 2011; Schmandt and Humphreys, 2010; Shen et al., 2013; Sigloch, 2011; Wagner et al., 2010]. Regardless of the ongoing debate as to the cause and depth extent of this anomaly [e.g. Fouch, 2012; James et al., 2011; Obrebski et al., 2011; Schmandt and Humphreys, 2010; Schmandt et al., 2012], it is clear that the lithosphere beneath the Snake River Plain has been heavily altered. Yellowstone–Snake River Plain magmatism is particularly interesting in this study as the silicic calderas have distinctly different ages. Thus, we can examine magmatic interactions with the lithosphere at small spatial (<100 km) and temporal (~1 Ma) scales.

A wide variety of models have been proposed to explain the magmatic history of the northwestern United States [see Long et al., 2012 for a summary]. Recently, models of subduction zone flow and, in some cases, its interaction with a mantle plume have been developed for the region [Druken et al., 2011; Faccenna et al., 2010; Kincaid et al., 2013; Liu and Stegman, 2012; Long et al., 2012] in response to the magmatic trends and tomographic results described above, and constraints on mantle anisotropy [Lin et al., 2011; Long et al., 2009; Yuan and Romanowicz, 2010b].

A goal of this study is to better understand how the continental lithosphere responds to tectonic and magmatic re-working by examining how shallow (<200 km) mantle discontinuity structure varies between cratonic and non-cratonic regions, and between non-cratonic regions with different magmatic histories. Due to their enhanced sensitivity to vertical velocity gradients, scattered waves such as Sp are an important complement to the constraints on volumetric heterogeneity provided by tomography. For example, while surface wave tomography typically cannot distinguish vertical velocity gradients over 50–70 km from those over smaller depth ranges, Sp phases at dominant periods of ~10 s will typically be clearly observed for velocity changes of less than ~8% only if they occur over less than ~30 km in depth [e.g. Ford et al., 2010; Rychert et al., 2007]. Conversely, if tomography shows that a significant (>4%) velocity gradient occurs but Sp phases are not observed, the velocity gradient must be distributed over a depth range of ~50 km or more.

A number of recent studies have used Ps and Sp phases to examine the western United States [Abt et al., 2010; Eagar et al., 2011; Hansen et al., 2013; Kumar et al., 2012; Lekić and Fischer, 2014; Lekić et al., 2011; Levander and Miller, 2012; Levander et al., 2011; Li et al., 2007; Schmandt et al., 2012; Sheehan et al., 2000]. Of these, several have investigated upper mantle discontinuities in study regions overlapping the one considered here [Abt et al., 2010; Kumar et al., 2012; Lekić and Fischer, 2014; Levander and Miller, 2012; Li et al., 2007].

Advantages provided by our study include a greater density of data over the study area; a new technique for more accurate automated phase picking [Lekić and Fischer, 2014] that allows more waveforms to be more correctly incorporated; a bandpass filter that minimizes interference between adjacent phases; and boot-strapping of the Sp-based image to determine which phases are robust.

One of the major results of these previous studies was Levander and Miller's [2012] observation of a pronounced change in depth of their observed phases across the Sevier Thrust Belt. We confirm this observation, and further explore the fundamental change in discontinuity character across this boundary. Furthermore, we observe pronounced variations in apparent lithospheric thickness between magmatic provinces of different ages. For example, the phase beneath the Columbia River is observed to be deeper than that beneath the High Lava Plains and northern Basin and Range. We also note the absence of a strong negative phase beneath the Moho in the vicinity of the active Yellowstone Caldera.

2. Data and methods

2.1. Sp waveforms

To avoid complications from crustal reverberations, we imaged shallow mantle discontinuities with Sp phases. S waveforms were obtained from the Incorporated Research Institutions for Seismology (IRIS) Data Management Center for events in the USGS National Earthquake Information Center catalog with $M_w > 5.8$. Data from all available broadband stations (804 stations from 31 permanent and temporary networks) within a ~1500 km by ~900 km region centered on the eastern Snake River Plain (Figure 1) were employed. Included are 247 Earthscope USArray Transportable Array stations, which crossed the area between 2006 and 2010; 118 High Lava Plains stations, which operated between 2006 and 2009; and 19 permanent stations of the U.S. National Seismic Network and IRIS Global Seismic Networks, some providing data for as many as 20 years. At short epicentral distances, Sp waves turn post-critical at smaller depths; the

critical depth increases with increasing epicentral distance. Based on the coherence of the final images, we found a distance range of $55\text{--}85^\circ$ and the exclusion of sources below 300 km [e.g. Wilson et al., 2006] to be the best compromise between reducing contamination and adding more data. Our stacks include 77,671 waveforms sourced from 1377 events with an uneven coverage distribution, matching the variable station distribution (Figure 2; Figure 1). In our dataset, the earthquakes are primarily located in the South American subduction zone, to the southeast of the study area, and in the Aleutian and Japan subduction zones, to the northwest. This strong back-azimuthal bias creates the southeast–northwest banding in the distribution of the number of phases contributing to CCP stack (Figure 2). To identify S phase windows for analysis, we used the automated array-based procedure of Lekić and Fischer [2014]. We employed a free surface transfer matrix to rotate the recorded wavefield into its P and SV components, suppressing the effects of the free surface [Bostock, 1998; Kennett, 1991]. An automated search was performed over V_p and V_p/V_s space to find the free-surface values that minimize the amplitude of the parent phase, SV, on the daughter component, P [e.g. Abt et al., 2010].

2.2. Deconvolution, migration, stacking and bootstrapping

For each event-station pair, we deconvolved the P by the SV component using the extended-time multi-taper cross-correlation method [Helffrich, 2006] with the deconvolution parameters of Lekić and Fischer [2014].

We migrated the deconvolved waveforms into a three-dimensional volume and stacked them with a common conversion point (CCP) approach and a spline function representation of the S_p Fresnel zone, more completely described in Lekić et al. [2011]. S_p times were corrected for lateral heterogeneity by ray-tracing through station averages of the crustal model of Lowry and Pérez-Gussinyé [2011] and mantle P-wave and S-wave velocities from Obrebski et al. [2011, 2010]. The Fresnel zones used were based on the dominant period of the waves; with the 4–33 s filter used for the images in this paper, we measured a dominant period of 9 s for the waveforms.

We excluded energy from depths where conversions are expected to be post-critical. We also reversed the polarity of the recorded phases to facilitate comparison with Ps phase results.

To assess the robustness of the phases observed in the Sp CCP stack, we calculated 50 versions of the stack each based on a different random sample of the Sp waveforms, as well as the mean and standard deviation of the 50 stacks. Figures shown in the main text of this paper all derive from the mean of the bootstrapped stack. Phases observed in the bootstrapped stack are very similar to those in the image based on the complete dataset, particularly in the western portion of the study region where a single clear mantle Sp phase is typically observed. In the east, where multiple mantle phases at different depths are common, comparable phases are observed in the bootstrapped stack and the stack containing all waveforms, although phase amplitudes sometimes differ (Supplementary Materials).

2.3. Discontinuity depths and uncertainties

The depth of the negative phase beneath the Moho was picked automatically as the mean depth of the 25 most negative points in the 35–200 km depth range, as described in Lekić et al. [2011]. Uncertainties in phase depth are a product of a) the scatter in the observed Sp waveforms, b) errors in the velocity model used to migrate the phases from time into the CCP stack volume, and c) the finite width of the phase peak and its interference with adjacent arrivals, both of which increase with longer dominant periods. Experimentation with different bandpass filters indicated the least interference between adjacent phases was achieved using a filter with a low frequency corner of 0.25 Hz or greater (Supplementary Materials). In the western half of our study region, uncertainties in phase depth from bootstrap testing (one standard deviation) are less than 5 km over ~70% of the area; in the eastern half, this drops to ~40% of the area (Figure S1). Due to the high quality crust and mantle models used to correct for lateral heterogeneity, uncertainties due to lateral heterogeneity will be <5 km for depths less than 150 km [e.g. Lekić et al., 2011]. In the

western half of our study region, where we interpret mantle Sp phase depths, net depth uncertainties are typically less than ~10 km.

3. Observed mantle discontinuities and their origin

We observe negative Sp phases at mantle depths throughout much of the study region. As we reversed Sp polarity to match the Ps sign convention, this negative phase corresponds to a velocity decrease with depth. Based on comparison of the depth of this phase to the high velocity lid seen in tomography [e.g. Obrebski et al., 2011; Wagner et al., 2010], the negative phase is classified as a lithosphere–asthenosphere boundary phase (LAB) if it is at least as deep as the mid-point between the peak velocity in the high velocity lid and the minimum velocity in the low velocity layer beneath. The phase is deemed a mid-lithospheric discontinuity (MLD) if it falls at depths shallower than this mid-point.

In general, we observe variations in the Sp phase properties between different tectonic provinces over a variety of spatial and temporal scales. At the longest spatial and temporal scales, pronounced differences in discontinuity character exist between the highly deformed region west of the Sevier Thrust Belt and the thicker, more stable lithosphere to its east. At smaller scales, differences in negative discontinuity depth are observed between the 16 Ma Columbia River Basalts and the High Lava Plains and the northwest Basin and Range, where more recent magmatism has occurred. At the shortest scales, the seismological LAB appears to have been completely disrupted beneath the youngest Yellowstone caldera with its active magmatism.

3.1. Cratonic lithosphere

3.1.1. Cratonic vs. more recently tectonized lithosphere

To the west of the Sevier Thrust Belt, a strong negative phase is commonly observed. South of 45°N this phase can be interpreted as the seismological LAB, based on comparisons of phase depth with tomography described earlier; north of 45°, clear association of this phase with the LAB becomes possible west of ~119°W. In contrast, in the cratonic regions to the east of the

Sevier Thrust Belt, weaker MLD phases are observed. In some areas a single MLD phase dominates the CCP stack, but often multiple MLD phases appear at different depths within the thick high velocity cratonic lithosphere. The contrast in mantle discontinuity character across the Sevier Thrust Belt is evident on profiles that cross the western edge of the Archean Wyoming Craton (Profiles A–C, Figure 3), although additional perturbations due to the Yellowstone hotspot track must also be considered (Profile B, Figure 3), as discussed in the next section. Strong laterally continuous negative phases within the potential LAB depth range are not observed beneath cratonic regions, although weak negative, intermittent phases sometimes occur at LAB depths. MLD phases within the cratonic lithosphere are almost exclusively negative, i.e. they appear to originate at a velocity decrease with depth. This observation may reflect real velocity structure, e.g. a series of velocity decreases or alternating velocity decreases and increases where the decreases are vertically localized and the increases are too distributed in depth to produce sharp phases. However, another possibility is that interference between phases from multiple discontinuities obscures aspects of the velocity gradient structure.

The change from a coherent LAB phase in the west to distributed MLDs within the craton does not correlate with a decrease in the density of contributing Sp phases. For example, in western regions of cross-section C–C' (Figure 3), a clear LAB is seen despite relatively sparse data collected largely from TA stations. In contrast, beneath the Wyoming craton where the distributed phase is observed, the TA is augmented by several temporary PASSCAL deployments (i.e. Deep Probe, CD-ROM, Lodore, Laramie), and more waveforms contribute to the image at a given node.

Given the distributed nature of the phase in the cratonic east, it can be misleading to make comparisons on the basis of depth and strength of a single phase between these two regions. Nonetheless, maps of the mean depth and amplitude of the strongest negative phases autopicked from the bootstrapped Sp CCP stacks (Figure 4) provide a useful synoptic view. Among the

distributed MLD phases within cratonic regions to the east of the Sevier Thrust Belt, the largest phase is typically deeper (>80 km) and lower amplitude than the phases interpreted as the LAB in the west. In the amplitude map (Figure 4b) the translucent white mask indicates areas where fewer than 50 weighted waveforms contribute to the image at a given model node. In these portions of the image, an artificial bias that enhances amplitude exists. Phase depth is more robust than phase amplitude in these zones, although these depths should still be viewed with greater skepticism than those where there is better sampling.

A comparable contrast in discontinuity character between cratonic and non-cratonic regions was also observed in the western U.S. to the south of our study region by Lekić and Fischer [2014] who used methods identical to those of this study. A change in the amplitude and depth of the largest negative phase across the Sevier Thrust Belt was first documented by Levander and Miller [2012], although aspects of their images, phase-picking approach and interpretation differ from ours. Broadly speaking, a deepening of the largest negative phase across the Sevier Thrust Belt also appears in the images of Kumar et al. [2012].

3.1.2. The origin of layering within the cratonic lithosphere

The variable number of mantle discontinuities within the lithosphere of the Wyoming craton indicates layering within the cratonic lithosphere, some of which is dipping or laterally discontinuous. Models for the formation of the cratonic mantle lithosphere include underthrusting and stacking of oceanic lithosphere [e.g. Canil, 2008, 2004; Lee, 2006; Lee et al., 2011; Simon et al., 2007]; thickening of arc lithosphere [Kelemen et al., 1998; Lee, 2006; Lee et al., 2011; Parman et al., 2004]; and a two-stage process involving growth of a “thermal blanket” at the base of an original highly depleted lithospheric layer [Cooper et al., 2004; Yuan and Romanowicz, 2010a]. The formation of cratonic mantle lithosphere as the residue of melting in large plume heads has also been proposed, but would predict compositions for cratonic peridotites consistent with high degrees of melting at large depths. As observed compositions suggest a low pressure

origin [Lee, 2006; Lee et al., 2011], we focus on the first three mechanisms. Of these, the lateral scale of the observed MLDs are most reminiscent of the imbrication of oceanic slab fragments, although this model would be more clearly supported if the MLDs were geometrically linked to sutures within the crust, as is the case with anisotropic Ps discontinuities in the Slave craton [Bostock, 1998; Mercier et al., 2008; Snyder, 2008]. Accretion of depleted mantle from beneath island arcs seems less likely to produce discontinuities that are laterally continuous over hundreds of kilometers as observed in parts of the craton; geodynamic modeling would be required to verify this point. On the other hand, the observed MLDs are more laterally variable than the two craton-wide lithospheric layers implied by the “thermal blanket” model [Cooper et al., 2004], although the relationship of the Sp-derived discontinuities and the vertical layering in azimuthal anisotropy used by Yuan and Romanowicz [2010a] in support of this model remains to be systematically explored.

3.2. Lithosphere to the west of the Sevier Thrust Belt

3.2.1. Columbia River flood basalts, the High Lava Plains and the northwest Basin and Range

Within the western, more recently tectonized portion of the study region, the depth of the LAB as defined by the Sp CCP stack shows pronounced variations at the boundaries of major magmatic provinces. Beneath the High Lava Plains, with its well-defined 0–10 Ma age-progressive silicic magmatic trend, and the adjacent northwest Basin and Range into which the age-progressive magmatism extends to a latitude of $\sim 42.25^\circ$ [Ford et al., 2013], a clear LAB phase lies at depths between 55 and 65 km (Figures 4, 5 and 6). However, a distinct deepening of the phase (10 km or more) occurs moving north across the boundary of the High Lava Plains with the northern lobe of the Columbia River Basalts, where significant magmatism has not occurred since ~ 15 Ma [Hooper et al., 2002]. This deepening is consistent with the ambient noise tomography of Gao and Shen [2014].

Beneath much of the High Lava Plains, a very strong and clear negative Sp phase is observed (Figure 6). The phase depth falls at the top of the low velocity asthenospheric layer seen in tomography models [Obrebski et al., 2011; Wagner et al., 2010], so we interpret it as the LAB. The combination of the Sp phase and the tomography indicate that a thin, high velocity mantle lid is present and possibly thickens slightly in the direction of the older silicic volcanism. The amplitude of the phase diminishes beneath the youngest magmatic ages at the northwest end of the age-progressive trend, including Newberry volcano (Figure 6); phase amplitudes are also typically low beneath the Cascades arc (Figure 4; Figure S7). It is tempting to suggest that in these volcanically active regions magmas and associated heat are abundant enough to significantly reduce velocities within the mantle lid and nearly erase any decrease in velocity at the LAB. However, interference between a potential LAB Sp phase and phases arising across the top of the subducting slab, which lies at depths of 90–100 km in this vicinity, may also be a factor (Figure S7).

In the High Lava Plains, the observed depth of the Sp-defined LAB (ranging from 55–65 km, with uncertainties of ~10 km) is approximately consistent with the depths of last equilibration of asthenospherically derived basaltic melts [Till et al., 2013a] which range from 40–58 km (with uncertainties of 5 km). Moreover, the Sp phase is likely produced by a velocity gradient over a finite depth range, where the nominal depth of the phase defined by its peak amplitude would lie at the depth range mid-point. If the velocity gradient occurred over 20 km, it could span depths as shallow as 45 km, without even considering uncertainties; therefore, the observed Sp phase depths agree with a model in which the basaltic melts are derived from magmas that collected near the base of the lithosphere.

Compared to the Ps migration image of Chen et al. [2013], the Sp CCP stack shows a much stronger and more continuous negative phase in the LAB depth range. A possible explanation for this discrepancy is that the longer wavelengths of the Sp phases allow them to

detect more gradual velocity gradients than the shorter period Ps phases. Alternatively, differences between the Sp and Ps images may reflect their different sensitivities to velocity anisotropy in the mantle, for example the high amplitude, uniform azimuthal anisotropy beneath the High Lava Plain reflected in teleseismic shear-wave splitting [Long et al., 2009]. Future work will investigate these possibilities.

3.2.2. Yellowstone and the Snake River Plain

In contrast to other recently tectonized regions, the most striking feature beneath the youngest Yellowstone calderas is the absence of a significant negative Sp phase. Cross-section F–F' (Figure 7) starts in the Owyhee Plateau, where Sp path density is reasonably good and a robust, perhaps double phase is observed. Continuing through the older Snake River Plain, a negative phase in the potential LAB depth range appears in the CCP stack, but path density is in general low, and the strongest and shallowest segments of this LAB phase (210 km and 340 km along the profile at 60 km depth) correspond to particularly sparse coverage and are not to be trusted (Figures 4 and 7). Between the 4 Ma and 2 Ma silicic magmas (470 to 520 km along profile F–F'), data density is locally high and a robust negative phase appears at depths of 75–100 km; its amplitude is lower than the LAB observed beneath the High Lava Plains and Basin and Range. Beneath the youngest and currently active calderas (550 km to 600 km along profile F–F'), the negative phase disappears completely. This finding differs from the Sp images of Levander and Miller [2012] and Kumar et al. [2012].

A possible interpretation for the lack of an LAB phase beneath Yellowstone is that elevated temperatures and associated partial melts have warmed and infiltrated the lithosphere, obliterating the high velocity lid, as we suggested for the Cascades arc. Tomography models showing very low velocities all the way up to the Moho beneath the Snake River Plain [e.g. Obrebski et al., 2011; Wagner et al., 2010] (Figure 7) support this interpretation, as does rheological modeling that indicates that the lower crust is less viscous beneath Yellowstone than

in surrounding areas, a finding that was attributed to the presence of fluid and/or melt [Chang et al., 2013].

3.2.3. Owyhee Plateau and Grouse Creek Block

The Owyhee Plateau has been interpreted to be Precambrian lithosphere that was further depleted by flood basalt volcanism. It remained relatively undeformed through Miocene extension in the western United States, with volcanism restricted largely to its margins. These observations have been attributed to a core of strong, depleted lithosphere [Shoemaker, 2004]. The crust of the Owyhee Plateau is anomalously thick [Eagar et al., 2011] and has high velocities [Hanson-Hedgecock et al., 2012].

We note subtle differences in the lithosphere on and off of the Owyhee Plateau. The negative Sp phase is observed to broaden and deepen beneath the Owyhee Plateau (Figures 6 and 7) with two distinct phases at 65 km and 80 km depth (Figure 6 in particular). When the negative phase is auto-picked (Figure 4), its depth is locally deeper beneath the center of the Owyhee Plateau, similar to the deeper LAB observed beneath the central portion of the Colorado Plateau [Kumar et al., 2012; Lekić and Fischer, 2014; Levander and Miller, 2012; Levander et al., 2011]. However, the persistence of the deeper negative phase to the southeast beneath the Snake River Plain calls the distinctiveness of the Owyhee Plateau lithosphere into question (Figure 7).

LAB depth also appears to increase to the east across the Sr 0.706 isopleth line into the Phanerozoically re-worked Archean Grouse Creek Block (Figure S3) south of the Snake River Plain (Figure 3c). However, paths are relatively sparse in the Grouse Creek Block to the east of 116°W (Figure 2).

3.3. The base of the low velocity zone

In portions of the study region, a positive Sp phase, indicating a velocity increase with depth, appears within the depth range where velocities increase with depth from their minimum in

the asthenospheric low velocity zone seen in tomography models [e.g. Obrebski et al., 2011; Wagner et al., 2010]. The localized velocity change necessary to create such a phase would require volatile content, melt fraction or grain size to change rapidly with depth. The mantle beneath the High Lava Plains provides one of the clearest examples (distances of 150 km to 500 km in Figure 6): positive Sp arrivals at 110 km to 150 km depth, albeit weaker and more diffuse than the LAB phase, follow the southeastward deepening of the base of the low velocity zone in the Obrebski et al. [2011] tomography. Other examples include the Owyhee Plateau and older Snake River Plain (distances of 0 km to 300 km in Figure 7). These observations suggest that the positive velocity gradient at the base of the asthenospheric low velocity zone is in places more localized in depth than it appears in the tomographic models.

3.4. The origins of the LAB

The distinct differences between shallow mantle discontinuities observed beneath the more recently tectonized portions of the northwestern U.S. and those observed within the Wyoming craton have significant implications for the physical and chemical factors that give rise to the drop in seismic velocity across the seismological LAB.

Beneath much of the Wyoming craton and the westernmost edge of the cratonic mantle beneath the Great Plains, the absence of an Sp phase from the tomographically-defined LAB depth range indicates that the drop in velocity from the cratonic lithosphere to the mantle beneath must occur over ~50 km or more [e.g. Ford et al., 2010; Rychert et al., 2007], so it could be as gradual as this gradient appears in the tomography models (e.g. Figure 7). Velocity gradients over these broad depth ranges can be entirely attributed to the effects of temperature and pressure alone [e.g. Faul and Jackson, 2005; Stixrude and Lithgow-Bertelloni, 2005], although gradual gradients in other properties cannot be ruled out. Where weak, intermittent sub-cratonic LAB Sp phases are observed, they suggest localized sharpening of negative shear velocity gradients over

vertical spatial scales of ~30 km or less, perhaps due to variations in bulk composition, volatile content, grain size or melt.

Turning to the western and tectonically active portion of our study region, the relatively well-known magmatic history of the High Lava Plains, Columbia River Basalts and Snake River Plain make this a particularly interesting area in which to test models for the origins of the LAB. Due to their higher Sp path densities and more robust Sp LAB phases (Figures 2, 5 and 7), we use the transition in LAB depth between the eastern High Lava Plains (LAB at 60–65 km) and the northern lobe of the Columbia River Basalts to their north (LAB at 70–80 km) to test two models. We restrict our analysis to the eastern High Lava Plains because we wish to compare model predictions against observations of equilibration depths and temperatures of anhydrous magmas; nominally anhydrous samples were collected largely from the Diamond and Jordan craters in the eastern High Lava Plains [Till et al., 2013a]. In the first model, we assume that the lithospheric mantle has higher shear velocities because it has been dehydrated and depleted by partial melting relative to a more hydrated and fertile asthenosphere [e.g. Hirth and Kohlstedt, 1996], and that LAB depth variations represent differences in mechanical deformation. In the second model, we assume that the seismological LAB is defined by mantle solidi and represents the top of a melt-rich layer.

The simplest models of mechanical deformation, ones in which a layer of dry, depleted lithosphere has a constant initial thickness and LAB depth variations represent differences in net pure shear extension, do not appear to be consistent with observed LAB depth variations. Extension in the High Lava Plains has been estimated at 17% from paleomagnetic data [Wells and Heller, 1988] and 16% based on crustal thickness estimates [Eagar et al., 2011]. If lithospheric extension beneath the northern Columbia River Basalts was ~0%, and the entire region had an initial lithospheric thickness of 70 km, 16–17% extension beneath the High Lava Plains could explain much of the observed LAB depth offset (e.g. an LAB at 60 km beneath the

High Lava Plains versus an LAB at 70 km beneath the northern Columbia River Basalts). However, this model fails on a broader basis. In regions of the northern Basin Range where extension has been estimated at 50% [McQuarrie and Wernicke, 2005], averaged LAB depths lie no shallower than ~65 km to 70 km [Lekić and Fischer, 2014]. Had 70 km thick lithosphere undergone 50% extension by simple pure shear stretching [e.g. McKenzie, 1978], we would instead expect the lithosphere to be less than 50 km thick.

Models in which the negative LAB velocity gradient is created by an increase in partial melt above the solidus do appear to be plausible. In such a model, partial melt generated at a range of depths in the asthenosphere buoyantly rises to collect in a layer whose upper boundary is defined by the solidus for that melt composition. Although estimates of partial melt volumes generated at any point in the oceanic asthenosphere may be too small to produce a significant reduction in shear velocity [Hirschmann, 2010; Karato, 2012], data from the High Lava Plains indicate 5–13% batch melting is occurring, generating enough partial melt to produce the required shear velocity gradient [Till et al., 2013b]. In addition, given that the pressure dependences of basaltic melt viscosity and density suggest rapid melt migration out of the depth range 90–150 km [Sakamaki et al., 2013], melt should tend to collect in the depth range in which we observe an LAB phase to the west of the Sevier Thrust Belt (50–80 km). Rising above the depth of its solidus, melt will tend to solidify rapidly; melt could also be inhibited from rising to shallower depths by a permeability barrier [Hirschmann, 2010; Till et al., 2010]. Some melt must still be able to make its way to the surface to produce the very young samples observed in the High Lava Plains [Till et al., 2013a], but not in the northern Columbia River Basalt region.

With a solidus-defined model and comparable asthenospheric compositions, the ~10 km shallower depth of the seismological LAB beneath the High Lava Plains indicates higher mantle temperatures, a reasonable inference given the High Lava Plains' active magmatism compared to magmatic quiescence in the northern Columbia River Basalts since 15 Ma, and the relatively low

mantle shear velocities observed beneath the High Lava Plains [e.g. Obrebski et al., 2011 in Figure 5]. In one scenario, the geodynamic model of Kincaid et al. [2013] shows that interactions between subducting lithosphere and a mantle plume can predict the timing of magmatism in the region. In this model, present-day temperatures at the base of the North American plate are up to 100°C higher beneath the High Lava Plains than the northern Columbia River Basalts.

Candidate geotherms for the eastern High Lava Plains and northern Columbia River Basalts illustrate the deeper geotherm-solidus intersection in the latter region. Peridotite solidi with 0–200 ppm water were assumed [Hirschmann et al., 2009], in keeping with the relatively anhydrous young basaltic magmas in the eastern High Lava Plains [Till et al., 2013a]. A present-day High Lava Plains geotherm is required to 1) intersect the temperatures and pressures of last equilibration for the young basalts [Till et al., 2013a] and 2) to cross the peridotite solidi such that melt would begin to solidify at depths overlapping with the negative velocity gradient imaged by the Sp phases (60 km \pm 10 km for the eastern High Lava Plains, assuming a velocity gradient over 20 km centered on the average depth of the phase). A geotherm for 37 km thick continental crust [Eagar et al., 2011] with a mantle potential temperature of 1380°C that has cooled over 1 My meets these criteria (Figure 8). With 15 My of cooling, the geotherm intersects the solidi in a depth range that intersects the Sp LAB velocity gradient for the northern Columbia River Basalts (75 km \pm 10 km). The equilibration ages of the geotherms are chosen to coincide with the timing of major magmatic events that may correspond to high temperature conditions in these areas. Newberry Volcano, the most recent major silicic crater of the High Lava Plains trend, dates to 1 Ma [Till et al., 2013a]; whereas the major outpouring of Columbia River Basalts ended 15 Ma [Hooper et al., 2002]. These simple conductive geotherms are not intended to precisely represent the thermal history of the region, which is almost certainly more complex. However, they do show that a time-dependent solidus-based model for the LAB is capable of explaining the LAB

depth variations observed between the High Lava Plains and the northern Columbia River Basalts.

4. Conclusions

Three-dimensional imaging with CCP stacking of Sp phases reveals strong variations in shallow mantle discontinuity structure across the northwestern United States over different spatial scales and tectonic time scales.

A coherent Sp phase that coincides with the LAB depth range in tomographic models is observed throughout the region to the west of the Sevier Thrust Belt, south of 45°N. In contrast, beneath stable cratonic regions, an Sp phase is typically absent at LAB depths, indicating that the negative LAB velocity gradient is gradual enough (distributed over >50 km) to be consistent with a purely thermal gradient; the presence of weak, intermittent Sp phases in the cratonic LAB depth range suggests localized sharpening of the LAB velocity gradient over vertical spatial scales of ~30 km or less, perhaps due to variations in bulk composition, volatile content, grain size or melt. MLDs exist within the cratonic mantle lithosphere and are often distributed in depth, but in places only a single MLD appears.

A ~10 km deepening of the LAB occurs at the transition between the High Lava Plains (with its <10 Ma magmatism) and the >15 Ma Columbia River Basalts to the north. This variation and observed melt equilibration temperatures and pressures [Till et al., 2013a] are consistent with a model in which a strong negative LAB velocity gradient is created by the presence of partial melt collected below a solidus-defined boundary. Underneath the Yellowstone Caldera, the LAB discontinuity disappears; there high melt volumes and elevated temperatures may have so completely permeated the lithosphere as to obliterate any LAB velocity contrast.

A positive Sp phase observed at depths consistent with the base of the asthenospheric low velocity zone suggests that this velocity gradient may be locally sharp.

Acknowledgements

Waveform data were obtained from the IRIS Data Management Center. Thanks to M. Obrebski for the tomographic models of Obrebski et al. [2010, 2011] and to C. Till for helpful discussion. We also thank P. Shearer, M. Hirschmann and an anonymous reviewer for their comments. This research was supported by the NSF EarthScope Program through award EAR-0844276.

References

- Abt, D.L., Fischer, K.M., French, S.W., Ford, H.A., Yuan, H., Romanowicz, B., 2010. North American lithospheric discontinuity structure imaged by Ps and Sp receiver functions. *J. Geophys. Res.* 115, B09301.
- Armstrong, R.L., Taubeneck, W.H., Hales, P.O., 1977. Rb–Sr and K–Ar geochronometry of Mesozoic granitic rocks and their Sr isotopic composition, Oregon, Washington, and Idaho. *Geol. Soc. Am. Bull.* 88, 397–411.
- Blackwell, D.D., Bowen, R.G., Hull, D.A., Riccio, J., Steele, J.L., 1982. Heat flow, arc volcanism, and subduction in northern Oregon. *J. Geophys. Res.* 87, 8735–8754.
- Bostock, M.G., 1998. Mantle stratigraphy and evolution of the Slave province. *J. Geophys. Res.* 103, 21183–21200.
- Burdick, S., Hilst, R.D., van der Vernon, F.L., Martynov, V., Cox, T., Eakins, J., Karasu, G.H., Tylell, J., Astiz, L., Pavlis, G.L., 2012. Model update March 2011: Upper mantle heterogeneity beneath North America from traveltimes tomography with global and USArray Transportable Array data. *Seismol. Res. Lett.* 83, 23–28.

Camp, V.E., Ross, M.E., 2004. Mantle dynamics and genesis of mafic magmatism in the intermontane Pacific Northwest. *J. Geophys. Res.* 109, B08204.

Camp, V.E., Ross, M.E., Hanson, W.E., 2003. Genesis of flood basalts and Basin and Range volcanic rocks from Steens Mountain to the Malheur River Gorge, Oregon. *Geol. Soc. Am. Bull.* 115, 105–128.

Canil, D., 2004. Mildly incompatible elements in peridotites and the origins of mantle lithosphere. *Lithos* 77, 375–393.

Canil, D., 2008. Canada's craton: A bottoms-up view. *GSA Today* 18 (6), 4.

Chang, W.-L., Smith, R.B., Puskas, C.M., 2013. Effects of lithospheric viscoelastic relaxation on the contemporary deformation following the 1959 Mw 7.3 Hebgen Lake, Montana, earthquake and other areas of the intermountain seismic belt. *Geochem. Geophys. Geosyst.* 14, 1–17.

Chen, C.-W., James, D.E., Fouch, M.J., Wagner, L.S., 2013. Lithospheric structure beneath the High Lava Plains, Oregon, imaged by scattered teleseismic waves. *Geochem. Geophys. Geosyst.* 14, 4835–4848. <http://dx.doi.org/10.1002/ggge.20284>.

Christiansen, R.L., Foulger, G.R., Evans, J.R., 2002. Upper-mantle origin of the Yellowstone hotspot. *Geol. Soc. Am. Bull.* 114, 1245–1256.

Coney, P.J., Jones, D.L., Monger, J.W.H., 1980. Cordilleran suspect terranes. *Nature* 288, 329–333.

Cooper, C.M., Lenardic, A., Moresi, L., 2004. The thermal structure of stable continental lithosphere within a dynamic mantle. *Earth Planet. Sci. Lett.* 222, 807–817.

Darold, A., Humphreys, E., 2013. Upper mantle seismic structure beneath the Pacific Northwest: A plume-triggered delamination origin for the Columbia River flood basalt eruptions. *Earth Planet. Sci. Lett.* 365, 232–242.

DeCelles, P.G., Coogan, J.C., 2006. Regional structure and kinematic history of the Sevier fold-and-thrust belt, central Utah. *Geol. Soc. Am. Bull.* 118, 841–864.

Dickinson, W.R., 2004. Evolution of the North American Cordillera. *Annu. Rev. Earth Planet. Sci.* 32, 13–45.

Druken, K.A., Long, M.D., Kincaid, C., 2011. Patterns in seismic anisotropy driven by rollback subduction beneath the High Lava Plains. *Geophys. Res. Lett.* 38, L13310.

Eagar, K.C., Fouch, M.J., James, D.E., Carlson, R.W., 2011. Crustal structure beneath the High Lava Plains of eastern Oregon and surrounding regions from receiver function analysis. *J. Geophys. Res.* 116, 141–153.

Faccenna, C., Becker, T.W., Lallemand, S., Lagabrielle, Y., Funicello, F., Piromallo, C., 2010. Subduction-triggered magmatic pulses: A new class of plumes?. *Earth Planet. Sci. Lett.* 299, 54–68.

Faul, U.H., Jackson, I., 2005. The seismological signature of temperature and grain size variations in the upper mantle. *Earth Planet. Sci. Lett.* 234, 119–134.

Fenneman, N.M., Johnson, D.W., 1946. Physical divisions of the United States: US geological survey map prepared in cooperation with the physiographic commission. *U.S. Geol. Surv.*, scale 1:7,000,000.

Ford, H.A., Fischer, K.M., Abt, D.L., Rychert, C.A., Elkins-Tanton, L.T., 2010. The lithosphere–asthenosphere boundary and cratonic lithospheric layering beneath Australia from Sp wave imaging. *Earth Planet. Sci. Lett.* 300, 299–310.

Ford, M.T., Grunder, A.L., Duncan, R.A., 2013. Bimodal volcanism of the High Lava Plains and northwestern Basin and Range of Oregon: The distribution and tectonic implications of age-progressive rhyolites. *Geochem. Geophys. Geosyst.* 14, 2836–2857. <http://dx.doi.org/10.1002/ggge.20175>.

Foster, D.A., Mueller, P.A., Mogk, D.W., Wooden, J.L., Vogl, J.J., 2006. Proterozoic evolution of the western margin of the Wyoming craton: implications for the tectonic and magmatic evolution of the northern Rocky Mountains. *Can. J. Earth Sci.* 43, 1601–1619.

Fouch, M.J., 2012. The Yellowstone hotspot: Plume or not?. *Geology* 40, 479–480.

Gao, H., Shen, Y., 2014. Upper mantle structure of the Cascades from full-wave ambient noise tomography: Evidence for 3D mantle upwelling in the back arc. *Earth Planet. Sci. Lett.* 390, 222–233.

Gaschnig, R.M., Vervoort, J.D., Lewis, R.S., Tikoff, B., 2011. Isotopic evolution of the Idaho batholith and Challis intrusive province, Northern US Cordillera. *J. Petrol.* 52, 2397–2429.

Hansen, S.M., Dueker, K.G., Stachnik, J.C., Aster, R.C., Karlstrom, K.E., 2013. A rootless Rockies – Support and lithospheric structure of the Colorado Rocky mountains inferred from CREST and TA seismic data. *Geochem. Geophys. Geosyst.* 14, 2670–2697. <http://dx.doi.org/10.1002/ggge.20143>.

Hanson-Hedgecock, S., Wagner, L.S., Fouch, M.J., James, D.E., 2012. Constraints on the causes of mid-Miocene volcanism in the Pacific Northwest US from ambient noise tomography. *Geophys. Res. Lett.* 39.

Helfrich, G., 2006. Extended-time multitaper frequency domain cross-correlation receiver-function estimation. *Bull. Seismol. Soc. Am.* 96, 344–347.

Hirschmann, M.M., 2000. Mantle solidus: Experimental constraints and the effects of peridotite composition. *Geochem. Geophys. Geosyst.* 1, 1042.

Hirschmann, M.M., 2010. Partial melt in the oceanic low velocity zone. *Phys. Earth Planet. Inter.* 179 (1), 60–71.

Hirschmann, M.M., Tenner, T., Aubaud, C., Withers, A.C., 2009. Dehydration melting of nominally anhydrous mantle: The primacy of partitioning. *Phys. Earth Planet. Inter.* 176, 54–68.

Hirth, G., Kohlstedt, D.L., 1996. Water in the oceanic upper mantle: implications for rheology, melt extraction and the evolution of the lithosphere. *Earth Planet. Sci. Lett.* 144, 93–108.

Hofmeister, A.M., 1999. Mantle values of thermal conductivity and the geotherm from phonon lifetimes. *Science* 283 (5408), 1699–1706.

Hooper, P.R., Binger, G.B., Lees, K.R., 2002. Ages of the Steens and Columbia River flood basalts and their relationship to extension-related calc-alkalic volcanism in eastern Oregon. *Geol. Soc. Am. Bull.* 114, 43–50.

James, D.E., Fouch, M.J., Carlson, R.W., Roth, J.B., 2011. Slab fragmentation, edge flow and the origin of the Yellowstone hotspot track. *Earth Planet. Sci. Lett.* 311, 124–135.

Jordan, B.T., Grunder, A.L., Duncan, R.A., Deino, A.L., 2004. Geochronology of age-progressive volcanism of the Oregon High Lava Plains: Implications for the plume interpretation of Yellowstone. *J. Geophys. Res.* 109, B10202.

Karato, S., 2012. On the origin of the asthenosphere. *Earth Planet. Sci. Lett.* 321–322, 95–103.

Kelemen, P.B., Hart, S.R., Bernstein, S., 1998. Silica enrichment in the continental upper mantle via melt/rock reaction. *Earth Planet. Sci. Lett.* 164, 387–406.

Kennett, B.L.N., 1991. The removal of free surface interactions from three-component seismograms. *Geophys. J. Int.* 104, 153–163.

Kincaid, C., Druken, K.A., Griffiths, R.W., Stegman, D.R., 2013. Bifurcation of the Yellowstone plume driven by subduction-induced mantle flow. *Nat. Geosci.* 6, 395–399.

Kumar, P., Kind, R., Yuan, X., Mechie, J., 2012. USArray receiver function images of the lithosphere–asthenosphere boundary. *Seismol. Res. Lett.* 83, 486–491.

Lee, C.-T.A., 2006. Geochemical/petrologic constraints on the origin of cratonic mantle. In: Benn, K., Mareschal, J.-C., Condie, K.C. (Eds.), *Archean Geodynamics and Environments*. In: *Geophys. Monogr.*, vol. 164. AGU, Washington, DC, pp. 89–114.

Lee, C.-T.A., Luffi, P., Chin, E.J., 2011. Building and destroying continental mantle. *Annu. Rev. Earth Planet. Sci.* 39, 59–90.

Lekić, V., Fischer, K., 2014. Contrasting lithospheric signatures across the western United States revealed by *Sp* receiver functions. *Earth Planet. Sci. Lett.* 402, 90–98. <http://dx.doi.org/10.1016/j.epsl.2013.11.026>.

Lekić, V., French, S.W., Fischer, K.M., 2011. Lithospheric thinning beneath rifted regions of Southern California. *Science* 334, 783–787.

Levander, A., Miller, M.S., 2012. Evolutionary aspects of lithosphere discontinuity structure in the western U.S. *Geochem. Geophys. Geosyst.* 13, Q0AK07.

Levander, A., Schmandt, B., Miller, M.S., Liu, K., Karlstrom, K.E., Crow, R.S., Lee, C.-T.A., Humphreys, E.D., 2011. Continuing Colorado plateau uplift by delamination-style convective lithospheric downwelling. *Nature* 472, 461–465.

Li, X., Yuan, X., Kind, R., 2007. The lithosphere–asthenosphere boundary beneath the western United States. *Geophys. J. Int.* 170, 700–710.

Lin, F.-C., Ritzwoller, M.H., Yang, Y., Moschetti, M.P., Fouch, M.J., 2011. Complex and variable crustal and uppermost mantle seismic anisotropy in the western United States. *Nat. Geosci.* 4, 55–61.

Liu, L., Stegman, D.R., 2012. Origin of Columbia River flood basalt controlled by propagating rupture of the Farallon slab. *Nature* 482, 386–389.

Long, M.D., Gao, H., Klaus, A., Wagner, L.S., Fouch, M.J., James, D.E., Humphreys, E., 2009. Shear wave splitting and the pattern of mantle flow beneath eastern Oregon. *Earth Planet. Sci. Lett.* 288, 359–369.

Long, M.D., Till, C.B., Druken, K.A., Carlson, R.W., Wagner, L.S., Fouch, M.J., James, D.E., Grove, T.L., Schmerr, N., Kincaid, C., 2012. Mantle dynamics beneath the Pacific Northwest and the generation of voluminous back-arc volcanism. *Geochem. Geophys. Geosyst.* 13, Q0AN01.

Lowry, A.R., Pérez-Gussinyé, M., 2011. The role of crustal quartz in controlling Cordilleran deformation. *Nature* 471, 353–357.

McCrory, P.A., Blair, J.L., Oppenheimer, D.H., Walter, S.R., 2006. Depth to the Juan de Fuca slab beneath the Cascadia subduction margin: A 3D model for sorting earthquakes. U.S. Geol. Surv. Digit. Data Ser. 91. Version 1.2.

McKenzie, D., 1978. Some remarks on the development of sedimentary basins. *Earth Planet. Sci. Lett.* 40 (1), 25–32.

McQuarrie, N., Wernicke, B.P., 2005. An animated tectonic reconstruction of southwestern North America since 36 Ma. *Geosphere* 1, 147–172.

Mercier, J.-P., Bostock, M.G., Audet, P., Gaherty, J.B., Garnero, E.J., Revenaugh, J., 2008. The teleseismic signature of fossil subduction: Northwestern Canada. *J. Geophys. Res.* 113, B04308.

Obrebski, M., Allen, R.M., Xue, M., Hung, S.-H., 2010. Slab-plume interaction beneath the Pacific Northwest. *Geophys. Res. Lett.* 37, L14305.

Obrebski, M., Allen, R.M., Pollitz, F., Hung, S.-H., 2011. Lithosphere–asthenosphere interaction beneath the western United States from the joint inversion of body-wave traveltimes and surface-wave phase velocities. *Geophys. J. Int.* 185, 1003–1021.

Parman, S.W., Grove, T.L., Dann, J.C., de Wit, M.J., 2004. A subduction origin for komatiites and cratonic lithospheric mantle. *S. Afr. J. Geol.* 107, 107–118.

Pierce, K.L., Morgan, L.A., 1992. The track of the Yellowstone hotspot: Volcanism, faulting, and uplift. In: Link, P.K., Kuntz, M.A., Platt, L.B. (Eds.), *Regional Geology of Eastern Idaho and Western Wyoming*. In: *GSA Mem.*, vol. 179, pp. 1–53.

Pierce, K.L., Morgan, L.A., 2009. Is the track of the Yellowstone hotspot driven by a deep mantle plume? – Review of volcanism, faulting, and uplift in light of new data. *J. Volcanol. Geotherm. Res.* 188, 1–25.

Rudnick, R.L., Fountain, D.M., 1995. Nature and composition of the continental crust: a lower crustal perspective. *Rev. Geophys.* 33, 267–309.

Rychert, C.A., Rondenay, S., Fischer, K.M., 2007. P-to-S and S-to-P imaging of a sharp lithosphere–asthenosphere boundary beneath eastern North America. *J. Geophys. Res.* 112, B08314.

Sakamaki, T., Suzuki, A., Ohtani, E., Terasaki, H., Urakawa, S., Katayama, Y., Funakoshi, K.-I., Wang, Y., Hernlund, J., Ballmer, M.D., 2013. Ponded melt at the boundary between the lithosphere and asthenosphere. *Nat. Geosci.* 6, 1041–1044.

Saleeby, J., 2003. Segmentation of the Laramide Slab—evidence from the southern Sierra Nevada region. *Geol. Soc. Am. Bull.* 115, 655–668.

Schmandt, B., Humphreys, E., 2010. Complex subduction and small-scale convection revealed by body-wave tomography of the western United States upper mantle. *Earth Planet. Sci. Lett.* 297, 435–445.

Schmandt, B., Dueker, K., Humphreys, E., Hansen, S., 2012. Hot mantle upwelling across the 660 beneath Yellowstone. *Earth Planet. Sci. Lett.* 331–332, 224–236.

Sheehan, A.F., Shearer, P.M., Gilbert, H.J., Dueker, K.G., 2000. Seismic migration processing of P-SV converted phases for mantle discontinuity structure beneath the Snake River Plain, western United States. *J. Geophys. Res.* 105, 19055–19065.

Shen, W., Ritzwoller, M.H., Schulte-Pelkum, V., 2013. A 3-D model of the crust and uppermost mantle beneath the Central and Western US by joint inversion of receiver functions and surface wave dispersion. *J. Geophys. Res.* 118, 262–276.

Shervais, J.W., Hanan, B.B., 2008. Lithospheric topography, tilted plumes, and the track of the Snake River–Yellowstone hot spot. *Tectonics* 27, 51–54.

Shoemaker, K.A., 2004. The tectonomagmatic evolution of the Late Cenozoic Owyhee Plateau, northwestern United States. Dissertation thesis. Miami Univ., Oxford, Ohio, 288 pp.

Sigloch, K., 2011. Mantle provinces under North America from multifrequency P wave tomography. *Geochem. Geophys. Geosyst.* 12.

Simon, N.S.C., Carlson, R.W., Pearson, D.G., Davies, G.R., 2007. The origin and evolution of the Kaapvaal cratonic lithospheric mantle. *J. Petrol.* 48, 589–625.

Smith, R.B., Jordan, M., Steinberger, B., Puskas, C.M., Farrell, J., Waite, G.P., Husen, S., Chang, W.-L., O'Connell, R., 2009. Geodynamics of the Yellowstone hotspot and mantle plume: Seismic and GPS imaging, kinematics, and mantle flow. *J. Volcanol. Geotherm. Res.* 188, 26–56.

Snyder, D.B., 2008. Stacked uppermost mantle layers within the Slave craton of NW Canada as defined by anisotropic seismic discontinuities. *Tectonics* 27, TC4006.

Stixrude, L., Lithgow-Bertelloni, C., 2005. Mineralogy and elasticity of the oceanic upper mantle: Origin of the low-velocity zone. *J. Geophys. Res.* 110, 610–632.

Tikoff, B., Maxson, J., 2001. Lithospheric buckling of the Laramide foreland during Late Cretaceous and Paleogene, western United States. *Rocky Mt. Geol.* 36, 13–35.

Till, C.B., Elkins-Tanton, L.T., Fischer, K.M., 2010. A mechanism for low-extent melts at the lithosphere–asthenosphere boundary. *Geochem. Geophys. Geosyst.* 11, Q10015. <http://dx.doi.org/10.1029/2010GC003234>.

Till, C.B., Grove, T.L., Carlson, R.W., Donnelly-Nolan, J.M., Fouch, M.J., Wagner, L.S., Hart, W.K., 2013a. Depths and temperatures of <10.5 Ma mantle melting and the lithosphere–asthenosphere boundary below southern Oregon and northern California. *Geochem. Geophys. Geosyst.* 14 (4), 864–879.

Till, C.B., Grove, T., Donnelly-Nolan, J., Carlson, R., 2013b. Depths and temperatures of mantle melt extraction in the Southern Cascadia subduction zone. Abstract S11C-07 Presented at 2013 Fall Meeting, AGU, San Francisco, Calif., 9–13 Dec.

Wagner, L., Forsyth, D.W., Fouch, M.J., James, D.E., 2010. Detailed three-dimensional shear wave velocity structure of the northwestern United States from Rayleigh wave tomography. *Earth Planet. Sci. Lett.* 299, 273–284.

Wells, R.E., Heller, P.L., 1988. The relative contribution of accretion, shear, and extension to Cenozoic tectonic rotation in the Pacific Northwest. *Geol. Soc. Am. Bull.* 100, 325–338.

Wilson, D.C., Angus, D.A., Ni, J.F., Grand, S.P., 2006. Constraints on the interpretation of S-to-P receiver functions. *Geophys. J. Int.* 165, 969–980.

Yuan, H., Romanowicz, B., 2010a. Lithospheric layering in the North American craton. *Nature* 466, 1063–1068.

Yuan, H., Romanowicz, B., 2010b. Depth dependent azimuthal anisotropy in the western US upper mantle. *Earth Planet. Sci. Lett.* 300, 385–394.

Yuan, H., Romanowicz, B., Fischer, K.M., Abt, D., 2011. 3-D shear wave radially and azimuthally anisotropic velocity model of the North American upper mantle. *Geophys. J. Int.* 184, 1237–1260.

Figures

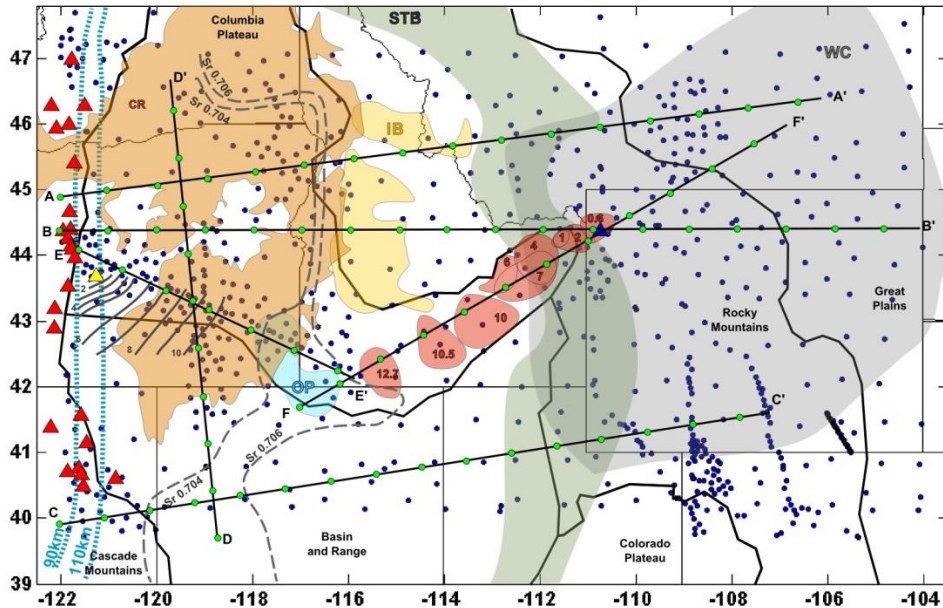


Figure 1: Map of the study area. Thick black lines with green circles: cross-section locations. Dark blue circles: broadband stations that contributed data to this study. Red triangles: arc volcanoes. Yellow triangle: Newberry Volcano. Blue triangle: Yellowstone Caldera. Red shaded areas: rhyolitic calderas in the eastern Snake River Plain, with age in Ma, after Smith et al. [2009]. Grey shaded area (WC): Wyoming Craton, after Foster et al. [2006]. Green shaded area (STB): Sevier fold and thrust belt, after DeCelles and Coogan [2006]. Orange shaded area (CR): Columbia River flood basalts and Steens basalts, after Camp and Ross [2004]. Yellow shaded area (IB): Idaho Batholith, after Gaschnig et al. [2011]. Blue shaded area (OP): Owyhee Plateau, after Shoemaker [2004]. Dashed grey lines (Sr 0.704 and Sr 0.706): Sr lines, after Eagar et al. [2011]. Solid grey lines: isochrons showing age progression of the High Lava Plains silicic volcanism, labeled with earliest age in Ma, after Eagar et al. [2011]. Hatched light blue lines: contours of depth to top of Juan de Fuca slab, labeled with depth, after McCrory et al. [2006]. Thick black lines: boundaries between tectonic provinces, labeled in black, from Fenneman and Johnson [1946].

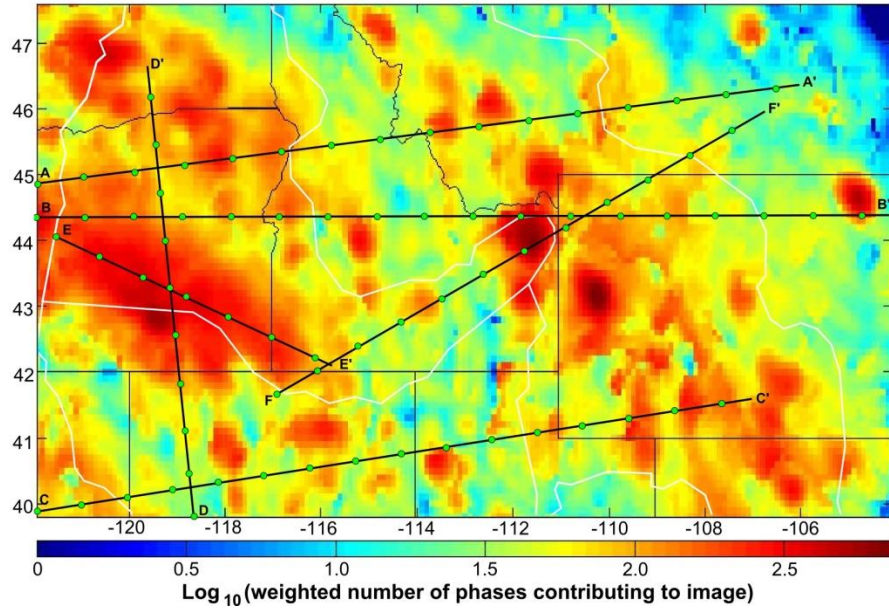


Figure 2: Spatial distribution of Sp phases. Logarithmically scaled plot of the number of phases contributing to the Sp CCP stack at a given point, taking into account the weighting factor applied to each phase by the spline function representation of its Fresnel zone [Lekić et al., 2011]. Values are taken from the depth at which the strongest negative phase was automatically picked. Where no phase was picked, the value is taken from the mean depth of all phases picked over the entire study area.

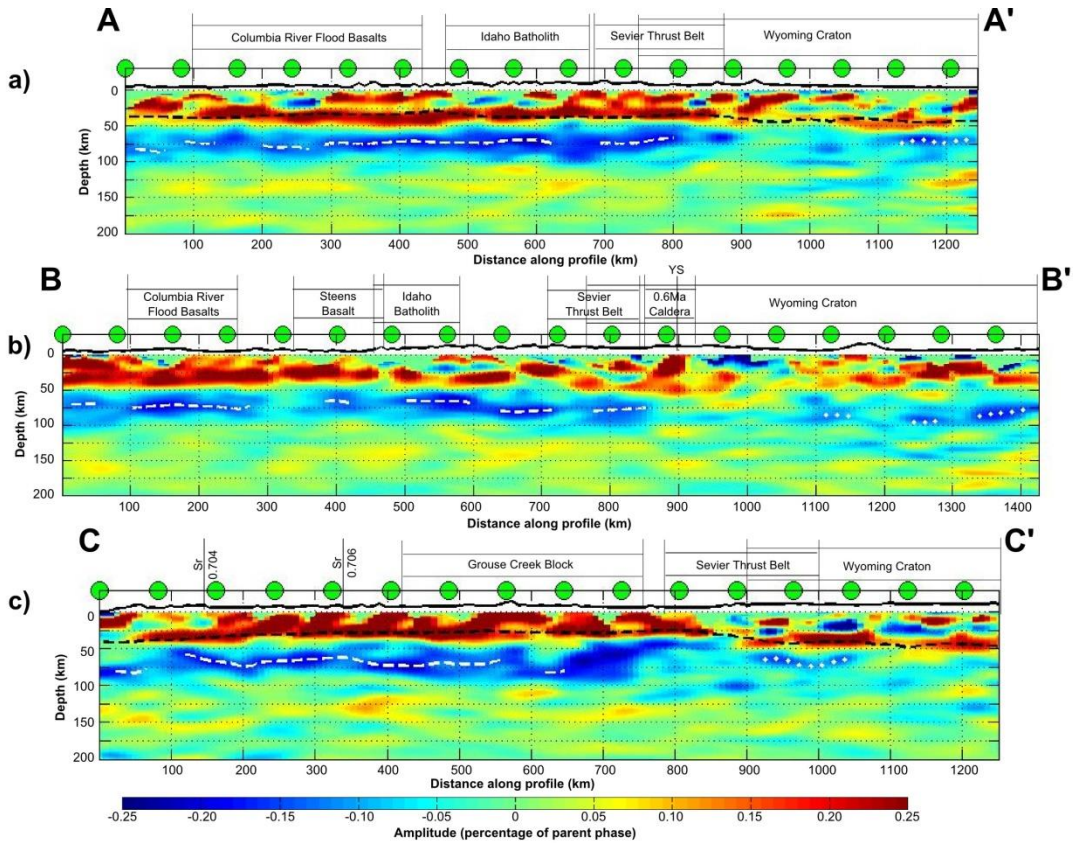


Figure 3: Cross-sections through mean of bootstrapped Sp CCP stack. Cross-section locations shown in Figure 1 with corresponding green circles. Where fewer than 35 unweighted paths contribute to a model point, zero amplitude is plotted. a) Cross-section A–A' runs from 44.9°N, 122°W to 46.4°N, 106.1°W. b) Cross-section B–B' runs from 44.4°N, 122°W to 44.4°N, 104°W. c) Cross-section C–C' runs from 39.9°N, 120.7°W to 41.6°N, 107.3°W. In all plots, CCP stack is from data filtered at 4–33 s, with a dominant period of 9 s. Thick black line: topography, at $5 \times$ vertical exaggeration. Dashed black line: Moho [Lowry and Pérez-Gussinyé, 2011]. Dashed white line: auto-picked negative phase, interpreted as LAB. Dotted white line: auto-picked negative phase, interpreted as MLD. Labels above sections give approximate locations of surface features.

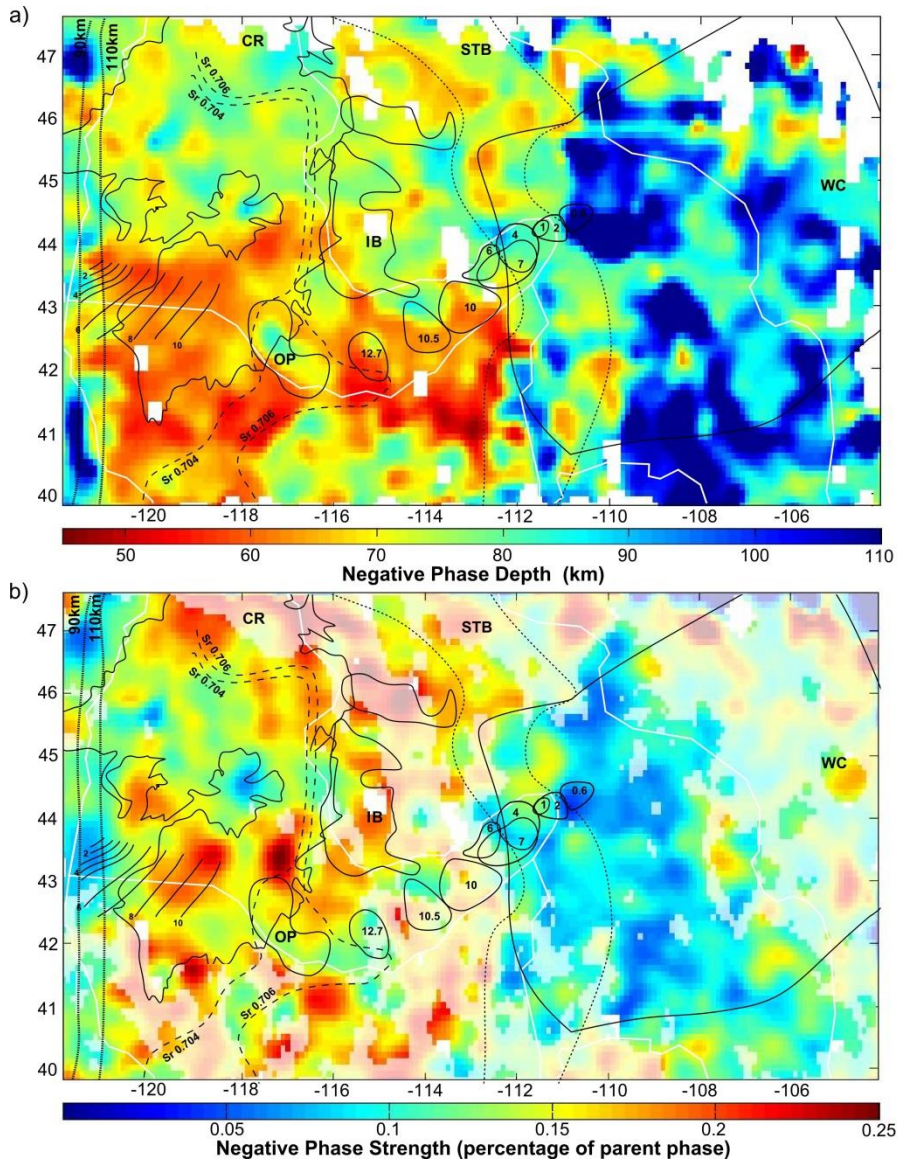


Figure 4: Mean depth and amplitude of largest negative Sp phase in the 50 bootstrapped stacks, as picked by automated picker. While maps appear to be showing variation in a single interface, the interpretation of the negative phase changes across the region. No value is given (i.e. pixel is white) where the phase was too weak to be picked. White lines: boundaries between tectonic provinces, as in Figure 1. Black lines: smaller scale tectonic features, labeled as in Figure 1. a) Depth map. b) Amplitude map. Translucent white mask indicates areas where fewer than 50 weighted waveforms contribute to the image at a given model node.

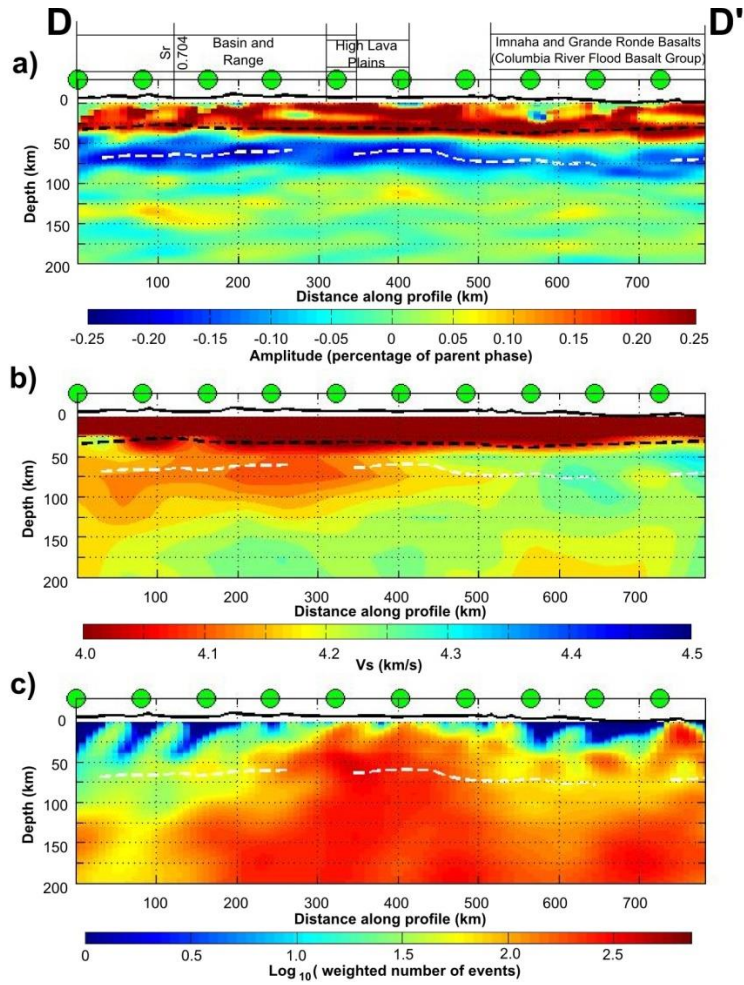


Figure 5: a) Cross-section D–D’ through mean of bootstrapped Sp CCP stack (4–33 s). b) Corresponding cross-section through the tomography model of Obrebski et al. [2011]. c) Cross-section of the weighted number of phases contributing to the image. Cross-section runs from 39.7°N, 118.7°W to 46.7°N, 119.7°W. Thick black line: topography, at 5 × vertical exaggeration. Dashed black line: Moho [Lowry and Pérez-Gussinyé, 2011]. Dashed white line: auto-picked negative phase, interpreted as LAB.

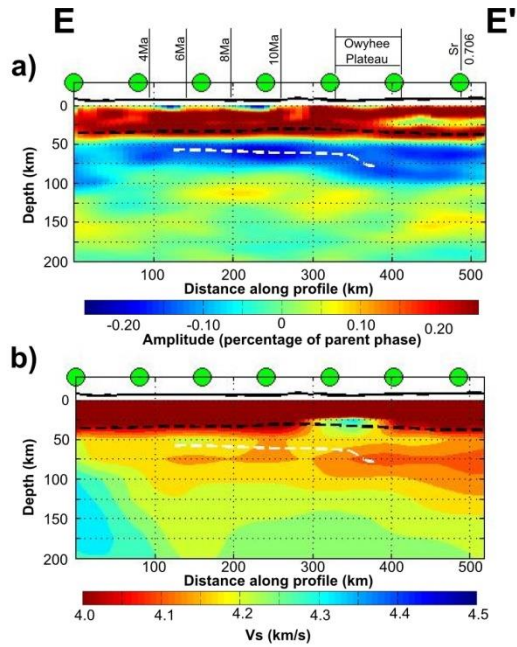


Figure 6: a) Cross-section E–E’ through mean of bootstrapped Sp CCP stack (4–33 s). b) Corresponding cross-section through the tomography model of Obrebski et al. [2011]. Cross-section runs from 44.11°N, 121.589°W to 42.142°N, 115.808°W. Thick black line: topography, at $5 \times$ vertical exaggeration. Dashed black line: Moho [Lowry and Pérez-Gussinyé, 2011]. Dashed white line: auto-picked negative phase, interpreted as LAB.

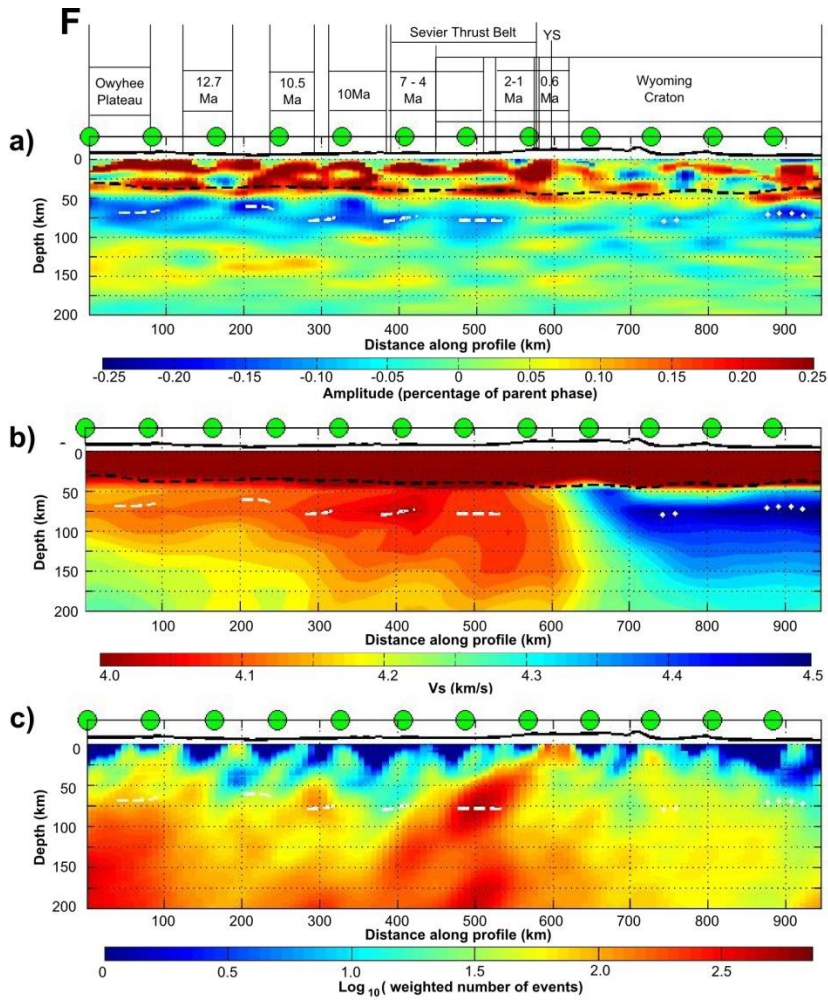


Figure 7: a) Cross-section F–F’ through mean of bootstrapped Sp CCP stack (4–33 s). b) Corresponding cross-section through the tomography model of Obrebski et al. [2011]. c) Cross-section of the weighted number of phases contributing to the image. Cross-section runs from 41.7°N, 117.0°W to 46.0°N, 106.8°W (F–F’ in Figure 1). Thick black line: topography, at 5 × vertical exaggeration. Dashed black line: Moho [Lowry and Pérez-Gussinyé, 2011]. Dashed white line: auto-picked negative phase, interpreted as LAB. Dotted white line: auto-picked negative phase, interpreted as MLD.

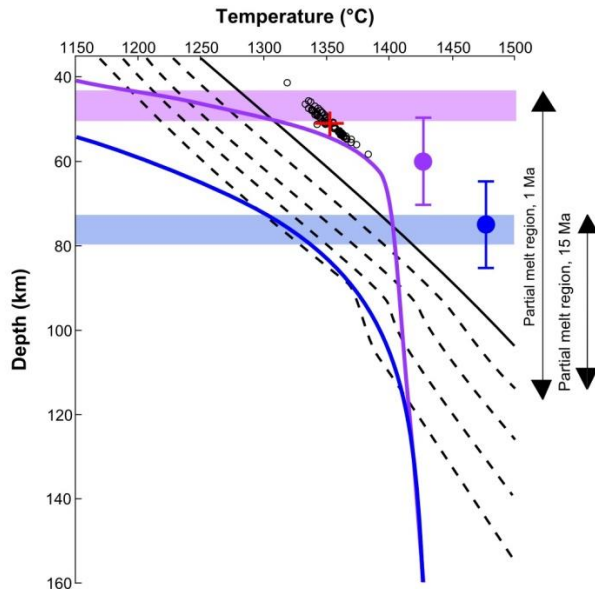


Figure 8: Shallowing of the top of a melt-rich layer with younger, hotter geotherm. Black solid line: dry peridotite solidus; dashed black lines: damp peridotite solidi, with water content increasing in 50 ppm increments from 50 to 200 ppm [Hirschmann et al., 2009; Hirschmann, 2000]. Purple solid line: candidate High Lava Plains geotherm for a mantle potential temperature of 1380°C that has cooled for 1 My. Blue solid line: candidate northern Columbia River Basalts geotherm for the same conditions except with cooling over 15 My. Crustal thickness is 37 km [Eagar et al., 2011]; crustal heat production is $0.93 \mu\text{W m}^{-3}$ (typical for continental crust; Rudnick and Fountain, 1995); initial surface heat flow is 95 mW m^{-2} (the upper end of values currently observed in High Lava Plains [Blackwell et al., 1982]); heat flow at infinite time is 40 mW m^{-2} ; thermal conductivity is $2.7 \text{ W m}^{-1} \text{ }^\circ\text{C}^{-1}$ (typical for oceanic lithosphere [Hofmeister, 1999]). Purple and blue shaded regions show the top of the region where partial melt is stable for the 1 My and 15 My geotherms, respectively. Arrows adjacent to figure show the entire extent of the partial melt region. Purple and blue circles show representative LAB velocity gradient depths observed in this study for the High Lava Plains and the northern Columbia River Basalts, respectively, assuming LAB velocity gradients are distributed over 20 km. Black circles: basalt magma equilibration temperatures in the eastern High Lava Plains [Till et al., 2013a]; red bars show the mean and standard deviation of these samples ($1353^\circ\text{C} \pm 11^\circ\text{C}$ and $51 \text{ km} \pm 3 \text{ km}$).

Supplementary Materials

Description of 1) the effects of different bandpass filters on the Sp CCP stacks and 2) bootstrap tests to assess uncertainties in the Sp CCP stacks.

Effects of different bandpass filters

In addition to the 4-33 s bandpass filters used in the images shown in the paper, we also applied 2-33 s and 6-33 s filters to our data, re-calculated the CCP stacks, and re-picked LAB depths. LAB phase depths from the 4-33 s filtered stack are not resolvably different from the 2-33 s filtered stack, but larger depth offsets exist for the 6-33 s filter. Based on modeling with synthetic Sp seismograms, the larger differences with the 6-33 s filter are created by interference between the Sp phase from the Moho with Sp phases from the shallow mantle that increases with the dominant period in the data.

Bootstrap Testing

To validate the statistical significance of our Sp CCP stacks, we performed bootstrap testing. The stacks were recalculated 50 times using a pseudorandom selection of the available waveforms with a uniform distribution. The same total number of waveforms went into each stack, but some waveforms would be repeated and some omitted. The images shown in the main text of the paper are based on the mean of these 50 stacks (hereafter called the mean stack). In the mean stack, the amplitude of the negative phases that we interpret are significantly greater than the standard deviation of the stack at the corresponding position. Hence, we are confident that the phases we interpret are robustly required by the Sp waveforms.

In Figure S1, we show the standard deviation of the mean of the depths of the largest negative mantle phase picked from each of the 50 stacks, and the standard deviation of the amplitude of the stack at the depth of the largest negative phase. In the western half of our study region where we interpret these values, phase depth uncertainties are less than 5 km for 70% of

the area, with 95% of the area having uncertainties less than 11 km. In addition, many of these data points with large uncertainties are associated with the subduction zone on the western margin. In the east of our study region, 70% of the area has an uncertainty less than 11 km; 95% has an uncertainty less than 22 km (Figure S1).

We also compared the mean stack to the single stack based on all of the data (hereafter called the single stack), both in terms of the depth and amplitude of the largest Sp negative phase (Figure S2) and the overall similarity of the images on selected profiles (Figures S4-S7). In addition, the profiles illustrate that the amplitudes of the interpreted negative phases are large relative to their standard deviations.

Overall, the depth and amplitude of the largest negative Sp phase are similar between the mean stack and the single stack. The mean difference in depth is 5.5 km for the entire study region. In the eastern half of our study region, the difference in depth is typically less than 5 km except in localized areas; in the western half, the difference in depth is less than 5 km over ~60% of the area, but larger elsewhere (Figure S2). The mean difference in the amplitude of the phase throughout the study area is less than 10% of the amplitude of the phase in portions of the study region such as the High Lava Plains.

When compared on individual profiles, the mean and single stacks in general are very similar (Figures S4-S7). The profile comparisons also illustrate that the larger differences between the Sp phase depths from the single and mean stacks in the cratonic eastern half of the study area (Figure S2) is due to the distributed nature of the phase in this area. As can be seen in Figure S4 east of 108°W, the overall character, amplitude, and approximate depths of the Sp phases are broadly similar between mean and single stacks, providing the same picture of layering within the cratonic lithosphere. However, slight changes in the relative strength of the distributed phases are sufficient to change the depth of the automatically picked phase

significantly. In the amplitude difference map (Figure S2), the largest variation between mean and single stacks where there is sufficient data coverage to be confident of the amplitude values occurs beneath the High Lava Plains. However, Figure S5 crosses through this region and clearly shows that, while the amplitude is slightly higher in the cross section through the mean of the bootstrapped data, the phase does appear to be very similar overall.

Comparison of additional profiles through the mean and single stacks provides a more complete view of their differences and similarities. In particular, the features interpreted in the main text appear clearly in both the mean stack and single stack. For example, the depth variation between the High Lava Plains (south of 43.5° N on Fig S5) and the Columbia River Basalts (north of 43.5° N on Figure S5) is very similar. The abrupt decrease in phase amplitude beneath Yellowstone seen in the single stack (Figure S4a) is also clear in the mean stack (Figure S4b). Beneath the less modified Wyoming craton (east of 109° W, Figure S4) where the phase is distributed, more variation between the mean and single stacks exists. However, even here, the depth and extent of the distributed phases are approximately equivalent.

The results of the bootstrapping also gave us more confidence in detailed features of the stacks. A pronounced gap in the LAB phase is observed beneath the Columbia River Basalts in the vicinity of 44.5° N, 118° W (see Figure S6). This gap is quasi-circular in map-view, with an approximate diameter of 50 km. It has been suggested that the uplift history of the Wallowa Mountains, 100-200 km to the northeast of the observed gap, can be explained by detachment of a dense root [Hales et al., 2005]. While the two observations are not precisely co-located, we find the proximity noteworthy.

The phases observed beneath the arc are also consistent between the mean and single stacks. Moving westward in the study region towards the arc, the clear negative Sp phase associated with the LAB in the western portion of the study area becomes more intermittent,

although the phase apparently remains strong between 44° N and 46.5° N. This weakening is particularly prominent beneath Newberry Volcano and the youngest High Lava Plains, (Figure S7, Figure 5). It is possible that this weakening is due to the elevated temperatures and partial melt fractions associated with the volcanism in this area. As postulated for the Yellowstone Caldera (Figure 7), heat and melt could reduce seismic velocities within the lithosphere, leading to a lesser contrast across the lithosphere-asthenosphere boundary. Another possibility is that the low amplitudes are caused by interference with a phase originating in the subducting slab. One additional complication in the interpretation of the phase beneath the arc is the observation in tomographic studies of a slab gap beneath Oregon. While teleseismic studies only observe this gap at greater depths [e.g. Schmandt and Humphreys, 2010], ambient noise tomography can resolve the weakening of the high velocity slab signature up to depths as shallow as 94 km [Gao and Shen, 2013]. The slab gap at these depths is observed between approximately 42.7°N and 45.2°N. In comparison to our observations, this overlaps in latitude with both the zone where the phase is weakest, beneath the youngest High Lava Plains, and where the amplitudes remain strong between 44° N and 46.5° N

Supplementary References

DeCelles, P.G., Coogan, J.C., 2006. Regional structure and kinematic history of the Sevier fold-and-thrust belt, central Utah. *Geol. Soc. Am. Bull.* 118, 841–864.

Foster, D.A., Mueller, P.A., Mogk, D.W., Wooden, J.L., Vogl, J.J., 2006. Proterozoic evolution of the western margin of the Wyoming craton: implications for the tectonic and magmatic evolution of the northern Rocky Mountains. *Can. J. Earth Sci.* 43, 1601–1619.

Gao, H., Shen, Y., 2013. Crust and upper mantle structure of the Cascades with full-wave ambient noise tomography: Seismic evidence for 3D decompressional melting in the back-arc. *Earth. Planet. Sci. Lett.*, submitted.

Hales, T. C., Abt, D. L., Humphreys, E. D., Roering, J. J. 2005. A lithospheric instability origin for Columbia River flood basalts and Wallowa Mountains uplift in northeast Oregon. *Nature* 438, 842-845.

Lowry, A.R., Pérez-Gussinyé, M., 2011. The role of crustal quartz in controlling Cordilleran deformation. *Nature* 471, 353–357.

Schmandt, B., Humphreys, E., 2010. Complex subduction and small-scale convection revealed by body-wave tomography of the western United States upper mantle. *Earth Planet. Sci. Lett.* 297, 435–445.

Supplementary Figures

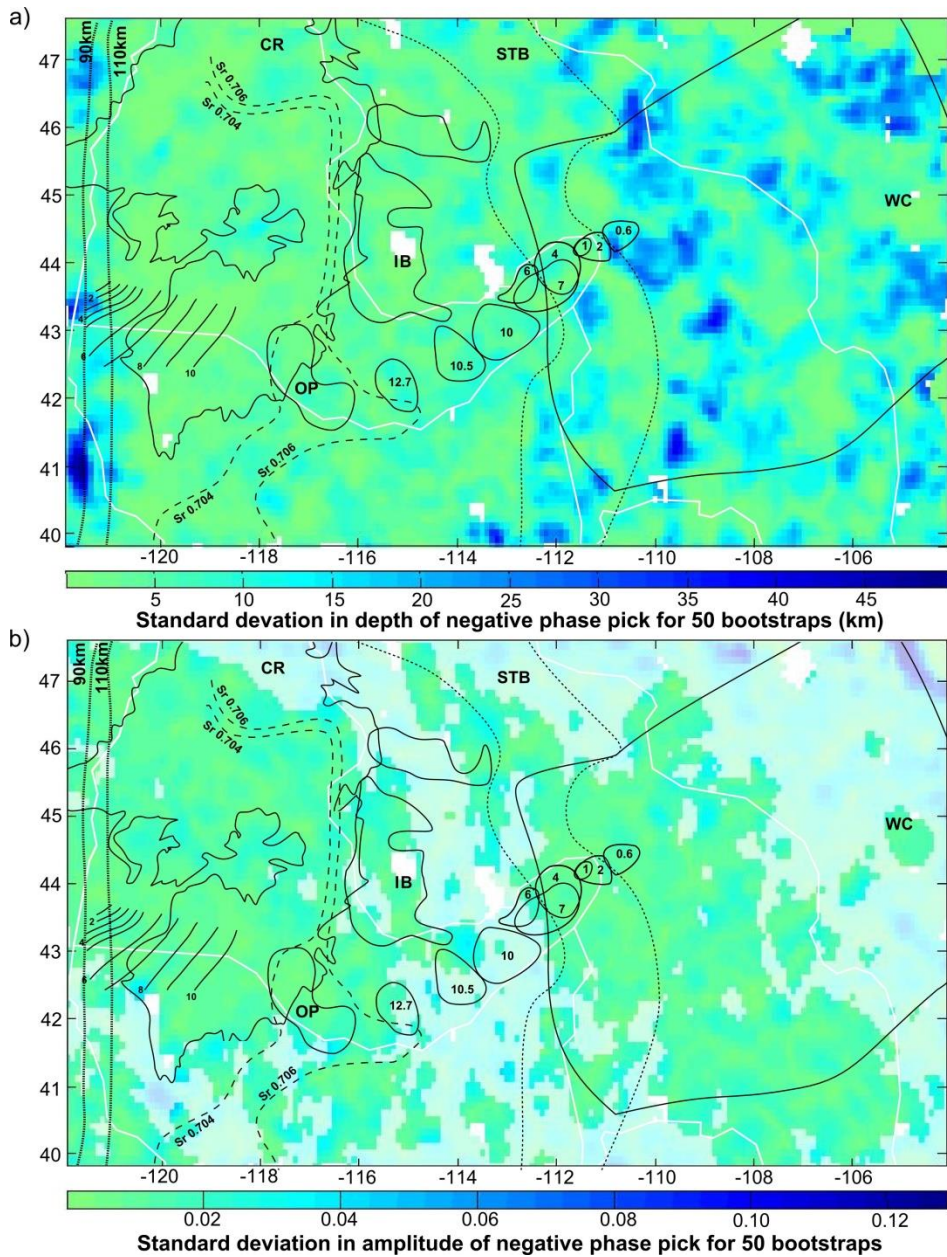


Figure S1: Standard deviation of the depth and amplitude of the auto-picked maximum negative phase over the 50 CCP bootstrap stacks. No value is given (i.e. pixel is white) where the phase was too weak to be picked. White lines: boundaries between tectonic provinces, as in Figure 1. Black lines: smaller scale tectonic features, labeled as in Figure 1. a) Depth map. b) Amplitude map. Translucent white mask indicates areas where fewer than 50 weighted waveforms contribute to the image at a given model node.

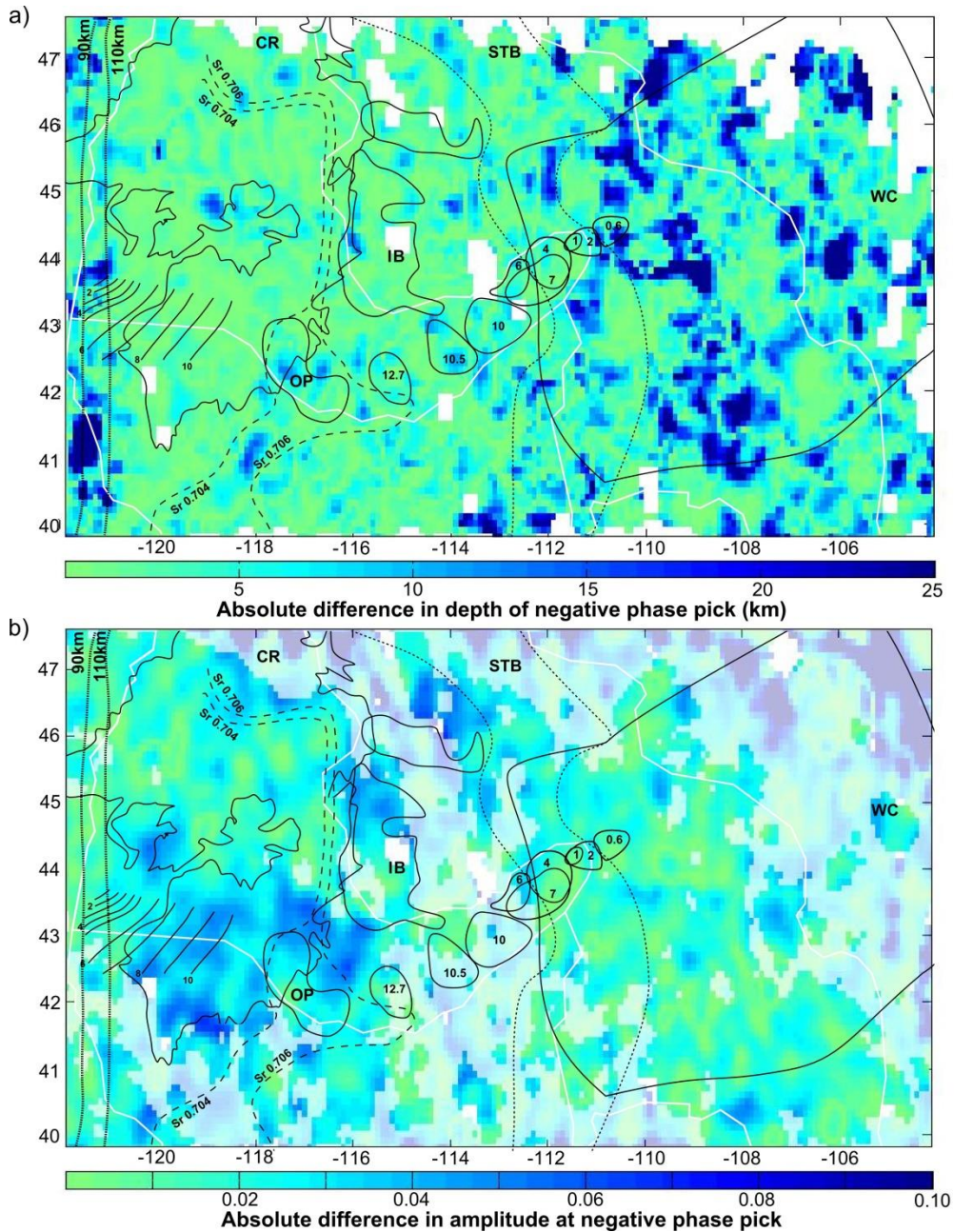


Figure S2: Absolute difference in depth and amplitude of the auto-picked maximum negative phase between the mean stack (the mean of the bootstrap stacks) and the single stack (based on all of the data). No value is given (i.e. pixel is white) where the phase was too weak to be picked. White lines: boundaries between tectonic provinces, as in Figure 1. Black lines: smaller scale tectonic features, labeled as in Figure 1. a) Depth map. b) Amplitude map. Translucent white mask indicates areas where fewer than 50 weighted waveforms contribute to the image at a given model node.

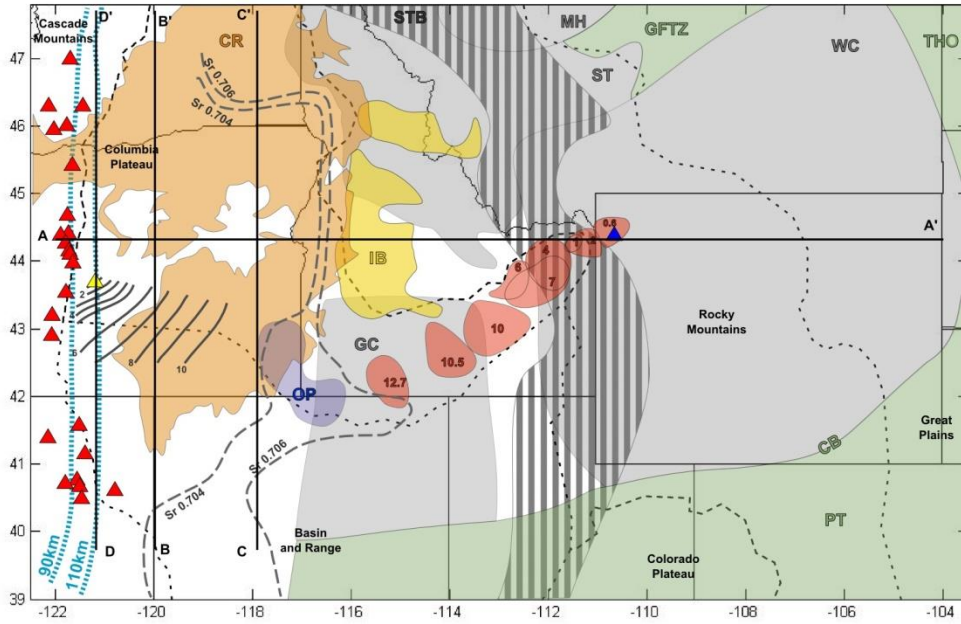


Figure S3: Basement map. Thick black lines: cross section locations. Grey shaded areas: the Archean Wyoming Craton (WC), Medicine Hat Block (MH), Grouse Creek Block (GC), and Selway Terrane (ST). Green shaded areas: the Proterozoic Great Falls Tectonic Zone (GFTZ), Trans-Hudson Orogen (THO), and accreted Proterozoic terranes (PT). CB: Cheyenne Belt suture. All after Foster et al. [2006]. Grey striped area (STB): Sevier fold and thrust belt, after DeCelles and Coogan [2006]. Other plot features described in Figure 1.

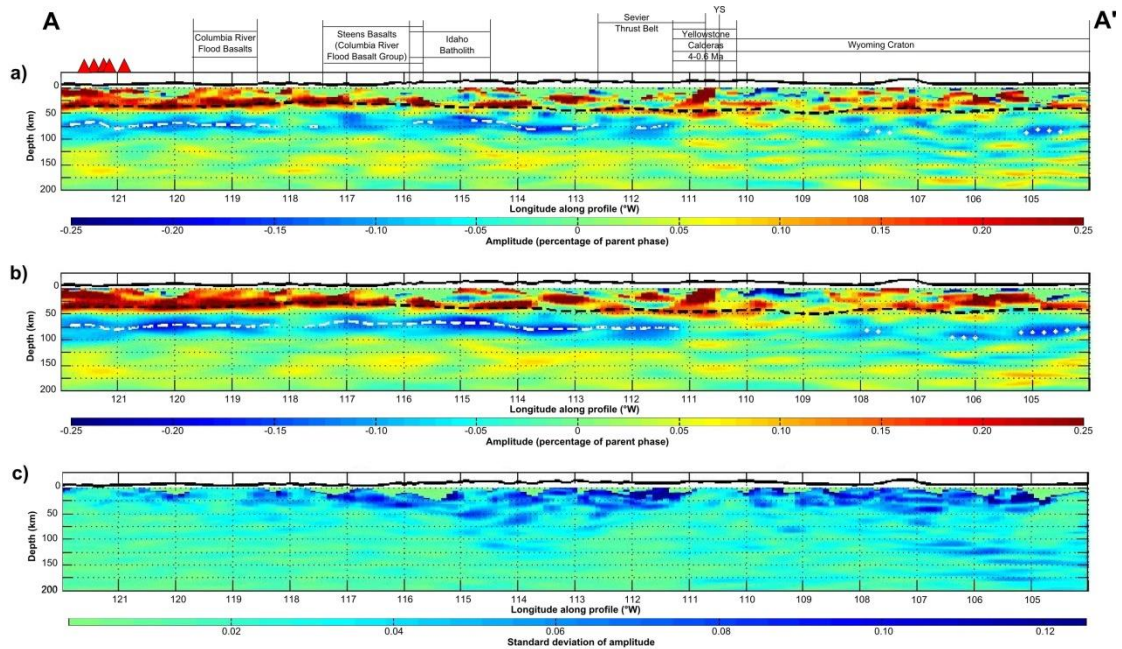


Figure S4: a) Cross section AA' through Sp CCP stack of all data (single stack). Location shown in Figure S3. Where fewer than 35 unweighted phases contribute to the image, zero amplitude is plotted. b) Corresponding cross section through Sp CCP stack of the mean of 50 bootstrapped models (mean stack). c) Corresponding cross section through the standard deviation of the mean stack. Cross section runs from 122° W to 104° W at a latitude of 44.4° N. In all plots, CCP stack is from data filtered at 4-33 s with a dominant period of 9 s. Thick black line: topography at 5x vertical exaggeration. Dashed black line: Moho [Lowry and Pérez-Gussinyé, 2011]. Dashed white line: auto-picked negative phase, interpreted as LAB. Dotted white line: auto-picked negative phase, interpreted as MLD. Labels above sections give approximate locations of surface features.

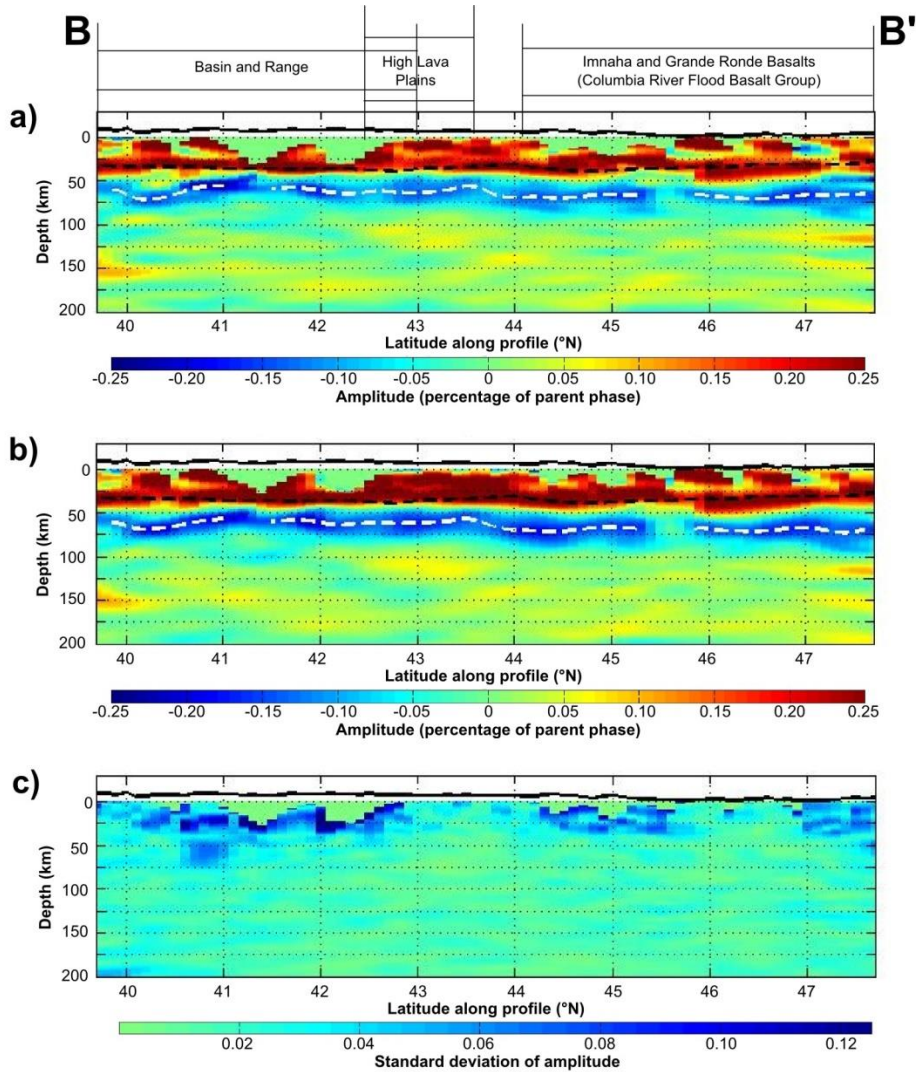


Figure S5: a) Cross section BB' through Sp CCP stack of all data (single stack). Location shown in Figure S3. Where fewer than 35 unweighted phases contribute to the image, zero amplitude is plotted. b) Corresponding cross section through Sp CCP stack of the mean of 50 bootstrapped models (mean stack). c) Corresponding cross section through the standard deviation of the mean stack. Cross section runs from 39.7° N to 47.7° N at a longitude of 120.0° W. Thick black line: topography at 5x vertical exaggeration. Dashed black line: Moho [Lowry and Pérez-Gussinyé, 2011]. Dashed white line: auto-picked negative phase, interpreted as LAB.

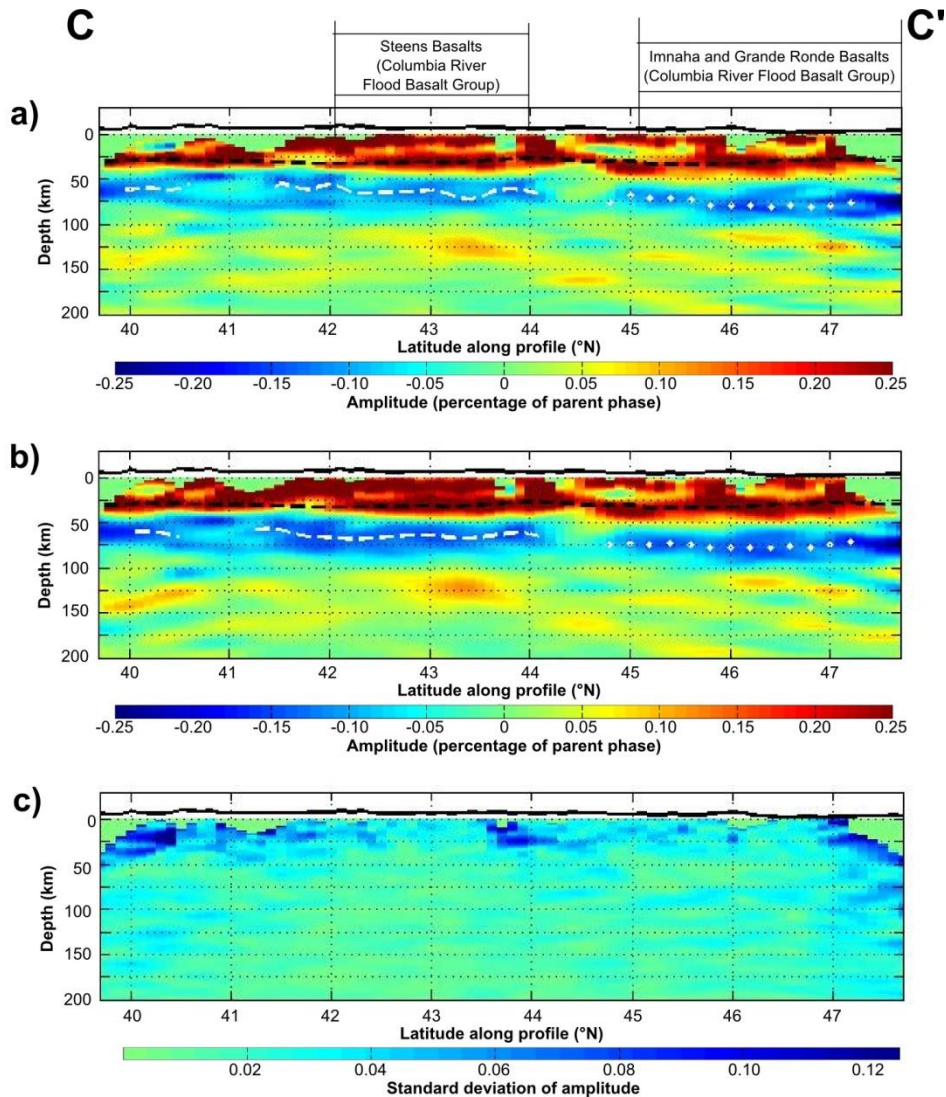


Figure S6: a) Cross section CC' through Sp CCP stack of all data (single stack). Location shown in Figure S3. Where fewer than 35 unweighted phases contribute to the image, zero amplitude is plotted. b) Corresponding cross section through Sp CCP stack of the mean of 50 bootstrapped models (mean stack). c) Corresponding cross section through the standard deviation of the mean stack. Cross section runs from 39.7° N to 47.7° N at a longitude of 117.9° W. Thick black line: topography at 5x vertical exaggeration. Dashed black line: Moho [Lowry and Pérez-Gussinyé, 2011]. Dashed white line: auto-picked negative phase, interpreted as LAB. Dotted white line: auto-picked negative phase, interpreted as MLD.

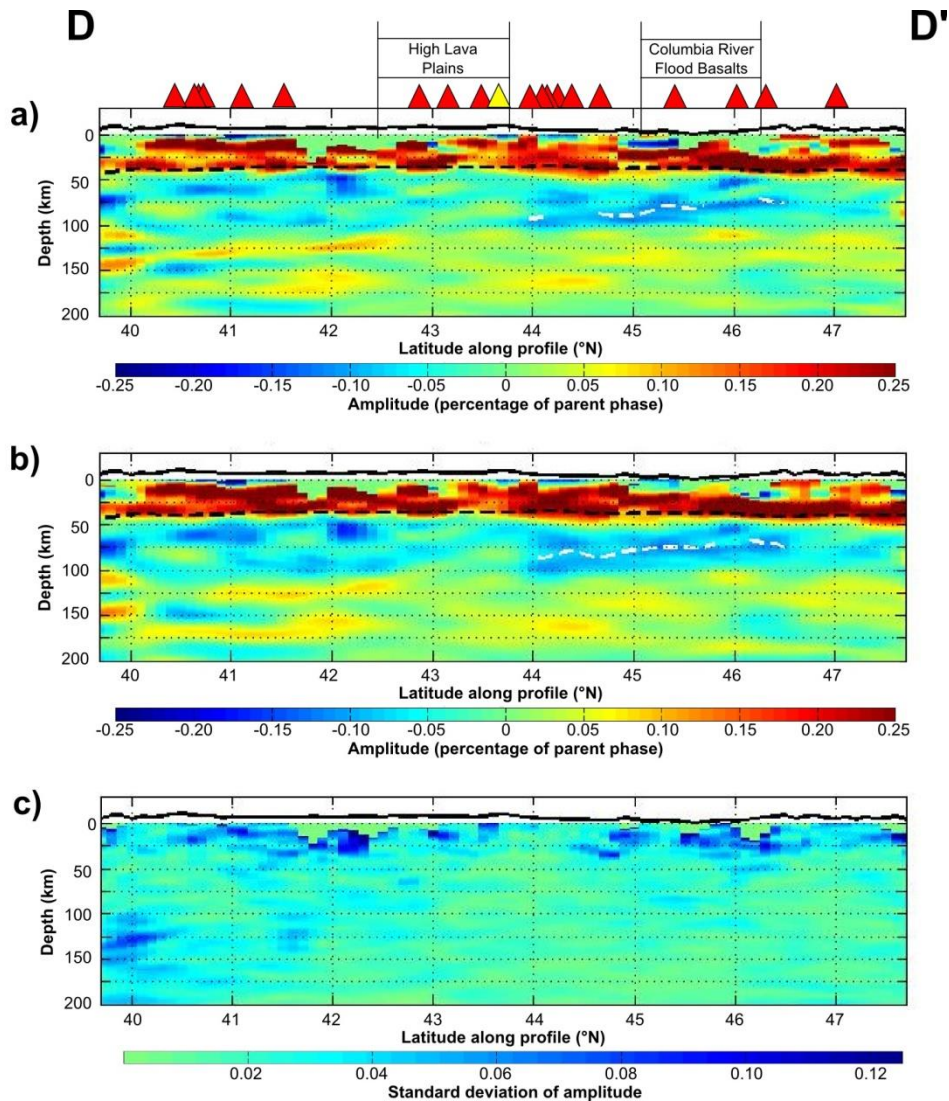


Figure S7: a) Cross section DD' through Sp CCP stack of all data (single stack). Location shown in Figure S3. Where fewer than 35 unweighted phases contribute to the image, zero amplitude is plotted. b) Corresponding cross section through Sp CCP stack of the mean of 50 bootstrapped models (mean stack). c) Corresponding cross section through the standard deviation of the mean stack. Cross section runs from 39.7° N to 47.7° N at a longitude of 121.2° W. Thick black line: topography at 5x vertical exaggeration. Dashed black line: Moho [Lowry and Pérez-Gussinyé, 2011]. Dashed white line: auto-picked negative phase, interpreted as LAB.

CHAPTER 2

Controls on lithospheric structures in the eastern United States: Tectonic inheritance and asthenospheric melts

Emily Hopper¹ and Karen M. Fischer¹

¹Department of Earth, Environmental and Planetary Sciences, Brown University, Providence, RI, USA

Abstract

The lithospheric mantle beneath the western and central contiguous United States has been well imaged in recent years. Here, we extend this analysis to the eastern U.S., using common conversion point stacking of Sp waveforms recorded at 682 broadband stations to characterize seismic discontinuities in the uppermost mantle. At lithosphere-asthenosphere boundary (LAB) depths, the strongest LAB phases observed are in areas of inferred enhanced upwelling, due to buoyant ‘hot spot’ asthenosphere, delamination, or sharp changes in lithospheric topography. The most prominent step in lithospheric topography as imaged by Sp waves occurs across the hinge zone, a late Proterozoic structure related to the rifting of Rodinia. Such Proterozoic rift structures have been invoked as controls on localizing later crustal deformation episodes, and the images presented here suggest such tectonic inheritance also influences current lithospheric topography. The imaging of the LAB by Sp waves requires that the velocity gradient is relatively sharp; that is, it cannot be a purely thermal boundary. In these areas of enhanced upwelling, increased fractions of partial melt ponded at the LAB may act to locally sharpen the velocity gradient, producing an Sp phase. Beneath the thick lithosphere of the continental interior, where temperatures are further below the solidus, no LAB phase is observed. This variation in LAB properties is compatible with observations of the LAB further west. Within the lithosphere, we observe a subhorizontal discontinuity at 90-100 km depth beneath the oldest, unmodified crust in the study area. This discontinuity is inferred to be generated by a volatile-rich layer within the lithosphere, and its restriction to the oldest crust in the study region implies the accumulation of sufficient volatiles in an upper lithospheric mantle layer is unique to ancient, unmodified lithosphere.

1. Introduction

1.1. Tectonic setting

The current quiescence of the eastern U.S. belies its rich tectonic history: the formation of Rodinia, its break-up by rifting to form the Iapetus Ocean, the closure of the ocean basins to form Pangea, and the rifting of that supercontinent to form the Atlantic are all recorded in the rocks and structures of the region [e.g. Thomas, 2006].

Near-continuous accretion to the southeastern and eastern margin of proto-North America took place over 800 My during the Proterozoic, building almost half of the North American continent as we know it today. Our study region (see Figure 1a) incorporates the Granite-Rhyolite province, a juvenile crustal block accreted between 1.5-1.3 Ga. Within this terrane, the Grenville Front marks the northwesternmost expression of the 1.3-1.0 Ga Grenville deformation, a sequence of orogenies resulting in the final assembly of Rodinia [e.g. Whitmeyer and Karlstrom, 2007]. Today, the Grenville Front is associated with a transition to thicker lithosphere (i.e. higher velocities to >150 km depth; see Figure 1b) in the upper mantle [Pollitz and Mooney, 2016].

The formation of the Iapetus Ocean broke Rodinia apart into Laurentia (proto-North America) and Gondwana, with significant rifting along the eastern margin of Laurentia beginning 620 Ma [Thomas, 2006; Whitmeyer and Karlstrom, 2007]. Although subsequently buried and deformed, the estimated limit of the rifted margin has been palinspastically restored with a zig-zag pattern of embayments and promontories [Thomas, 2006] (Figure 1a). Also preserved is the hinge zone: the transition to extreme crustal thinning, as marked by an abrupt change in the thickness and facies of contemporaneously deposited sediments [Wehr and Glover, 1985] (Figure 1).

The Appalachians were built during a series of Paleozoic orogenies, driven by the eventual collision of Gondwana with Laurentia to form the supercontinent Pangea [Hatcher, 2010; Hibbard et al., 2010]. Much of this deformation is thought to have been across relatively shallow, flat-lying detachments, transporting allochthonous thrust sheets hundreds of kilometers inboard of the rifted margin [Cook et al., 1979; Thomas, 2006]. Even the final suture between Gondwanan-affinity and Laurentian crust, preserved in Georgia, suggests >330 km overthrusting along a mid-crustal detachment [see Chapter 3].

The modern passive margin is a result of Mesozoic rifting, forming the Atlantic Ocean. Triassic-Jurassic rift basins extend along the east coast [Milici et al., 2012]. These sediments are interlayered with dykes, sills and lava flows: part of the Central Atlantic Magmatic Province (CAMP). These extensive tholeiitic basalts are thought to have a significant lithospheric mantle component, and to be the result of a large plume head impinging on the lithosphere [Marzoli et al., 1999].

1.1.1. Tectonic inheritance in the eastern U.S.

These superimposed tectonic processes have led many to speculate on the regional importance of tectonic inheritance: that is, the importance of pre-existing structures for subsequent episodes of deformation. At the crustal scale, tectonic inheritance has been cited as a control on localization of foreland basin deposits [Thomas, 1977], diachronous timing of Taconic tectonic loading [Bradley, 1989; Thomas, 2006], position of Appalachian salients and recesses [Thomas, 1977, 2006; Gates and Valentino, 1991; Benoit et al., 2014], and craton-ward extent of Appalachian thrusting above decollements [Thomas, 2006]. This is in addition to brittle reactivation of pre-existing faults, both during periods of deformation [e.g. Bobyarchick and Glover, 1979] and as a locus of modern intraplate seismicity [Powell and Thomas, 2016]. Many of these arguments for tectonic inheritance rest on the creation of a weakness which is repeatedly

exploited by later deformation. Thomas [2006] suggests the initial weaknesses are through-going lithospheric transform faults in the Iapetan rifted margin: this weakness localizes synorogenic sedimentation and subsidence, and these thick, weak sedimentary packages allow propagation of low-angle detachments further cratonwards. The possibility of lithospheric-scale tectonic inheritance is supported by observations of modern lithospheric mantle structures in actively deforming regions, e.g. the sharp transition in LAB properties across the San Andreas Fault [Ford et al., 2014]; the lithospheric thinning beneath the Salton Trough [Lekić et al., 2011]. In this study, we present converted wave images of the eastern U.S. in which observed structures support the notion that tectonic inheritance is indeed significant at a lithospheric scale.

1.2. The lithosphere-asthenosphere system

The continental mantle lithosphere varies hugely in character across the contiguous U.S. – from almost negligibly thin in the orogenic western U.S. [e.g. Schmandt and Humphreys, 2010; Till et al., 2013; Hopper et al., 2014] to the depleted, cold, thick, high velocity root typical of the cratonic interior [e.g. Carlson et al., 2005; Sigloch, 2011; Burdick et al., 2014; Porritt et al., 2014]. In this study, we investigate the lithosphere beneath the eastern U.S., a region intermediate in age [e.g. Thomas, 2006] and lithospheric thickness, as defined by seismic tomography [e.g. Schmandt and Lin, 2014; Pollitz and Mooney, 2016] and thermal modeling of heat flow data [e.g. Artemieva and Mooney, 2001]. We will examine both structures related to the lithosphere-asthenosphere boundary (LAB) and mid-lithospheric discontinuities (MLDs).

The seismological LAB is defined by the velocity drop at the base of the high velocity lid. While such a velocity drop can be observed in tomography models, converted wave imaging provides a way to probe this velocity gradient at high resolution. Sp waveforms, the data used in this study, are generated at a relatively sharp velocity gradient; a gradual velocity gradient, i.e. a 5-10% decrease over 50 km [Ford et al., 2010], will not produce a converted phase. Sp imaging has been used extensively beneath the contiguous U.S. to image lithospheric structures. In

general, there is a very strong, sharp, shallow LAB in the western U.S. [Abt et al., 2010; Levander and Miller, 2010; Lekić et al., 2011; Kumar et al., 2012; Ford et al., 2014; Lekić and Fischer, 2014; Hopper et al., 2014; Kind et al., 2015; Hansen et al., 2015]. Such a sharp negative velocity gradient (NVG) requires some additional factor, such as anisotropy, grain size, partial melt, bulk composition, or volatile content [e.g. Fischer et al., 2010]; our preferred mechanism, at least in the Pacific northwest, is partial melt [Hopper et al., 2014, and references therein]. This phase transitions eastward to a much more nebulous, deep LAB beneath the cratonic interior. While some studies do image intermittent NVGs at depths appropriate for a cratonic LAB [Hansen et al., 2013, 2015; Foster et al., 2014; Kind et al., 2015], many studies typically do not observe converted phases generated at these depths, consistent with a very broad velocity gradient as could be generated by temperature alone [e.g. Abt et al., 2010; Kumar et al., 2012; Levander and Miller, 2012; Lekić and Fischer, 2014; Hopper et al., 2014; Hopper et al., 2015].

While an LAB is not always observed beneath the thick lithosphere of the continental interior, phases are often generated by structures within the lithosphere. These MLDs are typically found at 60-150 km depth [Rychert and Shearer, 2009; Abt et al., 2010; Kind et al., 2012, 2015; Kumar et al., 2012; Hansen et al., 2013, 2015; Foster et al., 2014; Hopper et al., 2014; Lekić and Fischer, 2014; Wirth and Long, 2014], and may be generated by changes in depletion [Lee, 2003], anisotropy [e.g. Yuan and Romanowicz, 2010; Wirth and Long, 2014], partial melt [e.g. Kumar et al., 2012], volatile content [e.g. Hansen et al., 2015; Hopper and Fischer, 2015; Selway et al., 2015], or deformation mechanism [e.g. Karato et al., 2015]. Our preferred mechanism is a frozen-in layer of volatiles [Hopper and Fischer, 2015, and references therein]. In some cases, dipping MLDs are observed; these have been associated with ancient sutures, leaving remnant slabs embedded within the cratonic root [Bostock, 1998; Calvert et al., 1995; White et al., 2003; van der Velden and Cook, 2005; Mercier et al., 2008; Chen et al., 2009; Hopper and Fischer, 2015]. These structures can be linked to the mechanisms of cratonic root

formation involving sub-arc mantle thickening [e.g. Parman et al., 2004] or imbrication of oceanic lithosphere [e.g. Pearson and Wittig, 2008].

Based on these endmembers, what structures might we expect to find in the eastern U.S.? Here, the lithosphere ranges from >150 km thick beneath the Mesoproterozoic Granite-Rhyolite province to on the order of 100 km or less moving towards the coast beneath younger terranes (see Figure 1). Given the lack of recent volcanism [Mazza et al., 2014] and relatively low heat flow [Artemieva and Mooney, 2001] throughout the east coast, we do not expect significant volumes of melt in the asthenosphere [Hirschmann, 2010]. This is compatible with prior observations of a relatively weak (~5% velocity contrast) NVG at 90-120 km depth, interpreted as the LAB [Rychert et al., 2005, 2007; Abt et al., 2010]. The observations presented here confirm this pattern on a broader scale.

Our study region encompasses the relatively young cratonic lithosphere of the Granite-Rhyolite Province, providing an opportunity to characterize MLDs in such an environment. The Mesoproterozoic Granite-Rhyolite province, which was extensively reworked by the Grenville orogeny east of the Grenville Front (see Section 1.2), has a tomographically defined lithospheric thickness of ~150 km (Figure 1b) and is associated with a continental arc setting [e.g. Whitmeyer and Karlstrom, 2007]. Thus, one goal is to look for dipping interfaces potentially related to Mesoproterozoic collisions, analogous to the collision of the Yavapai with the Wyoming and Superior cratons [Hopper and Fischer, 2015]. We also might expect a subhorizontal NVG generated by a volatile-rich layer of frozen-in melt, as is indeed observed here. While such a layer may be initiated at the time of root formation [Rader et al., 2015], it seems possible that this layer is episodically or continuously added to throughout its history [Hopper and Fischer, 2015]. If this is so, this feature should not be limited to Archean lithosphere, but rather to any lithosphere thick enough to host it. Prior imaging, largely restricted to west of this study region, puts an MLD at 90-100 km [Abt et al., 2010; Kind et al., 2015; Hansen et al., 2015]. Here, we confirm

the MLD in this depth range beneath the Granite-Rhyolite province, although it is largely restricted to west of the Grenville Front

1.3. The impact of mantle dynamics

More recent alteration and destruction of lithospheric mantle is most spectacularly observed today as shallow, low velocity anomalies beneath New England and Virginia (i.e. very thin lithosphere; see Fig 1b) [Chu et al., 2013; Li et al., 2003; Pollitz and Mooney, 2016; Porter et al., 2016; Schmandt and Lin, 2014; van der Lee and Nolet, 1997; Villemare et al., 2012]. This is associated with the most recent volcanism on the east coast (Eocene volcanics in Virginia, 48 Ma) [Mazza et al., 2008], as well as Cretaceous intrusions in New England [Sleep, 1990], and Mesozoic kimberlites in Kentucky, New York, and Pennsylvania [Heaman et al., 2004]. These low velocity anomalies have been attributed by some to the remnant tracks of Cretaceous hot spots [Chu et al., 2013; Li et al., 2003; Pollitz and Mooney, 2016; Schmandt and Lin, 2014; van der Lee and Nolet, 1997; Villemare et al., 2012]. Although less well expressed tomographically [Pollitz and Mooney, 2016; Schmandt and Lin, 2014], the track of the Bermuda hotspot is also thought to have passed beneath southern Georgia [Cox and van Arsdale, 2002]; the track may extend northeast along the coast to North Carolina, before moving beneath the Atlantic [Chu et al., 2013]. Alternatively, the Virginia anomaly, at least, may be the result of lithospheric delamination – a hypothesis more consistent with calculated equilibration temperatures of the Virginia volcanics [Mazza et al., 2014] and the shape of the low velocity anomaly observed by body wave tomography [Schmandt and Lin, 2014]. In either case, some other mechanism, such as enhanced convection around the resulting lithospheric topography, is required to preserve the observed low velocity anomalies, preserved 10s-100s of million years after the purported perturbation [Schmandt and Lin, 2014].

Mantle dynamics may also be recorded by the rejuvenation of the southern and central Appalachians since the Miocene [Gallen et al., 2013; Miller et al., 2013], and an earlier episode

of rejuvenation of the central Appalachians during the Cretaceous (70 Ma) [McKeon et al., 2014]. The enhanced exhumation has been attributed to significant dynamic topography in the region [Miller et al., 2013; Moucha et al., 2008; Rowley et al., 2013], with upwellings associated with the low velocities beneath Virginia [Rowley et al., 2013] and extending west from the Bermuda swell [Forte et al., 2007; Rowley et al., 2013]. Alternatively, some authors prefer delamination e.g. beneath western North Carolina [Wagner et al., 2012; Gallen et al., 2013; Graw et al., 2015]; and some prefer surficial processes, such as changes in erosion rate related to climate change [Molnar, 2004] or drainage capture [Prince et al., 2013].

These focused zones of upwelling and enhanced melting are expected to produce a shallow, sharp LAB; the observations presented herein support this association.

2. Data and Methods

2.1. Data

We incorporated almost 70,000 Sp waveforms recorded at the 682 broadband stations with available data within the study region, including 400 of EarthScope's Transportable Array stations, 101 permanent stations, and data from 12 other temporary networks. Data coverage (Figure 2) is reasonable throughout the study area, but best beneath areas with focused temporary deployments (e.g. Georgia) or regional permanent arrays (e.g. the northeast). The data were obtained from the Incorporated Research Institutions for Seismology (IRIS) Data Management Center. All events with $M_w > 5.8$ as reported in the USGS National Earthquake Information Center catalog within a distance range of 55° - 85° and with a source depth < 300 km were used. Records from longer distances and greater depths are contaminated by other teleseismic arrivals [e.g. Wilson et al., 2006]; from shorter distances, the conversions become postcritical. Postcritical conversions occur when incidence angles are too large, i.e. below some depth that decreases with decreased epicentral distance. This critical depth is calculated from a station-

specific 1D velocity profile obtained from local 3D tomography [Schmandt et al., 2015; Schmandt and Lin, 2014], and any energy beneath it is excluded.

Sp conversions are generated at velocity discontinuities or relatively sharp velocity gradients. They are our preferred waveform with which to probe the lithospheric mantle as they are well separated in time from crustal multiples, arriving before the main S. For easier comparison with more common Ps studies, we reverse the polarity of the output such that a negative (blue) phase corresponds to a negative velocity gradient (NVG) with increasing depth, and a positive (red) phase to a positive velocity gradient (PVG).

2.2. Processing

We define S phase windows using an automated array-based procedure (Lekić and Fischer, 2014) so variations in mantle velocities within the study region are accounted for. The recorded waveforms were rotated into P and SV components with a free-surface transfer matrix [Kennet, 1991; Bostock, 1998], where the near-surface velocities were found by grid search [e.g. Abt et al., 2010]. The data were filtered at 4-33 s.

The daughter (P) phases were individually deconvolved by their parent (SV) phases using the extended-time multitaper cross-correlation method [Helffrich, 2006] with optimized parameters [Lekić and Fischer, 2014]. These receiver functions were migrated into the three-dimensional model volume using common conversion point stacking (CCP), where data were weighted by their proximity to the model points within a spline-representation of the Sp Fresnel zone [see Lekić et al., 2011], calculated for their measured 10 s dominant period. The velocity model used was station specific, and constructed from the crustal Vs of Schmandt et al. [2015], the crustal Vp/Vs of Parker et al. [2013] and French et al. [2009], and mantle Vp and Vs of Schmandt and Lin [2014].

The phases were bootstrapped by randomly resampling and recalculating the Sp CCP stack 30 times. The mean of these stacks is plotted in this paper, and the standard deviation was used as a criterion to identify robust phases by the picking algorithm.

2.3. Picking and classification of NVGs

An automated picking algorithm was used to isolate robust NVGs. For each depth column in the model, all phases meeting the following criteria were identified. 1) The minimum data coverage of weighted number of waveforms contributing to the model points in a column could not be less than 50 for 100 or more model points (equivalent to 50 km) between 50 and 300 km depth. 2) The minimum amplitude of the peak was 0.075; the width of the peak above this threshold had to exceed 5 km. If the coverage criterion was met and neither positive nor negative phases ever exceeded this threshold value, the location was marked as a gap (black crosses, Figures 3, 4). 3) The maximum allowable standard deviation was half of the peak phase amplitude. 4) The minimum separation between peaks was 10 km; for more closely spaced peaks, only the largest amplitude peak was retained. 5) A continuity threshold was applied within a 0.5° diameter around a phase pick. The Fresnel zone used to define the smoothing in these CCP stacks is approximately 50 km at 100 km depth; the 0.5° diameter continuity was chosen to be on the order of the Fresnel zone width. Picks were retained if more than half the model points within a circle 0.5° in diameter centered on the model point also had picks with overlapping depth ranges, where depth range was defined as the width at half maximum of the phase peak.

Once the phases were picked, they were classified as LABs or MLDs based on comparison to local tomography and to each other. The boundaries from local tomography (see Figure 1b) were restricted to the limit of thick lithosphere (blue shading, Fig 1b) and of thin lithosphere (red shading, Figure 1b). All other variations were ignored as too ambiguous between tomography models. This limits any bias in patterns of LAB thickness as defined by Sp waveforms. In the following description, maximum depth refers to the maximum depth at the half maximum of a

picked peak; regional LAB depth refers to the deepest phase within a 0.25° radius of the model point. Points within the region of thick lithosphere were defined as LABs if below 130 km; all other phases were defined as MLDs. For points inside the regions of thin lithosphere, anything below 110 km was classified as being within the asthenosphere; a maximum depth >60 km could be picked as an LAB; phases shallower than 60 km or in locations with a deeper identified LAB were defined as MLDs. In the rest of the study region, phases below 135 km were classed as within the asthenosphere; if the maximum depth exceeded the regional LAB depth or 80 km, whichever was greater, it was picked as an LAB; phases shallower than this or in locations with a deeper identified LAB were defined as MLDs.

The phases defined as ‘asthenospheric’ are not explored in this paper as they tend to be sparse and weak. These phases are not included in the maps of MLD and LAB depths (Figure 3), but are included in the unclassified NVG depth maps (Figure 4).

3. Observed LAB and MLD structures and their meaning

3.1. The lithosphere-asthenosphere boundary

Following variations in the depth of observed fast velocity anomalies [Pollitz and Mooney, 2016; Schmandt et al., 2015], we estimated the tomographically defined lid as varying from >150 km thick in the western part of the study region (the undeformed Granite-Rhyolite province west of the Grenville Front, as well as some of the region that underwent extensive Grenvillian deformation), to lithosphere of more intermediate thickness, to very thin lithosphere in the regions with the slow, shallow velocity anomalies in New England and Virginia (Figure 1b).

As observed in other parts of the U.S. (see Section 1.2), there is a relatively continuous, coherent LAB beneath the thinned lithosphere, but little indication of an LAB phase beneath the thicker lithosphere of the continental interior. In the intervening lithosphere of intermediate

thickness, we see somewhat discontinuous phases between 80 and 120 km depth, interpretable as the LAB. Such phases appear to be strongest around steps in lithospheric topography.

3.1.1. Shallow, low velocity anomalies associated with upwellings

The New England anomaly, the largest low velocity anomaly on the East Coast, is associated with a broad band of highly thinned lithosphere. NVGs are almost all shallower than 90 km, with the majority of picks in this region between 70 and 80 km depth (Figures 3, 4a). Some systematic variation seems to exist, with the shallowest depths in southern New England (Figures 3, 4a, 6d east of 73°W), a decrease in amplitudes in central New England (Figures 3, 4), and slightly deeper NVGs in northern New England (Figures 3, 4a, 5a east of 75°W). This zone of shallow phases is not restricted to the zone of lowest velocities identified tomographically, but rather extends throughout much of New York State (Figure 3b, 5a). The Great Meteor hot spot track is constrained by surface volcanism to extend northwest from southern New England through Vermont and into Quebec [Heaman et al., 2004]. This proposed track goes to the northeast of the zone of thinned lithosphere in New York, making the cause of the seemingly continuous linear lithospheric thinning from New England through New York obscure. However, recalculation of the Great Meteor hotspot track to better fit both the offshore trend and observed thinning of the mantle lithosphere suggests that the surface trace has been offset from the mantle trace of the hotspot track [Eaton and Frederiksen, 2007]. This may be due to horizontal lithospheric shearing driven by viscous coupling between the cratonic root and mantle flow. These authors' preferred lithospheric hotspot track runs through New York and into Ontario, much more compatible with our observations of the zone of thinned lithosphere.

The Virginia anomaly, in contrast, has a smaller footprint than defined tomographically, with phases remaining as deep as 100 km into the low velocity anomaly (e.g. Figure 4b in central Virginia; Figure 5b between 81° and 79.7°W). The thinning is localized (e.g. Figure 5b between

79.7° and 79°W), and the thinned zone is flanked by high amplitude phases at relatively unperturbed lithospheric depths (e.g. Fig 5b from 80.7° to 79.7°W and 78.3° to 76.5°W; Figure 7b east of 81°W) within the low velocity zone defined from tomography (Figure 1b, 3b). The localized nature of the thinning is compatible with the hypothesis that this anomaly is associated with delamination, rather than a hot-spot type upwelling [Mazza et al., 2014; Schmandt and Lin, 2014].

In the region of the predicted track of the Bermuda hotspot (southern Georgia, Figure 3a; south of 33°N, Figures 6e, f), LAB depths are also unusually shallow (70-80 km). Poor coverage along the coastline precludes distinguishing the possible hot spot tracks identified by Cox and van Arsdale [2002] and Chu et al. [2013] (see Section 1.3).

3.1.2. Changes across the hinge zone

Within the intermediate depth lithosphere, a distinct jump in phase depth is observed across the hinge zone (Figure 3b; Figure 6; Figure 7b; comparison of deepest phase depth between Figure 5b and 5c). This is perhaps shown the most clearly in Figure 4b, where phase depths below 100 km are restricted almost entirely to the zone between the Grenville Front and the hinge zone; the phases are particularly strong along the hinge zone, except where this is interrupted by the low velocity Virginia and New England anomalies. This sharp decrease in phase depth is typically on the order of 10 km (Figure 6), from 95-120 km west of the hinge zone to 80-100 km moving east. There is a possibility this shallowing extends into the region of the New England anomaly (Figure 6d), but the phase jump here is less abrupt and less well aligned with the surface trace of the hinge zone.

3.1.3. The thick lithosphere of the continental interior

Beneath the zone of thick lithosphere, there are isolated NVGs at depth (e.g. beneath Ohio and northwestern Pennsylvania in Figure 3b; Figure 6f at 150 km depth between 40.4° and 39.3°N; Figure 7a at 160-170 km depth between 82° to 81°W). While these phases are strong and continuous enough to meet our picking criteria, and could represent zones where the LAB beneath the continental interior has sharpened, they are insufficiently widespread for us to be confident in their interpretation as such. Moreover, there is not a clear reason why the NVG at the base of the lithosphere would be sharpened in these regions. There is no associated low velocity anomaly of note in the underlying lithosphere [Pollitz and Mooney, 2016], dynamic topography calculations predict mantle downwellings in these areas [Rowley et al., 2013], and there is no clear relation to tectonics exposed at the surface. However, if these are indeed LAB phases, they are well correlated with the depth of LAB phases reported to the west of the study region [Hansen et al., 2015].

3.1.4. Local strengthening of the LAB

The lithosphere is a rheological boundary, typically identified with the change from a conductive to a convective thermal regime moving into the asthenosphere. The broad velocity gradients predicted for a thermal boundary cannot produce an Sp phase, so an additional mechanism is required – our preferred explanation is partial melt (see Section 1.2). In the Pacific northwest, the LAB is thought to be defined by partial melt; this phase is very strong, and the depth is dependent on time since surface volcanism [Hopper et al., 2014]. How well does this mechanism translate to the east coast, where extensive mantle melting is not expected?

Where we see an LAB phase, the amplitudes are consistent with a velocity drop on the order of 5% [Rychert et al., 2005, 2007; comparison with phase amplitudes and synthetic modeling of Hopper and Fischer, 2015]. Given upper mantle shear velocities of approximately 4.45 km/s

[Pollitz and Mooney, 2016], this means a reduction to 4.23 km/s. This corresponds to a melt fraction [Schmerr, 2012; Priestley and McKenzie, 2006] of approximately 0.25% at a temperature of approximately 1350°C to account for the observed LAB phases at 80-120 km depth. This is comparable to estimates of 0.25%-1.25% melt beneath old Pacific lithosphere [Kawakatsu et al., 2009].

However, calculations by Hirschmann [2010] for an old (100 Ma) oceanic plate, with a mantle potential temperature of 1300°-1350°C and plate thickness of 125 km, conditions similar to the eastern U.S. lithosphere, predict much lower melt fractions (on the order of 0.025% melt for a depleted mantle source). Eocene volcanics suggest an enriched mantle source [Mazza et al., 2014] – not unexpectedly, given the recent history of hot spot volcanism [Cox and van Arsdale, 2002; Heaman et al., 2004] and suggested delamination episodes [Wagner et al., 2012; Mazza et al., 2014; Schmandt and Lin, 2014; Graw et al., 2015]. For an enriched mantle, the calculated asthenospheric melt fraction rises to over 0.1% [Hirschmann, 2010].

While this is significantly lower than the 0.25% melt required to generate observed phases, numerical modeling of porous flow within the asthenosphere coupled to dyke intrusion to the base of the lithosphere [Havlin et al., 2013] suggests that, at steady state, melt will tend to pond at the base of the lithosphere, with melt fractions 2.5 times higher than asthenospheric melt fractions. That is, predicted melt fractions at the LAB itself may be as high as 0.25%, as required to generate the observed Sp phases.

Given that the predicted melt quantity is just sufficient to match the strength of observed Sp phases, fluctuations in melt fraction may explain why the Sp LAB observations are limited in extent. The zones of low asthenospheric velocities in New England, Virginia, and Georgia are associated with enhanced mantle upwelling in dynamic topography calculations [Rowley et al., 2013], and unusually high mantle temperatures, as reflected by their low velocities. The other

region that we see a strong LAB is the hinge zone, where a step in topography may act to enhance small scale mantle convection. Given the motion of North America to the west or west-south-west, underlying asthenosphere is being forced to rise up this topographic step as the edge of the thicker lithosphere passes over it. This process has been modeled, and is predicted to generate significant upwelling dependent on the depth change of the topographic step, and the width over which it takes place [Till et al., 2010]. While the change in depth observed here is smaller than those modeled, the transition is also very sharp, which will act to enhance this effect. Enhancing small-scale convection and upwelling in this way is a possible mechanism to produce the additional partial melt required to generate the observed Sp phase. We suggest that the much larger topographic step at the edge of the thick continental root (Figure 1b) would also generate enhanced upwelling in this way; however, the colder temperatures relative to the solidus at these greater depths mean that no additional melt is produced by this small-scale convection. Hence, we do not observe a strong LAB around this step in topography.

Modeling of the melt ponding and migration processes [Havlin et al., 2013] also suggests that thermal erosion of the lithosphere by advection of heat through dyking will be negligible below melt fractions of 1.4% ponded below the LAB (0.6% within the asthenosphere). This is compatible with the preservation of relatively thick lithosphere and of the inherited step in lithospheric topography around the hinge zone: despite the continuous renewal of ponded melt over hundreds of millions of years, the melt fractions are too low to significantly thin or alter the lithosphere by thermal erosion. In the zone of thinned lithosphere along the Great Meteor hot spot track, the observed thermal erosion may have been caused by locally higher melt fractions in addition to hotter upwelling asthenosphere. The consequent step in lithospheric topography may have enhanced melt production, as discussed above, preserving it to the present day.

3.2. *Mid-lithospheric discontinuities*

A change in MLD character occurs parallel to the Grenville Front, running 50-100 km east of the surface trace of the front. There is a clear jump from relatively strong, continuous phases at 90-100 km depth in west central Kentucky and Tennessee (Figure 3a; Figure 4a; Figure 5a west of 83.8°W; Figure 6e between 39° to 36.5°N; Figure 7b west of 83.5°W) to shallower, more discontinuous phases. West of the Grenville Front, no phases shallower than 80 km are imaged.

The limited extent of this zone of strong, continuous MLD suggests that its formation mechanism may be unique to ancient, undeformed lithosphere. Such MLDs are observed in the U.S. within Archean cratons, Paleoproterozoic orogenic zones such as the Trans-Hudson Orogen, and in Mesoproterozoic accreted terranes [Rychert and Shearer, 2009; Abt et al., 2010; Kind et al., 2012, 2015; Kumar et al., 2012; Hansen et al., 2013, 2015; Foster et al., 2014; Hopper et al., 2014; Lekić and Fischer, 2014; Wirth and Long, 2014]. Our observations limit its approximate extent to west of the Grenville Front. The preferred mechanism to generate this phase, a frozen-in volatile-rich melt layer (see Section 1.2) suggests that this layer may have been created during initial lithospheric formation, and/or been added to since the stabilization of the lithosphere. Given that, does its absence in younger, more deformed lithosphere make sense? We think this pattern may be easily explained. One possibility is that the formation of this layer was in fact restricted to the Mesoproterozoic and older, perhaps due to the more efficient decarbonation of slab suggested for ancient mantle conditions [Dasgupta, 2013] providing greater volumes of carbonate-rich melt to percolate into the lithosphere. Alternatively, it may be a question of time – in order to accumulate sufficient low velocity volatile-rich material to the lithosphere by gradual accumulation over time, a greater age is required. Thus, the younger regions of the eastern U.S. may have an enriched upper mantle layer, but not of sufficient strength or volume to generate strong Sp phases. In either case, the lack of an MLD in Granite-Rhyolite aged rocks east of the Grenville Front means that crustal formation age alone is not sufficient to explain the pattern.

However, it seems likely that these structures are fragile and easily disrupted or destroyed. That is, extensive heating or deformation of the lithosphere will remobilize these volatile-rich layers, destroying or at least disrupting the strong, localized velocity reduction.

3.3. Gaps in the NVGs

The NVG maps show extensive regions where no sufficiently strong or continuous phase was found. We consider the lithosphere to be transparent to Sp waves (a gap) if amplitudes remain below the chosen threshold. These zones (marked with a black cross, Figure 3, 4) are concentrated around the Quebec/Ontario/New York border, throughout Pennsylvania (Figure 5a at 80° to 77°W; Figure 5b at 76.3° to 74.7°W; Figure 7a east of 80.5°W), a small gap around the Kentucky/Virginia/Tennessee border (Figure 6b west of 82.5°W; Figure 7b from 83.5° to 82°W), and a large zone of phase gaps interspersed with strong NVGs in western North Carolina, South Carolina and northeastern Georgia (Figure 7c east of 83°W). Of these zones, all have good data coverage (Figure 2), although it is particularly excellent in Pennsylvania and South Carolina/Georgia.

The region around South Carolina is interesting, in its juxtaposition of very strong with very weak lithospheric phases (Figure 7c). It should be noted that coverage here is extremely good and supplemented by several temporary arrays, so the fact that the spacing in the observed phases is similar to the spacing of the TA is purely coincidental, and not related to differential coverage. One possibility here is that the rifted Laurentian margin extends much further beneath the Appalachian allochthonous terranes than elsewhere [Thomas, 2006; Chapter 3]. These phases could be isolating topography in the rifted blocks of this underthrust lithosphere, with melt ponding beneath topographic highs.

The other NVG gaps, the regions around Quebec, Pennsylvania and Tennessee, align well with Appalachian salients (the Quebec, Pennsylvania, and Tennessee salients). Thomas [2010]

suggested the location of the Appalachian salients was controlled by the shape of the Iapetan rifted margin, and that these regions overlie areas of weakened lithosphere cut by Proterozoic transform faults (Section 1.1.1). The transparency of these regions is compatible with their interpretation as weak zones – their greater susceptibility to deformation means it is less likely that internal structures will be preserved (Section 3.2). While the seismic transparency could well be caused by thorough disruption of existing lithospheric structures, it is intriguing that the mountains in the vicinity of the Pennsylvania NVG gap [Miller et al., 2013; McKeon et al., 2014] and the eastern Tennessee gap [Gallen et al., 2013] have undergone Cenozoic rejuvenation, associated with delamination of at least the lower crust. Perhaps the inherited, Paleozoic weakness is still exerting a control on localizing delamination, and thus continued uplift of the Appalachians, today.

4. Conclusions

The Sp images of the eastern U.S. lithosphere presented here reveal LAB and MLD structures that vary across the study area. The LAB is strongest beneath lithosphere that has been extensively thermally eroded and where there is lithospheric topography that may enhance local convection. The MLD is strongest and most continuous within the oldest, unmodified terrane in the study area, the Granite-Rhyolite province.

4.1. Tectonic inheritance

Tectonic inheritance has been proposed as a significant control localizing crustal deformation; that is, weak zones created during older tectonism will act to localize subsequent deformation episodes. Our images suggest that such tectonic inheritance is significant at a lithospheric scale. The transition to extreme Proterozoic crustal thinning eastward across the hinge zone (black dashed line, Figure 1; Figures 3-7) is reflected by a sharp decrease in

lithospheric thickness of >10 km. That is, this 620 Ma rifting continues to influence lithospheric topography, and probably small-scale mantle flow and melting (see Section 3.1.4), today.

The large transform faults of the Proterozoic rifted margin have been linked to the localization of Appalachian salients in Quebec, Pennsylvania and Tennessee and associated enhanced sedimentation and subsidence [Thomas, 2006]; these vertical transform faults have been suggested to extend throughout the lithosphere, weakening it. This may be reflected in the much greater transparency to Sp waves in these regions (Figures 3-5, 7): any pre-existing structures here have been significantly disrupted if not destroyed.

4.2. The lithosphere-asthenosphere system

Assuming that the lithosphere can, to first order, be described as a thermal boundary, the LAB should be associated with a velocity gradient that is too gradual to be imaged by Sp waves. Ponding of melt at the base of the lithosphere is an effective means to generate the required sharp velocity gradient where an LAB is observed. Our observations in the eastern U.S. (Figures 3b, 5-7), where asthenospheric melt fraction is expected to be relatively low (Section 3.1.4), are compatible with this description. We observe intermittent, relatively weak LAB phases, primarily concentrated around steps in topography and asthenospheric low velocity anomalies, where upwelling and partial melt fractions may be enhanced. Beneath the thick lithosphere of the continental interior, where temperatures are much lower relative to the solidus, we do not unambiguously observe a broad-scale, deep LAB (Figures 3, 4).

Previously observed MLDs in the Archean Wyoming and Superior cratons are typically relatively shallow and near-horizontal, though some dipping MLDs at the cratonic margins have also been observed. Such dipping MLDs, associated with ancient remnant subducted slabs, are not observed in the eastern U.S. However, we do see a strong, continuous, sub-horizontal MLD within the lithosphere of the Mesoproterozoic Granite-Rhyolite province. This type of MLD has

been previously associated with a low-velocity volatile-rich layer. Furthermore, we observe a marked transition to shallower, more discontinuous MLDs moving east; the transition approximately parallels the Grenville Front, though is 50-100 km further east (Figure 3). This may indicate that the MLD, and therefore the presence of the suggested volatile-rich layer, is unique to old, undisturbed lithosphere.

4.3. The impact of mantle dynamics

Recent lithospheric disruption, whether by thermal erosion linked to hot spots or local replacement of delaminated material, is expected to enhance upwelling and thus melting. The shallow, anomalously low velocity asthenosphere seen in tomography models [Li et al., 2003; Pollitz and Mooney, 2016; Schmandt et al., 2015; van der Lee and Nolet, 1997] is compatible with their interpretation as melt-rich areas with enhanced thermal erosion of the lithosphere. Our results show that the observed LABs in this region are relatively shallow and strong, also compatible with this interpretation (Figures 3, 5, 7).

Acknowledgements

This study employed data from the following permanent networks: the Canadian National Seismic Network, the Central and Eastern US Network ([doi:10.7914/SN/N4](https://doi.org/10.7914/SN/N4)), the Global Seismograph Network ([doi:10.7914/SN/IU](https://doi.org/10.7914/SN/IU)), the Lamont-Doherty Cooperative Seismic Network (<http://www.ldeo.columbia.edu/LCSN>), the New England Seismic Network (<http://aki.bc.edu/nesn.htm>), the New Madrid Seismic Network (<http://www.eas.slu.edu/eqc/eqcnetworks.html>), the Penn State Network (<http://eqseis.geosc.psu.edu>) and the United States National Seismic Network ([doi:10.7914/SN/US](https://doi.org/10.7914/SN/US)); and data from the following temporary arrays: the Abitibi Experiment (XB), the Adirondack Broadband Array (XJ), AST (Z4), ENAM ([doi:10.7914/SN/YO_2014](https://doi.org/10.7914/SN/YO_2014)),

FLED (doi:10.7914/SN/XR_2001), MAGIC (doi:10.7914/SN/7A_2013), NOMAD (doi:10.7914/SN/XO_1997), PHRACCS (XQ), SCEPP (doi:10.7914/SN/SP), SESAME (doi:10.7914/SN/Z9_2010), USGS Networks (GS), XR (doi:10.7914/SN/XR_2012), and the TA (doi:10.7914/SN/TA). This work was supported by the NSF Geophysics Program under award EAR-1345143.

References

Abt, D. L., K. M. Fischer, S. W. French, H. A. Ford, H. Yuan, and B. Romanowicz (2010), North American lithospheric discontinuity structure imaged by Ps and Sp receiver functions, *J. Geophys. Res.*, 115, B09301, doi:10.1029/2009JB006914.

Artemieva, I. M., and W. D. Mooney (2001), Thermal thickness and evolution of Precambrian lithosphere: a global study, *J. Geophys. Res.*, 106(B8), 16387-16414.

Benoit, M. H., C. Ebinger and M. Crampton (2014). Orogenic bending around a rigid Proterozoic magmatic rift beneath the Central Appalachian Mountains, *Earth. Planet. Sci. Lett.*, 402, 197-208.

Bobyarchick, A. R. and L. Glover (1979), Deformation and metamorphism in the Hylas zone and adjacent parts of the eastern Piedmont in Virginia, *Geol. Soc. Am. Bull.*, 90(8), 739-752.

Bostock, M. G. (1998), Mantle stratigraphy and evolution of the Slave province, *J. Geophys. Res.*, 103(B9), 21,183–21,200, doi:10.1029/98JB01069.

Burdick, S., R. D. van der Hilst, F. L. Vernon, V. Martynov, T. Cox, J. Eakins, G. H. Karasu, J. Tylell, L. Astiz, and G. L. Pavlis (2014), Model update January 2013: Upper mantle

heterogeneity beneath North America from travel-time tomography with global and USArray transportable array data, *Seismol. Res. Lett.*, 85(1), 77–81, doi:10.1785/0220130098.

Calvert, A. J., E. W. Sawyer, W. J. Davis, and J. N. Ludden (1995), Archaean subduction inferred from seismic images of a mantle suture in the Superior Province, *Nature*, 375, 670–674, doi:10.1038/375670a0.

Carlson, R. W., D. G. Pearson, and D. E. James (2005), Physical, chemical and chronological characteristics of continental mantle, *Rev. Geophys.* 43(1).

Chen, C. W., S. Rondenay, R. L. Evans, and D. B. Snyder (2009), Geophysical detection of relict metasomatism from an Archean (~3.5 Ga) subduction zone, *Science*, 326(5956), 1089–1091, doi:10.1126/science.1178477.

Chu, R., W. Leng, D. V. Helmberger, and M. Gurnis (2013), Hidden hotspot track beneath the eastern United States, *Nat. Geosci.*, 6(11), 963-966.

Cook, F. A., D. S. Albaugh, L. D. Brown, S. Kaufman, J. E. Oliver, and R. D. Hatcher (1979), Thin-skinned tectonics in the crystalline southern Appalachians; COCORP seismic-reflection profiling of the Blue Ridge and Piedmont, *Geology*, 7(12), 563-567.

Cox, R. T., and R. B. Van Arsdale (2002), The Mississippi Embayment, North America: a first order continental structure generated by the Cretaceous superplume mantle event, *J. Geodyn.*, 34(2), 163-176.

Dasgupta, R. (2013), Ingassing, storage, and outgassing of terrestrial carbon through geologic time, *Rev. Mineral. Geochem.*, 75(1), 183–229, doi:10.2138/rmg.2013.75.7.

Eaton, D. W., and A. Frederiksen (2007), Seismic evidence for convection-driven motion of the North American plate, *Nature*, 446(7134), 428-431.

Fischer, K. M., H. A. Ford, D. L. Abt, and C. A. Rychert (2010), The lithosphere–asthenosphere boundary, *Annu. Rev. Earth Planet. Sci.*, 38, 551–575, doi:10.1146/annurev-earth-040809-152438.

Ford, H. A., K. M. Fischer, D. L. Abt, C. A. Rychert, and L. T. Elkins-Tanton (2010), The lithosphere–asthenosphere boundary and cratonic lithospheric layering beneath Australia from Sp wave imaging, *Earth Planet. Sci. Lett.*, 300(3), 299–310, doi:10.1016/j.epsl.2010.10.007.

Ford, H. A., K. M. Fischer, and V. Lekić (2014), Localized shear in the deep lithosphere beneath the San Andreas fault system, *Geology*, 42(4), 295-298.

Forte, A. M., J. X. Mitrovica, R. Moucha, N. A. Simmons, and S. P. Grand (2007), Descent of the ancient Farallon slab drives localized mantle flow beneath the New Madrid seismic zone, 34(4).

Foster, K., K. Dueker, B. Schmandt, and H. Yuan (2014), A sharp cratonic lithosphere–asthenosphere boundary beneath the American Midwest and its relation to mantle flow, *Earth Planet. Sci. Lett.*, 402, 82–89, doi:10.1016/j.epsl.2013.11.018.

French, S. W., K. M. Fischer, E. M. Syracuse, and M. E. Wysession (2008), Crustal structure beneath the Florida-to-Edmonton broadband seismometer array, *Geophys. Res. Lett.*, 36(8).

Gallen, S. F., K. W. Wegmann, and D. R. Bohnenstiehl (2013), Miocene rejuvenations of topographic relief in the southern Appalachians, *GSA Today*, 23(2), 4-10.

Gates, A. E., and D. W. Valentino (1991), Late Proterozoic rift control on the shape of the Appalachians: the Pennsylvania re-entrant, *J. Geol.*, 863-872.

Graw, J. H., C. A. Powell, and C. A. Langston (2015), Crustal and upper mantle velocity structure in the vicinity of the eastern Tennessee seismic zone based upon radial P wave transfer functions, *J. Geophys. Res.*, 120(1), 243-258.

Hansen, S. M., K. G. Dueker, J. C. Stachnik, R. C. Aster, and K. E. Karlstrom (2013), A rootless Rockies—Support and lithospheric structure of the Colorado Rocky Mountains inferred from CREST and TA seismic data, *Geochem. Geophys. Geosyst.*, 14, 2670–2695, doi:10.1002/ggge.20143.

Hansen, S. M., K. G. Dueker, and B. Schmandt (2015), Thermal classification of lithospheric discontinuities beneath USArray, *Earth Planet. Sci. Lett.*, 431, 36–47.

Hatcher, R. D. (2010), The Appalachian orogeny: A brief summary, *Geol. Soc. America Memoir*, 206, 1-19.

Havlin, C., E. M. Parmentier, and G. Hirth, Dike propagation driven by melt accumulation at the lithosphere-asthenosphere boundary, *Earth Planet. Sci. Lett.*, 376, 20-28.

Heaman, L. M., B. A. Kjarsgaard, and R. A. Creaser (2004), The temporal evolution of North American kimberlites, *Lithos*, 76(1), 377-397.

Helfrich, G. (2006), Extended-time multitaper frequency domain cross-correlation receiver-function estimation, *Bull. Seismol. Soc. Am.*, 96(1), 344–347, doi:10.1785/0120050098.

Hibbard, J. P., C. R. van Staal, and D. W. Rankin (2010), Comparative analysis of the geological evolution of the northern and southern Appalachian orogeny: Late Ordovician-Permian, *Geol. Soc. Am. Memoir*, 206, 51-69.

Hirschmann, M.M. (2010), Partial melt in the oceanic low velocity zone, *Phys. Earth Planet. Inter.*, 179(1), 60–71.

Hopper, E., H. A. Ford, K. M. Fischer, V. Lekić, and M. J. Fouch (2014), The lithosphere–asthenosphere boundary and the tectonic and magmatic history of the northwestern United States, *Earth Planet. Sci. Lett.*, 402, 69–81, doi:10.1016/j.epsl.2013.12.016.

Hopper, E., and Fischer, K. M. (2015), The meaning of midlithospheric discontinuities: A case study in the northern U.S. craton, *Geochem. Geophys. Geosyst.*, 16, 4057–4083, doi:10.1002/2015GC006030.

Karato, S. I., T. Ougboji, and J. Park (2015), Mechanisms and geologic significance of the mid-lithosphere discontinuity in the continents, *Nat. Geosci.*, 8, 509–514, doi:10.1038/ngeo2462.

Kawakatsu, H., P. Kumar, Y. Takei, M. Shinohara, T. Kanazawa, E. Araki and K. Suyehiro (2009), Seismic evidence for sharp lithosphere-asthenosphere boundaries of oceanic plates, *Science*, 324(5936), 499–502.

Kennett, B. L. N. (1991), The removal of free surface interactions from three-component seismograms, *Geophys. J. Int.*, 104(1), 153–163, doi:10.1111/j.1365-246X.1991.tb02501.x.

Kind, R., X. Yuan, and P. Kumar (2012), Seismic receiver functions and the lithosphere–asthenosphere boundary, *Tectonophysics*, 536, 25–43, doi:10.1016/j.tecto.2012.03.005.

Kind, R., X. Yuan, J. Mechie, and F. Sodoudi (2015), Structure of the upper mantle in the north-western and central United States from USArray S-receiver functions, *Solid Earth Discuss.*, 7, 1025–1057, doi:10.5194/sed-7-1025-2015.

Kumar, P., R. Kind, X. Yuan, and J. Mechie (2012), USArray receiver function images of the lithosphere-asthenosphere boundary, *Seismol. Res. Lett.*, 83(3), 486–491, doi:10.1785/gssrl.83.3.486.

Lee, C. T. A. (2003), Compositional variation of density and seismic velocities in natural peridotites at STP conditions: Implications for seismic imaging of compositional heterogeneities in the upper mantle, *J. Geophys. Res.*, 108(B9), 2441, doi:10.1029/2003JB002413.

Lekić, V., and K. M. Fischer (2014), Contrasting lithospheric signatures across the western United States revealed by S_p receiver functions, *Earth Planet. Sci. Lett.*, 402, 90–98, doi:10.1016/j.epsl.2013.11.026.

Lekić, V., S. W. French, and K. M. Fischer (2011), Lithospheric thinning beneath rifted regions of Southern California, *Science*, 334(6057), 783–787, doi:10.1126/science.1208898.

Levander, A., and M. S. Miller (2012), Evolutionary aspects of lithosphere discontinuity structure in the western US, *Geochem. Geophys. Geosyst.*, 13, Q0AK07, doi:10.1029/2012GC004056.

Li, A., D. W. Forsyth, and K. M. Fischer (2003), Shear velocity structure and azimuthal anisotropy beneath eastern North America from Rayleigh wave inversion, *J. Geophys. Res.*, 108(B8), doi:10.1029/2002JB002259.

Marzoli, A., P. R. Renne, E. M. Piccirillo, M. Ernesto, G. Bellieni, and A. De Min (1999), Extensive 200-million-year-old continental flood basalts of the Central Atlantic Magmatic Province, *Science*, 284(5414), 616-618.

Mazza, S. E., E. Gazel, E. A. Johnson, M. J. Kunk, R. McAleer, J. A. Spotila, M. Bizimis, and D. S. Coleman (2014), Volcanoes of the passive margin: The youngest magmatic event in eastern North America, *Geology*, 42(6), 483-486.

McKeon, R. E., P. K. Zietler, F. J. Pazzaglia, B. D. Idleman, and E. Enkelmann (2014), Decay of an old orogeny: Inferences about Appalachian landscape evolution from low-temperature thermochronology, *Geol. Soc. Am. Bull.*, 126(1-2), 31-46.

Mercier, J. P., M. G. Bostock, P. Audet, J. B. Gaherty, E. J. Garnero, and J. Revenaugh (2008), The teleseismic signature of fossil subduction: Northwestern Canada, *J. Geophys. Res.*, 113, B04308, doi:10.1029/2007JB005127.

Milici, R. C., J. L. Coleman, E. L. Rowan, T. A. Cook, R. R. Charpentier, M. A. Kirschbaum, T. R. Klett, R. M. Pollastro, and C. J. Schenk (2012), Assessment of undiscovered oil and gas resources of the East Coast Mesozoic basins of the Piedmont, Blue Ridge Thrust Belt, Atlantic Coastal Plain, and New England Provinces, 2011, USGS Fact Sheet 2012-3075.

Miller, S. R., P. B. Sak, E. Kirby, and P. R. Bierman (2013), Neogene rejuvenation of central Appalachian topography: Evidence for differential rock uplift from stream profiles and erosion rates, *Earth. Planet. Sci. Lett.*, 369, 1-12.

Molnar, P. (2004), Late Cenozoic increase in accumulation rates of terrestrial sediment: how might climate change have affected erosion rates?, *Annu. Rev. Earth. Planet. Sci.*, 32, 67-89.

Moucha, R., A. M. Forte, J. X. Mitrovica, D. B. Rowley, S. Quéré, N. A. Simmons, and S. P. Grand (2008), Dynamic topography and long-term sea-level variations: There is no such thing as a stable continental platform, *Earth. Planet. Sci. Lett.*, 271(1), 101-108.

Parman, S. W., T. L. Grove, J. C. Dann, and M. J. De Wit (2004), A subduction origin for komatiites and cratonic lithospheric mantle, *S. Afr. J. Geol.*, 107(1-2), 107–118, doi:10.2113/107.1-2.107.

Parker, E. H., R. B. Hawman, K. M. Fischer, and L. S. Wagner (2013), Crustal evolution across the southern Appalachians: Initial results from the SESAME broadband array, *Geophys. Res. Lett.*, 40(15), 3853-3857.

Pearson, D. G., and N. Wittig (2008), Formation of Archaean continental lithosphere and its diamonds: The root of the problem, *J. Geol. Soc.*, 165(5), 895–914, doi:10.1144/0016-76492008-003.

Pollitz, F. F., and W. D. Mooney (2016), Seismic velocity structure of the crust and shallow mantle of the Central and Eastern United States by surface wave imaging, *Geophys. Res. Lett.*

Porritt, R. W., R. M. Allen, and F. F. Pollitz (2014), Seismic imaging east of the Rocky Mountains with USArray, *Earth Planet. Sci. Lett.*, 402, 16–25, doi:10.1016/j.epsl.2013.10.034.

Porter, R., Y. Liu, and W. E. Holt (2016), Lithospheric records of orogeny within the continental U.S., *Geophys. Res. Lett.*, 43, 144-153, doi:10.1002/2015GL066950.

Powell, C. A., and W. A. Thomas (2016), Grenville basement structure associated with the Eastern Tennessee seismic zone, southeastern USA, *Geology*, 44(1), 39-42.

Priestley, K., and D. McKenzie (2006), The thermal structure of the lithosphere from shear wave velocities, *Earth. Planet. Sci. Lett.*, 244(1), 285-301.

Prince, P. S., J. A. Spotila, and W. S. Henika (2010), New physical evidence of the role of stream capture in active retreat of the Blue Ridge escarpment, southern Appalachians, *Geomorphology*, 123, 305-319.

Rader, E., E. Emry, N. Schmerr, D. Frost, C. Cheng, J. Menard, C. Q. Yu, and D. Geist (2015), Characterization and petrological constraints of the mid-lithospheric discontinuity, *Geochem. Geophys. Geosyst.*, 16(10), 3484-3504, doi:10.1002/2015GC005943.

Rowley, D. B., A. M. Forte, R. Moucha, J. X. Mitrovica, N. A. Simmons, and S. P. Grand (2013), Dynamic topography change of the eastern United States since 3 million years ago, *Science*, 340(6140), 1560-1563.

Rychert, C. A., and P. M. Shearer (2009), A global view of the lithosphere-asthenosphere boundary, *Science*, 324(5926), 495–498, doi:10.1126/science.1169754.

Rychert, C. A., K. M. Fischer, and S. Rondenay (2005), A sharp lithosphere–asthenosphere boundary imaged beneath eastern North America, *Nature*, 436(7050), 542–545, doi:10.1038/nature03904.

Rychert, C. A., S. Rondenay, and K. M. Fischer (2007), P-to-S and S-to-P imaging of a sharp lithosphere-asthenosphere boundary beneath eastern North America, *J. Geophys. Res.*, 112, B08314, doi:10.1029/2006JB004619.

Schmandt, B., and E. Humphreys (2010), Complex subduction and small-scale convection revealed by body-wave tomography of the western United States upper mantle, *Earth Planet. Sci. Lett.*, 297(3), 435–445, doi:10.1016/j.epsl.2010.06.047.

Schmandt, B., and F.-C. Lin (2014), P and S wave tomography of the mantle beneath the United States, *Geophys. Res. Lett.*, 41, 6342–6349, doi:10.1002/2014GL061231.

Schmandt, B., F.-C. Lin, and K. E. Karlstrom (2015), Distinct crustal isostasy trends east and west of the Rocky Mountain Front, *Geophys. Res. Lett.*

Schmerr, N. (2012), The Gutenberg discontinuity: Melt at the lithosphere-asthenosphere boundary, *Science*, 335(6075), 1480–1483, doi:10.1126/science.1215433.

Selway, K., H. Ford, and P. Kelemen (2015), The seismic mid-lithosphere discontinuity, *Earth Planet. Sci. Lett.*, 414, 45–57, doi:10.1016/j.epsl.2014.12.029.

Sigloch, K. (2011), Mantle provinces under North America from multifrequency P wave tomography, *Geochem. Geophys. Geosyst.*, 12, Q02W08, doi:10.1029/2010GC003421.

Sleep, N. H. (1990), Monterey hotspot track: A long-lived mantle plume, *J. Geophys. Res.*, 95(B13), 21983-21990.

Thomas, W. A. (1977), Evolution of Appalachian-Ouachita salients and recesses from reentrants and promontories in the continental margin, *Am. J. Sci.*, 277, 1233-1278.

Thomas, W. A. (2006), Tectonic inheritance at a continental margin, *GSA Today*, 16(2), 4-11.

Till, C. B., L. T. Elkins-Tanton, and K. M. Fischer (2010), A mechanism for low-extent melts at the lithosphere-asthenosphere boundary, *Geochem. Geophys. Geosyst.*, 11(10).

Till, C.B., T. L. Grove, R. W. Carlson, J. M. Donnelly-Nolan, M. J. Fouch, L. S. Wagner, W. K. Hart (2013), Depths and temperatures of <10.5 Ma mantle melting and the lithosphere–asthenosphere boundary below southern Oregon and northern California, *Geochem. Geophys. Geosyst.*, 14(4), 864–879.

van der Lee, S., and G. Nolet (1997), Upper mantle S velocity structure of North America, *J. Geophys. Res.*, 102(B10), 22,815–22,838.

van der Velden, A. J., and F. A. Cook (2005), Relict subduction zones in Canada, *J. Geophys. Res.*, 110, B08403, doi:10.1029/2004JB003333.

Villemaire, M., F. A. Darbyshire, and I. D. Bastow (2012), P-wave tomography of eastern North America: Evidence for mantle evolution from Archean to Phanerozoic, and modification during subsequent hot spot tectonism, *J. Geophys. Res.* 117(B12).

Wagner, L. S., K. Stewart, and K. Metcalf (2012), Crustal-scale shortening structures beneath the Blue Ridge Mountains, North Carolina, USA, *Lithosphere*, 4(3), 242-256.

Wehr, F. and L. Glover (1985), Stratigraphy and tectonics of the Virginia-North Carolina Blue Ridge: Evolution of a late Proterozoic-early Paleozoic hinge zone, *Geol. Soc. Am. Bull.*, 96(3), 285-295.

White, D. J., G. Musacchio, H. H. Helmstaedt, R. M. Harrap, P. C. Thurston, A. Van der Velden, and K. Hall (2003), Images of a lower-crustal oceanic slab: Direct evidence for tectonic accretion in the Archean western Superior province, *Geology*, 31(11), 997–1000, doi:10.1130/G20014.1.

Whitmeyer, S. J., and K. E. Karlstrom (2007), Tectonic model for the Proterozoic growth of North America, *Geosphere*, 3(4), 220–259, doi:10.1130/GES00055.1.

Wilson, D. C., D. A. Angus, J. F. Ni, and S. P. Grand (2006), Constraints on the interpretation of S-to-P receiver functions, *Geophys. J. Int.*, 165(3), 969–980, doi:10.1111/j.1365-246X.2006.02981.x.

Wirth, E. A., and M. D. Long (2014), A contrast in anisotropy across mid-lithospheric discontinuities beneath the central United States—A relic of craton formation, *Geology*, 42(10), 851–854, doi:10.1130/G35804.1.

Yuan, H., and B. Romanowicz (2010), Lithospheric layering in the North American craton, *Nature*, 466(7310), 1063–1068, doi:10.1038/nature09332.

Figures

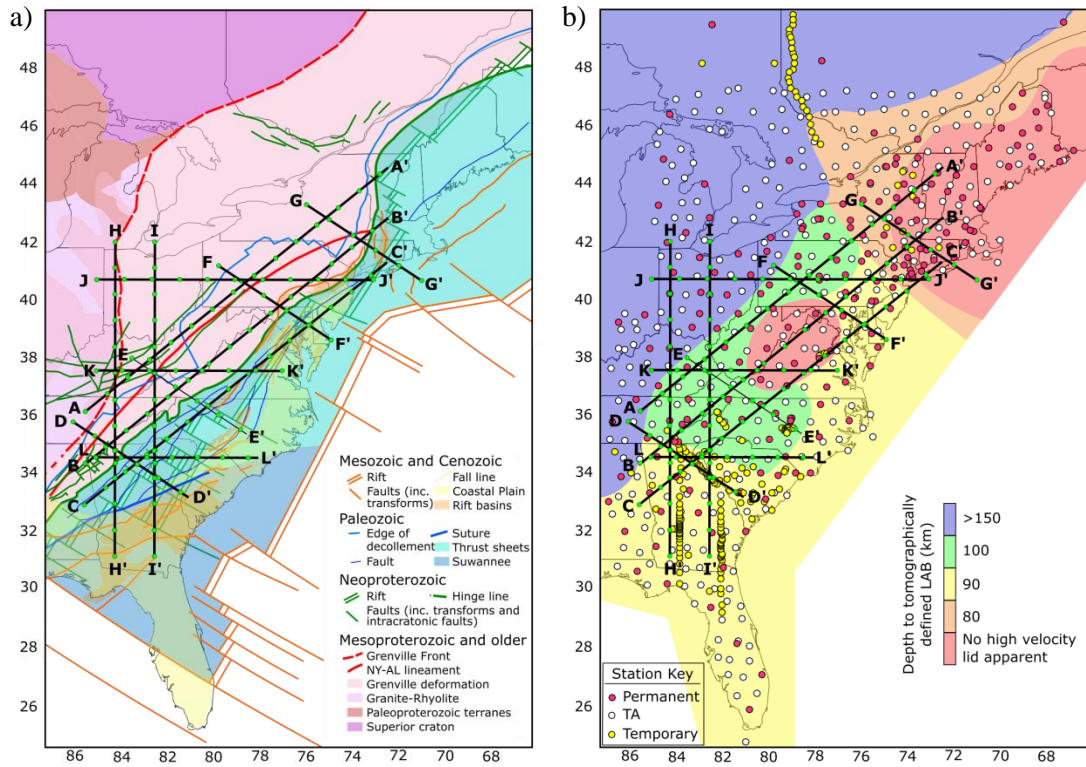


Figure 1: Maps of the study region. Thick black lines with green circles: cross section locations; small green circles correspond to circles in cross section figures. a) Simplified geological map, after Thomas [2006], showing the major terranes and faulted boundaries generated during the episodes of rifting and continental collision since the Mesoproterozoic. b) Lithospheric thickness map, estimated from local seismic tomography models based on the depth extent of fast velocity anomalies and the depth range of the largest negative gradient in seismic velocity [Villemaire et al., 2012; Pollitz and Mooney, 2016; Schmandt et al., 2015]. Circles show the station distribution.

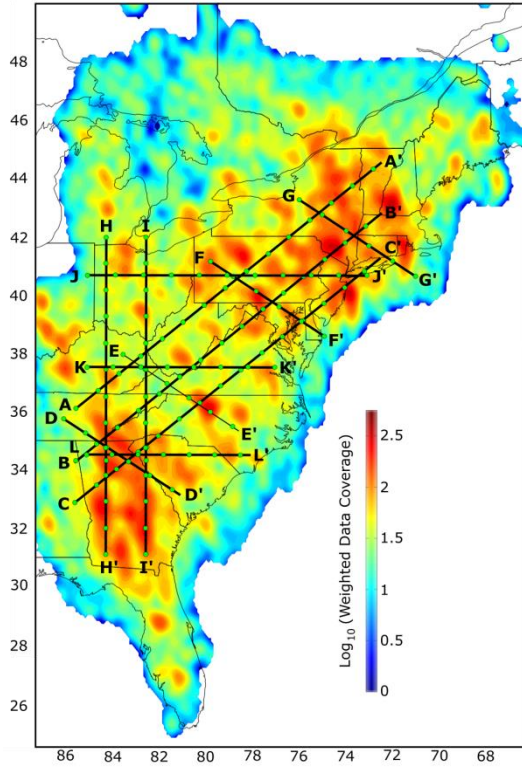


Figure 2: Spatial distribution of Sp phases at 100 km depth. Logarithmically scaled plot of the number of phases contributing to the Sp CCP stack at a given point, taking into account the weighting factor applied to each phase by the spline function representation of its Fresnel zone [Lekić et al., 2011].

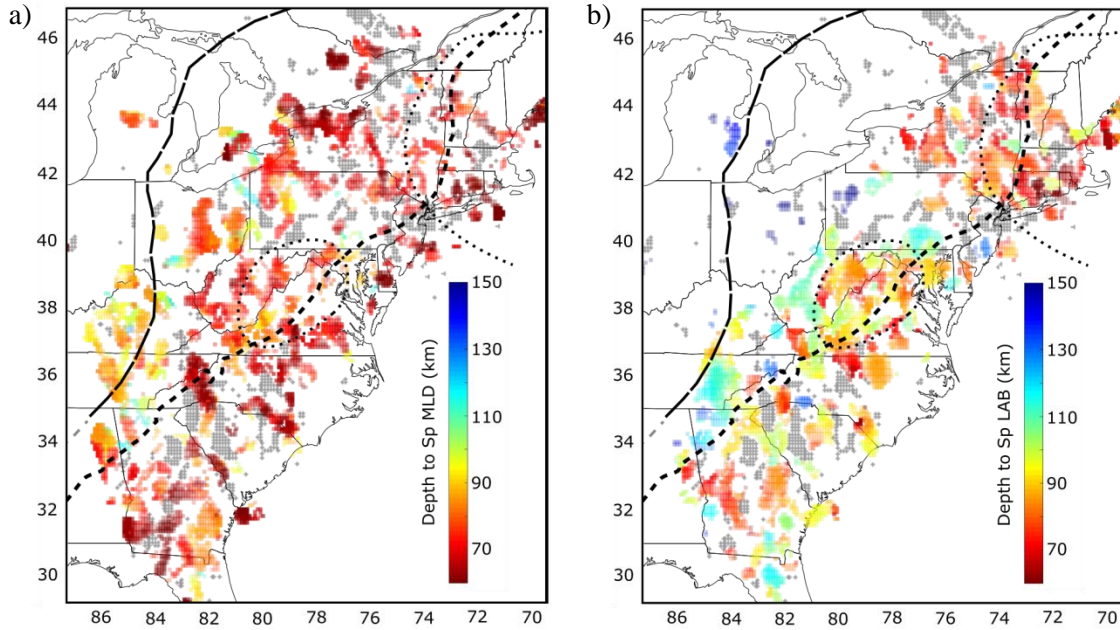


Figure 3: Depth map of automated Sp NVGs picks, separated into MLDs and LABs as described in Section 2.3. Plotted colored squares approximately correspond to the size of the model point (0.1° in latitude and longitude). Phase amplitude is indicated by the degree of transparency of the plotted point. The thick black lines correspond to significant boundaries shown in Figure 1. Long dashed line: Grenville Front, marking the northwestern limit of significant Grenville deformation (as red dashed line, Figure 1a). Short dashed line: hinge zone, marking the transition to highly extended crust during Proterozoic rifting (as green dashed line, Figure 1a). Dotted lines: regions of thinned lithosphere, as identified from seismic tomography (as Figure 1b). a) Phases classed as MLDs only. b) Phases classed as LABs only.

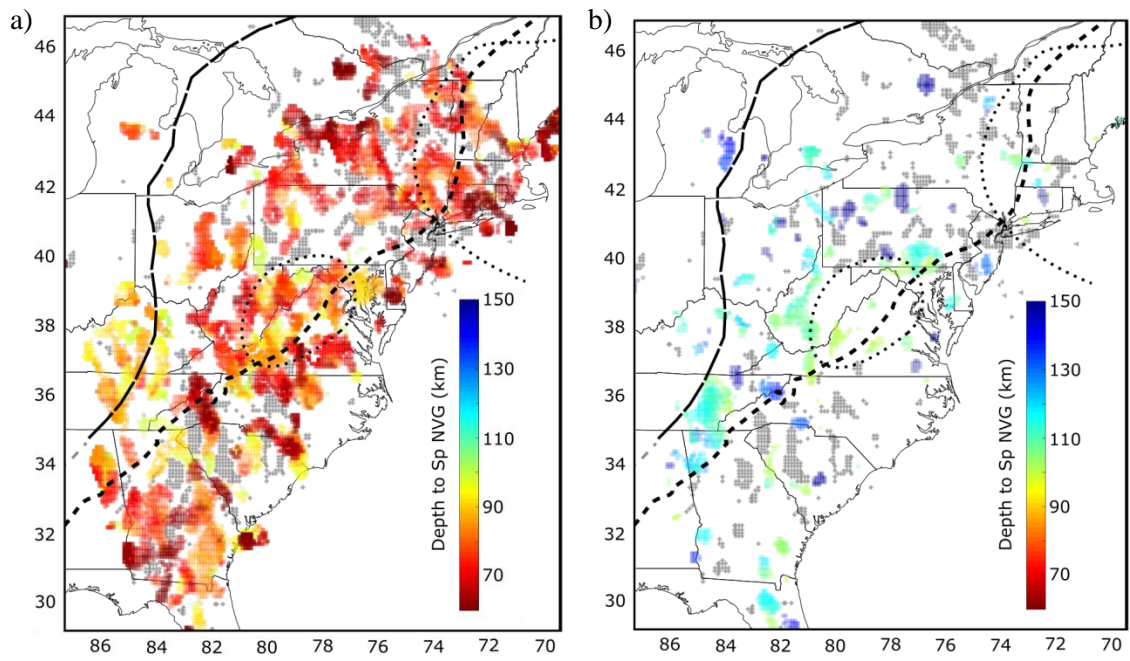


Figure 4: Depth map of automated Sp NVGs picks, as Figure 3. Here, all picked NVGs are plotted, and are separated only according to phase depth. Both panels use the same color scale as Figure 3. a) Sp NVGs shallower than 100 km depth. b) Sp NVGs deeper than 100 km depth.

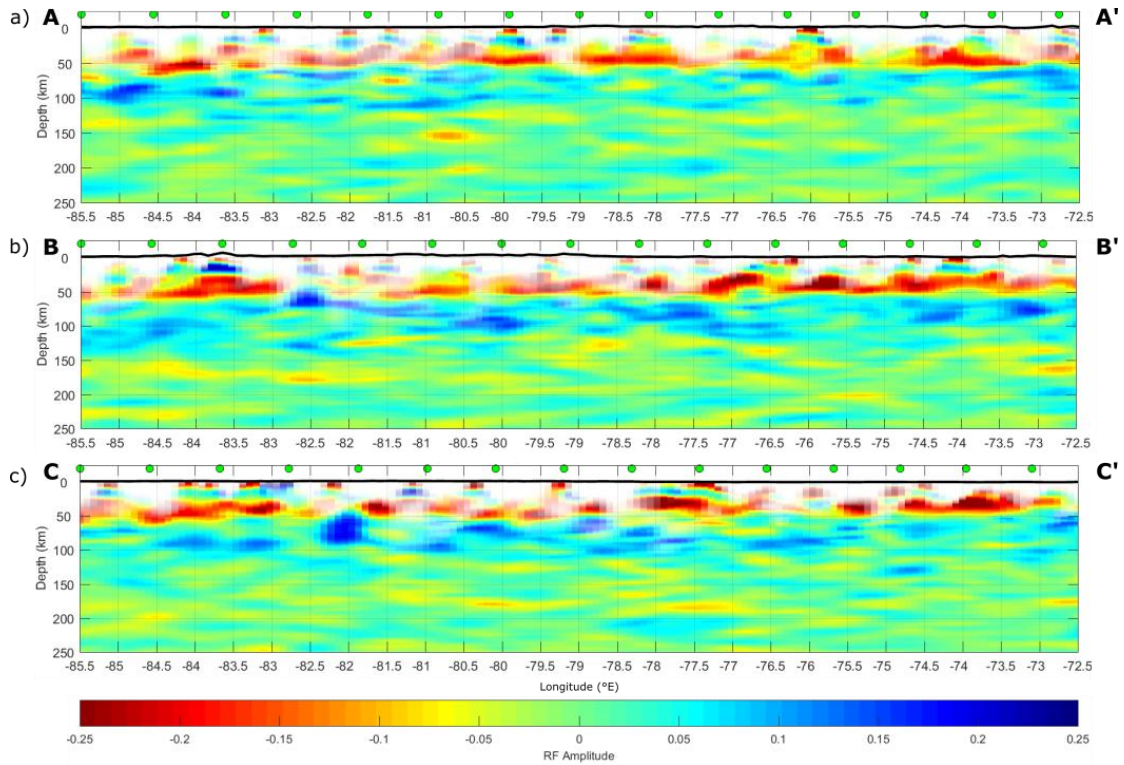


Figure 5: Cross-sections through mean of bootstrapped Sp CCP stack. Cross-section locations shown in Figures 1 and 2 with corresponding green circles. A white mask covers regions with poor data coverage, with the transparency of the mask increasing with increasing data coverage. This mask is completely transparent at model points with more than 50 total weighted waveforms contributing. The CCP stack is from data filtered at 4–33 s, with a dominant period of 10 s. Thick black line: topography, at $5 \times$ vertical exaggeration. a) Cross-section A–A’ traverses the undeformed Granite-Rhyolite province, the region of extensive Grenville deformation, and the New England low velocity anomaly. It runs from 36.2°N , 85.5°W to 44.5°N , 72.5°W . b) Cross-section B–B’ runs just northwest of the hinge zone, and traverses the Virginia low velocity anomaly. It runs from 34.4°N , 85.5°W to 42.7°N , 72.5°W . c) Cross-section C–C’ runs just southeast of the hinge zone, from 33°N , 85.5°W to 41.3°N , 72.5°W .

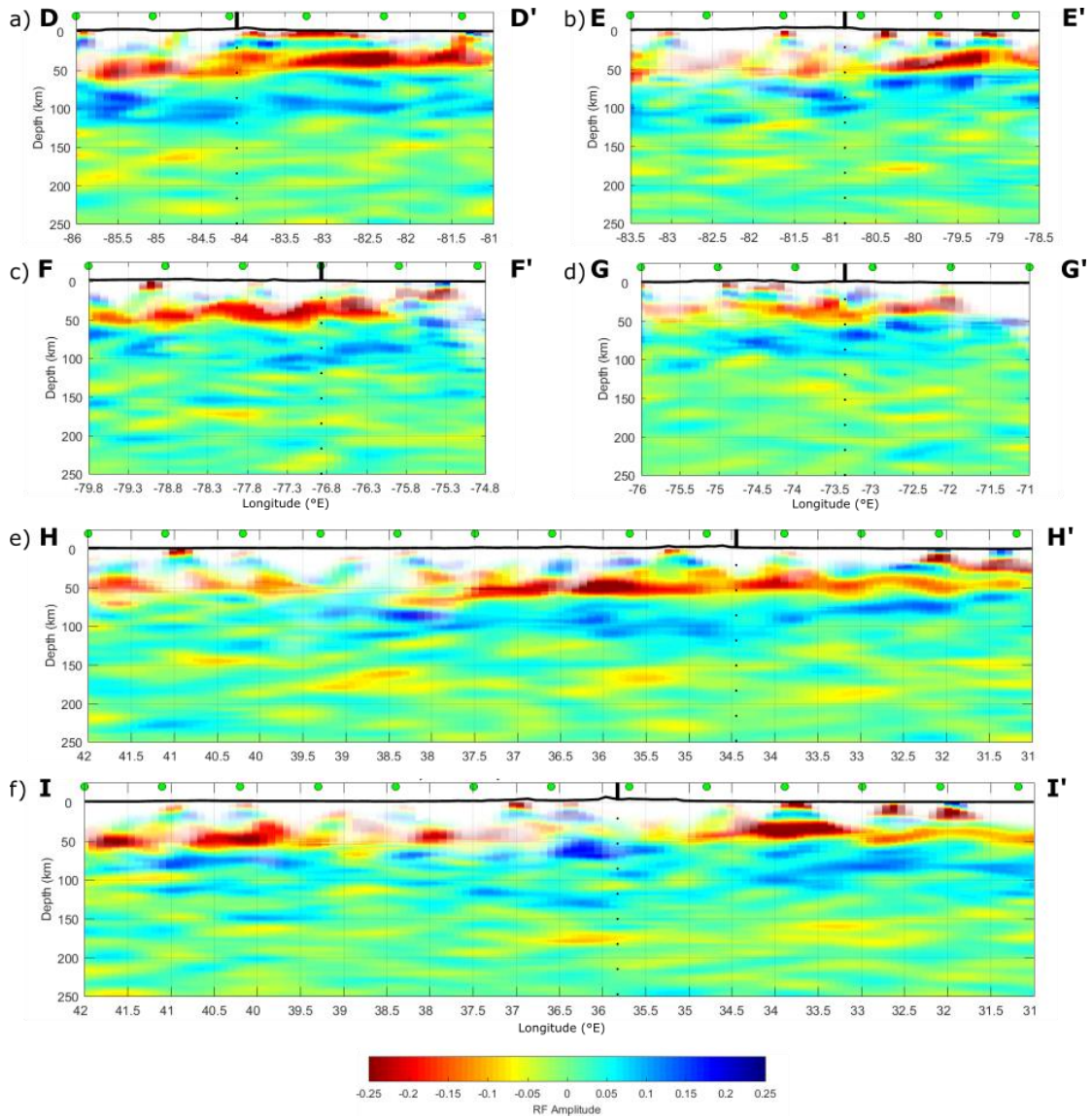


Figure 6: Cross-sections through mean of bootstrapped Sp CCP stack filtered at 4-33 s, as Figure 5. The vertical black, dashed line marks where the profile crosses the hinge zone, the Proterozoic rift boundary associated with a decrease in lithospheric thickness from west to east. Panels a-d run approximately perpendicular to the hinge zone; panels e and f run from north to south. a) Cross-section D-D' runs from 35.8°N, 86°W to 33.2°N, 81°W. b) Cross-section E-E' runs from 38°N, 83.5°W to 34.5°N, 78.5°W. c) Cross-section F-F' runs from 41.2°N, 79.8°W to 38.6°N, 74.8°W. d) Cross-section G-G' is on the margin of the New England low velocity anomaly; it runs from 43.3°N, 76°W to 40.7°N, 71°W. e) Cross-section H-H' runs from 42°N, 84.2°W to 31°N, 84.2°W. f) Cross-section I-I' runs from 42°N, 82.5°W to 31°N, 82.5°W.

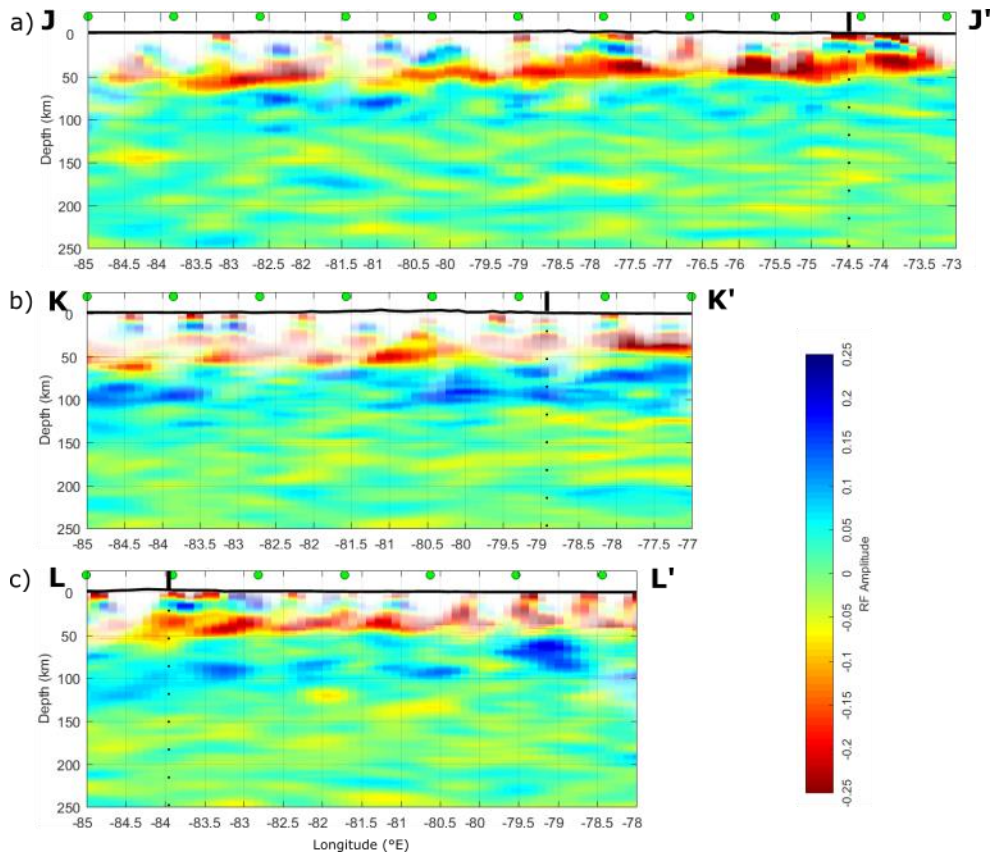


Figure 7: Cross-sections through mean of bootstrapped Sp CCP stack filtered at 4-33 s, as Figure 5. The vertical black, dashed line marks where the profile crosses the hinge zone. This is generally associated with a decrease in lithospheric thickness from west to east, but the lithosphere in these sections has been disrupted. a) Cross-section J-J' traverses the region of extensive Grenville deformation, including the seismically transparent region around the Pennsylvania salient. It runs from 40.7°N, 85°W to 40.7°N, 73°W. b) Cross-section K-K' traverses the Granite-Rhyolite province, the region of Grenville deformation and the margin of the Virginia low velocity anomaly, where the LAB is particularly strong. It runs from 37.6°N, 85°W to 37.6°N, 77°W. c) Cross-section L-L' traverses the rifted Iapetan margin in the zone of Appalachian deformation. The thinning across the hinge zone is clearly imaged here, as is the segmented LAB beneath South Carolina. It runs from 34.6°N, 85°W to 34.6°N, 78°W.

CHAPTER 3

Reimagining the end of the Appalachian Orogeny: Crustal structures in the southeast U.S.

Emily Hopper¹, Karen M. Fischer¹, Lara S. Wagner², Robert B. Hawman³

¹Department of Earth, Environmental and Planetary Sciences, Brown University, Providence, RI, USA

²Department of Terrestrial Magmatism, Carnegie Institution for Science, Washington, D.C., USA

³Department of Geology, University of Georgia, Athens, GA, USA

Abstract

The Appalachians were formed by tectonic plate convergence in a series of accretion episodes during the Paleozoic, but plate motions and deformation during the terminal collision between Laurentia (proto-North America) and Gondwana (proto-Africa/South America) have remained enigmatic [Hatcher, 2010; Hibbard et al., 2010; Mueller et al., 2014; Pollock et al., 2012]. Little of the suture that marks the ancient join between Laurentian and Gondwanan lithosphere is left on land today, and where it is preserved in the southeast U.S., it is buried beneath younger sediments. Here, we image the suture as a low angle ($<12^\circ$) southward-dipping interface that soles into a flat-lying mid-crustal decollement. The suture extends >330 km down dip and at least 360 km along strike. Previously, the suture was thought to be steeply dipping to Moho depths [McBride and Nelson, 1988; Nelson et al., 1985], and permitted a variety of final Laurentia-Gondwana collision models, ranging from largely strike-slip to head-on convergence [Hatcher, 2010; Hibbard et al., 2010; Mueller et al., 2014; Pollock et al., 2012]. The suture geometry observed in this study implies over 300 km of shortening, indicating that the culmination of Appalachian accretion in this location was highly convergent. The structure of this plate boundary is typical of many ongoing orogenies [Ammirati et al., 2015; Caldwell et al., 2013; Cook and Varsek, 1994; Huang et al., 2015; Lacombe and Mouthereau, 2002; Schulte-Pelkum et al., 2005], suggesting that this mode of deformation was and is fundamental in continental collisions.

Main Text

The Suwannee terrane, comprising Florida and parts of southern Georgia (Figure 1), is associated with Gondwana based on stratigraphic and paleontological affinities as identified in borehole samples [Chowns and Williams, 1983; Hatcher, 2010]. In the 1970s and 1980s, extensive reflection profiling in this region imaged dipping features that appeared to extend to the Moho, and these were interpreted to be caused by a steep (dip at least 30°), through-going crustal suture [Cook and Vasudevan, 2006; McBride and Nelson, 1988; McBride et al., 2005; Nelson et al., 1985] (pink dashed lines, Figure 1). The location of this suture zone has been debated; outcrop and borehole patterns instead suggest a northeastern suture zone strike [Thomas, 2010] (pink dotted lines, Figure 1). In contrast to the Suwannee suture, earlier accreted terranes that lie to the northwest are commonly interpreted as thin, allochthonous sheets that overthrust Paleozoic sediments of the Laurentian margin by hundreds of kilometers [Cook and Vasudevan, 2006; Cook et al. 1979; McBride et al., 2005].

This study obtained new constraints on crust and uppermost mantle structure from the Laurentian interior to the Suwannee terrane, including the geometry of the suture, using common conversion point (CCP) stacking of S-to-P (Sp) converted waves recorded by the 85 stations of the 2010-2014 EarthScope Southeastern Suture of the Appalachian Margin Experiment (SESAME), the EarthScope Transportable Array (TA), and other broadband stations (Figure 1). Higher resolution of crustal structure was enabled by the close spacing of SESAME stations (~5 km across the near-surface suture location, increasing to ~35 km) and the retention of shorter periods (1-33 s) than is commonly possible with Sp imaging (see Supplementary Materials). In the resulting images (Figure 2) positive (red) phases correspond to a localized positive velocity gradient (PVG) with increasing depth; negative (blue) phases correspond to a negative velocity gradient (NVG).

The Sp CCP stack reveals the large-scale structure of the crust beneath the southern Appalachians. The PVG at 35-55 km depth represents the Moho, seen to deepen beneath the mountains (Figure 2c at 60-150 km distance and the northern end of Figure 2a), as predicted by isostasy. Crustal thickness variations agree well with previous P-to-S imaging using SESAME [Parker et al., 2013] (Figure 2c) and TA data [Schmandt et al., 2015] (Figure 2a, b), demonstrating the ability of Sp waves to image crustal structure. Relatively thick crust beneath the Suwannee terrane (40 km at $\sim 31^\circ\text{N}$, Figure 2b) is also consistent with previous P-to-S results [French et al., 2009; Schmandt et al., 2015].

Within the crust, we observe a large amplitude PVG that extends from the surface at the northern limit of the Suwannee suture zone (32.8°N , Figure 2a; 33.2°N , Figure 2b), dips south-southeastward at a maximum of 12° (to 31.5°N , Figure 2a; 32°N Figure 2b), then levels out in the mid-to-lower crust (18-22 km depth) moving southward beneath the Suwannee terrane. This feature is imaged over >360 km along strike (Figure S1).

Given that this strong southward dipping crustal PVG reaches the near-surface within the suture zone defined by outcrop and borehole data [Thomas, 2010] (Figure 1) we interpret it as the suture between Laurentia and previously accreted peri-Gondwanan terranes with the Gondwanan-affinity Suwannee terrane. The shallow limit of the PVG approximately coincides with the northern edge of the Charleston magnetic anomaly terrane; this boundary was inferred to be the suture in early interpretations [Higgins and Zietz, 1983], in contrast to later studies [McBride and Nelson, 1988; Nelson et al., 1985] that associated the suture with the more southern negative Brunswick Magnetic Anomaly. We do not observe collisional structures within the mantle lithosphere that are consistent or analogous to the crustal PVG (Figure S2). The shallow limit of the crustal PVG is also spatially correlated with the northern edge of the thick sedimentary basins in this region. However, testing with synthetic seismograms indicates that the observed dipping

PVG cannot be explained by phases generated by sedimentary structures alone (Supplementary Materials; Figures S3 and S4).

The shallow dip of the suture interface we observe contrasts with the more steeply dipping structure ($>30^\circ$) interpreted from reflection profiles [McBride and Nelson, 1988; Nelson et al., 1985], which appears to intersect the Moho and could have accommodated significant strike-slip motion. However, re-migration of these observed reflections with more accurate models of crustal velocity [Schmandt et al., 2015] (also see Supplementary Materials) demonstrates that they are consistent with our images of a much lower angle boundary (Figure S5). Moreover, the dipping reflections in eastern Georgia are at comparable depths to the sub-horizontal portion of our observed suture phase, resolving the longstanding discrepancy between suture zone locations in eastern Georgia inferred from geological data [Thomas, 2010] versus reflection profiles [McBride and Nelson, 1988; Nelson et al., 1985] (Figure 1). The Sp CCP stack suture phase is also comparable to more recent active source observations. The deeper (>15 km) portion of this PVG coincides in depth with preliminary observations of wide-angle reflections from the active source SUGAR experiment [Shillington et al., 2015], indicating it is a sharp boundary in depth.

Due to its apparent continuity, we prefer to interpret the suture interface as a single, continuous lithological boundary. Alternative interpretations require greater complexity and coincidence. For example, a suture ramp that terminates at a mid-crustal velocity contrast within Suwannee crust would require 1) a prominent mid-crustal gradient in the Suwannee crust; 2) no such gradient in nearby Laurentian crust; 3) sufficiently similar lower crustal velocities in these juxtaposed terranes that the suture phase is invisible to Sp waves in the lower crust. Although this region experienced extension during the Mesozoic, the observed interface is poorly correlated with the rift basins and intruded sills documented by reflection and borehole data [McBride et al., 1989; McBride, 1991] (Figure 1), and does not appear to be a rift-generated structure. For

example, the interface is present north of the rift zone, and in eastern Georgia (Figure 2a) it extends >200 km south of the rift zone.

Low grade, andalusite-bearing lower Paleozoic shales retrieved from Suwannee boreholes [Milton, 1972] indicate that these now near-surface rocks were buried to no more than ~10 km, hence the suture detachment was at a maximum of ~30 km depth when active. A maximum depth of 20-30 km is comparable to detachments in modern orogens (e.g. 20-40 km in the Himalayas [Caldwell et al., 2013; Schulte-Pelkum et al., 2005], 13-17 km in Taiwan [Huang et al., 2015], 10-20 km in the Alps [Lacombe and Mouthereau, 2002], 20-30 km in the Sierras Pampeanas [Ammirati et al., 2015]).

The ramp-and-flat geometry of the shallowly dipping suture interface indicates that the final contact along this boundary was highly collisional, with the Suwannee terrane overthrusting the Laurentian basement or previously accreted terranes over a distance of at least 330 km. This geometry implies that any significant strike-slip motion during the late stages of the Appalachian orogeny occurred previous to this overthrusting, outside of this suture zone, or (implausibly) have faulted perfectly along strike of the dipping suture phase, such that no offset is visible in this structure.

The strong, sharp velocity contrast implied by the suture feature could be created by a juxtaposition of different lithologies across this apparent shear zone. Borehole samples of Suwannee basement are predominantly felsic and sedimentary lithologies [Chowns and Williams, 1983]; these may abut a sliver of the earlier accreted mafic arc volcanics of the Carolina terrane [Cook and Vasudevan, 2006; Hibbard et al., 2002; Steltenpohl et al., 2008] (Figure 3a). Laboratory measured seismic velocities show a 17-18% isotropic velocity contrast between andesite or metagreywackes and greenschist-facies basalt at PT conditions appropriate to 20 km depth [Christensen and Mooney, 1995], a contrast capable of generating the Sp phases from the

suture interface (Figure S3). Alternatively, a boundary representing this much thrusting might be expected to have some anisotropic character. However, the observed backazimuthal variation in the data is explained by suture dip (Figure S6) and does not require anisotropy.

North of the suture, the crystalline sheets of the Blue Ridge-Piedmont overthrust reflective, laminated platform sediments across an upper crustal detachment [Cook et al., 1979; Cook and Vasudevan, 2006; Parker et al., 2015]. At these latitudes we observe a positive/negative phase pair at comparable depths (PVG at <5 km depth and NVG at 10-15 km depth: 35.3-32.8°N, Figure 2a; 40-330 km along profile, Figure 2c; Figure S3). The observed phases could be generated by a radially anisotropic layer with a vertical or near-vertical slow symmetry axis, i.e. subhorizontal laminated sediments (white dotted line, Figure 2a; Figure S3), although we cannot rule out other models with these Sp observations alone (e.g. an isotropic fast layer). Such a layer of weak buried sediments may have localized slip at depth, allowing the formation of the observed long, near-flat detachment. Continuation of a layer of radially anisotropic sediments along the suture interface cannot generate the ramp section of the Sp suture phases (Figure S7), but the presence of underthrust platform sediments beneath the ramp section of the suture, as inferred from reflection data [McBride and Nelson, 1988], is possible.

Based on these results, we conclude that the final stages of the building of the southern Appalachians involved the north-northwestward overthrusting of the Gondwanan Suwannee terrane onto the Laurentian plate (Figure 3). At the beginning of the last phase of the orogeny (the Alleghanian), the Suwannee terrane collided with the Laurentian margin and the previously-docked Carolina terrane (Figure 3a, top panel). As the collision progressed, the Suwannee terrane overthrust Laurentian lower crust (Figure 3a, middle panel) along a mid-crustal detachment at 20-30 km depth that ramped up at a shallow angle to the near-surface. A sliver of Carolina terrane may be the origin of the strong velocity contrast required to generate the observed Sp phase. By the final stages of collision, the Suwannee terrane had overthrust the margin by >330 km (Figure

3a, lower panel). The extension of Laurentian basement this far south matches the Grenville (i.e. Laurentian) model ages calculated for the lower crust and/or lithosphere of the Suwannee terrane [Mueller et al., 2014]. This interpretation requires that the Proterozoic rifted margin of Laurentia lies further south than previously inferred [Thomas, 2010].

The geometry of the Suwannee suture precludes extensive strike-slip motion accommodated on the suture itself, negating models that include such motion [Mueller et al., 2014; Pollock et al., 2012] and supporting those that instead invoke significant shortening on the suture [Hatcher, 2010]. As such, while there may have been strike-slip motion accommodated elsewhere or earlier in time, the culmination of the Appalachian mountain building must have been driven by the near head-on collision of Laurentia and Gondwana, with the Suwannee terrane at the prow. The long, low-angle detachment formed by this collision is a deformation style common to orogens past and present [Ammirati et al., 2015; Caldwell et al., 2013; Cook and Varsek, 1994; Huang et al., 2015; Lacombe and Mouthereau, 2002; Schulte-Pelkum et al., 2005].

Acknowledgments

We thank the many people who made the SESAME array possible: the staff of the Incorporated Research Institutions for Seismology (IRIS) PASSCAL Instrument Center at New Mexico Tech, the student/postdoctoral field crews (in particular, Horry Parker), and the landowners who hosted stations. We also thank Donna Shillington for sharing early results from the SUGAR experiment. The instruments used in the field program were provided by the IRIS PASSCAL facility, and waveform data were accessed through the IRIS Data Management Center. This work was funded by the NSF EarthScope Program under the American Recovery and Reinvestment Act of 2009 (Public Law 111-S) through awards EAR-0844276 (K.M.F.), EAR-0844186 (L.S.W.), and EAR-0844154 (R.B.H.). Data from the TA network were made freely available as part of the

EarthScope USArray facility, operated by IRIS. IRIS is funded through the Seismological Facilities for the Advancement of Geoscience and EarthScope (SAGE) Proposal of the National Science Foundation under Cooperative Agreement EAR-1261681. In addition to SESAME (doi:10.7914/SN/Z9_2010) and TA (doi:10.7914/SN/TA) data, this study employed data from the following permanent networks: the Central and Eastern US Network (doi:10.7914/SN/N4), the Global Seismograph Network ([doi:10.7914/SN/IU](https://doi.org/10.7914/SN/IU)), the Penn State Network (<http://eqseis.geosc.psu.edu>) and the United States National Seismic Network ([doi:10.7914/SN/US](https://doi.org/10.7914/SN/US)); and data from the following temporary arrays: AST, FLED (doi:10.7914/SN/XR_2001), PHRACCS , and SCEPP (doi:10.7914/SN/SP).

References

Ammirati, J.-B., Alvarado, P. & Beck, S. A lithospheric velocity model for the flat slab region of Argentina from joint inversion of Rayleigh wave phase velocity dispersion and teleseismic receiver functions. *Geophysical Journal International* **202**, 224-241 (2015)

Caldwell, W. B., Klemperer, S. L., Lawrence, J. F., Rai, S. S. & Ashish, A. Characterizing the Main Himalayan Thrust in the Garhwal Himalaya, India with receiver function CCP stacking. *Earth and Planetary Science Letters* **367**, 15-27 (2013)

Chowns, T. M. & Williams, C. T. Pre-Cretaceous rocks beneath the Georgia Coastal Plain – Regional implications. In Gohn, G. S., ed., *Studies related to the Charleston, South Carolina, earthquake of 1886 – Tectonics and seismicity: USGS Professional Paper 1313-L*, L1-L42 (1983)

Christensen, N. I. & Mooney, W. D. Seismic velocity structure and composition of the continental crust: A global view. *Journal of Geophysical Research* **100**, 9761-9788 (1995)

Cook, F. A. *et al.* Thin-skinned tectonics in the crystalline southern Appalachians; COCORP seismic-reflection profiling of the Blue Ridge and Piedmont. *Geology* **7**, 563-567 (1979)

Cook, F. A., & Varsek, J. L. Orogen-scale decollements. *Reviews of Geophysics* **32**, 37-60 (1994)

Cook, F. A. & Vasudevan, K. Reprocessing and enhanced interpretation of the initial COCORP Southern Appalachians traverse. *Tectonophysics* **420**, 161-174 (2006)

French, S. W., Fischer, K. M., Syracuse, E. M. & Wyssession, M. E. Crustal structure beneath the Florida-to-Edmonton broadband seismometer array. *Geophysical Research Letters* **36**, L08309 (2008)

Hatcher, R. D. The Appalachian orogeny: A brief summary. *Geol. Soc. America Memoir* **206**, 1-19 (2010)

Hibbard, J. P., Stoddard, E. F., Secor, D. T. & Dennis, A. J. The Carolina Zone: overview of Neoproterozoic to Early Paleozoic peri-Gondwanan terranes along the eastern flank of the southern Appalachians. *Earth-Science Reviews* **57**, 299-339 (2002)

Hibbard, J. P., van Staal, C. R. & Rankin, D. W. Comparative analysis of the geological evolution of the northern and southern Appalachian orogeny: Late Ordovician-Permian. *Geological Society of America Memoir* **206**, 51-69 (2010)

Higgins, M.W. & Zietz, I. Geologic interpretation of geophysical maps of the pre-Cretaceous "basement" beneath the Coastal Plain of the Southeastern United States. *Geological Society of America Memoirs* **158**, 125-130 (1983)

Huang, T.-Y., Gung, Y., Kuo, B.-Y., Chiao, L.-Y. & Chen, Y.-N. Layered deformation in the Taiwan orogeny. *Science* **349**, 720-723 (2015)

Lacombe, O. & Mouthereau, F. Basement-involved shortening and deep detachment tectonics in forelands of orogens: Insights from recent collision belts (Taiwan, Western Alps, Pyrenees). *Tectonics* **21**, doi:10.1029/2001TC901018 (2002)

McBride, J. H. Constraints on the structure and tectonic development of the early Mesozoic south Georgia rift, southeastern United States; seismic reflection data processing and interpretation. *Tectonics* **10**, 1065-1083 (1991)

McBride, J. H. & Nelson, K. D. Integration of COCORP deep reflection and magnetic anomaly analysis in the southeastern United States: Implications for origin of the Brunswick and East Coast magnetic anomalies. *Geological Society of America Bulletin* **100**, 436-445 (1988)

McBride, J. H., Nelson, K. D. & Brown, L. D. Evidence and implications of an extensive early Mesozoic rift basin and basalt/diabase sequence beneath the southeast Coastal Plain. *Geological Society of America Bulletin* **101**, 512-520 (1989)

McBride, J. H., Hatcher, R. D., Stephenson, W. J. & Hooper, R. J. Integrating seismic reflection and geological data and interpretations across an internal basement massif: The southern Appalachian Pine Mountain window, USA. *Geological Society of America Bulletin* **117**, 669-686 (2005)

Milton, C. Igneous and metamorphic basement rocks of Florida. *Florida Bureau of Geology Bulletin* **55**, 125 (1972)

Mueller, P. A., Heatherington, A. L., Foster, D. A., Thomas, W. A. & Wooden, J. L. The Suwannee suture: Significance for Gondwana-Laurentia terrane transfer and formation of Pangaea. *Gondwana Research* **26**, 355-373 (2014)

Nelson, K. D. *et al.* New COCORP profiling in the southeastern United States. Part I: Late Paleozoic suture and Mesozoic rift basin. *Geology* **13**, 714-718 (1985)

Parker, E. H. Jr., Hawman, R. B., Fischer, K. M. & Wagner, L. S. Crustal evolution across the Southern Appalachians: Initial results from the SESAME broadband array. *Geophysical Research Letters* **40**, 3853-3857 (2013)

Parker, E. H. Jr., Hawman, R. B., Fischer, K. M. & Wagner, L. S. Constraining lithologic variability along the Alleghanian detachment in the southern Appalachians using passive-source seismology. *Geology* **43**, 431-434 (2015)

Pollock, J. C., Hibbard, J. P. & van Staal, C. R. A paleogeographical review of the peri-Gondwanan realm of the Appalachian orogeny. *Canadian Journal of Earth Science* **49**, 259-288 (2012)

Schmandt, B. F., Lin, F.-C. & Karlstrom, K. E. Distinct crustal isostasy trends east and west of the Rocky Mountain Front. *Geophysical Research Letters* **42**, 10,290-10,298 (2015)

Schulte-Pelkum, V. *et al.* Imaging the Indian subcontinent beneath the Himalaya. *Nature* **435**, 1222-1225 (2005)

Shillington, D. *et al.* Extension and magmatism across the Suwannee Suture and South Georgia Basin from the SUGAR seismic refraction experiment. *Abstract T14A-07 presented at 2015 Fall Meeting, AGU, San Francisco, California, 14-18 Dec* (2015)

Steltenpohl, M. G., Mueller, P. M., Heatherington, A. L., Hanley, T. B. & Wooden, J. L. Gondwanan/peri-Gondwanan origin for the Uchee terrane, Alabama and Georgia: Carolina zone or Suwannee terrane (?) and its suture with Grenvillian basement of the Pine Mountain window. *Geosphere* **4**, 131-144 (2008)

Thomas, W. A. Interactions between the southern Appalachian-Ouachita orogenic belt and basement faults in the orogenic footwall and foreland. *Geological Society of America Memoirs* **206**, 897-916 (2010)

Figures

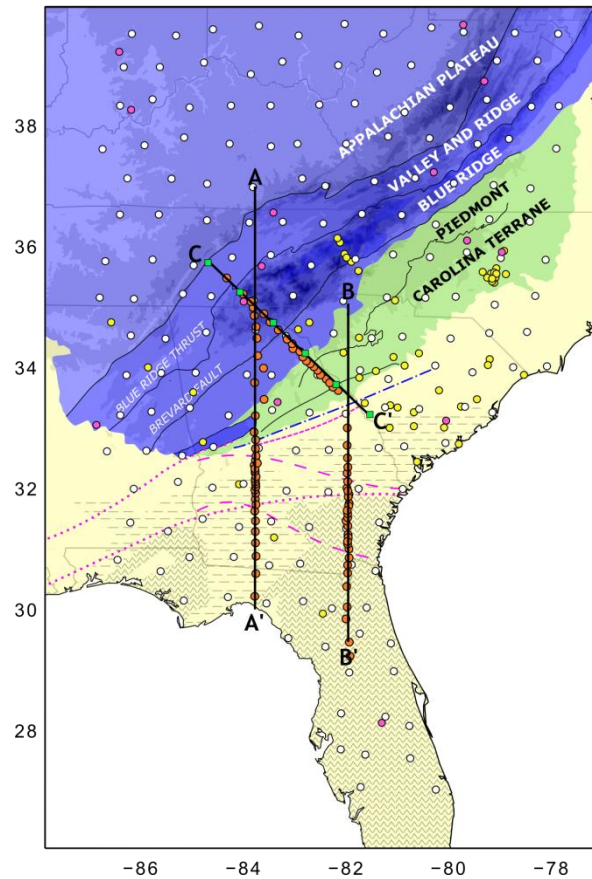


Figure 1: Study region. Simplified geological map with topographic shading (blue: Laurentian affinity terranes; green: exotic or suspect terranes; yellow: Cenozoic sedimentary cover) [Steltenpohl et al., 2008]; subsurface (dashes: Mesozoic rift basin; carets: Gondwanan affinity Suwannee terrane) [Chows and Williams, 1983]; previously inferred Suwannee suture zones (pink dotted line, from outcrop/borehole patterns [Thomas, 2010]; pink dashed line, from reflection profiling [McBride and Nelson, 1988; Nelson et al., 1985]); intersection of Sp CCP suture with surface (blue dash-dotted line). Broadband station locations (orange: SESAME; white: EarthScope TA; pink: permanent; yellow: other temporary); and cross section locations (thick black lines).

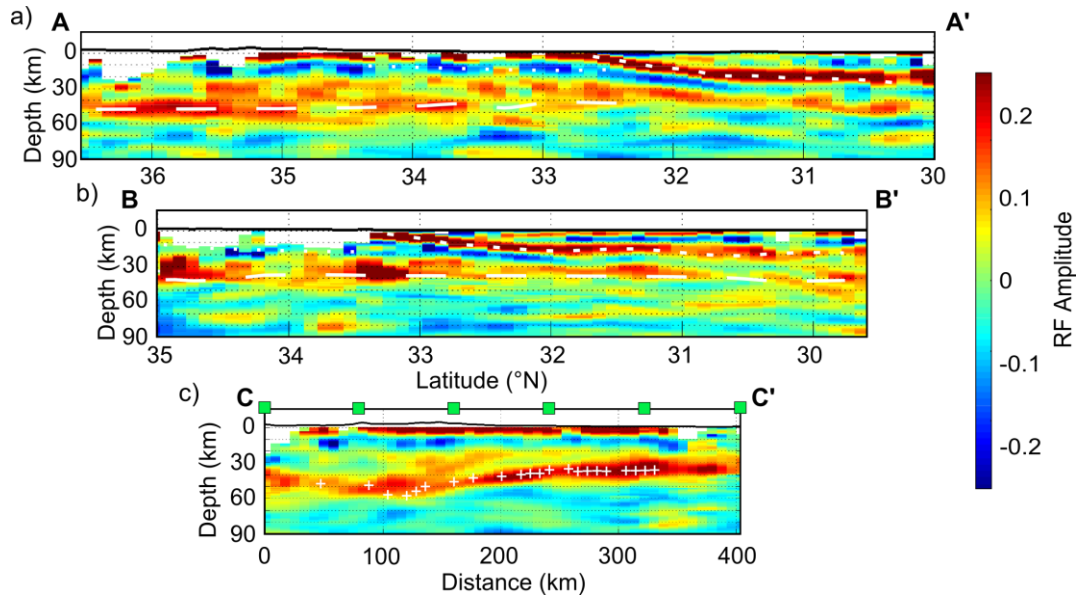


Figure 2: Crustal structure along SESAME lines. Cross sections through the mean bootstrapped 1-33 s Sp CCP stack. Points with fewer than 35 contributing waveforms are plotted as white. Black line: topography with 5x vertical exaggeration. Cross section locations are shown on Figure 1. a and b) White lines show depth of three of the phases produced by synthetics. Long dashed line: Moho, depth from Ps imaging [Schmandt et al., 2015]; short dashed line: suture phase, depths picked from Sp images; dotted line: base of layered sediments, depth from reflection profiles [Cook et al., 1979; Cook and Vasudevan, 2006]. c) Green squares correspond to green square locations in Figure 1. White crosses show Ps Moho depths [Parker et al., 2013].

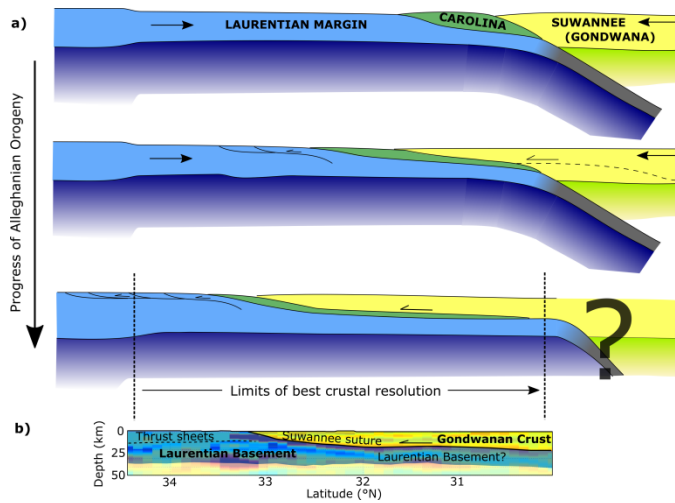


Figure 3: Interpretation of images. a) Schematic showing proposed progression of the Alleghanian orogeny, from the Mississippian [Hatcher, 2010; Hibbard et al., 2010] (top panel) to the end stages of the collision in the Permian [Hatcher, 2010] (bottom panel). In these panels, the far left edge of the lithosphere represents a fixed point. b) Interpretative overlay on a portion of Sp CCP stack section B-B', showing crustal structure today.

Supplementary Materials

Data

We downloaded data from the Incorporated Research Institutions for Seismology (IRIS) Data Management Center, choosing events with reported $M_w > 5.8$ in the USGS National Earthquake Information Center catalogue. The epicentral distance of the sources was restricted to 55° - 85° , which limits postcritical conversions and overlap with other teleseismic phases. These data were recorded at 374 broadband stations within the study area, including 85 SESAME (SouthEastern Margin of the Appalachian Mountains Experiment) stations, 181 Earthscope USArray Transportable Array (TA) stations, 55 permanent stations, and data from five other temporary arrays (see Acknowledgements for network details). Our final stacks incorporate 28,123 S-to-P waveforms sourced from 6,173 events.

Processing

S-to-P (Sp) converted waves are generated at sharp seismic velocity gradients, such as lithological contrasts or changes in anisotropy. The offset in time of the Sp conversions depends on the depth of the boundary, and phase amplitude on the size of the velocity contrast. As P waves travel faster than S waves, these converted waves arrive before the main S arrival. As such, they are uncontaminated by sedimentary basin multiples and are more suitable for this region, with its extensive sedimentary cover, than the more commonly used P-to-S converted waves.

To isolate these converted phases, data was processed as follows. Phase windows were defined using an automated array-based procedure [Lekić and Fischer, 2014] to account for varying mantle velocities. Waveforms were rotated using a free-surface transfer matrix [Bostock, 1998; Kennet, 1991], with free-surface velocity structure found by grid search [Abt et al., 2010]. We deconvolved S components from P components using the extended-time multitaper cross-correlation method [Helffrich, 2006], with optimized parameters [Lekić and Fischer, 2014]. The

resulting individual receiver functions were migrated to depth using common conversion point (CCP) stacking [Lekić et al., 2011]. We filtered the data at 1-33 s to target small-scale crustal structures. Fresnel zones used to map Sp receiver functions to stack nodes were calculated using a 5.5 s dominant period, as measured for this dataset. For the mantle-focused stacks (Figure S2), we filtered at 4-33 s to target larger scale mantle features (dominant period: 9 s).

The raypaths used in migration were calculated using a 1D velocity model for each station extracted from a combined crustal model (a Rayleigh wave data model incorporating Ps receiver functions) [Schmandt et al., 2015] and mantle model (a body wave model of Vp and Vs) [Schmandt and Lin, 2014]. P wave velocities were calculated in the crust using Vp/Vs ratios (mean: 1.76) constrained by local H-k stacking of Ps waves [French et al., 2009; Parker et al., 2013].

In order to be consistent with Ps studies, we reverse the polarities of our observed phases such that a positive phase corresponds to a positive velocity and a negative phase to a negative velocity gradient.

Bootstrapping

We bootstrapped the Sp CCP stacks by computing the mean and standard deviation of 50 CCP stacks based on different random samples of the waveforms [Lekić and Fischer, 2014]. In general, standard deviation is much lower than mean phase amplitude, especially directly beneath the SESAME array in the vicinity of the suture phase (Figure S8). We only interpret phases whose mean bootstrap amplitudes exceed 2 times their standard deviation.

Forward modeling

We tested three types of models: those containing crustal interfaces consistent with our interpretation (Figure S3), those to rule out sedimentary features as the source of our observations

(Figure S4), and those that indicate a dipping layer of radial anisotropy cannot reproduce the observed suture phase (Figure S7).

We generated synthetics using station-specific velocity models using the RAYSUM method [Frederiksen and Bostock, 2002] for all stations in our dataset, assuming the same backazimuthal and epicentral distance distribution in the real data. Both incident SV and incident SH motion was calculated, though incident SH motion contributes little to the output waveforms for the velocity models used. Sp CCP stacks were calculated from synthetic waveforms in the same way as with the real data. When incorporating anisotropic layers, a shape factor of 0.7 was used, appropriate for deformed crustal rocks [Schulte-Pelkum and Mahan, 2014].

Modeling of Sedimentary Basins

Our simpler models incorporate Mesozoic and Tertiary sediments and the Moho only. These were calculated to address concerns that we may be imaging the base of the sediments poorly migrated in depth. We compiled a sediment isopach map from an interpolation of borehole data [Chowns and Williams, 1983; Virginia Division of Geology and Mineral Resources, 2012] and depth estimates from reflection profiling [McBride et al., 1987], where two-way travel-time was converted to depth based on our input sediment velocities. These velocities were estimated based on local down-borehole measurements of Vp [Virginia Division of Geology and Mineral Resources, 2012] and local modeling of refraction and reflection data [Shillington et al., 2015]. We use a Vp of 3.5 km/s for the Coastal Plain sediments, and a Vp of 5 km/s for the South Georgia rift basin. We assume a Vp/Vs ratio of 2; this ratio was chosen as an endmember high Vp/Vs, which will cause a greater offset in the Sp arrival time, so phases will be migrated to the greatest depths reasonable. We find that the suture PVG observed in the stack of real Sp phases is too deep and does not have the expected spatial variation to have been generated by sediments alone (Figure S4). This also holds true for synthetics calculated using slower

sedimentary velocities (V_p of 2.4 km/s for the Coastal Plain sediments and 3.5 km/s for the South Georgia rift basin).

While it does not match our observed suture phase, the strong base-of-sediments phase seen in these synthetics (Figure S3) implies that there should be a significant phase at shallow depths – indeed, we may be resolving it in parts of our images (3-6 km depth, 32.3°-30.5°N, Figure 2b).

Modeling anisotropic structures at single stations

To take a more detailed look at potential anisotropic structures, we compared single station stacks. These are made up of data processed in the same way as for the CCP stacks, but stacked by station then bootstrapped (100 random resamplings). Anisotropic (or dipping) structure should manifest itself as a variation in converted phase amplitude (and potentially polarity) with backazimuth. The incomplete backazimuthal distribution of our dataset limits us to two primary backazimuthal ranges – from the northwest and from the south (Figure S6a).

When stacks are recalculated using only data from these backazimuths, we see a significant difference in the amplitude of the suture phase between backazimuthal ranges. However, this variation is modeled by the dip of the interface alone (Figure S6b), and does not require anisotropy.

Supplementary References

Abt, D. L. *et al.* North American lithospheric discontinuity structure imaged by Ps and Sp receiver functions. *Journal of Geophysical Research* **115**, B09301 (2010)

Bostock, M. G. Mantle stratigraphy and evolution of the Slave province. *Journal of Geophysical Research* **103**, 21,183-21,200 (1998)

Frederiksen, A. W. & Bostock, M. G. Modelling teleseismic waves in dipping anisotropic structures. *Geophysical Journal International* **141**, 401-412 (2002)

Helfrich, G. Extended-time multitaper frequency domain cross-correlation receiver-function estimation. *Bulletin of the Seismological Society of America* **96**, 344-347 (2006)

Kennett, B. L. N. The removal of free surface interactions from three-component seismograms. *Geophysical Journal International* **104**, 153-163 (1991)

Lekić, V. & Fischer, K. M. Contrasting lithospheric signatures across the western United States revealed by S_p receiver functions. *Earth and Planetary Science Letters* **402**, 90-98 (2014)

Lekić, V., French, S. W. & Fischer, K. M. Lithospheric thinning beneath rifted regions of Southern California. *Science* **334**, 783-787 (2011)

McBride, J. H., Nelson, K. D. & Brown, L. D. Early Mesozoic basin structure and tectonics of the southern United States as revealed from COCORP reflection data and the relation to Atlantic rifting. *Canadian Society of Petroleum Geologists Memoir* **12**, 173-184 (1987)

McBride, J. H. & Nelson, K. D. Deep seismic reflection constraints on Paleozoic crustal structure and definition of the Moho in the buried Southern Appalachian orogeny. *Continental Lithosphere: Deep Seismic Reflections* 9-20 (1991)

Pollitz, F. F., & Mooney, W. D. Seismic velocity structure of the crust and shallow mantle of the Central and Eastern United States by seismic surface wave imaging. *Geophysical Research Letters* (2016).

Schmandt, B. & Lin, F.-C. P and S wave tomography of the mantle beneath the United States. *Geophysical Research Letters* **41**, 6342-6349 (2014)

Schulte-Pelkum, V. & Mahan, K. H. Imaging faults and shear zones using receiver functions. *Pure and Applied Geophysics* **171**, 2967-2991 (2014)

Virginia Division of Geology and Mineral Resources, 2012. Georgia Well Logs. AASG *Geothermal Data Repository* (2012) June 2015.

Wehr, F. & Glover, L. Stratigraphy and tectonics of the Virginia-North Carolina Blue Ridge: Evolution of a late Proterozoic-early Paleozoic hinge zone. *Geological Society of America Bulletin* **96**, 285-295 (1985).

Supplementary Figures

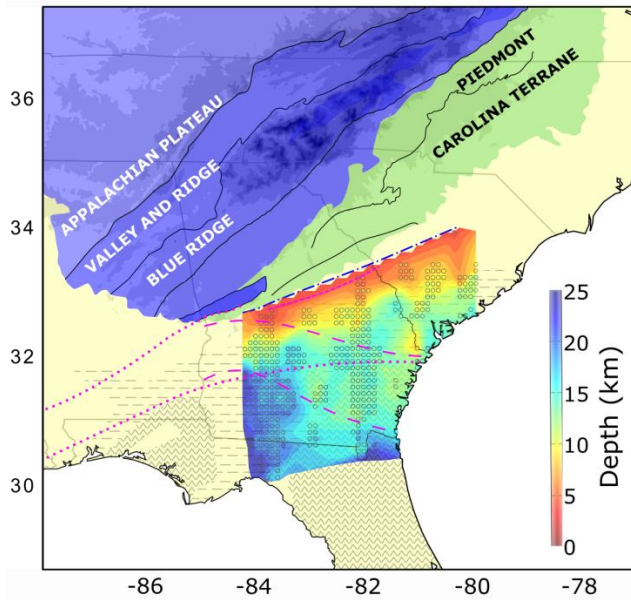


Figure S1: Depth map of suture phase. Map as in Figure 1 with interpolated surface of suture phase depth. Black circles on top of surface show locations of actual hand-picked depths; in all cases, these phases are at least twice the amplitude of the standard deviation. This feature is continuous over 360 km along strike.

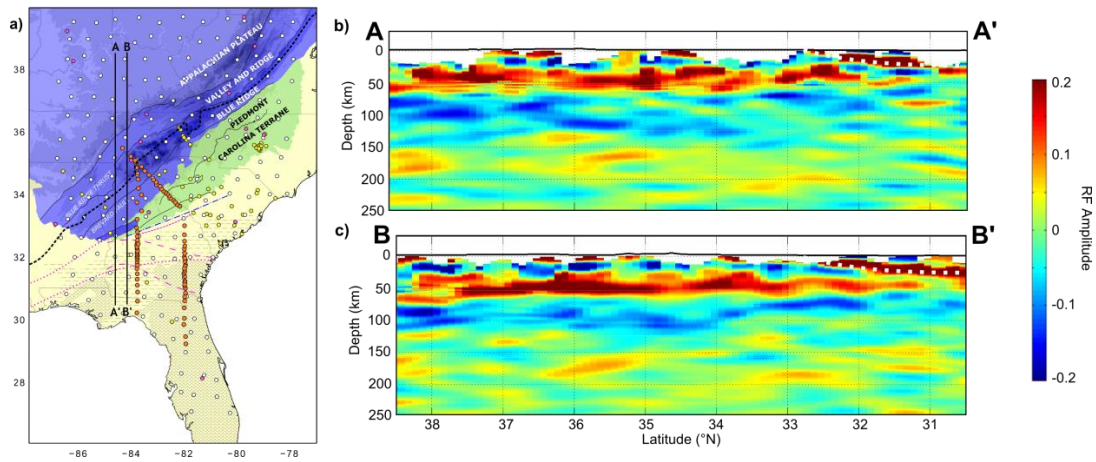


Figure S2: Sp CCP stack including mantle depths. a) Location map, similar to Figure 1. Thick dashed black line: the hinge zone (boundary between western and eastern Blue Ridge), marking the northwest edge of extensively thinned crust from the Proterozoic rifting of Rodinia [Steltenpohl et al., 2008; Wehr and Glover, 1985]. Thick black lines: locations of cross sections in other panels. b and c) Sp mean CCP stacks, filtered at 4-33 s and stacked assuming a dominant period of 9 s. White dotted line: location of crustal suture phase. South of 37°N, comparison with surface wave tomography [Pollitz and Mooney, 2016; Schmandt et al., 2015] indicates that the mantle NVG at depths of 80-120 km can be interpreted as the lithosphere-asthenosphere boundary (LAB). In (b), there are hints of a southward dipping segment of the LAB from 100 km depth (36.5°N) to 150 km depth (33°N). However, this feature is very limited in lateral extent (<50 km), raising questions about its significance. Overall, the mantle lacks evidence for widespread structures that are obviously collisional and related to the crustal PVG. In contrast, LAB depth consistently shallows southeastward across the hinge zone, suggesting a correlation between lithospheric thickness and Proterozoic rifting processes [see Chapter 4].

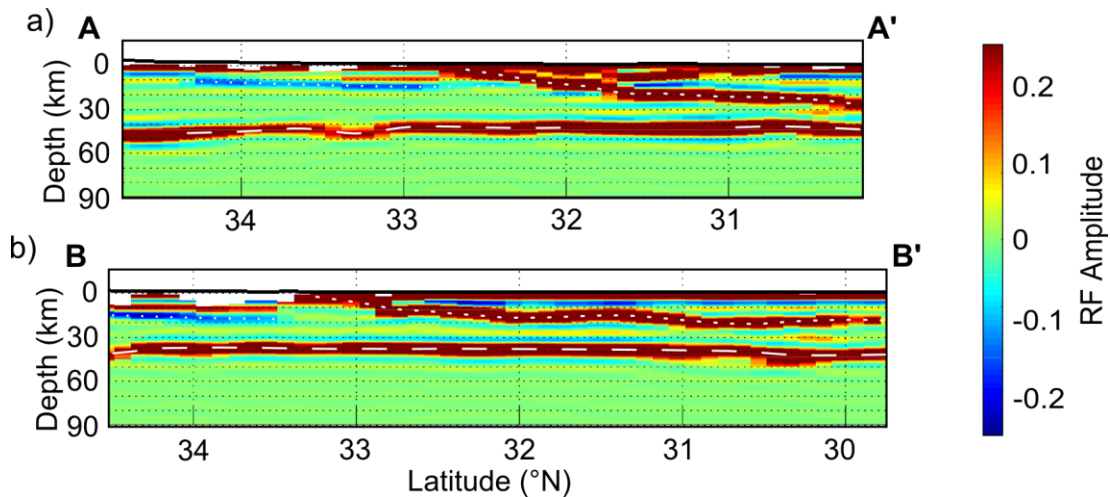


Figure S3: Synthetic Sp CCP stack calculated using the preferred crustal model. This model incorporates the Moho (long dashed white line), buried Laurentian sediments beneath the thin crystalline thrust sheets of the Blue Ridge and Piedmont (north of 33°N; dotted white line), a 20% isotropic contrast across the suture interface (short dashed white line), and Mesozoic and Tertiary sedimentary basins. Synthetic waveforms were calculated using the RAYSUM package [Frederiksen and Bostock 2002], using rays corresponding to all waveforms in the real dataset. The sedimentary basin thicknesses and velocities were constrained by active source and borehole data (see Supplementary Materials). In the north, the Blue Ridge and Piedmont overthrust the Laurentian margin along a shallow, low angle detachment. The buried sediments beneath this detachment are represented as a 20% anisotropic layer with a vertical slow axis; this hexagonal isotropy is typical of laminated sediments. The depth of this phase was picked from the depth extent of the observed laminated sediment layer beneath the Blue Ridge and Piedmont from published reflection profiles [Cook et al., 1979; Cook and Vasudevan, 2006] and extrapolated assuming the northeasterly-strike typical of structures in the Blue Ridge and Inner Piedmont. The depth of the suture phase was picked from our Sp CCP stacks, and we used a published Moho depth map derived from P-to-S receiver functions [Schmandt et al., 2015]. The input background crustal velocity model was the same as that used to migrate the data [Schmandt et al., 2015; Schmandt and Lin, 2014]. Synthetics were processed in the same way as the data. These plots show cross sections through the Sp CCP stack of synthetic data. a) Corresponds to cross section A-A' (Figure 2a). b) Corresponds to cross section B-B' (Figure 2b).

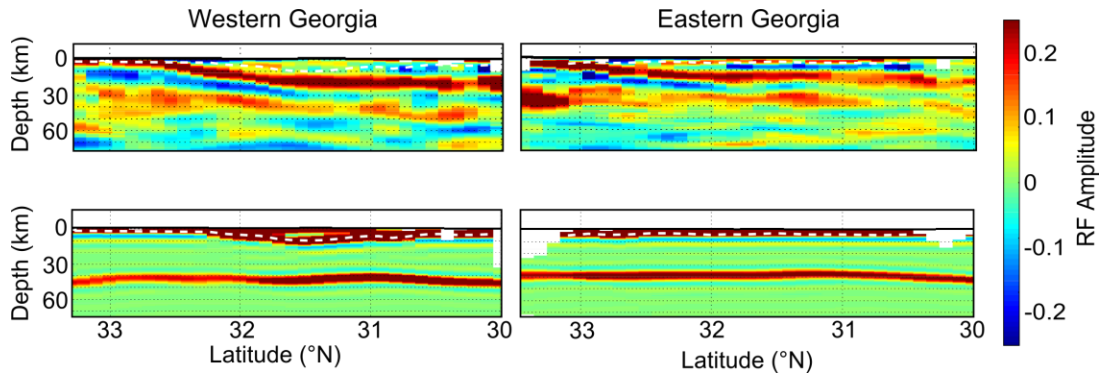


Figure S4: Comparison of observed Sp CCP stack and synthetic stack generated with only sediment layers and basins. Left column corresponds to a portion of cross section A-A' (Figure 2a). Right column corresponds to a portion of cross section B-B' (Figure 2b). First row: cropped subsection of mean bootstrapped Sp CCP stack, as Figure 2. Second row: Same cross sections through Sp CCP stack of synthetic data. Synthetic dataset is equivalent to all waveforms recorded by the SESAME array. This model includes Coastal Plain and South Georgia Rift Basin sediments and the Moho. In all panels, dashed white line is traced from the base-of-sediments phase in the synthetics. Sp phases generated at sedimentary interfaces are too shallow to explain the observed PVG interpreted as the southward dipping crustal suture.

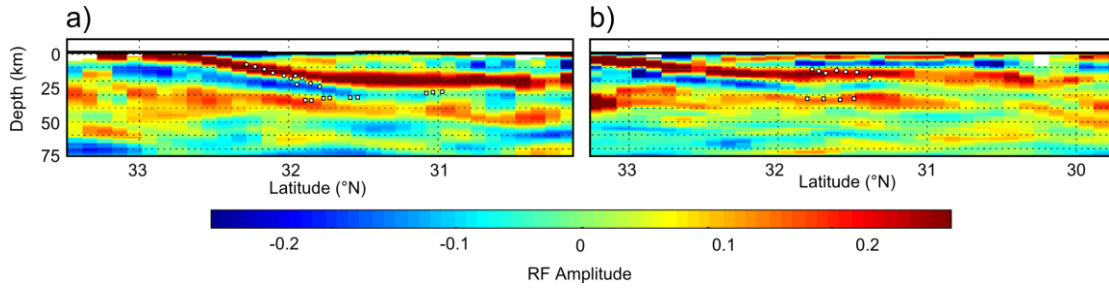


Figure S5: Comparison of Sp CCP images to re-migrated reflections. For both panels, Sp mean CCP stacks are plotted, with overlain white points picked from two-way travel time reflection profiles [McBride and Nelson, 1988]. On all sections, white circles: top of band of dipping reflectors; white squares: phase interpreted as ‘Moho’. We migrated these times assuming the same velocity model that we used to migrate the CCP stacks [Schmandt et al., 2015] (also see Supplementary Materials). When originally published [McBride and Nelson, 1988], the reflection profiles were mapped to depth assuming a constant crustal velocity of 6 km/s. The velocity model we employ [Schmandt et al., 2015] has slower velocities in the upper crust moving southwards beneath the Coastal Plain – possibly due to the combination of sedimentary basins and lower velocity overthrust Suwannee crust. This means that, moving southward, the two-way travel time observations are pulled up to shallower depths, resulting in a more shallowly dipping feature that matches our observed phase depth quite well. Alternatively, if we superimpose the sedimentary velocity model used in synthetic seismogram calculations (see Supplementary Materials) onto this crustal model, we get comparable results. The reflection ‘Moho’, previously described as ‘anomalously shallow’ [McBride and Nelson, 1991], is found to be at a similar depth to the relatively flat continuation of our dipping PVG. With our larger scale images, we can interpret this as a mid-crustal feature, rather than the Moho. That is, when re-migrated using a modern 3D tomography model incorporating ambient noise data, the COCORP reflection profiles are compatible with a more shallowly dipping phase that does not reach the Moho, but rather a strong, mid-crustal feature that we interpret as the down-dip continuation of the suture phase. a) Portion of cross section A-A’ (Figure 2a). Reflection phase picks taken from lines GA-11 through GA-15 [McBride and Nelson, 1988]. b) Portion of cross section B-B’ (Figure 2b). Reflection phase picks taken from lines GA-16 and GA-17 [McBride and Nelson, 1988].

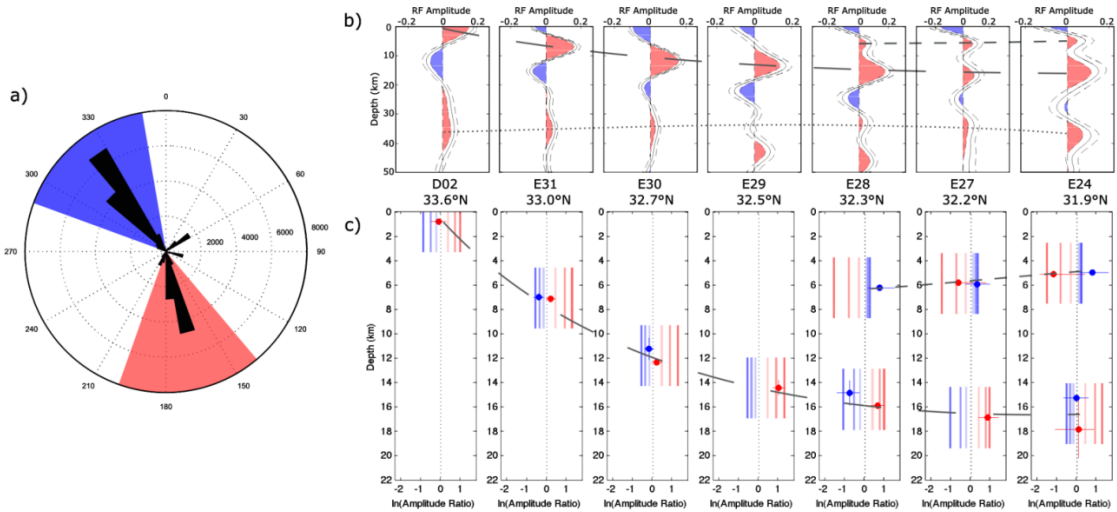


Figure S6: Comparison of backazimuthally restricted single station stacks showing the suture phase in eastern Georgia to synthetics calculated for various phase dips. While significant amplitude variation with backazimuth exists, it can be readily explained by a structure dip of $<10^\circ$; we cannot definitively identify anisotropic structure. a) Rose diagram showing the backazimuthal distribution of data used in this study. Red and blue shading corresponds to backazimuthally-restricted data bins used in panel (c). b) Single station stacks for SESAME stations D02, E31, E30, E29, E28, E27, and E24. These stations are at longitudes of 82.3 - 82.1°W , so this sequence approximates a north-south profile (latitudes labelled on figure). Solid black line: mean bootstrap stack; dashed black line: mean ± 1 standard deviation; blue and red shading shows where the single station stack phases are significant. Overlain grey lines show crustal phases consistent between stations. Short dashed line: associated with base of sediments; long dashed line: suture phase; dotted line: Moho. c) Comparison of amplitude variation with backazimuth. Single station stacks were calculated for backazimuthally restricted datasets. Red: data from 140 - 200° only; blue: data from 290 - 350° only. For each station, the circles show the natural log of the amplitude ratio of the phase on the backazimuthally-restricted stack to the all-data stack. Error bars in amplitude ratio show the maximum and minimum amplitude ratios within 1 standard deviation; error bars in depth show the range in phase depth between the backazimuthally-restricted and all-data stacks. In many cases, error bars are smaller than the symbol. Vertical bars show calculated amplitude ratios from synthetics incorporating a southward-dipping phase at 5° , 10° or 15° (pale to dark bars). For the southern stations, the vertical bars in the upper 10 km are for a northward-dipping phase. Interface dips of 5° - 10° are capable of explaining the observed backazimuthal amplitude variation.

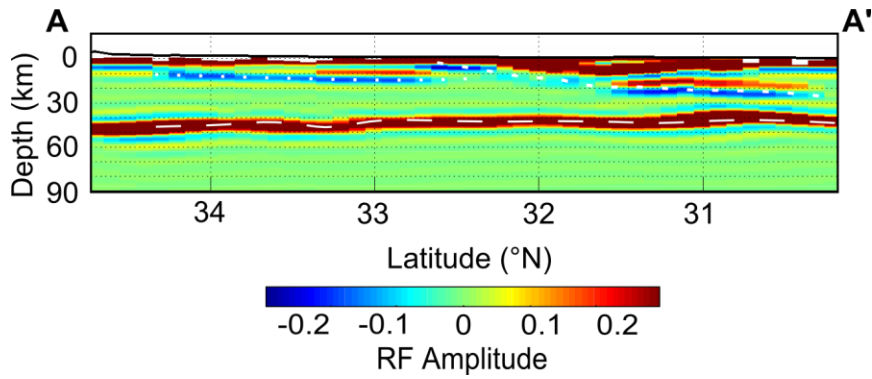


Figure S7: Synthetic Sp CCP stack calculated using a continuous layer of radial anisotropy from the Southern Appalachian Detachment along the Suwannee suture. This model incorporates the Moho, buried Laurentian sediments along the Southern Appalachian Detachment and the Suwannee suture, and Mesozoic and Tertiary sedimentary basins. Synthetics were calculated in the same way as for Figure S3, except that the Suwannee suture phase was modeled as a 5 km thick anisotropic layer of radial anisotropy, with the slow axis perpendicular to phase dip. White dashed and dotted lines correspond to those from Figure S3a (also Figure 2a). In the ramp part of the Suwannee suture, this model does not reproduce the observed Sp phases from the suture interface. This section corresponds to cross section A-A' (Figure 2a).

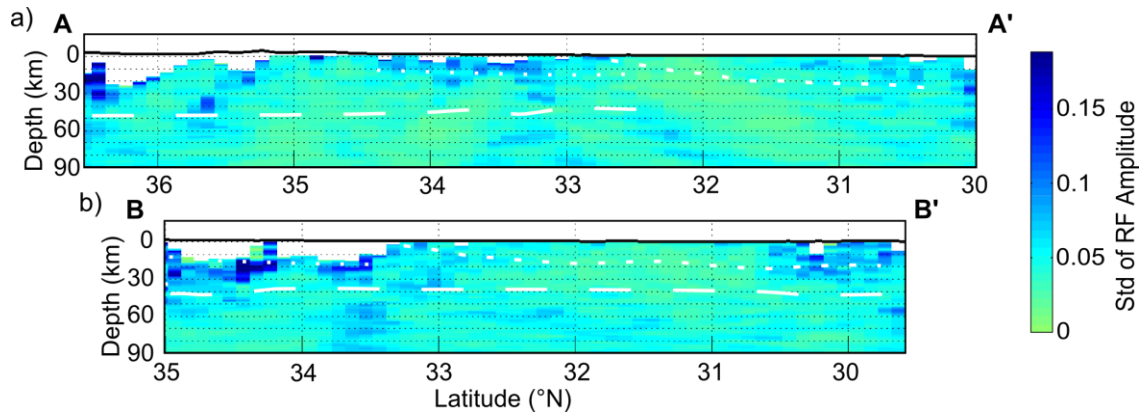


Figure S8: Standard deviation of mean bootstrapped Sp CCP stack. Cross sections A-A' and B-B' locations are those in Figure 2. White lines show the location of the Southern Appalachian detachment, the suture phase, and the Moho (as in Figure 2). In the vicinity of the major crustal phases, standard deviation is low.

CHAPTER 4

Imaging of crustal structures in the southeast U.S. by scattered wavefield migration

Emily Hopper¹, Karen M. Fischer¹, Stéphane Rondenay²,
Lara S. Wagner³, Robert B. Hawman⁴

¹Department of Earth, Environmental and Planetary Sciences, Brown University, Providence, RI, USA

²Department of Earth Science, University of Bergen, Norway

³Department of Terrestrial Magmatism, Carnegie Institution for Science, Washington, D.C., USA

⁴Department of Geology, University of Georgia, Athens, GA, USA

Abstract

To constrain crustal structures in the southern Appalachians and the suture zone with the Gondwanan-affinity Suwannee terrane, we analyzed the scattered incident P wavefield as recorded by EarthScope's Southeastern Suture of the Appalachian Margin Experiment and adjacent Transportable Array stations using the 2D GRT wavefield migration method. We confirm the presence of a thickened crustal root beneath the high topography of the Blue Ridge mountains and observations of the gently south-southeastward dipping crustal suture. Localized weakening of the Moho coincides with the thickest crust, and could be related to an ongoing delamination of the lower crust, perhaps contributing to local tectonic rejuvenation. The geometry of the crustal suture implies over 300 km of crustal shortening at the final stages of the Appalachian orogeny.

1. Introduction

The building of the southern Appalachians occurred over a series of Paleozoic orogenies, culminating in the formation of the supercontinent Pangea [Hatcher, 2010; Hibbard et al., 2010]. The accretionary structures of this orogenesis are still observable in the crust today, providing insight into the mechanics of ancient continental collisions. Allochthonous crystalline thrust sheets in the Blue Ridge and Inner Piedmont overlie a shallow detachment (5-15 km depth), which accommodated hundreds of kilometers of shortening [Cook and Vasudevan, 2006; Cook et al., 1979; McBride et al., 2005]. The final amalgamation of Pangea, as inferred from the relict suture between Laurentia and Gondwana, also occurred by thrusting over hundreds of kilometers [Chapter 3]. This suture, preserved in Georgia as the boundary with the Gondwanan-affinity Suwannee terrane (Figure 1) [Chowns and Williams, 1983], was thought to be a steeply dipping feature that accommodated significant strike-slip motion [McBride and Nelson, 1988; Nelson et al., 1985; Mueller et al., 2013]. However, recent crustal imaging suggests the suture is a low-angle detachment preserving at least 330 km of overthrusting [Chapter 3].

Today, the Appalachians are a tectonically quiescent, decaying orogen, yet many studies of landscape evolution, geomorphology and thermochronology [Gallen et al., 2013; McKeon et al., 2014; Miller et al., 2013; Prince et al., 2013; Prince and Spotila, 2013; Willett et al., 2014] indicate recent topographic rejuvenation of these mountains. Conventional wisdom states that as the isostatic crustal root is progressively consumed by erosion, topography should become muted and erosion rates decrease. So what is causing the observed rejuvenation? Possible forcing mechanisms include dynamic topography [Forte et al., 2007; Liu, 2014; Rowley et al., 2013] and lower crustal delamination [Wagner et al., 2012; Gallen et al., 2013; Graw et al., 2015]. As such, accurate retrieval of the structure of the crustal root and uppermost mantle is important to our understanding of the ongoing evolution of the Appalachians.

Studies utilizing Ps receiver functions [French et al., 2009; Parker et al., 2013; Schmandt et al., 2015] and active source reflections [Hawman, 2008; Hawman et al., 2012] have previously imaged the crustal root beneath the southern Appalachians. The thickness of the crustal root relative to topography and gravity implies a relatively low density contrast between the lower crust and uppermost mantle, consistent with postorogenic increases in crustal root density postulated for old orogens [French et al., 2009; Fischer, 2002]. Here, we present new images using a full wavefield migration technique that accurately retrieves structure geometry and material property perturbations. The results are consistent with previous observations of crustal thickness, and show a pronounced variation in the strength of the velocity contrast across the Moho where the crust is thickest. Additionally, we observe upper crustal structures that we associate with the collisions that formed the Appalachians.

2. Data and Methods

2.1. Data

The Southeastern Suture of the Appalachian Margin Experiment (SESAME), a targeted temporary seismic network deployed between 2010 and 2014, collected a dense dataset suitable (Section 2.3) for the full wavefield migration technique that we apply here. We performed a migration for each of the three legs of the SESAME array, hereafter referred to as the W, E and D lines (Figure 1). We also incorporated data from nearby broadband stations deployed contemporaneously, including 47 of EarthScope's Transportable Array stations, and 3 permanent stations. For the W line profile, we use 41 events recorded at 74 stations. For the E line profile, we use 59 events recorded at 63 stations. For the D line profile, we used 18 events recorded at 24 stations. Given the backazimuthal distribution of events from both the northwest and south-southeast, dipping structures within the migration plane should be well retrieved [Rondenay et al., 2005].

2.2. *Inversion of scattered waves*

The waveforms are inverted for model properties (e.g. V_s perturbation) via the scattering potential of a given model point. This calculation involves analytical inversion of the scattered wavefield, cast as a generalized Radon transform (GRT). The inversion has been simplified to two dimensions (2D GRT), as 3D structures are not well resolved by data recorded on linear arrays such as SESAME, but can incorporate incident waves from any backazimuth and waveforms recorded from stations adjacent to the inversion plane [Bostock et al., 2001; Rondenay et al., 2001, 2005]. The 2D simplification requires that the inversion plane (i.e. cross section planes in Figures 3-7) is perpendicular to local geological strike. The 2D GRT incorporates several scattered modes, both forward and back-scattered (Figure 2); this increases resolution in the inversion as a whole, and comparison of the results from individual modes allows testing of the robustness of observed phases (see Section 3.1.2).

The benefits of this methodology over receiver function imaging [e.g. Chapters 2, 3; French et al., 2009; Parker et al., 2013, 2015; Schmandt et al., 2015] include accurate imaging of dipping structures, higher resolution images, explicit incorporation of multiples (i.e. back-scattered modes), and inversion for actual material properties. Unlike receiver functions, which are commonly migrated to depth assuming horizontal discontinuities in velocity structure, scattered wavefield migration methodologies such as the 2D GRT make no such prior assumptions about structure. In addition to improved dip resolution, the volume resolution is substantially improved by the inclusion of back-scattered modes. The data used here has a measured dominant period of 3.5 s; for typical crustal velocities of 6km/s (i.e. wavelengths of ~21 km), forward-scattered modes have a resolution of ~10 km; this is reduced to ~5 km for back-scattered waves. The inclusion of the back-scattered waves means that multiples are explicitly included in the inversion, improving the interpretation of scattered incident P waves in regions with high amplitude multiples. Finally, unlike receiver functions which need to be calibrated

against synthetic waveforms, the 2D GRT inverts for material properties, specifically the perturbations to V_s , V_p and density. V_s perturbations are the best resolved [Bostock, 1999; Rondenay et al., 2008; Rondenay, 2009]. V_p perturbations are calculated from the back-scattered P_{pp} mode only.

The data were filtered at 1-17 s, and were visually inspected to remove records with a low signal-to-noise ratio. Waveforms were rotated into P-SV by the free surface transfer matrix. For each event, phases were aligned by cross-correlation [VanDecar and Crosson, 1990] of the hand-picked incident P arrival. The incident wavefield was isolated by principal component analysis and removed. The remaining scattered wavefield was deconvolved by the incident wavefield in the frequency domain. The resultant waveforms were then rotated into an inversion plane-specific coordinate system: vertical, parallel and perpendicular to the plane. These waveforms are inverted for scattering potential, and then for model perturbations. Model perturbations are calculated individually for each scattering mode (Figure 2); resulting images containing all reverberations (i.e. higher resolution back-scattered modes only) or all modes are the equally weighted mean of these individual modes. The inversions were first performed for data from individual earthquakes. Visual inspection of each mode inversion determined its inclusion in the final inversion of all earthquake data. Migration to depth assumed a simple, two-layer 1D velocity model containing crust (V_s of 3.8 km/s; V_p of 6.6 km/s) over mantle (V_s of 4.8 km/s; V_p of 8.2 km/s). An artificially thick crust (60 km) was assumed to avoid introducing artefacts in the vicinity of the true Moho.

2.3. Suitability of the dataset

The limitation of the 2D GRT is its much stricter data requirements. Namely, the data must be sufficiently dense and the structures that it is imaging must conform to the assumption of 2D geometry [Rondenay et al., 2005, 2008].

Array geometry constrains the resolution of the final inversion. The three legs of the SESAME array provide the necessary dense station spacing, improved by the addition of TA stations. The W and E lines are ~600 km long, with a station spacing of 6.3 and 7.7 km respectively over the most densely spaced central section, and 23.5 and 22 km respectively outside of this. The D line is ~300 km long, with ~11 km station spacing. Typically, operator aliasing occurs at depths ≤ 2 times the station spacing [Rondenay et al., 2005]. Hence, this dataset gives good resolution of crustal structure beneath 13-20 km where station spacing is densest, and good resolution of the Moho and uppermost mantle elsewhere. This dataset is also sufficient to avoid spatial aliasing, which occurs if the station spacing is more than half the wavelength of the data (~10 km; Section 2.2). Acceptable dip resolution is maintained to a depth equivalent to ~half the length of the array, i.e. throughout the lithospheric mantle in this region [e.g. Pollitz and Mooney, 2016].

Previous imaging of the region by receiver functions allows us to estimate the lateral variability of local structure. The requirement for out-of-plane structures to be homogeneous along strike is depth-dependent, with shallower features requiring less continuity [Rondenay et al. 2005]. Within the crust, a large, low angle south-southeastward dipping feature (strike of 18°) associated with the late Paleozoic Gondwana-Laurentia suture is observed [Chapter 3]. This structure is imaged from the surface to depths of 20 km, so the out-of-plane continuity is required to be ~5-10 km on either side of the inversion plane [Rondenay et al., 2005]. Given that the suture phase is observed to be relatively smooth and continuous over ~360 km along strike, out-of-plane heterogeneities should not be problematic. The Moho has been imaged by Ps receiver functions [Parker et al., 2013; Schmandt et al., 2015], with an increase in crustal thickness beneath the Blue Ridge mountain and the Piedmont. The Moho depth ranges from 40-60 km depth, increasing the continuity requirement to ~25 km. The approximate strike of the crustal thickness variations is northeastward (~45°), parallel to the D line. In the uppermost mantle, Sp imaging [Chapter 2]

reveals relatively discontinuous, laterally variable features. Additionally, mantle features were not well resolved by Sp phases with higher frequency contents [Chapter 3], implying that the velocity gradients observed may be too gradual to generate scattered phases incorporated by this method. As such, we do not expect to image mantle lithospheric phases well.

3. Observed discontinuities

In the 2D GRT images (Figures 3-7), a velocity discontinuity is marked by a juxtaposition of anomalously fast and slow material: white-to-blue corresponds to a positive velocity gradient (PVG) with depth, such as the Moho. As they are based on scattering potential, the output material perturbations show the contrast across a velocity discontinuity, not volumetric velocity perturbations.

The Moho across the study region is relatively well imaged, and is at comparable depths to previous results [e.g. Parker et al., 2013]. Beneath the W line, there is a robust dipping crustal feature at comparable depths to the suture phase observed with Sp waveforms [Chapter 3]. No structures are well imaged within the lithospheric mantle.

3.1. Crustal structure beneath the Blue Ridge and Inner Piedmont: the D line

3.1.1. Moho topography and strength variations

The D line traverses the most significant surface topography of the profiles presented here, and has the largest crustal root. In these images, the PVG marking the Moho is observed at 50-60 km depth beneath the Blue Ridge mountains (<120 km along profile, Figure 3), and shallows moving to the southeast (green dashed line, Figure 3). As expected, the structure is much clearer in the output Vs perturbation (Figures 3a, b) than Vp perturbation (Figure 3c). The structure observed here is very consistent with previous Ps results (black crosses, Figure 1a), and the size of the isostatic crustal root implies a density contrast of 100-180 kg/m³ between the lower crust and upper mantle [French et al., 2009; Parker et al., 2013; Schmandt et al., 2015]. These

previous Ps results make use of the forward scattered Ps mode (Figure 4a), which is incorporated into Figure 3b only, as well as the back-scattered phases which are used in Figure 3a and 3b.

Along most of the profile, the velocity contrast across the Moho is relatively uniform, but there is a marked drop in amplitude at <125 km along the profile, particularly at 55-125 km (Figure 3a, b). Such a weakening is also observable in previously published Ps [Parker et al., 2013] and Sp results [Chapter 3]. This decreased contrast across the Moho could be due to elevated lower crustal velocities or anomalously low uppermost mantle velocities. Elevated lower crustal velocities would result from the postorogenic densification due to garnet growth suggested to occur in old crustal roots [Fischer, 2002]; this process could account for the reduced contrast across the Moho where the crustal root is thickest. However, anomalously low uppermost mantle velocities are indeed observed with local Pn measurements [MacDougall et al., 2015], and could instead explain this reduced contrast across the Moho. MacDougall et al. [2015] suggest that their observed low velocity region could be Laurentian lithosphere (here observed to be ~90-100 km thick, Chapter 2) that is volatile-rich and partially serpentinized. Alternatively, these authors suggest that eclogitized lower crust may extend beneath their Ps defined Moho, such that their observations are of a local, deep, highly eclogitized crustal root rather than anomalously slow mantle.

How does this relate to the observed tectonic rejuvenation at the surface? Given that low velocities beneath the Moho at the northern end of the D line do not appear to extend deeper [Pollitz and Mooney, 2016; Schmandt et al., 2015], it seems unlikely that the addition of volatiles and serpentinization would have happened recently. While still a viable explanation for the seismic observations, it therefore cannot explain the rejuvenation of the past few million years [e.g. Willett et al., 2014], although the enhanced mantle buoyancy would contribute to the support of the topography in the long term. If, instead, these low Pn velocities and Moho gap are related to the initial stages of crustal foundering, the enhanced erosion may be due to the onset of

delamination. This would generate dynamic topography, and is one possible contribution to local topographic rejuvenation. In essence, this zone would represent the first step in the type of well-developed delamination that has been suggested beneath the Sierra Nevada [Zandt et al., 2004].

3.1.2. Robustness of the Moho

We consider the observed Moho to be robust, as it is imaged on the individual mode inversions (Figure 4) in addition to the mean mode inversion (Figure 3). The individual mode inversions migrate the scattered wavefield assuming that all energy is generated by that scattering mode. This migration also accounts for the different radiation patterns, phase shifts, and amplitude decay calculated for each mode by weighting and filtering the waveforms. Therefore, to first order, the same data is plotted for each mode, but with different timing. As such, there will be mismigrated energy on each mode plot. While a wide array of scattering angles and incidence angles are considered in the migration, we can simplify to the minimum offset in distance for these crustal multiples, i.e. assuming vertical paths between the scatterer and the surface. Given the input crustal velocities (V_p of 6.6 km/s; V_s of 3.8 km/s), we expect the PPs multiple to be mismigrated to depths of >2.15 times the Ps depth; PSs multiples will be at depths of >2.58 times the Ps depth. Given that we are imaging relatively shallow structures, we do not necessarily expect to be able to distinguish PPs and PSs in depth in these plots.

We show the mode inversions for the forward scattered Ps mode (Figure 4a), and the back-scattered PPs (Figure 4b) and PSs modes (Figure 4c). In all panels, there is a strong velocity contrast observed at the interpreted Moho depth. Additionally, in the Ps and PPs modes at the least, the mismigrated other modes are observed at depths consistent with the simple calculation above (Figure 4). The Moho gap is less robust, and is most evident on the PSs mode (Figure 4c). The PPs mode inversion (Figure 4b) implies there is still a strong contrast, but it is offset from the inferred Moho depth, perhaps indicating layering or other complex structures near the base of the crust.

3.1.3. Upper crustal structure beneath the thrust sheets

The shallow crust in this region is thought to consist of thin, crystalline thrust sheets separated from autochthonous Laurentian sediments by a shallow crustal detachment. Previous imaging of the upper crust in this region has been related to sediments of the Laurentian margin: reflection profiles contain a series of layered reflections interpreted as sedimentary interfaces [e.g. Cook et al., 1979]; Ps imaging reveals a sequence of shallow positive and negative velocity gradients interpreted as variable sedimentary features in the different terranes [Parker et al., 2015]; Sp imaging shows a shallow positive and negative velocity gradient phase pair, related to a radially anisotropic layer of laminated sediments [Chapter 3].

In the wavefield migration presented here, we observe some structure at shallow depths (8-16 km). We tentatively interpret these phases with the following caveats. 1) Such shallow interfaces are not well imaged with the 2D GRT method, which is prone to operator aliasing at shallow depths (<2 times the station spacing; Section 2.3). Even the deeper upper crustal interfaces (10-16 km) are affected. We do not expect to be able to image the shallow detachment beneath the Blue Ridge (5-10 km). 2) The phase is disrupted, and it is unclear whether it represents many distinct scatterers or a single velocity discontinuity. While the most continuous interpretation would be a single negative velocity gradient (NVG) with depth, there are places where a deeper PVG seems possible, e.g. 160-200 km along profile at ~15 km depth. 3) The phase is not clear on the individual mode inversions (Figure 4; see Section 3.1.2). No such upper crustal NVG is observed from the Ps or PPs modes (Figure 4a, b); these observations in the mean mode inversion are exclusively from backscattered S modes. Additionally, the deeper PVG that is sometimes observed may be mismatched direct Ps energy (Figure 4b).

These phases may have been generated from a single, continuous NVG (orange dashed line, Figure 3a), shallowing from 14 to 10 km moving southeast along the profile. This NVG is within error of the observed NVG in Sp images (12 to 10 km over the same profile, Chapter 3). If

this feature is real, it is at least consistent with the Sp observations, which do not suffer from the issues outlined above when imaging shallow structures.

However, the disrupted nature of the observed phase means that we cannot rule out the interpretation of several distinct sedimentary interfaces beneath the different terranes, as in Parker et al. [2015]. Where they interpret deeper phases (>10 km) that we may be able to resolve with this method, they report a PVG at 11-13 km depth beneath the Inner Piedmont (equivalent to 170-220 km along the profile, where we see a weak PVG at 14-16 km depth; Figure 4a, b) and an NVG at 5-12 km beneath the Carolina Terrane (equivalent to 230-280 km along the profile, where we see a weak NVG at 6-10 km depth). We cannot rule out this interpretation, but it is not strongly supported by our observations.

3.2. Crustal structure beneath the Coastal Plain: the W line

3.2.1. Moho topography

As beneath the D line, we observe a crustal root beneath the mountains that is very consistent with Ps observations (Figure 5) [Parker et al., 2013; Schmandt et al., 2015]. The Moho is much weaker than beneath the D line, although this may be due to the greater station spacing outside of the dense station spacing over the suture zone, or due to interference from more complex overlying crustal structure. As such, we do not interpret variations in Moho strength on this profile.

3.2.2. The Suwannee suture

The southern portion of the W line profile (>350 km along profile; Figures 5, 6) is much more complex within the crust than the seismically transparent northern W line crust. Here, the profile moves beneath the thick sediments of the Mesozoic South Georgia rift basin (locally up to 8 km deep) [McBride et al., 1987] and the Coastal Plain (locally up to 2.5 km deep) [Chowns and Williams, 1983] and also into the suture zone. At these latitudes, Sp observations show a very

strong, south-southeastward dipping PVG interpreted as the Suwannee suture [Chapter 3], separating the Laurentian margin from the Gondwanan-affinity Suwannee terrane.

The V_s perturbation image looks very complex (Figure 5a, b), but analysis of individual modes indicates that the imaged feature is robust and corresponds to the suture phase identified by Sp imaging. The depth of the feature on the Ps mode corresponds very well with the observed depth from Sp imaging (pink dashed line; Figure 6a). On this profile, the structure appears simple, although the multiples are strong (on this profile, mismapped to greater depths). On the reverberated modes, the forward scattered Ps phase is seen at shallower depths on the profiles (Figures 6b, c). Additional complexity at greater depths in the image may be due to multiples reflected several times at the free surface, which are not modeled here. On the mean mode V_s inversion, the apparent complexity of the structure arises because there is not total destructive interference of the mismapped scattering modes. The modeled V_p perturbation beneath the W line (Figure 5c) has a clear Moho at consistent depths, and appears to be robust. This mode shows the dipping PVG very clearly.

The inferred suture interface agrees well with previous Sp observations [Chapter 3]. Not only do the depth and lateral extent match very well, the amplitudes appear comparable: this mid-crustal suture phase has as much larger amplitude than either the Moho or any phase associated with the base of the sediments. However, it should be noted that the velocity models used to migrate these datasets are very different. The Sp CCP stack is migrated using local tomography that incorporates ambient noise data [Schmandt et al., 2015], and includes very low shallow crustal velocities in the southern portion of the W line. Here, we assume a single velocity throughout the crust, which will increase the apparent depth of the phase. Even so, we do not think this phase can have been generated at the base of the sediments, as these basins have a different geometry than the observed phase [Chapter 3]. Future work will constrain the effect of varying the input velocity model.

3.3. Crustal structure beneath the Coastal Plain: the E line

The E line was the last section of the SESAME array to be deployed, and has one fewer years of data than the D or W line. Also, visual inspection of these waveforms showed them to be consistently noisier than those recorded on other parts of the array, perhaps because the E line is completely within the soft sediments of the Coastal Plain. As such, it is not surprising that the migration of E line data is messy and hard to interpret.

The Moho is relatively strong in the northern part of the profile (green dashed line <120 km along profile; Figures 7a, b). Further south (260-375 km along profile; Figures 7a, b), a weaker phase at comparable depths to the previously reported Ps Moho [Schmandt et al., 2015] is observed. The Moho deepens southwards into northern Florida, as previously observed [French et al., 2009; Schmandt et al., 2015].

4. Conclusions

The 2D GRT wavefield migration of scattered P waves recorded by SESAME is very consistent with previous results from Ps and Sp receiver function imaging. This agreement is particularly meaningful given that the 2D GRT approach is capable of generating higher resolution images with more accurate retrieval of dipping structures, and the data used in this study are completely independent of the Sp phases employed in Chapter 3.

The deep Moho beneath the highest topography is compatible with the assumption of isostasy, given a modest density difference between crust and mantle, and its geometry matches previous Ps results. A zone of weaker contrast at Moho depths is consistent with nascent delamination of the lower crust, possibly linked to ongoing regional tectonic rejuvenation. Within the crust, these observations confirm the strength and geometry of a low-angle, south-southeastward dipping structure associated with the late Paleozoic suture between Laurentia and Gondwana. The geometry of this suture implies the final collision in the assembly of Pangea involved significant shortening.

Acknowledgements

We thank the many people who made the SESAME array possible: the staff of the Incorporated Research Institutions for Seismology (IRIS) PASSCAL Instrument Center at New Mexico Tech, the student/postdoctoral field crews (in particular, Horry Parker), and the landowners who hosted stations. The instruments used in the field program were provided by the IRIS PASSCAL facility, and waveform data were accessed through the IRIS Data Management Center. This work was funded by the NSF EarthScope Program under the American Recovery and Reinvestment Act of 2009 (Public Law 111-S) through awards EAR-0844276 (K.M.F.), EAR-0844186 (L.S.W.), and EAR-0844154 (R.B.H.). Data from the TA network were made freely available as part of the EarthScope USArray facility, operated by IRIS. IRIS is funded through the Seismological Facilities for the Advancement of Geoscience and EarthScope (SAGE) Proposal of the National Science Foundation under Cooperative Agreement EAR-1261681. In addition to SESAME ([doi:10.7914/SN/Z9_2010](https://doi.org/10.7914/SN/Z9_2010)) and TA ([doi:10.7914/SN/TA](https://doi.org/10.7914/SN/TA)) data, this study employed data from the United States National Seismic Network ([doi:10.7914/SN/US](https://doi.org/10.7914/SN/US)).

References

Bostock, M. G., S. Rondenay, and J. Shragge (2001), Multiparameter two-dimensional inversion of scattered teleseismic body waves 1. Theory for oblique incidence, *J. Geophys. Res.*, 106(B12), 30771-30782.

Chowns, T. M. and C. T. Williams (1983), Pre-Cretaceous rocks beneath the Georgia Coastal Plain – Regional implications, in Gohn, G. S., ed., *Studies related to the Charleston, South Carolina, earthquake of 1886 – Tectonics and seismicity: USGS Professional Paper*, 1313-L, L1-L42.

Cook, F. A., D. S. Albaugh, L. D. Brown, S. Kaufman, J. E. Oliver, and R. D. Hatcher (1979), Thin-skinned tectonics in the crystalline southern Appalachians; COCORP seismic-reflection profiling of the Blue Ridge and Piedmont, *Geology*, 7(12), 563-567.

Cook, F. A. and K. Vasudevan (2006), Reprocessing and enhanced interpretation of the initial COCORP Southern Appalachians traverse, *Tectonophysics*, 420, 161-174.

Fischer, K. M. (2002), Waning buoyancy in the crustal roots of old mountains, *Nature*, 417(6892), 933-936.

Forte, A. M., J. X. Mitrovica, R. Moucha, N. A. Simmons, and S. P. Grand (2007), Descent of the ancient Farallon slab drives localized mantle flow beneath the New Madrid seismic zone, *Geology*, 34(4).

French, S. W., K. M. Fischer, E. M. Syracuse, and M. E. Wysession (2008), Crustal structure beneath the Florida-to-Edmonton broadband seismometer array, *Geophys. Res. Lett.*, 36(8).

Gallen, S. F., K. W. Wegmann, and D. R. Bohnenstiehl (2013), Miocene rejuvenations of topographic relief in the southern Appalachians, *GSA Today*, 23(2), 4-10.

Graw, J. H., C. A. Powell, and C. A. Langston (2015), Crustal and upper mantle velocity structure in the vicinity of the eastern Tennessee seismic zone based upon radial P wave transfer functions, *J. Geophys. Res.*, 120(1), 243-258.

Hatcher, R. D. (2010), The Appalachian orogeny: A brief summary, *Geol. Soc. America Memoir*, 206, 1-19.

Hibbard, J. P., C. R. van Staal, and D. W. Rankin (2010), Comparative analysis of the geological evolution of the northern and southern Appalachian orogeny: Late Ordovician-Permian, *Geol. Soc. Am. Memoir*, 206, 51-69.

Hawman, R. B. (2008), Crustal thickness variations across the Blue Ridge Mountains, southern Appalachians: An alternative procedure for migrating wide-angle reflection data, *Bull. Seism. Soc. Am.*, 98(1), 469-475.

Hawman, R. B., M. O. Khalifa, and M. S. Baker (2012), Isostatic compensation for a portion of the Southern Appalachians: Evidence from a reconnaissance study using wide-angle, three-component seismic soundings, *Geol. Soc. Am. Bull.*, 124(3-4), 291-317.

Hibbard, J. P., C. R. van Staal, and D. W. Rankin (2010), Comparative analysis of the geological evolution of the northern and southern Appalachian orogeny: Late Ordovician-Permian, *Geol. Soc. Am. Memoir*, 206, 51-69.

Liu, L. (2014), Rejuvenation of Appalachian topography caused by subsidence-induced differential erosion, *Nat. Geosci.*, 7(7), 518-523.

MacDougall, J. G., K. M. Fischer, D. W. Forsyth, R. B. Hawman, and L. S. Wagner (2015), Shallow mantle velocities beneath the southern Appalachians from Pn phases, *Geophys. Res. Lett.*, 42(2), 339-345.

McBride, J. H., K. D. Nelson, and L. D. Brown (1987), Early Mesozoic basin structure and tectonics of the southern United States as revealed from COCORP reflection data and the relation to Atlantic rifting, *Can. Soc. Petr. Geol. Mem.*, 12, 173-184.

McBride, J. H., R. D. Hatcher, W. J. Stephenson, and R. J. Hooper (2005), Integrating seismic reflection and geological data and interpretations across an internal basement massif: The southern Appalachian Pine Mountain window, USA, *Geol. Soc. Am. Bull.*, 117, 669-686.

McBride, J. H. and K. D. Nelson (1988), Integration of COCORP deep reflection and magnetic anomaly analysis in the southeastern United States: Implications for origin of the Brunswick and East Coast magnetic anomalies, *Geol. Soc. Am. Bull.*, 100, 436-445.

McKeon, R. E., P. K. Zietler, F. J. Pazzaglia, B. D. Idleman, and E. Enkelmann (2014), Decay of an old orogeny: Inferences about Appalachian landscape evolution from low-temperature thermochronology, *Geol. Soc. Am. Bull.*, 126(1-2), 31-46.

Miller, S. R., P. B. Sak, E. Kirby, and P. R. Bierman (2013), Neogene rejuvenation of central Appalachian topography: Evidence for differential rock uplift from stream profiles and erosion rates, *Earth. Planet. Sci. Lett.*, 369, 1-12.

Mueller, P. A., A. L. Heatherington, D. A. Foster, W. A. Thomas, and J. L. Wooden (2014), The Suwannee suture: Significance for Gondwana-Laurentia terrane transfer and formation of Pangaea, *Gondwana Res.*, 26, 355-373.

Nelson, K. D., J. A. Arnow, J. H. McBride, J. H. Willemin, J. Huang, L. Zheng, J. E. Oliver, L. D. Brown, and S. Kaufman (1985), New COCORP profiling in the southeastern United States. Part I: Late Paleozoic suture and Mesozoic rift basin, *Geology*, 13(10), 714-718.

Parker, E. H., R. B. Hawman, K. M. Fischer, and L. S. Wagner (2013), Crustal evolution across the southern Appalachians: Initial results from the SESAME broadband array, *Geophys. Res. Lett.*, 40(15), 3853-3857.

Parker, E. H., R. B. Hawman, K. M. Fischer, and L. S. Wagner (2015), Constraining lithologic variability along the Alleghanian detachment in the southern Appalachians using passive-source seismology, *Geology*, 43(5), 431-434.

Pollitz, F. F., and W. D. Mooney (2016), Seismic velocity structure of the crust and shallow mantle of the Central and Eastern United States by surface wave imaging, *Geophys. Res. Lett.*

Prince, P. S., and J. A. Spotila (2013), Evidence of transient topographic disequilibrium in a landward passive margin river system: knickpoints and paleo-landscapes of the New River basin, southern Appalachians, *Earth Surface Processes and Landforms*, 38(14), 685-1699.

Prince, P. S., J. A. Spotila, and W. S. Henika (2010), New physical evidence of the role of stream capture in active retreat of the Blue Ridge escarpment, southern Appalachians, *Geomorphology*, 123, 305-319.

Rondenay, S (2009), Upper mantle imaging with array recordings of converted and scattered teleseismic waves, *Surv. Geophys.*, 30(4-5), 377-405.

Rondenay, S., M. G. Bostock, and J. Shragge (2001), Multiparameter two-dimensional inversion of scattered teleseismic body waves 3. Application to the Cascadia 1993 data set, *J. Geophys. Res.*, 106(B12), 30795-30807.

Rondenay, S., M. G. Bostock, and K. M. Fischer (2005), Multichannel inversion of scattered teleseismic body waves: practical considerations and applicability, *in Seismic Earth: array analysis of broadband seismograms*, 187-203.

Rondenay, S., G. A. Abers, and P. E. Van Keken (2008), Seismic imaging of subduction zone metamorphism, *Geology*, 36(4), 275-278.

Rowley, D. B., A. M. Forte, R. Moucha, J. X. Mitrovica, N. A. Simmons, and S. P. Grand (2013), Dynamic topography change of the eastern United States since 3 million years ago, *Science*, 340(6140), 1560-1563.

Schmandt, B., F.-C. Lin, and K. E. Karlstrom (2015), Distinct crustal isostasy trends east and west of the Rocky Mountain Front, *Geophys. Res. Lett.*

Steltenpohl, M. G., P. M. Mueller, A. L. Heatherington, T. B. Hanley, and J. L. Wooden (2008), Gondwanan/peri-Gondwanan origin for the Uchee terrane, Alabama and Georgia: Carolina zone or Suwannee terrane (?) and its suture with Grenvillian basement of the Pine Mountain window, *Geosphere*, 4, 131-144.

VanDecar, J. C., and R. S. Crosson (2002), Determination of teleseismic relative phase arrival times using multi-channel cross-correlation and least squares, *Bull. Seism. Soc. Am.*, 80(1), 150-169.

Wagner, L. S., K. Stewart, and K. Metcalf (2012), Crustal-scale shortening structures beneath the Blue Ridge Mountains, North Carolina, USA, *Lithosphere*, 4(3), 242-256.

Willett, S. D., S. W. McCoy, J. T. Perron, L. Goren, and C.-Y. Chen (2014), Dynamic reorganization of river basins, *Science*, 343(6175), 1248765.

Zandt, G., H. Gilbert, T. J. Owens, M. Ducea, J. Saleeby, and C. H. Jones (2001), Active foundering of a continental arc root beneath the southern Sierra Nevada in California, *Nature*, 431(7004), 41-46.

Figures

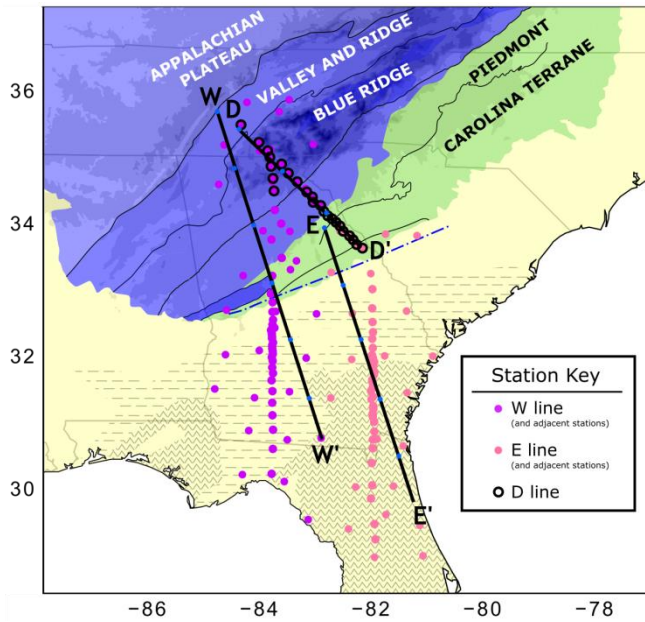


Figure 1: Simplified geological map with topographic shading (blue: Laurentian affinity terranes; green: exotic or suspect terranes; yellow: Cenozoic sedimentary cover) [Steltenpohl et al., 2008]; subsurface (dashes: Mesozoic rift basin; carets: Gondwanan affinity Suwannee terrane) [Chows and Williams, 1983]; intersection of Sp CCP suture with surface (blue dash-dotted line) [Chapter 3]. Circles show broadband station locations: stations used for both the D line profile and either the W or E line profiles are shaded accordingly with a black outline. Cross section locations are shown by thick black lines with light blue circles.

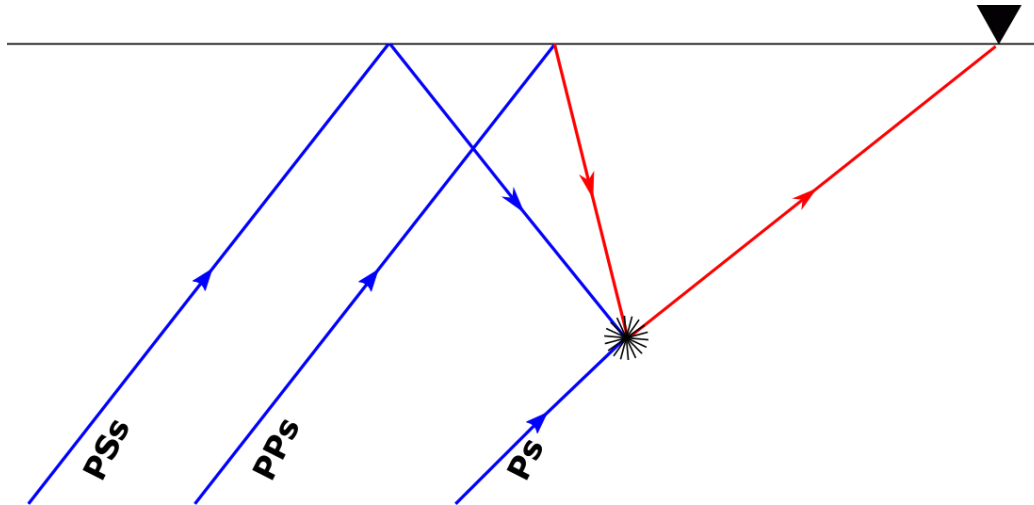


Figure 2: Ray diagram showing different scattering modes, where blue lines represent P waves and red lines represent S waves. The incident P wavefield approaches the region at a uniform angle of incidence. It can directly interact with the scatterer (black symbol), generating forward scattered P-to-P (P, not shown) and P-to-S (Ps, shown) modes. Alternatively, it may reflect off the free surface, generating back-scattered P-to-P-to-P (PPp, not shown), P-to-P-to-S (PPs, shown), P-to-S-to-P (PSp, not shown), P-to-S-to-S (PSs, shown) modes. The PSs modes are calculated for both SH and SV waves, but the PSs mode shown in Figures 4 and 6 is the SV only mode. Multiples that reflect off the free surface more than once exist in the wavefield, but are not modeled here.

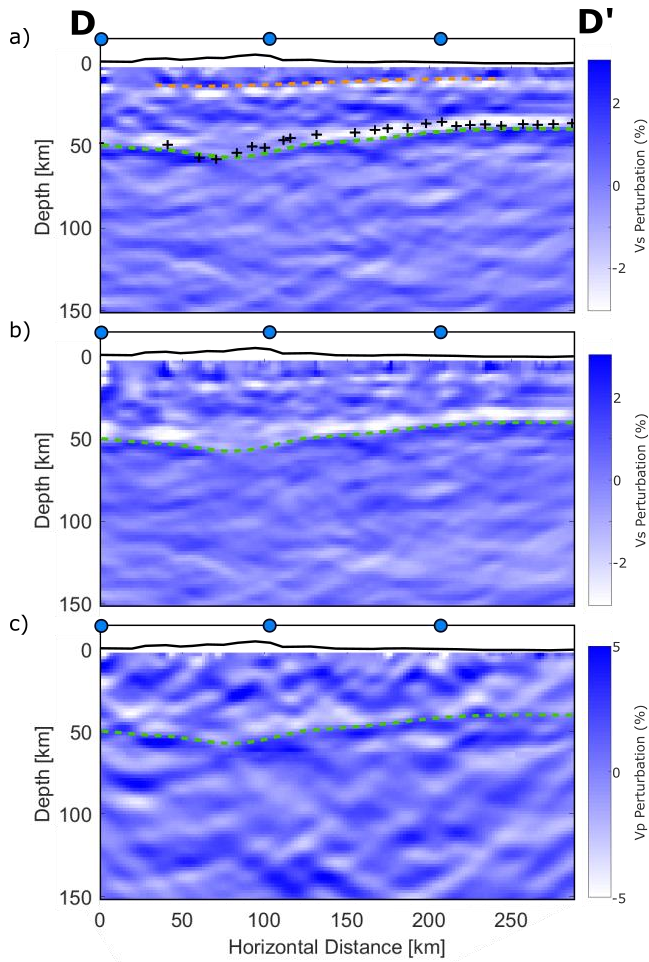


Figure 3: Inversion profiles beneath the D line (D-D' in Figure 1). In all panels, the green dashed line marks the Moho picked from the back-scattered mean mode Vs inversion (panel a). a) Mean mode inversion for Vs perturbation, consisting of all relevant back-scattered modes (PPs, PSp, PSsv, PSsh). All modes are equally weighted. Orange dashed line: possible upper crustal feature, picked from this profile. Black crosses show Moho depths calculated from Ps observations at SESAME stations [Parker et al., 2013]. b) Mean mode inversion for Vs perturbation, consisting of all relevant modes. This includes the forward scattered Ps mode in addition to the back-scattered modes utilized in panel (a). c) Mode inversion for Vp perturbation, consisting of the back-scattered Ppp mode.

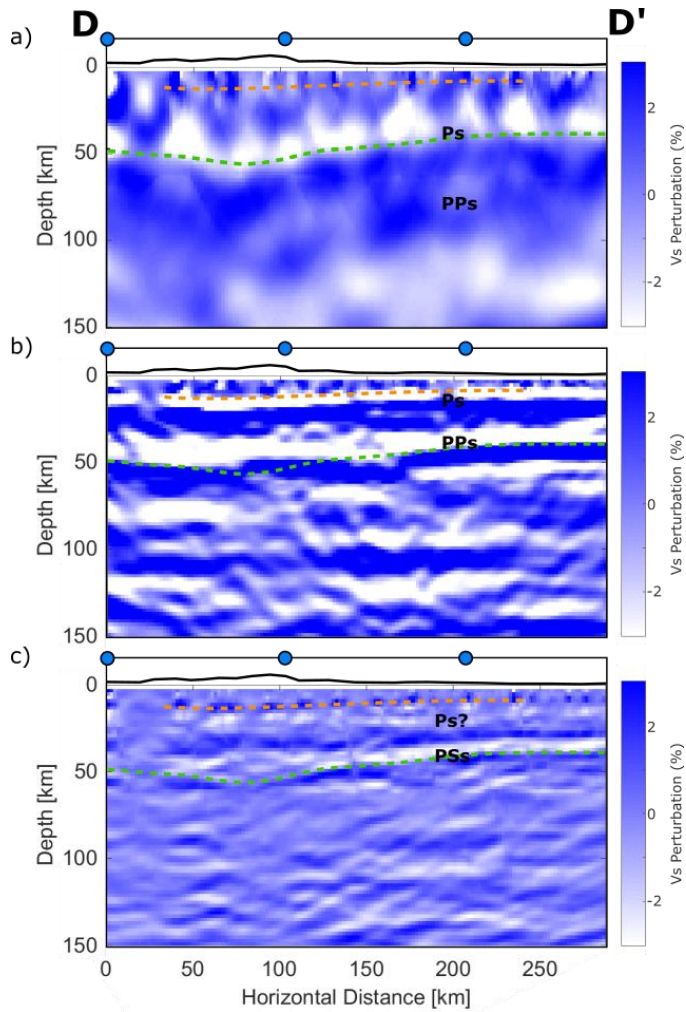


Figure 4: Individual mode inversion profiles beneath the D line (D-D' in Figure 1). In all panels, the green dashed line: Moho; orange dashed line: possible upper crustal feature. Both are picked from the back-scattered mean mode Vs inversion (Figure 3a). In all panels, the correctly migrated mode is labeled, as well other, mismigrated modes. a) Ps mode inversion for Vs perturbation. b) PPs mode inversion for Vs perturbation. c) PSs mode inversion for Vs.

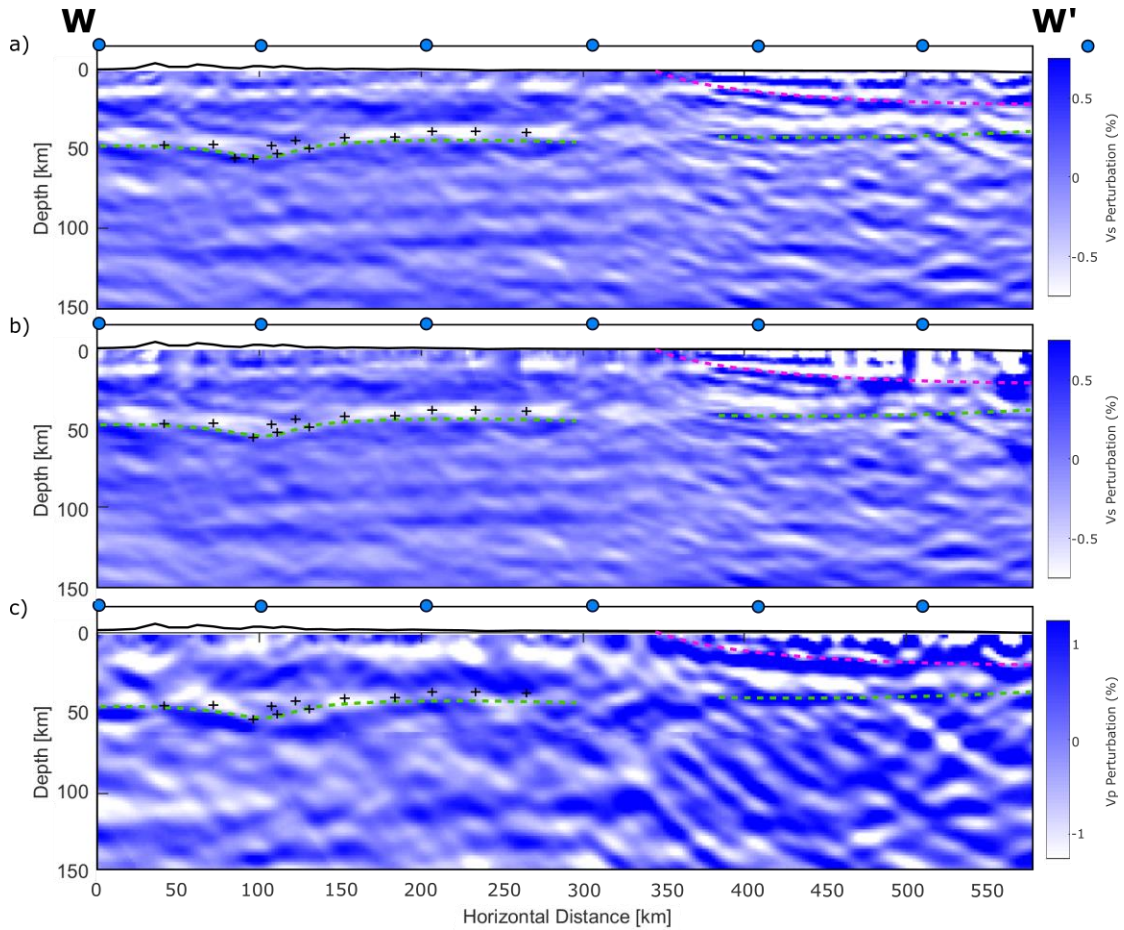


Figure 5: Inversion profiles beneath the W line (W-W' in Figure 1). In all panels, the green dashed line marks the Moho picked from the back-scattered mean mode Vs inversion (panel a). The orange dashed line marks the dipping crustal suture phase from Sp observations [Chapter 3]. a) Mean mode inversion for Vs perturbation, consisting of all relevant back-scattered modes (PPs, PSp, PSsv, PSsh). Black crosses show Moho depths calculated from Ps observations at SESAME stations [Parker et al., 2013]. b) Mean mode inversion for Vs perturbation, consisting of all relevant modes (Ps, PPs, PSp, PSsv, PSsh). c) Mode inversion for Vp perturbation, consisting of the back-scattered PPs mode.

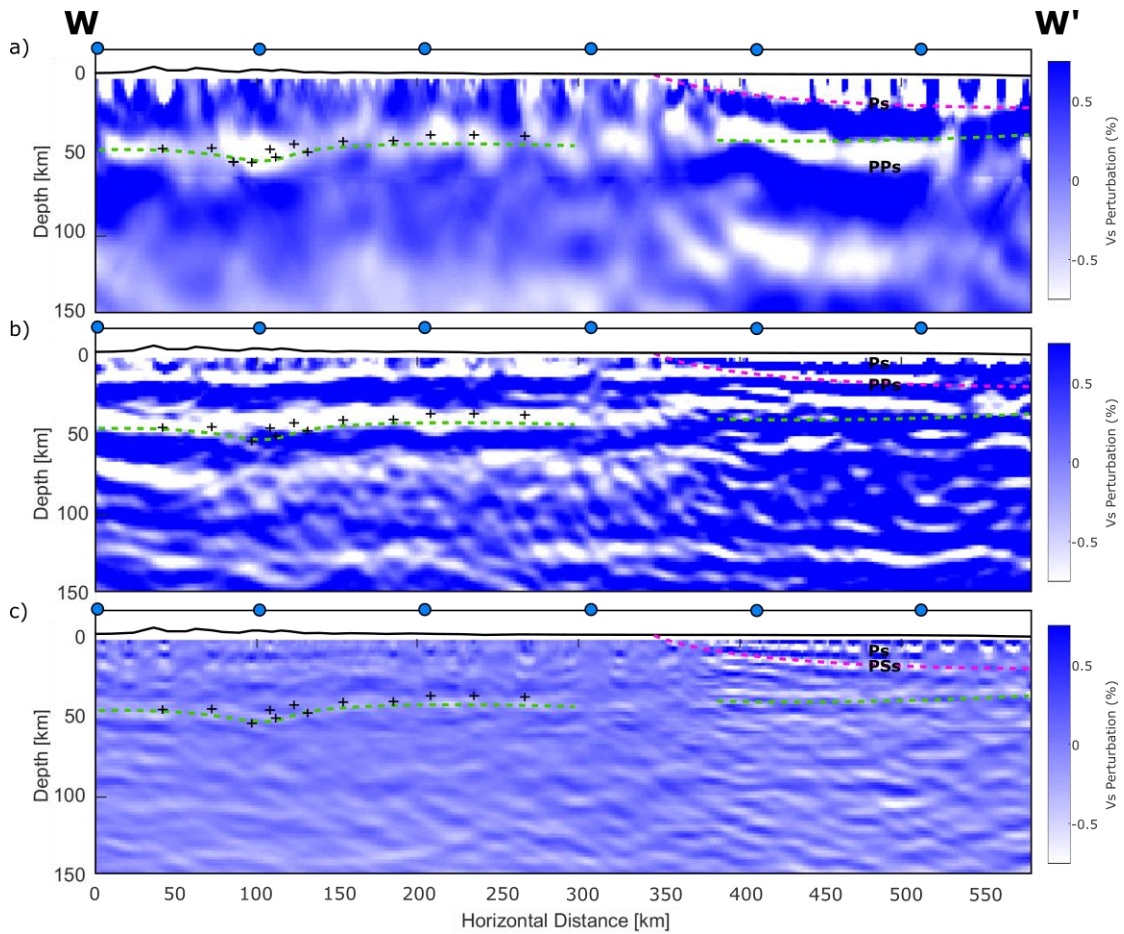


Figure 6: Individual mode inversion profiles beneath the W line (W-W' in Figure 1). In all panels, the green dashed line: Moho picked from the back-scattered mean mode Vs inversion (Figure 5a); orange dashed line: dipping crustal suture phase from Sp observations [Chapter 3]. In all panels, the correctly migrated mode is labeled, as well other, mismigrated modes. a) Ps mode inversion for Vs perturbation. b) PPs mode inversion for Vs perturbation. c) PSs mode inversion for Vs.

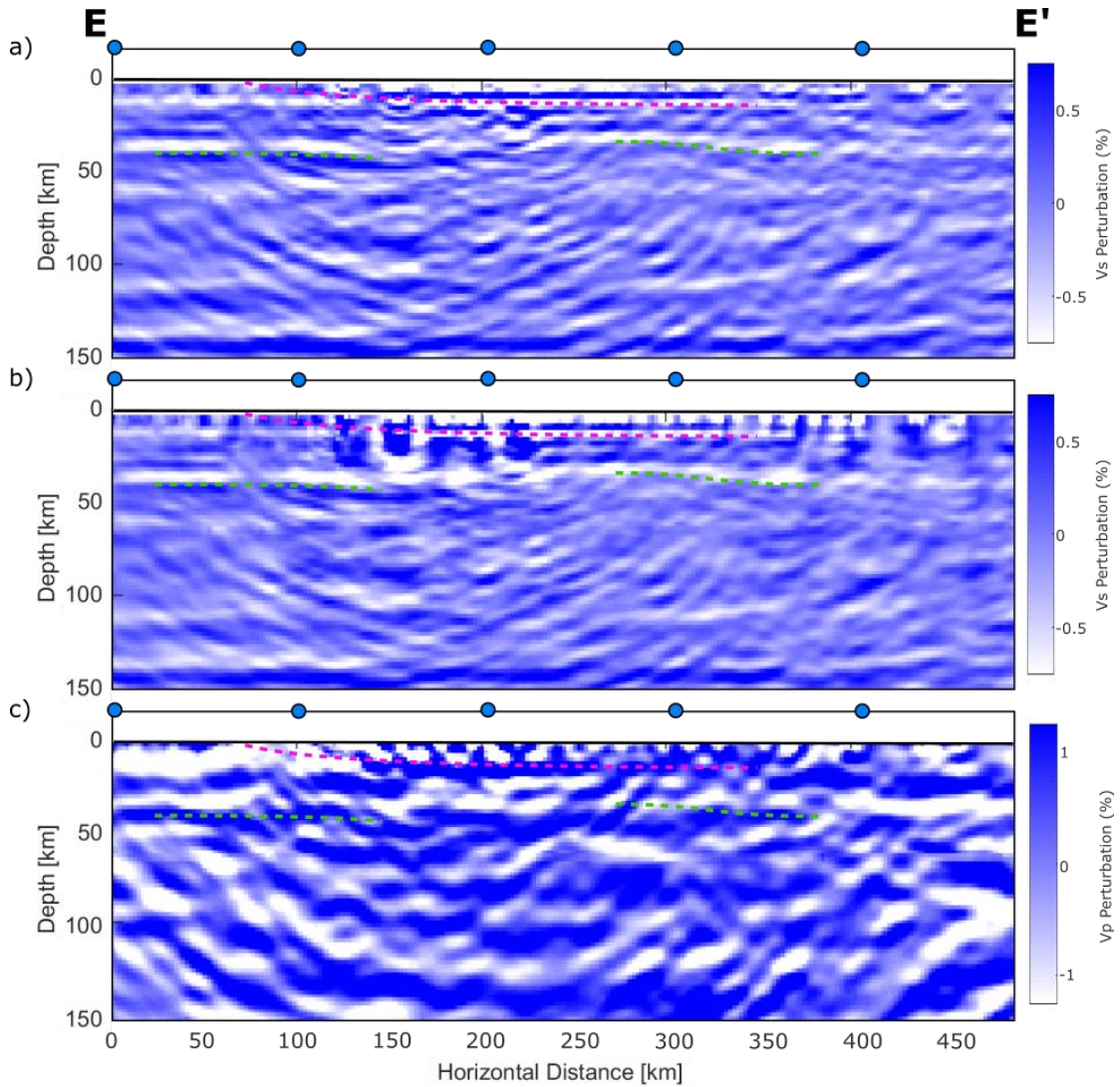


Figure 7: Inversion profiles beneath the E line (E-E' in Figure 1). In all panels, the green dashed line marks the Moho picked from the back-scattered mean mode Vs inversion (panel a). The orange dashed line marks the dipping crustal suture phase from Sp observations [Chapter 3]. a) Mean mode inversion for Vs perturbation, consisting of all relevant back-scattered modes (PPs, PSp, PSsv, PSsh). b) Mean mode inversion for Vs perturbation, consisting of all relevant modes (Ps, PPs, PSp, PSsv, PSsh). c) Mode inversion for Vp perturbation, consisting of the back-scattered P-to-P mode.

CHAPTER 5

The meaning of midlithospheric discontinuities: A case study in the northern U.S. craton

Emily Hopper¹ and Karen M. Fischer¹

¹Department of Earth, Environmental and Planetary Sciences, Brown University, Providence, RI, USA

This chapter has been published in:

Geochemistry, Geophysics, Geosystems

Citation: **Hopper, E.**, and Fischer, K. M. (2015), The meaning of midlithospheric discontinuities: A case study in the northern U.S. craton, *Geochem. Geophys. Geosyst.*, 16, 4057-4083, doi:10.1002/2015GC006030.

Abstract

Converted wave imaging has revealed significant negative velocity gradients, often termed midlithospheric discontinuities, within the thick, high-velocity mantle beneath cratons. In this study, we investigate the origins and implications of these structures with high-resolution imaging of mantle discontinuities beneath the Archean Wyoming, Superior and Medicine Hat, and Proterozoic Yavapai and Trans-Hudson terranes. Sp phases from 872 temporary and permanent broadband stations, including the EarthScope Transportable Array, were migrated into three-dimensional common conversion point stacks. Four classes of discontinuities were observed. (1) A widespread, near-flat negative velocity gradient occurs largely at 70–90 km depth beneath both Archean and Proterozoic cratons. This structure is consistent with the top of a frozen-in layer of volatile-rich melt. (2) Dipping negative velocity gradients are observed between 85 and 200 km depth. The clearest examples occur at the suture zones between accreted Paleoproterozoic Yavapai arc terranes and the Wyoming and Superior cratons. These interfaces could represent remnant subducting slabs, and together with eclogite in xenoliths, indicate that subduction-related processes likely contributed to cratonic mantle growth. (3) Sporadic positive velocity gradients exist near the base of the lithospheric mantle, perhaps due to laterally variable compositional layering. (4) In contrast to off-craton regions, clear Sp phases are typically not seen at lithosphere-asthenosphere boundary depths beneath Archean and Proterozoic terranes, consistent with a purely thermal contrast between cratonic mantle lithosphere and asthenosphere.

1. Introduction

1.1. Cratonic mantle seismic velocity discontinuities

Cratonic mantle lithosphere is typically characterized by an anomalously thick layer of cold mantle that has been highly depleted by melt extraction [e.g., Jordan, 1978; Boyd, 1989; Griffin et al., 1999; Lee, 2006; Lee et al., 2011], with low surface heat flows [e.g., Pollack et al., 1993; Rudnick and Nyblade, 1999; Mareschal and Jaupart, 2004] and seismic velocities that are significantly higher than average to depths of at least 200 km [e.g., Gung et al., 2003; Jordan and Paulson, 2013].

Within the overall high-velocity cratonic mantle, seismic discontinuities or vertically localized seismic velocity gradients have been found by a range of seismic studies. In particular, converted wave studies have imaged negative velocity gradients (often termed midlithospheric discontinuities, or MLDs) on a widespread basis, typically at depths of 60–150 km [e.g., Zurek and Dueker, 2005; Wittlinger and Farra, 2007; Savage and Silver, 2008; Chen et al., 2009; Rychert and Shearer, 2009; Abt et al., 2010; Ford et al., 2010; Geissler et al., 2010; Miller and Eaton, 2010; Kind et al., 2012, 2015; Kumar et al., 2012; Wölbern et al., 2012; Hansen et al., 2013, 2015; Bodin et al., 2013; Cooper and Miller, 2014; Foster et al., 2014; Hopper et al., 2014; Lekić and Fischer, 2014; Porritt et al., 2015], and discontinuities at comparable depths have also been characterized as anisotropic boundaries [Bostock, 1998; Levin and Park, 2000; Saul et al., 2000; Mercier et al., 2008; Sodoudi et al., 2013; Wirth and Long, 2014]. Evidence for a midlithospheric low-velocity zone is also found in diverse studies based on reflected waves [Revenaugh and Sipkin, 1994], surface waves [e.g., Weeraratne et al., 2003; Chen et al., 2007; Romanowicz, 2009; Yuan and Romanowicz, 2010; Yuan et al., 2011], long-range seismic profiles [Thybo and Perchuc', 1997; Nielsen et al., 2002; Thybo, 2006] and regional P waveforms [Chu et al., 2012].

However, while some interpretations of MLDs have treated these features as a single negative velocity gradient, increasingly high-resolution imaging within various cratonic mantles has shown that while a single MLD may dominate discontinuity structure in some regions, in others multiple discontinuities exist [e.g., Lekić and Fischer, 2014; Hopper et al., 2014]. In addition, the relationship of MLDs to dipping structures observed in cratonic mantle by both Ps studies [Bostock, 1998; Moorkamp et al., 2007; Mercier et al., 2008; Snyder, 2008; Chen et al., 2009] and reflection profiles [Calvert et al., 1995; Steer et al., 1998; White et al., 2003] requires further exploration.

The sharpness of the negative seismic velocity gradient from the cold cratonic mantle lithosphere to the underlying hot asthenosphere is another question of interest. Beneath noncratonic continental regions, the lithosphere-asthenosphere boundary (LAB) velocity gradient typically generates significant converted body waves, and thus is localized over ~30 km or less and cannot be produced by a thermal gradient alone; additional factors such as volatile content, bulk composition, partial melt, grain size, or anisotropic fabrics must also vary between the (seismologically defined) lithosphere and asthenosphere [e.g., Rychert et al., 2007; Eaton et al., 2009; Fischer et al., 2010; Fischer, 2015]. In contrast, LAB velocity gradients at the base of the cratonic mantle are typically more gradual, or at least more debated. Beneath North America, some prior studies found that converted phases are not typically observed at depths consistent with the base of the lithosphere as defined by comparison to local tomography, or are weak and intermittent, when seen [e.g., Abt et al., 2010; Kumar et al., 2012; Kind et al., 2012; Levander and Miller, 2012; Lekić and Fischer, 2014; Hopper et al., 2014]. The absence of clear converted phases (at the frequencies used in these studies) is consistent with a LAB velocity gradient that is distributed over 50–70 km or more and that can be explained by a purely thermal boundary [e.g., Abt et al., 2010; Ford et al., 2010]. However, other studies do report converted phases from LAB

depths beneath portions of the North American craton [Miller and Eaton, 2010; Hansen et al., 2013; Foster et al., 2014; Porritt et al., 2015; Kind et al., 2015].

The goals of this investigation are to better define lithospheric mantle velocity discontinuities beneath the Archean Wyoming, Medicine Hat, and Superior cratons in the U.S. and the Proterozoic terranes that surround them, and to explore the origins of the discontinuities by comparing their properties to a variety of models that relate to the formation and evolution of the cratonic mantle lithosphere.

1.2. Tectonic, geophysical, and geochemical setting

The northern Rockies and Great Plains of the U.S. are made up of a mosaic of Archean continental blocks: the Wyoming craton, Medicine Hat Block, and the westernmost Superior craton. Parts of the Wyoming craton date back to >3.0 Ga [Mueller et al., 1992; Chamberlain et al., 2003]. However, final assembly of the Wyoming craton did not occur until the latest Archean after several episodes of inferred lateral accretion (2.7–2.5 Ga) with associated calcalkaline magmatism [Frost et al., 1998; Chamberlain et al., 2003; Mueller and Frost, 2006]. Accretion was followed by extensive 2.3–2.0 Ga rifting in southern Wyoming [Karlstrom and Houston, 1984; Cox et al., 2000; Whitmeyer and Karlstrom, 2007].

The Archean blocks were knitted together along Paleoproterozoic orogenic zones including the Trans-Hudson orogen, the Great Falls Tectonic Zone, and the suture zone on the southern margin of the Wyoming craton, the Cheyenne Belt (Figure 1a). Arc accretion at the Cheyenne Belt started at 1.74–1.78 Ga [Karlstrom and Houston, 1984; Chamberlain, 1998]. Continued accretion of ~1300 km of Proterozoic terranes onto this margin between 1.8 and 1.6 Ga created a large portion of the central U.S. [e.g., Nelson and DePaolo, 1985; Hoffman, 1988; Whitmeyer and Karlstrom, 2007].

In the Mesozoic, deformation associated with the Sevier Orogeny extended only onto the western margin of the Wyoming craton, ending at the Sevier Fold and Thrust Belt (Figure 1a) [DeCelles and Coogan, 2006]. Within the Wyoming craton, both pre-Laramide deformation, thought to be recorded by Moho topography [Yeck et al., 2014], and Laramide crustal shortening [Erslev and Koenig, 2009] occurred. However, xenolith data indicate that the mantle lithosphere appears to have remained intact [Eggler et al., 1987a; Carlson et al., 1999], except in the northern Wyoming craton where the mantle lithosphere deeper than 150 km may have been replaced [Carlson et al., 1999], possibly due to Laramide subduction [Humphreys et al., 2015].

In many recent studies that employ data from EarthScope's USArray Transportable Array, the Archean and Proterozoic terranes in our study region are underlain by thick layers of high-velocity mantle [e.g., Schmandt and Humphreys, 2010; Sigloch, 2011; Tian and Zhao, 2012; Shen et al., 2013; Burdick et al., 2014; Lou and van der Lee, 2014; Porritt et al., 2014; Schaeffer and Lebedev, 2014; Schmandt and Lin, 2014].

However, the cratonic mantle is not uniform. For example, while the mantle lithosphere beneath the Wyoming craton is high velocity relative to adjacent regions of the western U.S., its maximum velocities are typically less than found in other parts of the North American craton [Burdick et al., 2014; Porritt et al., 2014; Schaeffer and Lebedev, 2014; Yuan et al., 2014]. Lower velocities have also been observed beneath craton accreted in the Proterozoic i.e., the Trans-Hudson orogen [e.g., Yuan et al., 2014], and the Cheyenne Belt and Great Falls Tectonic Zone are correlated with high conductivity anomalies [Meqbel et al., 2014].

Mantle xenoliths in our study area are found near the north and south margins of the Wyoming craton (Figures 1a and 1c). Xenoliths sourced from up to 250 km depth show that much of the root is defined by a cold geotherm ($35\text{--}44\text{ mW m}^{-2}$) and was depleted in Archean or Paleoproterozoic times down to ~ 200 km depth [Eggler et al., 1987a; Carlson and Irving, 1994;

Carlson et al., 1999, 2004; Kuehner and Irving, 1999; Hearn, 2004; Aschepkov et al., 2013]. However, extensive metasomatism and refertilization has also occurred in multiple episodes from the Archean to the Cenozoic [Carlson and Irving, 1994; Carlson et al., 1999, 2004; Downes et al., 2004; Hearn, 2004].

2. Data and methods

2.1. Data

We collected data for earthquakes in the USGS National Earthquake Information Center catalog with $M_w > 5.8$ from the Incorporated Research Institutions for Seismology (IRIS) Data Management Center. We utilized data from all 872 available broadband stations in the study area, including 407 Earthscope USArray Transportable Array stations, 13 other temporary arrays, and 48 permanent stations (see Figure 1b for details). Using S_p waveforms provides an image of the uppermost mantle that is uncontaminated by crustal multiples. However, this phase becomes postcritical at depth, with the critical depth decreasing with decreasing epicentral distance. We limit the minimum epicentral distance of our sources, and also exclude energy migrated to depths below the critical depth based on a station-specific 1D velocity profile extracted from local 3-D tomography models [see Porritt et al., 2014, section 2.2; Shen et al., 2013]. Overlap in arrival time with other phases further restricts which sources are useable [e.g., Wilson et al., 2006]. We therefore use sources from above 300 km depth in the distance range 55° – 85° . The distribution in back azimuth is highly skewed toward events sourced from the northwest (47.5% of waveforms sourced from a back azimuth of 300° – 320°) and southeast (24.5% of waveforms sourced from a back azimuth of 140° – 160°). Our final stacks incorporate 77,349 waveforms sourced from 6,198 events.

2.2. Phase processing: picking, deconvolution, migration, and stacking

To mitigate the effects of large variations in mantle velocity across the study region, we used the automated array-based procedure of Lekić and Fischer [2014] to define S phase windows. The data were rotated into its P and SV components using a free-surface transfer matrix

which suppresses the effects of the free surface [Kennett, 1991; Bostock, 1998]. The free-surface values for V_p and V_p/V_s were found by grid search, aiming to minimize the amplitude of the parent SV phase on the daughter P component [e.g., Abt et al., 2010]. The data were filtered at 4–33 s, found to minimize interference between shallow mantle and Moho phases while maintaining coherency in imaged mantle discontinuities [Hopper et al., 2014].

We deconvolved the P by the SV component using the extended-time multitaper cross-correlation method [Helffrich, 2006], with the parameters found to be optimal by Lekić and Fischer [2014]. We then migrated into a three-dimensional volume using a station-specific velocity profile constructed from a combination of local velocity models. For the crust, the average shear velocity was taken from Shen et al. [2013]. Average crustal V_p was calculated using the V_p/V_s ratio of the crust (A. R. Lowry, personal communication, 2014). Within the mantle, P wave and S wave velocity anomalies from Porritt et al. [2014] were used; due to the heavy damping of this model (R. W. Porritt, personal communication, 2014), we scaled the perturbations by 1.5X, which we found best matched the amplitude of variations seen by Obrebski et al. [2010]. The waveforms were stacked by common conversion point (CCP) using a spline function representation of the Sp Fresnel zone [see Lekić et al., 2011]. These Fresnel zones were calculated using the measured 9 s average dominant period of the waveforms. We also reversed the polarity of the phases for consistency with Ps studies; a positive phase indicates a positive velocity gradient (PVG) with depth, and a negative phase indicates a negative velocity gradient (NVG) with depth.

2.3. Bootstrapping and uncertainties

To ensure we only interpret robust phases, we bootstrapped the Sp CCP stacks. That is, we randomly resampled the waveforms and recalculated the Sp CCP stack 50 times and determined the mean and standard deviation of these 50 stacks. The mean stack is plotted throughout the paper. The standard deviation allows us to discern robust phases arising from

observable structures within the lithosphere from phases that are not resolvable from the noise of the data set. This approach is particularly important where discontinuities appear to be relatively complex, such as in the cratonic mantle.

Our criteria for determining whether a feature in the stack is robust are as follows. (1) Converted phase amplitude must be greater than 10% that of the parent phase. (2) Bootstrap testing shows the phase to be significant, here defined as the standard deviation of the stack being less than 5% of the parent phase amplitude (i.e., less than half the amplitude of the minimum interpretable converted phase). (3) The phase must have a consistent depth or shape over at least 0.5° in latitude or longitude and be visible on perpendicularly oriented cross sections. An example showing phases selected and rejected by these criteria is shown in supporting information Figure S1.

3. Observed mantle discontinuities

3.1. Summary of observed mantle discontinuity types

In the cratonic mantle, we observe several types of discontinuity structure: (1) a widespread negative discontinuity (NVG) in the 65–105 km depth range; (2) dipping NVG's in the 85–200 km depth range; (3) sporadic positive phases (PVGs) at the greater depths (>125 km); (4) a typical absence of clear NVGs in the LAB depth range, with a few exceptions. From comparison to the high-velocity lid [Porritt et al., 2014], the layering represented by the first three types of discontinuities falls largely within the lithospheric mantle (Figures 2–4). These classes of discontinuities are described more completely in the remainder of this section.

3.2. Observed shallow, subhorizontal NVG

At 65–105 km depth, a quasi-horizontal NVG is observed over much of the study area. This band of scattering crosses multiple terrane boundaries, although the character of the phase varies in detail. For example, an NVG at 70–90 km depth exists almost everywhere east of 108°W (Figures 2a and 3). Within the core of the Wyoming craton (between 110°W and 105°W ,

Figure 3), the phase is relatively localized in depth, although laterally variable in both depth (83 ± 6 km) and strength. The phase broadens near the eastern margin of the Wyoming craton, perhaps due to the juxtaposition of two NVGs sufficiently close in depth that they are difficult to resolve with relatively long-period Sp phases (east of 105°W , Figure 3a; east of 103°W , Figures 3b and 3c).

3.3. Dipping structures within the lithosphere

3.3.1. Observed dipping NVGs

Beneath the subhorizontal NVG zone described in Section 3.2, we observe more discontinuous, intermittent NVGs, many of which are dipping. The most extensive dipping NVGs occur at the boundary between the Proterozoic Yavapai terrane and the Archean Wyoming and Superior cratons. The NVGs dip toward the center of the Archean cratons, as is observed in the Canadian shield [Bostock, 1998; Calvert et al., 1995; Mercier et al., 2008; van der Velden and Cook, 2005; White et al., 2003].

3.3.2. The Cheyenne Belt

The Sp stacks in this study document mantle discontinuities dipping toward the center of the Wyoming craton. The most prominent NVG (dotted line, Figure 5) dips northward directly beneath the surface expression of the Cheyenne Belt, the suture between Proterozoic Yavapai and Archean Wyoming lithosphere. This NVG appears to continue as a relatively flat-lying phase beneath the interior of the Wyoming craton. A secondary dipping NVG further to the south (dash-dotted line, Figure 5) dips in a similar direction to the first. These interfaces are overlain by a flat-lying NVG, as characterized in Section 3.2 (dashed line, Figure 5). These three surfaces were handpicked on perpendicular cross sections between 38°N and 45°N , and 111°W and 101°W , with interpolated surfaces shown in Figure 6.

The primary dipping NVG wraps around the Wyoming craton, such that its steepest dips underlie the Cheyenne Belt and the eastern boundary with the Trans-Hudson orogen (Figure 6b). There is an overall northwesterly dip to this surface, although dip varies across the region in detail. The NVG flattens at 120–140 km depth, and extends several hundred kilometers beneath the interior of the Wyoming craton. As shown in Figure 6d, the three NVGs are distinct in depth. All lie within the lithosphere as defined by regional tomography (supporting information Figure S2).

The northward polarity of subduction implied by the dipping NVGs is consistent with mantle structures seen in prior work beneath the Cheyenne Belt, including a northwestward dipping band of high velocities along the southern margin of the Wyoming craton in tomographic studies [Yuan and Dueker, 2005a; MacCarthy et al., 2014; Porritt et al., 2014], northward directed underthrusting inferred from converted waves [Poppeliers and Pavlis, 2003], and a high conductivity anomaly, interpreted as deeply underthrust metasediments in the suture zone, that extends to ~100 km depth [Meqbel et al., 2014]. In addition, the lack of an Archean sediment contribution to the isotopic signature of the first arc accreted here suggests it formed above a northward dipping subduction zone [Jones et al., 2011]. At crustal depths, the Cheyenne Belt has been associated with thickened crust interpreted to be a zone of crustal imbrication [Snelson et al., 1998; Henstock et al., 1998; Poppeliers and Pavlis, 2003; Crosswhite and Humphreys, 2003; Hansen and Dueker, 2009; Hansen et al., 2013], with some studies preferring northward underthrusting of the Proterozoic crust beneath the Wyoming craton [Zurek and Dueker, 2005; Hansen and Dueker, 2009]. On the other hand, southward dipping subduction has been inferred based on the orientation of deformed structures, comparison of metamorphic grade, the southward transportation of Archean isotopic signatures [Karlstrom and Houston, 1984; Chamberlain, 1998], and seismically imaged southeastward dipping crustal reflectors [Allmendinger et al., 1982; Crosswhite and Humphreys, 2003; Poppeliers and Pavlis, 2003]. Shallow S-dipping and deeper

N-dipping structures could be reconciled by “wedge” tectonism, suggested to be typical of Archean-Proterozoic boundaries globally based on deep seismic reflection profiles [Snyder, 2002].

3.3.3. The Yavapai-Superior craton boundary

The suture zone marking the Yavapai-Superior boundary, the Spirit Lake tectonic zone, marks the northern extent of Yavapai-aged crust from SE South Dakota to Wisconsin [Holm et al., 2007; Van Schmus et al., 2007]. Here we observe a clear NVG dipping to the northeast on the southwest margin of the Superior craton. Examples include a strike-perpendicular view of the NVG between 100 and 150 km depth from 400 to 750 km along the cross section in Figure 7, and an oblique view of the NVG east of 102°W in Figure 2a.

The northeast-dipping NVG is consistent with Yavapai-interval magmatism north of the Spirit Lake tectonic zone that suggests northward dipping subduction [Holm et al., 2005; Van Schmus et al., 2007]. Although recent local tomography does not resolve dipping high-velocity mantle features at this margin [Frederiksen et al., 2013], P-to-S receiver functions are interpreted to show a northwest-dipping relict subduction zone just beneath the Moho [Turner et al., 2015].

3.3.4. Other Proterozoic and Archean collision zones

We do not observe clear mantle discontinuities that can be unambiguously associated with other zones of Proterozoic accretion. Although seismic reflection surveys image prominent dipping crustal reflectors at the margins of the Trans-Hudson orogen [Lewry et al., 1994; Nelson et al., 1993], we cannot distinguish interpretable structures within the mantle lithosphere beyond a broad band of negative energy in the Sp CCP stacks (e.g., between 103°W and 99°W; Figure 3). While the origins of the Great Falls Tectonic Zone are debated [Boerner et al., 1998; Mueller et al., 2002; Ross, 2002], calcalkaline rocks of the Little Belt arc [Mueller et al., 2002] and dipping upper mantle reflectors imaged by seismic refraction [Gorman et al., 2002] support the idea of a

suture associated with subduction. However, our Sp CCP stacks are insufficiently well resolved to contribute to the debate, especially this close to the edge of our study region.

Dipping interfaces could also have formed within the interiors of the Archean cratons, either by Archean subduction, or alternatively by imbrication of the continental lithosphere through Neoproterozoic orogenic thickening [Gray and Pysklywec, 2010]. However, while some dipping features are observed within the interior of the Wyoming craton (e.g., at 108°, Figure 4), they are less laterally extensive than those associated with Proterozoic sutures and cannot be confidently linked with any feature of surface geology.

3.4. Base of the lithosphere

The Sp CCP stacks show a strong LAB beneath Phanerozoic regions in the western U.S. (e.g., west of the Sevier Thrust Belt at ~112°W in Figures 2a, 3b, and 3c) and beneath the thinned high-velocity lid of the High Rockies (Figure 6a). In cratonic regions, however, a coherent NVG is not in general observed at depths within the lithosphere-asthenosphere transition range defined by the Porritt et al. [2014] seismic tomography (Figures 2 and 4-7). The one location where we observe a clear, deep LAB NVG is beneath the eastern Great Plains, between 39°N and the southern boundary of our study region. The NVG dips from 100 km depth at 103.5°W to 200 km depth at 98°W, at which point it levels off, extending to 96°W (Figure 8a), and it coincides with an increase in the thickness of the high-velocity lid (Figure 8b).

The presence of a clear NVG at lithosphere-asthenosphere transition depths west of the Sevier Thrust Belt and the typical, although not universal, absence of a NVG at lithosphere-asthenosphere transition depths to the east of the Sevier Thrust Belt are consistent with a number of prior analyzes of Sp phases that overlap with our study region [e.g., Abt et al., 2010; Levander and Miller, 2012; Kumar et al., 2012; Kind et al., 2012; Lekić and Fischer, 2014; Hopper et al., 2014]. However, other studies overlapping with our study region have argued for a more

widespread NVG at tomographically defined LAB depths [e.g., Hansen et al., 2013; Foster et al., 2014; Kind et al., 2015].

3.5. Sporadic PVGs

At depths of 150–220 km beneath cratonic regions, the most coherent features seen in our CCP stacks correspond to positive velocity gradients, or PVGs. While weaker and more sporadic than either of the two classes of NVGs first described, bootstrap testing shows some of this energy is robust. In general, the PVGs concentrate near the base of the lithosphere (107°W–103°W, Figures 3b and 4; 500–850 km along profile, Figure 7), but their sporadic character implies that they do not represent a ubiquitous component of the mantle lithosphere.

4. The origin of lithospheric layering

4.1. Summary of observational constraints

We have documented that the mantle lithosphere beneath the Wyoming craton and adjacent cratonic regions contains not a single MLD, but rather two distinct categories of NVGs, and, at greater depth, sporadic PVGs. A lithosphere-asthenosphere boundary NVG is in general not observed. In this section, we explore possible origins for these features and their implications for the formation and/or alteration of the mantle lithosphere. We conclude that the observed discontinuities were formed by a combination of processes.

4.2. Widespread NVG in the shallow upper mantle

4.2.1. Possible origins: chemical composition, rock fabric and deformation mechanism

The shallowest NVG lies across most of the study region, is relatively flat lying, and largely occurs between 70 and 90 km depth. It appears to be simpler and more localized in depth in the core of the Wyoming craton, but spans both Archean and Proterozoic terranes. Given its widespread nature, a mechanism that affects cratonic mantle of varied age is required.

Layering in fertility cannot explain the flat-lying NVG. The observed decrease in velocity would be consistent with an increase in fertility with depth, given that melt depletion in

peridotites increases velocity [e.g., Lee, 2003]. However, xenoliths do not show a downward increase in fertility that correlates with NVG depths of 70–90 km. Xenoliths from the Williams kimberlite, at the northern edge of the Wyoming craton, show depleted compositions on both sides of the 70–90 km NVG range [Carlson et al., 1999] and those from the State Line District just south of the Wyoming craton actually show a decrease in fertility at >100 km [Eggler et al., 1987a]. This lack of correlation between depletion variations and midlithospheric NVGs is typical of other cratons worldwide; observed vertical changes in Mg# are in general not at the right depth range, nor sufficiently large to generate observed NVGs [Selway et al., 2015, and references therein].

The top of a low-velocity layer that is rich in volatiles (Figure 10) could explain the 70–90 km NVG. Low-velocity layers with high concentrations of phlogopite [Rader et al., 2015] or amphibole [Selway et al., 2015] have been proposed as the mechanism for shallow MLDs globally. Here we explore the possibility of this type of structure in the context of the Wyoming craton, and in Section 4.4, we show that velocity models with volatile-rich layers are consistent with the Sp observations.

How might such a layer form? A layer of partial melt or frozen-in melt could have a sufficiently sharp upper limit if it were to pond at the nearly isobaric kink in the solidus observed for carbonated peridotites [Falloon and Green, 1989; Wyllie, 1995; Dasgupta and Hirschmann, 2010; Dasgupta et al., 2013]. Using a nominally anhydrous system with relatively fertile peridotite, this kink occurs at approximately 50–65 km depth [Falloon and Green, 1989; Dasgupta and Hirschmann, 2010; Dasgupta et al., 2013], shallower than the observed widespread NVGs. However, the addition of water to the system could increase the depth of the solidus kink [Brey et al., 1983; Wyllie, 1987], and recent experiments suggest that the kink would also be deeper in depleted mantle compositions more typical of cratons [R. Dasgupta et al., personal communication, 2015].

Would such a layer contain partial melt in the present day, or would be the melt be frozen? The cool geotherms estimated for the Wyoming craton in the 65–100 km depth range (less than ~800°C from xenolith [Eggler et al., 1987a; Humphreys et al., 2015] and xenocryst data [Griffin et al., 2004]) provide conditions in which the volatile-rich melt could easily be subsolidus. For example, Rader et al. [2015] propose a model in which (1) volatile-rich melts collect below the solidus kink at the base of thin, hot continental Archean mantle lithosphere and (2) the melt layer solidifies at midlithospheric depths as the mantle lithosphere cools and thickens. Such a mechanism may have been facilitated by the efficient decarbonation of subducting slabs that is thought to have occurred during the Archean and Paleoproterozoic [Dasgupta, 2013]. Alternatively, even in an already formed and cool cratonic mantle lithosphere, carbonated melts from the asthenosphere might be able to rise rapidly enough through the mantle lithosphere to remain out of thermal equilibrium and supersolidus, thus enabling them to reach the depth of the solidus kink and then freeze into the volatile-rich layer. Given the possibility of both scenarios, a frozen-in volatile-rich layer could have formed at any time during or since root formation. On the other hand, certain melt compositions may remain supersolidus even at cold cratonic conditions. For example, with the right oxygen fugacity, a carbonated and hydrated fertile peridotite melt may remain stable in the shallow NVG depth range [Dasgupta, 2014] and sulfur-rich melts also have anomalously low melting temperatures [Helffrich et al., 2011].

Geochemical and petrological data support the presence of a frozen-in layer of hydrated and carbonated minerals. Globally, xenoliths sourced from the MLD depth range are consistent with the presence of a hydrous and/or carbonated mineral layer at these depths [Rader et al., 2015]. Within the Wyoming craton and its surroundings, abundant evidence exists for phlogopite in the mantle and multiple episodes of metasomatism. (1) Phlogopite is commonly observed as an accessory mineral rimming phases in upper mantle xenoliths across the Wyoming craton [Buhlmann et al., 2000; Carlson et al., 2004; Downes et al., 2004; Eggler et al., 1987b; Hearn,

1999, 2004; Lester and Farmer, 1998] (Figure 1c). (2) Refertilization (modal metasomatism) is common in many of the mantle samples [Carlson et al., 2004; Carlson and Irving, 1994; Eggler et al., 1987a]. (3) The extensive Montana alkalic province is often modeled as having one source component of metasomatically enriched mantle lithosphere [Buhlmann et al., 2000; Dudas et al., 1987; O'Brien et al., 1995; Wooden and Mueller, 1988]. (4) Carbonatites in the Bearpaw Mountains [Macdonald et al., 1992], the Bear Lodge alkali complex [Moore et al., 2015], and the Porcupine Dome carbonate-rich mica peridotites [Hearn, 1999] are thought to be sourced from the lithospheric mantle, i.e., there is abundant carbonate mineralization at depth. (5) Alkalic rocks in the Bearpaw Mountains are consistent with melting of a phlogopite-bearing mantle assemblage at pressures of 3 GPa, i.e., approximately 90 km depth [Macdonald et al., 1992].

Another mechanism for generating a localized zone of hydrous minerals in the shallow NVG depth range would be the stabilization of amphibole, which occurs at approximately 80–90 km depth over a wide temperature range [Selway et al., 2015]. Upward percolating hydrous fluids or melt might be expected to crystallize amphibole rapidly once within the amphibole stability zone, generating a thin low-velocity layer. However, while amphibole-rich xenoliths have been found in a number of cratons, and in some cases, the amphibole-bearing xenoliths sample the 70–90 km depth range where we observe the shallowmost NVG [Selway et al., 2015], the absence of evidence for an amphibole-rich layer on a global basis [Selway et al., 2015] poses a challenge for this model.

Vertical variations in radial and azimuthal anisotropy cannot be ruled out as explanations for the observed NVG at 70–90 km, but neither are they required by the data. If vertical variations in azimuthal or radial anisotropy are sufficiently large and localized, they can easily generate coherent Sp and Ps phases at amplitudes comparable to observations [e.g., Ford, 2013; Sodoudi et al., 2013; Wirth and Long, 2014; Selway et al., 2015], with periodic back azimuthal variations in

Sp amplitudes from azimuthal anisotropy and constant Sp amplitude in back azimuth from radial anisotropy.

To look for the effects of azimuthal anisotropy in the observed mantle discontinuities, we recalculated the CCP stacks using data from the two dominant limited back azimuthal ranges in our data (135° – 175° and 300° – 340°) and found no well-resolved variation in the NVG at 70–90 km, or in fact in any of the mantle phases (supporting information Figure S5). While this result does not provide evidence for azimuthal anisotropy as the source of the NVG, it also does not rule out azimuthal anisotropy. Because the back azimuth ranges in these images are nearly 180° apart, many azimuthally anisotropic models would predict comparable amplitudes for the two subsets of the data.

However, the NVG at 70–90 km is not obviously consistent with existing models for azimuthal anisotropy in the region, for example, the layering in azimuthal anisotropy in the long-period waveform tomography of Yuan and Romanowicz [2010]. The Yuan and Romanowicz [2010] model contains two layers with distinct fast-axis orientations in the mantle lithosphere of the North American craton, plus a third layer at greater depths that they interpret as ongoing flow in the asthenosphere. While the gradient in direction of azimuthal anisotropy fast axis in the Yuan and Romanowicz model is quite broad, the maximum rotation in fast axis with depth is typically deeper than 70–90 km, the depth of the observed NVG. In addition, the mid-lithospheric gradients in azimuthal anisotropy from Yuan and Romanowicz [2010] in general predict PVGs for the range of Sp back azimuths in our data, as opposed to the NVGs seen in the Sp stacks. Thus, in order to be compatible with the Sp stacks, the vertical gradients in azimuthal anisotropy in the Yuan and Romanowicz [2010] must be gradual enough in depth to not produce clear Sp arrivals.

Vertical variations in radial anisotropy, for example, a fast horizontal plane and a slow vertical axis (the “SH > SV” anisotropy commonly observed with Love and Rayleigh waves), could also produce a shallow NVG, and such a model has been proposed both in the mantle of continents [Ford, 2013; Selway et al., 2015] and oceans [Becker et al., 2014]. The polarity of the Sp phases generated at a vertical transition in radial anisotropy depends on the relative strength of S wave versus P wave anisotropy. Assuming that radial anisotropy is produced by horizontal olivine a-axes that are randomly aligned in azimuth and that the material above this layer is isotropic with the same average velocity, a NVG comparable to the observations could be produced. However, it is unclear how such a laterally extensive, subhorizontal layer with horizontal yet azimuthally random olivine a-axes could have formed so consistently across varied cratonic terranes. Another possibility is that the radially anisotropic layer is created not by aligned olivine, but instead by a compositional fabric, for example, fine-scale, subhorizontal layering with different isotropic velocities. Again, however, the possible origins of this type of compositional heterogeneity are opaque. In addition, full waveform tomography indicates that suture zones, such as the Trans-Hudson orogen, are associated with large anomalies in radial anisotropy [Yuan et al., 2014], a result that further complicates radial anisotropy as an explanation for a consistent NVG across both Archean and Proterozoic mantle.

Elastically accommodated grain-boundary sliding has also been proposed as an explanation for MLDs globally [Karato, 2012; Olugboji et al., 2013; Karato et al., 2015]. In this model, as temperature rises, a shift occurs between elastic deformation of mineral grains to a mode in which grain-boundary sliding occurs while accommodated by elastic grain deformation [e.g., Karato et al., 2015]. The depth at which the shift occurs depends on temperature, water content, grain size, and the time scale (inverse frequency) of deformation, and seismic waves at comparable frequencies will experience a drop in shear velocity at this depth. This mechanism is appealing because it has potential to generate an NVG at a relatively consistent depth over a wide

variety of cratonic terranes. However, recent studies modeling converted phase amplitudes [Selway et al., 2015; Karato et al., 2015] disagree as to whether the shear-velocity drop with depth produced by elastically accommodated grain-boundary sliding is large enough to match the amplitudes of the observed shallow NVGs.

4.2.2. Relationship of large-scale, shallow negative phase to lithospheric mantle seismicity

An intriguing correlation exists between the upper NVG within the Wyoming craton and several earthquakes that are highly unusual for this tectonic environment because they occurred at mantle depths: a September 2013 event and its aftershock beneath Wyoming at ~75 km depth [Pechmann et al., 2014; Froment et al., 2014; Craig and Heyburn, 2015; Frohlich et al., 2015] and a February 1979 event beneath Utah between 80 and 90 km depth [Zandt and Richins, 1979] (Section 4 of the supporting information). The hypocenters of both earthquakes coincide with the upper NVG (Figure 9), suggesting a relationship between the source of the velocity decrease imaged by the converted waves and the mechanism that enabled these mantle earthquakes.

Several mechanisms have been proposed as explanations for mantle-depth earthquakes in continental settings. One hypothesis is that with sufficiently cold (<600°C) and anhydrous mantle, brittle fracture is possible at mantle depths [McKenzie et al., 2005; Boettcher et al., 2007; Sloan and Jackson, 2012]. However, mantle temperatures in the source regions of the Wyoming and Utah mantle earthquakes are likely too high for brittle failure to be relevant, a conclusion also reached for the Utah event by Wong and Chapman [1990]. While some xenoliths from the Wyoming craton and its margins suggest temperatures approaching 600°C in the ~75 km depth range [Eggler et al., 1987a; Griffin et al., 2004; Humphreys et al., 2015] most xenoliths from these depths indicate higher temperatures (700–800°C) [Eggler et al., 1987a]. Moreover, the deep earthquakes occurred at the edge of the high-velocity cratonic mantle (Figure 1a and supporting information Figures S4b and S4d), close to adjacent regions of lower velocity associated with the actively deforming western U.S., whereas the xenoliths sampled mantle further into the interior of

the cratonic mantle, suggesting the mantle near the earthquake hypocenters may be even hotter than the xenolith geotherms.

Two popular hypotheses for intermediate depth earthquakes in subducting slabs provide alternative explanations for the Wyoming and Utah mantle earthquakes: (1) dehydration embrittlement, where pore fluids are released by dehydration of hydrous minerals, thus reducing effective pressure and allowing faulting to occur [e.g., Green and Houston, 1995; Hacker et al., 2003]; (2) thermal shear runaway, where if shear is initially localized (e.g., along a preexisting fine-grained shear zone), the viscosity reduction caused by shear heating will cause a positive-feedback loop, allowing substantial slip [Ogawa, 1987; Wiens, 2001; Kelemen and Hirth, 2007; Prieto et al., 2013].

Based on the correlation of the Wyoming and Utah earthquake depths and the shallowmost NVG, we propose that the velocity reduction associated with the NVG represents a rheological contrast that enables either thermal shear runaway or dehydration embrittlement. In the case of our preferred model, a frozen-in layer of volatile-rich melt, either model for intermediate depth earthquakes is feasible. Strain rates might be higher within the layer due to the weaker hydrous phases than in the surrounding mantle, thus enhancing the probability of initiating rupture via a shear heating instability. Alternatively, the hydrous phases in a volatile-rich frozen melt layer could represent a source of enhanced dehydration embrittlement.

In either case, the Wyoming and Utah earthquakes suggest that the properties of the NVG promote rapid shear processes. The agreement between the T and P axes of the Wyoming mantle earthquakes and nearby crustal events [Frohlich et al., 2015; Craig and Heyburn, 2015] is consistent with deformation of the crust and mantle at the edge of the cratonic lithosphere due to similar stresses imposed by more active deformation to the west. Localization of mantle strain within the NVG in response to these stresses would explain the occurrence of the observed

earthquakes. The lack of earthquakes within the shallowmost NVG further into the craton would in turn reflect lower stresses and strain rates within the cratonic interior.

4.3. Dipping NVGs within the lithospheric mantle

4.3.1. Possible origins: chemical composition, rock fabric and deformation mechanism

The dipping NVGs observed at 85–200 km depth are most prominent at the boundaries between the Proterozoic Yavapai and the Archean Wyoming and Superior terranes (Sections 3.3.2 and 3.3.3). While we do not image compelling examples of dipping phases that relate to Archean sutures, such phases have been observed elsewhere in North America [Calvert et al., 1995; White et al., 2003; Chen et al., 2009]. The dipping phases we observe are consistent with imbrication or lateral accretion of oceanic lithosphere, but a number of other origins cannot be ruled out.

While there is a correlation between the suture zone marking the northern limit of Yavapai-aged arc material and dipping mantle phases, there is not a perfect correlation between all surface suture zones across the study region and dipping phases (Section 3.3.4). Assuming that imbrication of subducted lithosphere was common in the cratonic mantle, the absence of dipping NVGs at known sutures could indicate extensive deformation or alteration of these structures such that they no longer generate converted waves.

Xenolith data are consistent with the hypothesis that the dipping NVGs are related to subduction. Deeply underthrust oceanic crust is expected to eclogitize, and abundant eclogite xenoliths are found in the State Line and Iron Mountain kimberlite Districts near the Cheyenne Belt (Figure 1c) [Ater et al., 1984; Eggler et al., 1987a; Lester and Farmer, 1998; McCallum et al., 1975]. The high $\delta^{18}\text{O}$ measured for the State Line eclogites has been related to seawater alteration, evidence for their origin as subducted oceanic crust [Jacob, 2004; Schulze et al., 2003].

Eclogites from the Cedar Mountain breccia pipes within the Wyoming craton have also been tied to a seawater-altered mafic protolith [Kuehner and Irving, 1999].

One model is that the dipping NVG represents the base of high-velocity eclogitized oceanic crust (Figure 10). Based on modern subduction zone settings, where eclogitized oceanic crust has velocities that are indistinguishable from the surrounding mantle lithosphere [Bostock et al., 2002; Rondenay et al., 2008], an eclogitic layer might not be expected to produce a negative phase of the correct amplitude. However, calculation of expected assemblage velocities and forward modeling of the observed converted phases suggests that the required velocity contrast would be feasible, especially given the uppermost subducted oceanic mantle may be hydrated (Section 4.4).

An alternative model is that a frozen-in volatile-rich layer is preserved at the base of dipping underthrust lithosphere. Options include subducted oceanic lithosphere (Figure 10), or imbricated segments of continental lowermost crust and lithosphere resulting from orogenic thickening [e.g., Gray and Pysklywec, 2010]. We prefer the oceanic lithosphere model, given the evidence for subduction outlined above. In addition, models involving imbrication of pre-existing continental mantle lithosphere require elevated, Archean geotherms [Gray and Pysklywec, 2010]. Under such conditions, a volatile-rich layer seems unlikely to survive. The oceanic lithosphere model is also supported by the inference of a partial melt layer at the base of modern oceanic lithosphere [Kawakatsu et al., 2009; Schmerr, 2012], including currently subducting oceanic plates [Kumar and Kawakatsu, 2011; Naif et al., 2013; Stern et al., 2015]. In this model, the melt layer would need to be preserved as further mantle was added to the craton, indicating that the melt layer would need to cool and solidify before the next mantle accretion event. We note that a frozen melt layer at the base of an oceanic plate is consistent with the relative depths of the dipping NVG we observe beneath the Superior craton (120–150 km depth, 500–700 km along profile F-F', Figure 7) and Ps observations interpreted as a relict subducted oceanic Moho at 45–

65 km [Turner et al., 2015]. Alternative explanations for dipping NVGs in the observed 85–200 km depth range include other types of layering associated with subduction or underthrusting of lithosphere beneath pre-existing continental mantle lithosphere. Possibilities include: layers of localized anisotropy created by shear at the boundary of underthrust and overriding lithosphere; ponding of subduction-derived metasomatic fluids to generate a phlogopite-rich layer [Chen et al., 2009].

4.3.2. Timing of dipping and shallowmost NVGs

The geometry of most of the dipping NVGs relative to the shallowmost, quasi-horizontal NVG (Figures 2a, 5, and 6) is consistent with the interpretation that the shallower NVG formed first, within the Archean mantle lithosphere, and that the dipping NVGs represent later growth of the cratonic mantle from subduction, or possibly lateral compression and imbrication of the lithospheric mantle. However, this relative timing is not necessarily the case. For example, the shallowmost NVG could have formed by freezing of a volatile-rich melt layer at the base of an originally thinner lithosphere, and/or by later additions of volatile-rich melt that ponded at the base of the carbonated peridotite solidus (Section 4.2.1). Given the long history of metasomatism in the region, these later additions could have occurred before and/or after the tectonic event likely associated with the most prominent of the dipping NVGs, the Proterozoic convergence of Yavapai lithosphere with the Wyoming and Superior cratons. The enrichment of the Wyoming craton lithospheric mantle has been proposed as early as 2.79 Ga [Wooden and Mueller, 1988; O'Brien et al., 1995]. Major metasomatic events have been dated between 1.9 and 1.5 Ga [Dudas et al., 1987; Macdonald et al., 1992], including the formation of mica-rich veins within the lithospheric mantle at 1.8 Ga [Carlson and Irving, 1994]. Other age estimates for metasomatism range through the Proterozoic [e.g., Carlson and Irving, 1994; Downes et al., 2004] to the Cenozoic [e.g., Carlson and Irving, 1994; Downes et al., 2004; O'Brien et al., 1995].

4.4. Modeling of NVG depths and amplitudes

Our preferred mechanism for generating the upper NVG is a layer of frozen-in volatile-rich melt (Figure 10). In global MLD studies, such volatile-rich layers have been suggested to consist of 5–15% phlogopite (giving a 2–7% reduction in shear velocity [Rader et al., 2015]), or a 25% amphibole layer (giving a 4.5% reduction in shear velocity [Selway et al., 2015]). Our preferred models for the deeper and dipping NVG involve subduction; the NVG either represents underthrust oceanic crust or a preserved layer of frozen volatile-rich melt that was originally at the base of the oceanic lithosphere (Figure 10).

To test these hypotheses, we compared observations of receiver functions stacked at six individual stations to receiver functions predicted for candidate velocity models (Figures 10–12). Predicted receiver functions were calculated using the method of Frederiksen and Bostock [2000] for distances and back azimuths comparable to those in the real data. The models include a Moho whose absolute velocity increase is well constrained by wide-angle refraction data [Snelson et al. 1998], and we assumed a V_p/V_s ratio of 1.78 in both crust and mantle. The absolute velocities at lithospheric mantle depths are compatible with velocities reported by local tomography models at the modeled station locations [Shen et al., 2013; Porritt et al., 2014; Yuan et al., 2014]. The six stations chosen for modeling (three of which are shown in Figures 11 and 12) follow a profile that crosses the Cheyenne Belt and show either just the shallowest NVG or both the shallow and dipping NVGs, depending on their location.

For models that assume both NVGs represent frozen-in melt layers whose upper boundaries are flat and instantaneous in depth, the best fitting models for all six modeled stations include shear velocity drops of 7–12% for the upper NVG, and a 6.5–11% shear velocity drop for the deeper NVG (Figures 10a and 11). These velocity drops imply 12–23 vol % phlogopite, based on velocity-composition calculations from Hacker and Abers [2004]. However, the apparent dip of the deeper NVG where it is intersected by the S_p conversion points for the six modeled

stations is $\sim 2^\circ$, although elsewhere the dip of this interface may be as much as 10° . If the deeper interface is assumed to have a dip of 2° , a 13% velocity drop and 30 vol % phlogopite are required. The 12–30 vol % phlogopite is not unreasonable, given xenolith lithologies from the Wyoming craton region that include glimmerites (>80 vol % mica) and mica-rich xenoliths, most of which contain >30 vol % phlogopite [Carlson and Irving, 1994; Downes et al., 2004]. Other aspects of the model introduce additional nonuniqueness in shear velocity structure. If the depth over which the velocity drop occurs increases, so does the required velocity contrast (supporting information Figures S6 and S7). In addition, these models contain a gradual positive velocity gradient between the two NVGs, representing the decreasing volume of low velocity, volatile-rich minerals. This increase must be gradual, as we do not observe a large positive phase between the two NVGs. The presence and size of this positive velocity gradient also has an impact on the velocity drop required at the deeper NVG (supporting information Figure S6).

We also tested models in which the deeper, dipping NVG represents subducted oceanic crust, while the shallower NVG still represents a volatile-rich layer (Figures 10b and 12). For the subducted crust, we calculated seismic velocities based on predicted mineral assemblages [Connolly, 2009] along two geotherms [Eggler et al., 1987a; Griffin et al., 2004] given the major element compositions of several distinct classes of eclogites [Ater et al., 1984] and peridotites [Eggler et al., 1987a], again using both *Perple_x* and Hacker and Abers [2004]. Clinopyroxene compositions can be used to distinguish true eclogites from cumulates [Lee et al., 2006]. The eclogites identified in this way have seismic velocities that exceed the peridotite velocities by as much as 4.5% in the depth range of interest. Forward modeling shows that a 7.5–11% velocity drop is required by the amplitudes of the deeper NVGs at the six stations, for a flat interface, and a drop of as much as 14.5% for an interface with a 2° dip. These velocity decreases are much higher than the 4.5% drop for the base of an eclogitic oceanic crust inferred from the xenolith compositions. However, if we assume that the uppermost oceanic mantle is hydrated [e.g., Hacker

et al., 2003; Syracuse et al., 2008], some of the required velocity drop can be accommodated on the mantle side of the discontinuity by low-velocity hydrous minerals such as talc and/or serpentine. If the oceanic crust is 4.5% fast, a further velocity drop of 3–6.5% is required in the uppermost oceanic mantle for a flat interface, and up to 10% for the 2° case. These values imply 6–13 vol % talc or 5–11 vol % serpentine (flat) and up to 21.5 vol % talc or 18.5 vol % serpentine (2° dip), assuming talc and serpentine replace enstatite and forsterite, respectively. These models do not include a positive velocity gradient between the two NVGs for simplicity; although one is likely to exist, it must be sufficiently gradual that no positive phase is generated.

4.5. Lithosphere-asthenosphere boundary

The absence of a consistent NVG at LAB depths in the Sp CCP stacks, given the 33–4 s band-pass filter employed in our analysis, implies that the velocity decrease at the lithosphere-asthenosphere boundary is gradual (distributed over >50 km; e.g., supporting information Figure S7 and Ford et al. [2010]). Such a gradual NVG could be due to the effects of temperature and pressure alone [e.g., Rychert et al., 2005, 2007, 2012; Stixrude and Lithgow-Bertelloni, 2005; Faul and Jackson, 2005]. Enhanced volatile or melt content in the asthenosphere relative to a dry, depleted, and melt-free mantle lithosphere is not required, but a gradual gradient in volatile or melt content cannot be ruled out.

The apparently gradual velocity gradient beneath much of the craton is consistent with models in which a cool thermal boundary layer develops beneath thick, chemically depleted cratonic mantle [Cooper et al., 2004], creating a layer of relatively undepleted mantle that cools to the point where it represents lithosphere as opposed to asthenosphere, potentially with a distinct orientation of azimuthal anisotropy [Yuan and Romanowicz, 2010]. This type of multistage evolution is also consistent with seismic layering in the cratonic mantle beneath Hudson Bay [Darbyshire et al., 2013].

In the southernmost portion of our study region, where we do image a clear NVG at LAB depths (Figure 8a), we suggest that the LAB velocity gradient is unusually sharp due to anomalously low-velocity asthenosphere, as seen in the Porritt et al. [2014] model (Figure 8b), and other studies [e.g., Schmandt and Humphreys, 2010; Shen et al., 2013; MacCarthy et al., 2014]. This region coincides with the northern end of the Rio Grande Rift [e.g., Chapin, 1979], and the juxtaposition of warm, upwelling asthenosphere at the base of the cratonic mantle explains why the LAB velocity gradient is sharp enough to generate significant Sp phases.

4.6. Positive phases near the base of the lithosphere

The origin of the PVGs observed at depths of 150–220 km is uncertain. These less well constrained features are small-scale, low-amplitude, sporadic, and do not have a consistent relationship with surface geology. One possibility is that they reflect the tops of refertilized zones within the deepest mantle, and that this layer is chemically heterogeneous. For example, xenolith stratigraphy within the Slave craton has shown the existence of thin, highly refertilized layers at depth in which the high proportion of pyroxene and garnet would increase velocities, despite a reduced Mg# [Kopylova and Russell, 2000]. We are not aware of xenolith data from regions where we observe the clearest deep PVGs, but we assumed the websterite compositions found amongst xenoliths from the State Line District [Eggler et al., 1987a] to be analogous. *Perple_x* calculations of the velocities for the websterite xenolith stable assemblages at 150–220 km depth indicate that they would be up to 3% higher than velocities for State Line peridotites [Eggler et al., 1987a]. To explain the PVGs, the refertilized zone would need to have a sharp upper boundary and a gradual transition at its base.

We also note that one zone of the PVGs occurs at 150–160 km beneath the northern Wyoming craton (107°W to 103°W, Figure 3b) where the replacement of the original mantle lithosphere by subducted Farallon plate (the Shatsky Rise conjugate) has been proposed by Humphreys et al. [2015]. This tectonic scenario would explain the relatively young Re-Os ages

found for the high-temperature mantle xenoliths that emanated from depths of more than 150 km. The PVG could be associated with the contact between original Wyoming craton mantle and the adhered oceanic lithosphere. However, PVGs of comparable strength also occur elsewhere.

4.7. Relationship of MLDs and LAB to cratonic mantle formation models

A wide variety of models have been proposed for the formation of the thick cratonic mantle lithosphere, including: (1) orogenic thickening of depleted mantle in a subduction zone [Kelemen et al., 1998; Parman et al., 2004] or intracontinental setting [Gray and Pysklywec, 2010; Lee and Chin, 2014]; (2) stacking or imbrication of oceanic lithosphere beneath the continent [e.g., Canil, 2004; Pearson and Wittig, 2008]; (3) stabilization of a thick, cool thermal boundary layer beneath a chemically isolated root [Cooper et al., 2004; Yuan and Romanowicz, 2010]; (4) depletion of the mantle root in situ, as from the passage of a mantle plume [e.g., Griffin et al., 2003; Arndt et al., 2009] or decompression melting following continental collapse [Rey et al., 2014].

The clearest connection between our results and prior models is the support provided by the observed dipping NVGs for mechanisms of cratonic root formation that invoke subduction, either accretion of subducted oceanic lithosphere to the base of the continental lithospheric mantle [Canil, 2004; Pearson and Wittig, 2008], or thickening and underthrusting of highly depleted subarc mantle [Kelemen et al., 1998; Parman et al., 2004]. Since the latter case would occur as subduction zones are subsumed by continent-continent collisions, remnant subducting slabs could still be present within the accreted mantle. The observation of dipping NVGs along Archean/Proterozoic boundaries and their interpretation as preserved subducted oceanic crust or the base of subducted oceanic lithosphere (Sections 4.3 and 4.4) supports these mechanisms of cratonic root growth, at least in the Proterozoic.

Another implication of our results for craton formation is that the gradual velocity gradient typical of the LAB in our Sp stacks is consistent with the idea that a cool, thermal

boundary layer underlies the chemically depleted portion of the cratonic mantle [e.g., Cooper et al., 2004; Yuan and Romanowicz, 2010] (Section 4.5).

Our results do not shed much light on the processes that created chemically depleted cratonic mantle in the Archean. Sporadic dipping NVGs in the Archean core of the Wyoming craton could represent subduction or shortening processes, but this interpretation is nonunique (Section 3.3.4). Other proposed models include: the formation of a thick mantle root by extensive partial melting due to the impact of a mantle plume [e.g., Griffin et al., 2003; Arndt et al., 2009] and decompression melting under an extending continent [Rey et al., 2014]. However, while these models could produce the depleted mantle indicated by xenoliths [Eggler et al., 1987a; Carlson and Irving, 1994; Carlson et al., 1999, 2004; Downes et al., 2004; Hearn, 2004], they are inconsistent with the geochemical evidence that the cratonic lithospheric mantle was formed by melting at shallow depths, but now lies at higher pressures and colder temperatures [e.g., Canil, 2004; Wittig et al., 2008; Lee and Chin, 2014]. Lee and Chin [2014] provide an alternative hypothesis that involves melting and convergence over a downwelling. The deep highly depleted layer implied by this model does not explain the observed NVGs, but neither can it be ruled out by our results.

4.8. Evolution of the Wyoming lithospheric mantle

Although aspects of our interpretation are nonunique, we conclude this paper with a model for the evolution of the southern Wyoming craton that is consistent with both the mantle discontinuities imaged in this study and prior geological and geophysical constraints (Figure 13).

Extensive Archean deformation (Section 1.2) and metasomatism (Section 4.3.2) likely generated relict mantle structures (left side of Figure 13a). While we cannot unambiguously attribute any of the observed mantle discontinuities to Archean events, if the shallow, subhorizontal NVG does correspond to a layer of frozen volatile-rich melt (Section 4.2.1), it may have formed, or at least begun to form in the Archean. In addition, some of the dipping NVGs

observed in the interior of the Wyoming craton (Section 3.3.4) may relate to Archean accretion events, and their fragmentary character could reflect their disruption and modification by later tectonism and metasomatism.

The Paleoproterozoic Yavapai orogeny is a likely candidate for the formation of the most extensive dipping NVGS – those observed beneath the Cheyenne Belt (Section 3.3.2) and the Yavapai-Superior boundary (Section 3.3.3). Extensive arc systems existed to the south of the Wyoming craton margin prior to the Yavapai orogeny [Whitmeyer and Karlstrom, 2007] (Figure 13a). When this material collided with the Wyoming and Superior cratons at 1.78–1.75 Ga [Whitmeyer and Karlstrom, 2007] (Figure 13b), the subducting lithosphere (the probable origin of the dipping NVGs) and depleted subarc mantle could have been accreted to the preexisting Archean mantle. Both prior to and during accretion, the subduction zones would have been a source of fluids involved in the major metasomatic events at 1.9–1.5 Ga [Dudas et al., 1987; Macdonald et al., 1992; Carlson and Irving, 1994], and this metasomatism and related melts could have contributed to a volatile-rich melt layer associated with the shallow, horizontal NVG (Section 4.3.2) in the Wyoming, Superior, and Yavapai terranes.

From Yavapai accretion into the Cenozoic, multiple episodes of magmatism and metasomatism [e.g., Harlan et al., 1997, 2003; Whitmeyer and Karlstrom, 2007; Carlson and Irving, 1994; Downes et al., 2004; O'Brien et al., 1995] could have added to the frozen-in melt layer (Figure 13c). Late Mesozoic Laramide tectonism deformed Wyoming craton crust, and may have replaced mantle lithosphere in the northern Wyoming craton [Humphreys et al., 2015] (not shown in Figure 13). Throughout the history of the region, a thermal boundary layer below the depleted cratonic mantle [e.g., Cooper et al., 2004] likely formed, was disrupted, and regenerated, resulting in a gradual LAB velocity gradient that in general does not produce clear Sp phases.

5. Conclusions

Across the Archean and Proterozoic terranes of the northern U.S., a widespread, largely subhorizontal NVG typically appears between 70 and 90 km depth. The ubiquity of this feature suggests a process that has operated in both Archean and Proterozoic terranes. The NVG could be generated at the top of a low-velocity layer of frozen-in volatile-rich melt. Such a layer is compatible with the widespread phlogopite found in mantle xenoliths in this region, and with the inference of an enriched lithospheric source from the geochemistry of local magmas. This layer may have formed concurrent with original cratonic mantle, and/or may have been added to throughout its history by upward percolating melts. The association of this layer with rare upper mantle seismicity suggests that this layer enables deep faulting on localized shear zones. Refertilization of isolated patches of deep lithospheric mantle may also be the source of sporadically distributed positive phases.

Dipping NVGs are observed between 85 and 200 km depth. These interfaces are clearest at the southern margin of the Archean terranes, where they are sutured with Proterozoic Yavapai-interval arc terranes and dip northward beneath the cratonic interior. Together with abundant eclogite in xenoliths, these structures indicate that the cratonic mantle likely grew through a process involving subduction, at least in the Proterozoic.

The lack of a vertically localized NVG at the cratonic LAB across most of the study region suggests that this transition is gradual (distributed over more than 60 km). Unlike younger continental regions, where a sharp LAB velocity gradient requires volatiles or melt in the asthenosphere, the base of the cratonic seismological lithosphere may be controlled by temperature alone. The one exception is a localized region with a sharp LAB velocity gradient at the southern edge of our study region that could be explained by anomalously warm asthenosphere associated with the northern Rio Grande Rift. The typically gradual LAB velocity

gradient suggests that the chemically depleted root in this region may stabilize an underlying thermal boundary layer.

Acknowledgements

Thanks to Emily Chin and Ben Parks for their insights on mantle xenoliths and to Greg Hirth, Steve Parman, Colleen Dalton, Alberto Saal, Don Forsyth, and Marc Parmentier for discussions about cratonic processes. We also thank Alan Levander, an anonymous reviewer, and G3 Editor Thorsten Becker for their constructive comments, which improved the quality of this manuscript. This research was supported by the NSF CSEDI Program through award EAR-1361487. The facilities of IRIS Data Services, and specifically the IRIS Data Management Center, were used for access to waveforms, related metadata, and/or derived products used in this study. Data from the TA network were made freely available as part of the EarthScope USArray facility, operated by IRIS. IRIS is funded through the Seismological Facilities for the Advancement of Geoscience and EarthScope (SAGE) Proposal of the National Science Foundation under Cooperative Agreement EAR-1261681. This study also employed data from the following permanent networks: the Central and Eastern U.S. Network, the Global Seismograph Network (doi:10.7914/SN/IU), the Intermountain West network, the Leo Brady Network, the Montana Regional Seismic Network, the PDAR Pinedale network, the United States National Seismic Network (doi:10.7914/SN/US), and the University of Utah Regional Network and data from the following temporary arrays: YISA [Waite et al., 2006], Laramie Array [Hansen and Dueker, 2009], Rocky Mountain Front Array [Sheehan et al., 1995], Colorado Plateau—Great Basin Network [Sheehan et al., 1997], Eastern Snake River Plain Experiment [Walker et al., 2004], CD-ROM [Karlstrom and the Continental Dynamics of the Rocky Mountain Working Group, 2002], RISTRA 1.5 [Sine et al., 2008], Deep Probe [Dueker and Yuan, 2004], CREST [Hansen et al., 2013], FLED [French et al., 2009], Billings Array [Yuan and Dueker, 2005b], Lodore Array [Crosswhite and Humphreys,

2003], Bighorn Broadband Experiment [Yeck et al., 2014], and NOISY [Seats and Lawrence, 2014].

References

Abt, D. L., K. M. Fischer, S. W. French, H. A. Ford, H. Yuan, and B. Romanowicz (2010), North American lithospheric discontinuity structure imaged by Ps and Sp receiver functions, *J. Geophys. Res.*, 115, B09301, doi:10.1029/2009JB006914.

Allmendinger, R. W., J. A. Brewer, L. D. Brown, S. Kaufman, J. E. Oliver, and R. S. Houston (1982), COCORP profiling across the Rocky Mountain Front in southern Wyoming, Part 2: Precambrian basement structure and its influence on Laramide deformation, *Geol. Soc. Am. Bull.*, 93(12), 1253–1263.

Arndt, N. T., N. Coltice, H. Helmstaedt, and M. Gregoire (2009), Origin of Archean subcontinental lithospheric mantle: Some petrological constraints, *Lithos*, 109(1), 61–71, doi:10.1016/j.lithos.2008.10.019.

Aschepkov, I. V., H. Downes, R. Mitchell, N. V. Vladykin, H. Coopersmith, and S. V. Palessky (2013), Wyoming Craton mantle lithosphere: Reconstructions based on xenocrysts from Sloan and Kelsey Lake kimberlites, in *Proceedings of 10th International Kimberlite Conference*, vol. 1, pp. 13–27, Geol. Soc. of India, Springer, New Delhi, India, doi:10.1007/978-81-322-1170-9_2.

Ater, P. C., D. H. Egger, and M. E. McCallum (1984), Petrology and geochemistry of mantle eclogite xenoliths from Colorado-Wyoming kimberlites: Recycled ocean crust, in *Kimberlites II: The Mantle and Crust-Mantle Relationships*, pp. 309–318, Elsevier, Amsterdam.

Becker, T. W., C. P. Conrad, A. J. Schaeffer, and S. Lebedev (2014), Origin of azimuthal seismic anisotropy in oceanic plates and mantle, *Earth Planet. Sci. Lett.*, 401, 236–250, doi:10.1016/j.epsl.2014.06.014.

Bodin, T., H. Yuan, and B. Romanowicz (2013), Inversion of receiver functions without deconvolution – Application to the Indian craton, *Geophys. J. Int.*, 196, 1025–1033, doi:10.1093/gji/ggt431.

Boerner, D. E., J. A. Craven, R. D. Kurtz, G. M. Ross, and F. W. Jones (1998), The Great Falls Tectonic Zone: Suture or intracontinental shear zone?, *Can. J. Earth Sci.*, 35(2), 175–183, doi:10.1139/e97-104.

Boettcher, M. S., G. Hirth, and B. Evans (2007), Olivine friction at the base of oceanic seismogenic zones, *J. Geophys. Res.*, 112, B01205, doi:10.1029/2006JB004301.

Bostock, M. G. (1998), Mantle stratigraphy and evolution of the Slave province, *J. Geophys. Res.*, 103(B9), 21,183–21,200, doi:10.1029/98JB01069.

Bostock, M. G., R. D. Hyndman, S. Rondenay, and S. M. Peacock (2002), An inverted continental Moho and serpentinization of the forearc mantle, *Nature*, 417(6888), 536–538, doi:10.1038/417536a.

Boyd, F. R. (1989), Compositional distinction between oceanic and cratonic lithosphere, *Earth Planet. Sci. Lett.*, 96(1), 15–26.

Brey, G., W. R. Brice, D. J. Ellis, D. H. Green, K. L. Harris, and I. D. Ryabchikov (1983), Pyroxene-carbonate reactions in the upper mantle, *Earth Planet. Sci. Lett.*, 62(1), 63–74, doi:10.1016/0012-821X(83)90071-7.

Buhlmann, A. L., P. Cavell, R. A. Burwash, R. A. Creaser, and R. W. Luth (2000), Minette bodies and cognate mica-clinopyroxenite xenoliths from the Milk River area, southern Alberta: Records of a complex history of the northernmost part of the Archean Wyoming craton, *Can. J. Earth Sci.*, 37(11), 1629–1650, doi:10.1139/e00-058.

Burdick, S., R. D. van der Hilst, F. L. Vernon, V. Martynov, T. Cox, J. Eakins, G. H. Karasu, J. Tylell, L. Astiz, and G. L. Pavlis (2014), Model update January 2013: Upper mantle heterogeneity beneath North America from travel-time tomography with global and USArray transportable array data, *Seismol. Res. Lett.*, 85(1), 77–81, doi:10.1785/0220130098.

Calvert, A. J., E. W. Sawyer, W. J. Davis, and J. N. Ludden (1995), Archean subduction inferred from seismic images of a mantle suture in the Superior Province, *Nature*, 375, 670–674, doi:10.1038/375670a0.

Canil, D. (2004), Mildly incompatible elements in peridotites and the origins of mantle lithosphere, *Lithos*, 77(1), 375–393, doi:10.1016/j.lithos.2004.04.014.

Carlson, R. W., and A. J. Irving (1994), Depletion and enrichment history of subcontinental lithospheric mantle: An Os, Sr, Nd and Pb isotopic study of ultramafic xenoliths from the northwestern Wyoming Craton, *Earth Planet. Sci. Lett.*, 126(4), 457–472, doi:10.1016/0012-821X(94)90124-4.

Carlson, R. W., A. J. Irving, and B. C. Hearn Jr. (1999), Chemical and isotopic systematics of peridotite xenoliths from the Williams kimberlite, Montana: Clues to processes of lithosphere formation, modification and destruction, in *Proceedings of the VIIth International Kimberlite Conference*, vol. 1, pp. 90–98, Red Roof Design, Cape Town, South Africa.

Carlson, R. W., A. J. Irving, D. J. Schulze, and B. C. Hearn (2004), Timing of Precambrian melt depletion and Phanerozoic refertilization events in the lithospheric mantle of

the Wyoming Craton and adjacent Central Plains Orogen, *Lithos*, 77(1), 453–472, doi:10.1016/j.lithos.2004.03.030.

Chamberlain, K. R. (1998), Medicine Bow orogeny timing of deformation and model of crustal structure produced during continent-arc collision, ca. 1.78 Ga, southeastern Wyoming, *Rocky Mt. Geol.*, 33(2), 259–277, doi:10.2113/33.2.259.

Chamberlain, K. R., C. D. Frost, and B. R. Frost (2003), Early Archean to Mesoproterozoic evolution of the Wyoming Province: Archean origins to modern lithospheric architecture, *Can. J. Earth Sci.*, 40(10), 1357–1374, doi:10.1139/e03-054.

Chapin, C. E. (1979), Evolution of the Rio Grande rift—A summary, in *Rio Grande Rift: Tectonics and Magmatism*, edited by R. E. Riecker, pp. 1–6, AGU, Washington, D. C., doi:10.1029/SP014p0001.

Chen, C. W., S. Rondenay, D. S. Weeraratne, and D. B. Snyder (2007), New constraints on the upper mantle structure of the Slave craton from Rayleigh wave inversion, *Geophys. Res. Lett.*, 34, L10301, doi:10.1029/2007GL029535.

Chen, C. W., S. Rondenay, R. L. Evans, and D. B. Snyder (2009), Geophysical detection of relict metasomatism from an Archean (~3.5 Ga) subduction zone, *Science*, 326(5956), 1089–1091, doi:10.1126/science.1178477.

Chu, R., B. Schmandt, and D. V. Helmberger (2012), Upper mantle P velocity structure beneath the Midwestern United States derived from triplicated waveforms, *Geochem. Geophys. Geosyst.*, 13, Q0AK04, doi:10.1029/2011GC003818.

Connolly, J. A. D. (2009), The geodynamic equation of state: What and how, *Geochem. Geophys. Geosyst.*, 10, Q10014, doi:10.1029/2009GC002540.

Cooper, C. M., and M. S. Miller (2014), Craton formation: Internal structure inherited from closing of the early oceans, *Lithosphere*, 6(1), 35–42, doi:10.1130/L321.1.

Cooper, C. M., A. Lenardic, and L. Moresi (2004), The thermal structure of stable continental lithosphere within a dynamic mantle, *Earth Planet. Sci. Lett.*, 222(3), 807–817, doi:10.1016/j.epsl.2004.04.008.

Cox, D. M., C. D. Frost, and K. R. Chamberlain (2000), 2.01-Ga Kennedy dike swarm, southeastern Wyoming Record of a rifted margin along the southern Wyoming province, *Rocky Mt. Geol.*, 35(1), 7–30, doi:10.2113/35.1.7.

Craig, T. J., and R. Heyburn (2015), An enigmatic earthquake in the continental mantle lithosphere of stable North America, *Earth Planet. Sci. Lett.*, 425, 12–23, doi:10.1016/j.epsl.2015.05.048.

Crosswhite, J. A., and E. D. Humphreys (2003), Imaging the mountainless root of the 1.8 Ga Cheyenne belt suture and clues to its tectonic stability, *Geology*, 31(8), 669–672, doi:10.1130/G19552.1.

Darbyshire, F. A., D. W. Eaton, and I. D. Bastow (2013), Seismic imaging of the lithosphere beneath Hudson Bay: Episodic growth of the Laurentian mantle keel, *Earth Planet. Sci. Lett.*, 373, 179–193, doi:10.1016/j.epsl.2013.05.002.

Dasgupta, R. (2013), Ingassing, storage, and outgassing of terrestrial carbon through geologic time, *Rev. Mineral. Geochem.*, 75(1), 183–229, doi:10.2138/rmg.2013.75.7.

Dasgupta, R. (2014), Lithosphere and asthenosphere properties beneath oceans and continents and their relationship with domains of partial melt stability in the mantle, Abstract DI43B-03 presented at 2014 Fall Meeting, AGU, San Francisco, Calif., 15-19 Dec.

Dasgupta, R., and M. M. Hirschmann (2010), The deep carbon cycle and melting in Earth's interior, *Earth Planet. Sci. Lett.*, 298(1), 1–13, doi:10.1016/j.epsl.2010.06.039.

Dasgupta, R., A. Mallik, K. Tsuno, A. C. Withers, G. Hirth, and M. M. Hirschmann (2013), Carbon-dioxide-rich silicate melt in the Earth's upper mantle, *Nature*, 493(7431), 211–215, doi:10.1038/nature11731.

DeCelles, P. G., and J. C. Coogan (2006), Regional structure and kinematic history of the Sevier fold-and-thrust belt, central Utah, *Geol. Soc. Am. Bull.*, 118(7-8), 841–864, doi:10.1130/B25759.1.

Downes, H., R. Macdonald, B. G. J. Upton, K. G. Cox, J. L. Bodinier, P. R. D. Mason, D. James, P. G. Hill, and B. C. Hearn (2004), Ultramafic xenoliths from the Bearpaw Mountains, Montana, USA: Evidence for multiple metasomatic events in the lithospheric mantle beneath the Wyoming craton, *J. Petrol.*, 45(8), 1631–1662.

Dudás, F. Ö., R. W. Carlson, and D. H. Eggler (1987), Regional Middle Proterozoic enrichment of the subcontinental mantle source of igneous rocks from central Montana, *Geology*, 15(1), 22–25.

Dueker, K., and H. Yuan (2004), Upper mantle P-wave velocity structure from PASSCAL teleseismic transects across Idaho, Wyoming and Colorado, *Geophys. Res. Lett.*, 31, L08603, doi:10.1029/2004GL019476.

Eaton, D. W., F. Darbyshire, R. L. Evans, H. Grütter, A. G. Jones, and X. Yuan (2009), The elusive lithosphere–asthenosphere boundary (LAB) beneath cratons, *Lithos*, 109(1), 1–22, doi:10.1016/j.lithos.2008.05.009.

Eggler, D. H., M. E. McCallum, and M. B. Kirkley (1987a), Kimberlite-transported nodules from Colorado-Wyoming; A record of enrichment of shallow portions of an infertile lithosphere, *Spec. Pap. Geol. Soc. Am.*, 215, 77–90, doi:10.1130/SPE215-p77.

Eggler, D. H., J. K. Meen, F. Welt, F. O. Dudas, K. P. Furlong, M. E. McCallum, and R. W. Carlson (1987b), Tectonomagmatism of the Wyoming Province, *Colo. Sch. Mines Q.*, 83(2), 25–40.

Erslev, E. A., and N. V. Koenig (2009), Three-dimensional kinematics of Laramide, basement-involved Rocky Mountain deformation, USA: Insights from minor faults and GIS-enhanced structure maps, *Geol. Soc. Am. Memo.*, 204, 125–150, doi:10.1130/2009.1204(06).

Falloon, T. J., and D. H. Green (1989), The solidus of carbonated, fertile peridotite, *Earth Planet. Sci. Lett.*, 94(3), 364–370, doi:10.1016/0012-821X(89)90153-2.

Faul, U., and I. Jackson (2005), The seismological signature of temperature and grain size variations in the upper mantle, *Earth Planet. Sci. Lett.*, 234, 119–134, doi:10.1016/j.epsl.2005.02.008.

Fischer, K. M. (2015), Crust and lithospheric structure—Seismological constraints on the lithosphere-asthenosphere boundary, in *Treatise on Geophysics*, 2nd ed., edited by G. Schubert, pp. 587–612, Elsevier, Oxford, U. K., doi:10.1016/B978-0-444-53802-4.00026-9.

Fischer, K. M., H. A. Ford, D. L. Abt, and C. A. Rychert (2010), The lithosphere-asthenosphere boundary, *Annu. Rev. Earth Planet. Sci.*, 38, 551–575, doi:10.1146/annurev-earth-040809-152438.

Ford, H. A., K. M. Fischer, D. L. Abt, C. A. Rychert, and L. T. Elkins-Tanton (2010), The lithosphere–asthenosphere boundary and cratonic lithospheric layering beneath Australia from Sp wave imaging, *Earth Planet. Sci. Lett.*, 300(3), 299–310, doi:10.1016/j.epsl.2010.10.007.

Ford, H. A. (2013), A seismological perspective on the lithosphere-asthenosphere boundary (Doctoral dissertation), Retrieved from Brown Digital Repository (bdr:320544).

Foster, K., K. Dueker, B. Schmandt, and H. Yuan (2014), A sharp cratonic lithosphere–asthenosphere boundary beneath the American Midwest and its relation to mantle flow, *Earth Planet. Sci. Lett.*, 402, 82–89, doi:10.1016/j.epsl.2013.11.018.

Frederiksen, A. W., and M. G. Bostock (2000), Modelling teleseismic waves in dipping anisotropic structures, *Geophys. J. Int.*, 141(2), 401–412, doi:10.1046/j.1365-246x.2000.00090.x.

Frederiksen, A. W., T. Bollmann, F. Darbyshire, and S. Lee (2013), Modification of continental lithosphere by tectonic processes: A tomographic image of central North America, *J. Geophys. Res. Earth Sci.*, 118, 1051–1066, doi:10.1002/jgrb.50060.

French, S. W., K. M. Fischer, E. M. Syracuse, and M. E. Wysession (2009), Crustal structure beneath the Florida-to-Edmonton broadband seismometer array, *Geophys. Res. Lett.*, 36, L08309, doi:10.1029/2008GL036331.

Frohlich, C., W. Gan, and R. B. Herrmann (2015), Two deep earthquakes in Wyoming, *Seismol. Res. Lett.*, 86(3), 810–818, doi:10.1785/0220140197.

Froment, B., G. A. Prieto, and R. E. Abercrombie (2014), Source parameters of the upper-mantle September 21, 2013 Mw4.8 Wyoming earthquake, Abstract S53B-4506 presented at 2014 Fall Meeting, AGU, San Francisco, Calif., 15–19 Dec.

Frost, C. D., B. R. Frost, K. R. Chamberlain, and T. P. Hulsebosch (1998), The Late Archean history of the Wyoming province as recorded by granitic magmatism in the Wind River Range, Wyoming, *Precambrian Res.*, 89(3), 145–173, doi:10.1016/S0301-9268(97)00082-X.

Geissler, W. H., F. Sodoudi, and R. Kind (2010), Thickness of the central and eastern European lithosphere as seen by S receiver functions, *Geophys. J. Int.*, 181(2), 604–634, doi:10.1111/j.1365-246X.2010.04548.x.

Gorman, A. R., et al. (2002), Deep Probe: Imaging the roots of western North America, *Can. J. Earth Sci.*, 39(3), 375–398, doi:10.1139/e01-064.

Gray, R., and R. N. Pysklywec (2010), Geodynamic models of Archean continental collision and the formation of mantle lithosphere keels, *Geophys. Res. Lett.*, 37, L19301, doi:10.1029/2010GL043965.

Green, H. W., and H. Houston (1995), The mechanics of deep earthquakes, *Annu. Rev. Earth Planet. Sci.*, 23, 169–214.

Griffin, W. L., S. Y. O'Reilly, and C. G. Ryan (1999), The composition and origin of sub-continental lithospheric mantle, in *Mantle Petrology: Field Observations and High-Pressure Experimentation: A Tribute to Francis R. (Joe) Boyd*, edited by Y. Fei, C. M. Bertka, and B. O. Mysen, *Geochem. Soc. Spec. Publ.*, 6, 13–45.

Griffin, W. L., S. Y. O'Reilly, N. Abe, S. Aulbach, R. M. Davies, N. J. Pearson, B. J. Doyle, and K. Kivi (2003), The origin and evolution of Archean lithospheric mantle, *Precambrian Res.*, 127(1), 19–41, doi:10.1016/S0301-9268(03)00180-3.

Griffin, W. L., S. Y. O'Reilly, B. J. Doyle, N. J. Pearson, H. Coopersmith, K. Kivi, V. Malkovets, and N. Pokhilenko (2004), Lithosphere mapping beneath the North American plate, *Lithos*, 77(1), 873–922, doi:10.1016/j.lithos.2004.03.034.

Gung, Y., M. Panning, and B. Romanowicz (2003), Global anisotropy and the thickness of continents, *Nature*, 422(6933), 707–711, doi:10.1038/nature01559.

Hacker, B. R., and G. A. Abers (2004), Subduction factory 3: An Excel worksheet and macro for calculating the densities, seismic wave speeds, and H₂O contents of minerals and rocks at pressure and temperature, *Geochem. Geophys. Geosyst.*, 5, Q01005, doi:10.1029/2003GC000614.

Hacker, B. R., S. M. Peacock, G. A. Abers, and S. D. Holloway (2003), Subduction factory 2. Are intermediate-depth earthquakes in subducting slabs linked to metamorphic dehydration reactions?, *J. Geophys. Res.*, 108(B1), 2030, doi:10.1029/2001JB001129.

Hansen, S., and K. Dueker (2009), P- and S-wave receiver function images of crustal imbrication beneath the Cheyenne Belt in southeast Wyoming, *Bull. Seismol. Soc. Am.*, 99(3), 1953–1961, doi:10.1785/0120080168.

Hansen, S. M., K. G. Dueker, J. C. Stachnik, R. C. Aster, and K. E. Karlstrom (2013), A rootless Rockies—Support and lithospheric structure of the Colorado Rocky Mountains inferred from CREST and TA seismic data, *Geochem. Geophys. Geosyst.*, 14, 2670–2695, doi:10.1002/ggge.20143.

Hansen, S. M., K. G. Dueker, and B. Schmandt (2015), Thermal classification of lithospheric discontinuities beneath USArray, *Earth Planet. Sci. Lett.*, 431, 36–47.

Harlan, S. S., J. W. Geissman, and L. W. Snee (1997), Paleomagnetic and ⁴⁰Ar/³⁹Ar geochronologic data from late Proterozoic mafic dikes and sills, Montana and Wyoming, U.S. Geol. Surv. Prof. Pap., 1580, pp. 1–16.

Harlan, S. S., L. Heaman, A. N. LeCheminant, and W. R. Premo (2003), Gunbarrel mafic magmatic event: A key 780 Ma time marker for Rodinia plate reconstructions, *Geology*, 31(12), 1053–1056, doi:10.1130/G19944.1.

Hearn, B. C. (1989), Introduction: T346 Montana high-potassium igneous province, in Montana High-Potassium Igneous Province: Crazy Mountains to Jordan, Montana. Field Trip Guidebook T346, pp.1–5, AGU, Washington, D. C.

Hearn, B. C., Jr. (1999), Peridotite xenoliths from Porcupine Dome, in Montana, USA: Depleted subcontinental lithosphere samples in an olivine–phlogopite–carbonate magma, in Proceedings of the VIIth International Kimberlite Conference, vol. 1, edited by J. J. Gurney et al., pp. 353–360, Red Roof Design, Cape Town, South Africa.

Hearn, B. C. (2004), The Homestead kimberlite, central Montana, USA: Mineralogy, xenocrysts, and upper-mantle xenoliths, *Lithos*, 77(1), 473–491, doi:10.1016/j.lithos.2004.04.030.

Hearn, B. C., and F. R. Boyd (1975), Garnet peridotite xenoliths in a Montana, USA, kimberlite, *Phys. Chem. Earth*, 9, 247–255.

Helfrich, G. (2006), Extended-time multitaper frequency domain cross-correlation receiver-function estimation, *Bull. Seismol. Soc. Am.*, 96(1), 344–347, doi:10.1785/0120050098.

Helfrich, G., J. M. Kendall, J. O. S. Hammond, and M. R. Carroll (2011), Sulfide melts and long-term low seismic wavespeeds in lithospheric and asthenospheric mantle, *Geophys. Res. Lett.*, 38, L11301, doi:10.1029/2011GL047126.

Henstock, T. J., A. Levander, C. M. Snelson, G. R. Keller, K. C. Miller, S. H. Harder, A. R. Gorman, R. M. Clowes, M. J. A. Burianyk, and E. D. Humphreys (1998), Probing the Archean and Proterozoic lithosphere of western North America, *GSA Today*, 8(7), 1–5.

Hoffman, P. F. (1988), United Plates of America, the birth of a craton-Early Proterozoic assembly and growth of Laurentia, *Annu. Rev. Earth Planet. Sci.*, 16, 543–603.

Holm, D. K., W. R. Van Schmus, L. C. MacNeill, T. J. Boerboom, D. Schweitzer, and D. Schneider (2005), U-Pb zircon geochronology of Paleoproterozoic plutons from the northern midcontinent, USA: Evidence for subduction flip and continued convergence after geon 18 Penokean orogenesis, *Geol. Soc. Am. Bull.*, 117(3-4), 259–275, doi:10.1130/B25395.1.

Holm, D. K., R. Anderson, T. J. Boerboom, W. F. Cannon, V. Chandler, M. Jirsa, J. Miller, D. A. Schneider, K. J. Schulz, and W. R. Van Schmus (2007), Reinterpretation of Paleoproterozoic accretionary boundaries of the north-central United States based on a new aeromagnetic-geologic compilation, *Precambrian Res.*, 157(1), 71–79, doi:10.1016/j.precamres.2007.02.023.

Hopper, E., H. A. Ford, K. M. Fischer, V. Lekić, and M. J. Fouch (2014), The lithosphere–asthenosphere boundary and the tectonic and magmatic history of the northwestern United States, *Earth Planet. Sci. Lett.*, 402, 69–81, doi:10.1016/j.epsl.2013.12.016.

Humphreys, E. D., B. Schmandt, M. J. Bezada, and J. Perry-Houts (2015), Recent craton growth by slab stacking beneath Wyoming, *Earth Planet. Sci. Lett.*, 429, 170–180, doi:10.1016/j.epsl.2015.07.066.

Jacob, D. E. (2004), Nature and origin of eclogite xenoliths from kimberlites, *Lithos*, 77(1), 295–316, doi:10.1016/j.lithos.2004.03.038.

Jones, D. S., C. G. Barnes, W. R. Premo, and A. W. Snoke (2011), The geochemistry and petrogenesis of the Paleoproterozoic Green Mountain arc: A composite (?), bimodal, oceanic, fringing arc, *Precambrian Res.*, 185(3), 231–249, doi:10.1016/j.precamres.2011.01.011.

Jordan, T. H. (1978), Composition and development of the continental tectosphere, *Nature*, 274(5671), 544–548.

Jordan, T. H., and E. M. Paulson (2013), Convergence depths of tectonic regions from an ensemble of global tomographic models, *J. Geophys. Res. Solid Earth*, 118, 4196–4225, doi:10.1002/jgrb.50263.

Karato, S. I. (2012), On the origin of the asthenosphere, *Earth Planet. Sci. Lett.*, 321, 95–103, doi:10.1016/j.epsl.2012.01.001.

Karato, S. I., T. Ougboji, and J. Park (2015), Mechanisms and geologic significance of the mid-lithosphere discontinuity in the continents, *Nat. Geosci.*, 8, 509–514, doi:10.1038/ngeo2462.

Karlstrom, K. E., and the Continental Dynamics of the Rocky Mountain Working Group (2002), Structure and evolution of the lithosphere beneath the Rocky Mountains: Initial results from the CD-ROM experiment, *GSA Today*, 12, 4–10.

Karlstrom, K. E., and R. S. Houston (1984), The Cheyenne belt: Analysis of a Proterozoic suture in southern Wyoming, *Precambrian Res.*, 25(4), 415–446, doi:10.1016/0301-9268(84)90012-3.

Kawakatsu, H., P. Kumar, Y. Takei, M. Kanazawa, E. Araki, and K. Suyehiro (2009), Seismic evidence for sharp lithosphere-asthenosphere boundaries of oceanic plates, *Science*, 324(5926), 499–502, doi:10.1126/science.1169499.

Kelemen, P. B., and G. Hirth (2007), A periodic shear-heating mechanism for intermediate-depth earthquakes in the mantle, *Nature*, 446(7137), 787–790, doi:10.1038/nature05717.

Kelemen, P. B., S. R. Hart, and S. Bernstein (1998), Silica enrichment in the continental upper mantle via melt/rock reaction, *Earth Planet. Sci. Lett.*, 164(1), 387–406, doi:10.1016/S0012-821X(98)00233-7.

Kennett, B. L. N. (1991), The removal of free surface interactions from three-component seismograms, *Geophys. J. Int.*, 104(1), 153–163, doi:10.1111/j.1365-246X.1991.tb02501.x.

Kind, R., X. Yuan, and P. Kumar (2012), Seismic receiver functions and the lithosphere–asthenosphere boundary, *Tectonophysics*, 536, 25–43, doi:10.1016/j.tecto.2012.03.005.

Kind, R., X. Yuan, J. Mechie, and F. Sodoudi (2015), Structure of the upper mantle in the north-western and central United States from USArray S-receiver functions, *Solid Earth Discuss.*, 7, 1025–1057, doi:10.5194/sed-7-1025-2015.

Kopylova, M. G., and J. K. Russell (2000), Chemical stratification of cratonic lithosphere: Constraints from the Northern Slave craton, Canada, *Earth Planet. Sci. Lett.*, 181(1), 71–87, doi:10.1016/S0012-821X(00)00187-4.

Kuehner, S. M., and A. J. Irving (1999), Eclogite and metabasite xenoliths of subducted slab origin from the Paleogene Cedar Mountain diatremes, southwestern Wyoming, USA, in *Proceedings of the International Kimberlite Conference*, vol. 1, pp. 485–493, Red Roof Design, Cape Town, South Africa.

Kumar, P., and H. Kawakatsu (2011), Imaging the seismic lithosphere-asthenosphere boundary of the oceanic plate, *Geochem. Geophys. Geosyst.*, 12, Q01006, doi:10.1029/2010GC003358.

Kumar, P., R. Kind, X. Yuan, and J. Mechie (2012), USArray receiver function images of the lithosphere-asthenosphere boundary, *Seismol. Res. Lett.*, 83(3), 486–491, doi:10.1785/gssrl.83.3.486.

Lee, C. T. A. (2003), Compositional variation of density and seismic velocities in natural peridotites at STP conditions: Implications for seismic imaging of compositional heterogeneities in the upper mantle, *J. Geophys. Res.*, 108(B9), 2441, doi:10.1029/2003JB002413.

Lee, C. T. A. (2006), Geochemical/petrologic constraints on the origin of cratonic mantle, in *Archean Geodynamics and Environments*, AGU Monogr. Ser., vol. 164, pp. 89–114, AGU, Washington, D. C., doi:10.1029/164GM08.

Lee, C. T. A., and E. J. Chin (2014), Calculating melting temperatures and pressures of peridotite protoliths: Implications for the origin of cratonic mantle, *Earth Planet. Sci. Lett.*, 403, 273–286, doi:10.1016/j.epsl.2014.06.048.

Lee, C. T. A., X. Cheng, and U. Horodyskyj (2006), The development and refinement of continental arcs by primary basaltic magmatism, garnet pyroxenite accumulation, basaltic recharge and delamination: Insights from the Sierra Nevada, California, *Contrib. Mineral. Petrol.* 151(2), 222–242, doi:10.1007/s00410-005-0056-1.

Lee, C. T. A., P. Luffi, and E. J. Chin (2011), Building and destroying continental mantle, *Annu. Rev. Earth Planet. Sci.*, 39, 59–90, doi:10.1146/annurev-earth-040610-133505.

Lekić, V., and K. M. Fischer (2014), Contrasting lithospheric signatures across the western United States revealed by Sp receiver functions, *Earth Planet. Sci. Lett.*, 402, 90–98, doi:10.1016/j.epsl.2013.11.026.

Lekić, V., S. W. French, and K. M. Fischer (2011), Lithospheric thinning beneath rifted regions of Southern California, *Science*, 334(6057), 783–787, doi:10.1126/science.1208898.

Lester, A., and G. L. Farmer (1998), Lower crustal and upper mantle xenoliths along the Cheyenne belt and vicinity, *Rocky Mt. Geol.*, 33(2), 293–304, doi:10.2113/33.2.293.

Levander, A., and M. S. Miller (2012), Evolutionary aspects of lithosphere discontinuity structure in the western US, *Geochem. Geophys. Geosyst.*, 13, Q0AK07, doi:10.1029/2012GC004056.

Levin, V., and J. Park (2000), Shear zones in the Proterozoic lithosphere of the Arabian Shield and the nature of the Hales discontinuity, *Tectonophysics*, 323(3), 131–148, doi:10.1016/S0040-1951(00)00105-0.

Lewry, J. F., Z. Hajnal, A. Green, S. B. Lucas, D. White, M. R. Stauffer, K. E. Ashton, W. Weber, and R. Clowes (1994), Structure of a Paleoproterozoic continent-continent collision zone: A LITHOPROBE seismic reflection profile across the Trans-Hudson Orogen, Canada, *Tectonophysics*, 232(1), 143–160, doi:10.1016/0040-1951(94)90081-7.

Lou, X., and S. van der Lee (2014), Observed and predicted North American teleseismic delay times, *Earth Planet. Sci. Lett.*, 402, 6–15, doi:10.1016/j.epsl.2013.11.056.

MacCarthy, J. K., R. C. Aster, K. Dueker, S. Hansen, B. Schmandt, and K. Karlstrom (2014), Seismic tomography of the Colorado Rocky Mountains upper mantle from CREST: Lithosphere–asthenosphere interactions and mantle support of topography, *Earth Planet. Sci. Lett.*, 402, 107–119, doi:10.1016/j.epsl.2014.03.063.

Macdonald, R., B. G. J. Upton, K. D. Collerson, B. C. Hearn, and D. James (1992), Potassic mafic lavas of the Bearpaw Mountains, Montana: Mineralogy, chemistry, and origin, *J. Petrol.*, 33(2), 305–346, doi:10.1093/petrology/33.2.305.

Mareschal, J. C., and C. Jaupart (2004), Variations of surface heat flow and lithospheric thermal structure beneath the North American craton, *Earth Planet. Sci. Lett.*, 223(1), 65–77, doi:10.1016/j.epsl.2004.04.002.

McCallum, M. E., D. H. Eggler, and L. K. Burns (1975), Kimberlitic diatremes in northern Colorado and southern Wyoming, *Phys. Chem. Earth*, 9, 149–161, doi:10.1016/0079-1946(75)90014-2.

McKenzie, D., J. Jackson, and K. Priestley (2005), Thermal structure of oceanic and continental lithosphere, *Earth Planet. Sci. Lett.*, 233(3), 337–349, doi:10.1016/j.epsl.2005.02.005.

Meqbel, N. M., G. D. Egbert, P. E. Wannamaker, A. Kelbert, and A. Schultz (2014), Deep electrical resistivity structure of the northwestern US derived from 3-D inversion of USArray magnetotelluric data, *Earth Planet. Sci. Lett.*, 402, 290–304, doi:10.1016/j.epsl.2013.12.026.

Mercier, J. P., M. G. Bostock, P. Audet, J. B. Gaherty, E. J. Garnero, and J. Revenaugh (2008), The teleseismic signature of fossil subduction: Northwestern Canada, *J. Geophys. Res.*, 113, B04308, doi:10.1029/2007JB005127.

Miller, M. S., and D. W. Eaton (2010), Formation of cratonic mantle keels by arc accretion: Evidence from S receiver functions, *Geophys. Res. Lett.*, 37, L18305, doi:10.1029/2010GL044366.

Moore, M., A. R. Chakhmouradian, A. N. Mariano, and R. Sidu (2015), Evolution of rare-earth mineralization in the Bear Lodge carbonatite, Wyoming: Mineralogical and isotopic evidence, *Ore Geology Reviews*, 64, 499–521, doi:10.1016/j.oregeorev.2014.03.015.

Moorkamp, M., A. G. Jones, and D. W. Eaton (2007), Joint inversion of teleseismic receiver functions and magnetotelluric data using a genetic algorithm: Are seismic velocities and electrical conductivities compatible?, *Geophys. Res. Lett.*, 34, L16311, doi:10.1029/2007GL030519.

Mueller, P. A., and C. D. Frost (2006), The Wyoming Province: A distinctive Archean craton in Laurentian North America, *Can. J. Earth Sci.*, 43(10), 1391–1397, doi:10.1139/e06-075.

Mueller, P. A., J. L. Wooden, and A. P. Nutman (1992), 3.96 Ga zircons from an Archean quartzite, Beartooth Mountains, Montana, *Geology*, 20(4), 327–330, doi:10.1130/0091-7613(1992)020<0327:GZFAAQ>2.3.CO;2.

Mueller, P. A., A. L. Heatherington, D. M. Kelly, J. L. Wooden, and D. W. Mogk (2002), Paleoproterozoic crust within the Great Falls tectonic zone: Implications for the assembly of southern Laurentia, *Geology*, 30(2), 127–130, doi:10.1130/0091-7613(2002)030<0127:PCWTGF>2.0.CO;2.

Naif, S., K. Key, S. Constable, and R. L. Evans (2013), Melt-rich channel observed at the lithosphere-asthenosphere boundary, *Nature*, 495(7441), 356–359, doi:10.1038/nature11939.

Nelson, B. K., and D. J. DePaolo (1985), Rapid production of continental crust 1.7 to 1.9 by ago: Nd isotopic evidence from the basement of the North American mid-continent, *Geol. Soc. Am. Bull.*, 96(6), 746–754, doi:10.1130/0016-7606(1985)96<746:RPOCCT>2.0.CO;2.

Nelson, K. D., D. J. Baird, J. J. Walters, M. Hauck, L. D. Brown, J. E. Oliver, J. L. Ahern, Z. Hajnal, A. G. Jones, and L. L. Sloss (1993), Trans-Hudson orogen and Williston basin in Montana and North Dakota: New COCORP deep-profiling results, *Geology*, 21(5), 447–450, doi:10.1130/0091-7613(1993)021<0447:THOAWB>2.3.CO;2.

Nielsen, L., H. Thybo, and A. V. Egorkin (2002), Implications of seismic scattering below the 8 discontinuity along PNE profile Kraton, *Tectonophysics*, 358(1), 135–150, doi:10.1016/S0040-1951(02)00421-3.

Obrebski, M., R. M. Allen, M. Xue, and S. H. Hung (2010), Slab-plume interaction beneath the Pacific Northwest, *Geophys. Res. Lett.*, 37, L14305, doi:10.1029/2010GL043489.

O'Brien, H. E., A. J. Irving, I. S. McCallum, and M. F. Thirlwall (1995), Strontium, neodymium, and lead isotopic evidence for the interaction of post-subduction asthenospheric

potassic mafic magmas of the Highwood Mountains, Montana, USA, with ancient Wyoming craton lithospheric mantle, *Geochim. Cosmochim. Acta*, 59(21), 4539–4556, doi:10.1016/0016-7037(95)99266-J.

Ogawa, M. (1987), Shear instability in a viscoelastic material as the cause of deep focus earthquakes, *J. Geophys. Res.*, 92(B13), 13,801–13,810, doi:10.1029/JB092iB13p13801.

Olugboji, T. M., S. I. Karato, and J. Park (2013), Structures of the oceanic lithosphere-asthenosphere boundary: Mineral-physics modelling and seismological signatures, *Geochem. Geophys. Geosyst.*, 14, 880–901, doi:10.1002/ggge.20086.

Parman, S. W., T. L. Grove, J. C. Dann, and M. J. De Wit (2004), A subduction origin for komatiites and cratonic lithospheric mantle, *S. Afr. J. Geol.*, 107(1-2), 107–118, doi:10.2113/107.1-2.107.

Pearson, D. G., and N. Wittig (2008), Formation of Archaean continental lithosphere and its diamonds: The root of the problem, *J. Geol. Soc.*, 165(5), 895–914, doi:10.1144/0016-76492008-003.

Pechmann, J. C., K. D. Koper, R. B. Herrmann, K. M. Whidden, H. M. Benz, K. L. Pankow, F. Lin, and D. S. Chapman (2014), An M 4.8 earthquake in the upper mantle beneath the Wind River Range, Wyoming, *Seismol. Res. Lett.*, 85, 507.

Pollack, H. N., S. J. Hurter, and J. R. Johnson (1993), Heat flow from the Earth's interior: Analysis of the global data set, *Rev. Geophys.*, 31(3), 267–280, doi:10.1029/93RG01249.

Poppeliers, C., and G. L. Pavlis (2003), Three-dimensional, prestack, plane wave migration of teleseismic P-to-S converted phases: 2. Stacking multiple events, *J. Geophys. Res.*, 108(B5), 2267, doi:10.1029/2001JB001583.

Porritt, R. W., R. M. Allen, and F. F. Pollitz (2014), Seismic imaging east of the Rocky Mountains with USArray, *Earth Planet. Sci. Lett.*, 402, 16–25, doi:10.1016/j.epsl.2013.10.034.

Porritt, R. W., M. S. Miller, and F. A. Darbyshire (2015), Lithospheric architecture beneath Hudson Bay, *Geochem. Geophys. Geosyst.*, 16, 2262–2275, doi:10.1002/2015GC005845.

Prieto, G. A., M. Florez, S. A. Barrett, G. C. Beroza, P. Pedraza, J. F. Blanco, and E. Poveda (2013), Seismic evidence for thermal runaway during intermediate-depth earthquake rupture, *Geophys. Res. Lett.*, 40, 6064–6068, doi:10.1002/2013GL058109.

Rader, E., E. Emry, N. Schmerr, D. Frost, C. Cheng, J. Menard, C. Q. Yu, and D. Geist (2015), Characterization and petrological constraints of the mid-lithospheric discontinuity, *Geochem. Geophys. Geosyst.*, doi:10.1002/2015GC005943, in press.

Revenaugh, J., and S. A. Sipkin (1994), Mantle discontinuity structure beneath China, *J. Geophys. Res.*, 99(B11), 21,911–21,927.

Rey, P. F., N. Coltice, and N. Flament (2014), Spreading continents kick-started plate tectonics, *Nature*, 513(7518), 405–408, doi:10.1038/nature13728.

Romanowicz, B. (2009), The thickness of tectonic plates, *Science*, 324(5926), 474–476, doi:10.1126/science.1172879.

Rondenay, S., G. A. Abers, and P. E. Van Keken (2008), Seismic imaging of subduction zone metamorphism, *Geology*, 36(4), 275–278, doi:10.1130/G24112A.1.

Ross, G. M. (2002), Evolution of Precambrian continental lithosphere in Western Canada: Results from Lithoprobe studies in Alberta and beyond, *Can. J. Earth Sci.*, 39(3), 413–437, doi:10.1139/e02-012.

Rudnick, R. L., and A. A. Nyblade (1999), The thickness and heat production of Archean lithosphere: Constraints from xenolith thermobarometry and surface heat flow, in *Mantle Petrology: Field Observations and High-Pressure Experimentation: A Tribute to Francis R. (Joe) Boyd*, vol. 6, edited by Y. Fei, C. M. Bertka, and B. O. Mysen, *Geochem. Soc. Spec. Publ.*, 6, 3–12.

Rychert, C. A., and P. M. Shearer (2009), A global view of the lithosphere-asthenosphere boundary, *Science*, 324(5926), 495–498, doi:10.1126/science.1169754.

Rychert, C. A., K. M. Fischer, and S. Rondenay (2005), A sharp lithosphere–asthenosphere boundary imaged beneath eastern North America, *Nature*, 436(7050), 542–545, doi:10.1038/nature03904.

Rychert, C. A., S. Rondenay, and K. M. Fischer (2007), P-to-S and S-to-P imaging of a sharp lithosphere-asthenosphere boundary beneath eastern North America, *J. Geophys. Res.*, 112, B08314, doi:10.1029/2006JB004619.

Rychert, C. A., N. Schmerr, and N. Harmon (2012), The Pacific lithosphere-asthenosphere boundary: Seismic imaging and anisotropic constraints from SS waveforms, *Geochem. Geophys. Geosyst.*, 13, Q0AK10, doi:10.1029/2012GC004194.

Saul, J., M. R. Kumar, and D. Sarkar (2000), Lithospheric and upper mantle structure of the Indian Shield, from teleseismic receiver functions, *Geophys. Res. Lett.*, 27(16), 23,57–23,60, doi:10.1029/1999GL011128.

Savage, B., and P. G. Silver (2008), Evidence for a compositional boundary within the lithospheric mantle beneath the Kalahari craton from S receiver functions, *Earth Planet. Sci. Lett.*, 272(3), 600–609, doi:10.1016/j.epsl.2008.05.026.

Schaeffer, A. J., and S. Lebedev (2014), Imaging the North American continent using waveform inversion of global and USArray data, *Earth Planet. Sci. Lett.*, 402, 26–41, doi:10.1016/j.epsl.2014.05.014.

Schmandt, B., and E. Humphreys (2010), Complex subduction and small-scale convection revealed by body-wave tomography of the western United States upper mantle, *Earth Planet. Sci. Lett.*, 297(3), 435–445, doi:10.1016/j.epsl.2010.06.047.

Schmandt, B., and F.-C. Lin (2014), P and S wave tomography of the mantle beneath the United States, *Geophys. Res. Lett.*, 41, 6342–6349, doi:10.1002/2014GL061231.

Schmerr, N. (2012), The Gutenberg discontinuity: Melt at the lithosphere-asthenosphere boundary, *Science*, 335(6075), 1480–1483, doi:10.1126/science.1215433.

Schulze, D. J., J. W. Valley, K. F. Viljoen, and M. J. Spicuzza (2003), Oxygen isotope composition of mantle eclogites, paper presented at 8th International Kimberlite Conference, Victoria, British Columbia, June 22–27th.

Schulze, D. J., H. G. Coopersmith, B. Harte, and L. A. Pizzolato (2008), Mineral inclusions in diamonds from the Kelsey Lake Mine, Colorado, USA: Depleted Archean mantle beneath the Proterozoic Yavapai province, *Geochim. Cosmochim. Acta*, 72(6), 1685–1695, doi:10.1016/j.gca.2007.09.037.

Seats, K. J., and J. F. Lawrence (2014), The seismic structure beneath the Yellowstone Volcano Field from ambient seismic noise, *Geophys. Res. Lett.*, 41, 8277–8282, doi:10.1002/2014GL061913.

Selway, K., H. Ford, and P. Kelemen (2015), The seismic mid-lithosphere discontinuity, *Earth Planet. Sci. Lett.*, 414, 45–57, doi:10.1016/j.epsl.2014.12.029.

Sheehan, A. F., G. A. Abers, A. L. Lerner-Lam, and C. H. Jones (1995), Crustal thickness variations across the Colorado Rocky Mountains from teleseismic receiver functions, *J. Geophys. Res.*, 100(B10), 20,391-20,404.

Sheehan, A. F., C. H. Jones, M. K. Savage, S. Ozalaybey, and J. M. Schneider (1997), Contrasting lithospheric structure beneath the Colorado Plateau and Great Basin: Initial results from Colorado Plateau—Great Basin PASSCAL experiment, *Geophys. Res. Lett.*, 24(21), 2609–2612.

Shen, W., M. H. Ritzwoller, and V. Schulte-Pelkum (2013), A 3-D model of the crust and uppermost mantle beneath the Central and Western US by joint inversion of receiver functions and surface wave dispersion, *J. Geophys. Res. Solid Earth*, 118, 262–276, doi:10.1029/2012JB009602.

Sigloch, K. (2011), Mantle provinces under North America from multifrequency P wave tomography, *Geochem. Geophys. Geosyst.*, 12, Q02W08, doi:10.1029/2010GC003421.

Sine, C. R., D. Wilson, W. Gao, S. P. Grand, R. Aster, J. Ni, and W. S. Baldrige (2008), Mantle structure beneath the western edge of the Colorado Plateau, *Geophys. Res. Lett.*, 35, L10303, doi:10.1029/2008GL033391.

Sloan, R. A., and J. A. Jackson (2012), Upper-mantle earthquakes beneath the Arafura Sea and south Aru Trough: Implications for continental rheology, *J. Geophys. Res. Solid Earth*, 117(B5), B05402, doi:10.1029/2011JB008992.

Smith, R. B., M. Jordan, B. Steinberger, C. M. Puskas, J. Farrell, G. P. Waite, S. Hansen, W. L. Change, and R. O'Connell (2009), Geodynamics of the Yellowstone hotspot and mantle plume: Seismic and GPS imaging, kinematics, and mantle flow, *J. Volcanol. Geother. Res.*, 188(1), 26–56, doi:10.1016/j.jvolgeores.2009.08.020.

Snelson, C. M., T. J. Henstock, G. R. Keller, K. C. Miller, and A. Levander (1998), Crustal and uppermost mantle structure along the Deep Probe seismic profile, Rocky Mt. Geol., 33(2), 181–198.

Snyder, D. B. (2002), Lithospheric growth at margins of cratons, *Tectonophysics*, 355(1), 7–22, doi:10.1016/S0040-1951(02)00131-2.

Snyder, D. B. (2008), Stacked uppermost mantle layers within the Slave craton of NW Canada as defined by anisotropic seismic discontinuities, *Tectonics*, 27, TC4006, doi:10.1029/2007TC002132.

Soudoudi, F., X. Yuan, R. Kind, S. Lebedev, J. M. C. Adam, E. Kästle, and F. Tilmann (2013), Seismic evidence for stratification in composition and anisotropic fabric within the thick lithosphere of Kalahari Craton, *Geochem. Geophys. Geosyst.*, 14, 5393–5412, doi:10.1002/2013GC004955.

Steer, D. N., J. H. Knapp, and L. D. Brown (1998), Super-deep reflection profiling: Exploring the continental mantle lid, *Tectonophysics*, 286, 111–121, doi:10.1016/S0040-1951(97)00258-8.

Stern, T. A., S. A. Henrys, D. Okaya, J. N. Louie, M. K. Savage, S. Lamb, H. Sato, R. Sutherland, and T. Iwasaki (2015), A seismic reflection image for the base of a tectonic plate, *Nature*, 518(7537), 85–88, doi:10.1038/nature14146.

Stixrude, L., and C. Lithgow-Bertelloni (2005), Thermodynamics of mantle minerals - I. Physical properties, *Geophys. J. Int.*, 162(2), 610–632, doi:10.1111/j.1365-246X.2005.02642.x.

Syracuse, E. M., G. A. Abers, K. M. Fischer, L. MacKenzie, C. A. Rychert, M. Protti, V. Gonzalez, and W. Strauch (2008), Seismic tomography and earthquake locations in the

Nicaraguan and Costa Rican upper mantle, *Geochem. Geophys. Geosyst.*, 9(7), doi:10.1029/2008GC001963.

Thurner, S., R. Margolis, A. Levander, and F. Niu (2015), PdS receiver function evidence for crustal scale thrusting, relic subduction, and mafic underplating in the Trans-Hudson Orogen and Yavapai province, *Earth Planet. Sci. Lett.*, 426, 13–22, doi:10.1016/j.epsl.2015.06.007.

Thybo, H. (2006), The heterogeneous upper mantle low velocity zone, *Tectonophysics*, 416(1), 53–79, doi:10.1016/j.tecto.2005.11.021.

Thybo, H., and E. Perchuc (1997), The seismic 8 discontinuity and partial melting in continental mantle, *Science*, 275(5306), 1626–1629, doi:10.1126/science.275.5306.1626.

Tian, Y., and D. Zhao (2012), P-wave tomography of the western United States: Insight into the Yellowstone hotspot and the Juan de Fuca slab, *Phys. Earth Planet. Inter.*, 200, 72–84, doi:10.1016/j.pepi.2012.04.004.

van der Velden, A. J., and F. A. Cook (2005), Relict subduction zones in Canada, *J. Geophys. Res.*, 110, B08403, doi:10.1029/2004JB003333.

Van Schmus, W. R., D. A. Schneider, D. K. Holm, S. Dodson, and B. K. Nelson (2007), New insights into the southern margin of the Archean–Proterozoic boundary in the north-central United States based on U–Pb, Sm–Nd, and Ar–Ar geochronology, *Precambrian Res.*, 157(1), 80–105, doi:10.1016/j.precamres.2007.02.011.

Waite, G. P., R. B. Smith, and R. M. Allen (2006), Vp and Vs structure of the Yellowstone hot spot from teleseismic tomography: Evidence for an upper mantle plume, *J. Geophys. Res.*, 111, B04303, doi:10.1029/2005JB003867.

Walker, K., G. Bokelmann, and S. Klemperer (2004), Shear-wave splitting beneath the Snake River suggests a mantle upwelling beneath eastern Nevada, USA, *Earth Planet. Sci. Lett.*, 222, 529–542.

Weeraratne, D. S., D. W. Forsyth, K. M. Fischer, and A. A. Nyblade (2003), Evidence for an upper mantle plume beneath the Tanzanian craton from Rayleigh wave tomography, *J. Geophys. Res.*, 108(B9), 2427, doi:10.1029/2002JB002273.

White, D. J., G. Musacchio, H. H. Helmstaedt, R. M. Harrap, P. C. Thurston, A. Van der Velden, and K. Hall (2003), Images of a lower-crustal oceanic slab: Direct evidence for tectonic accretion in the Archean western Superior province, *Geology*, 31(11), 997–1000, doi:10.1130/G20014.1.

Whitmeyer, S. J., and K. E. Karlstrom (2007), Tectonic model for the Proterozoic growth of North America, *Geosphere*, 3(4), 220–259, doi:10.1130/GES00055.1.

Wiens, D. A. (2001), Seismological constraints on the mechanism of deep earthquakes: Temperature dependence of deep earthquake source properties, *Phys. Earth Planet. Inter.*, 127(1), 145–163, doi:10.1016/S0031-9201(01)00225-4.

Wilson, D. C., D. A. Angus, J. F. Ni, and S. P. Grand (2006), Constraints on the interpretation of S-to-P receiver functions, *Geophys. J. Int.*, 165(3), 969–980, doi:10.1111/j.1365-246X.2006.02981.x.

Wirth, E. A., and M. D. Long (2014), A contrast in anisotropy across mid-lithospheric discontinuities beneath the central United States—A relic of craton formation, *Geology*, 42(10), 851–854, doi:10.1130/G35804.1.

Wittig, N., D. G. Pearson, M. Webb, C. J. Ottley, G. J. Irvine, M. Kopylova, S. M. Jensen, and G. M. Nowell (2008), Origin of cratonic lithospheric mantle roots: A geochemical

study of peridotites from the North Atlantic Craton, West Greenland. *Earth Planet. Sci. Lett.*, 274(1), 24–33, doi:10.1016/j.epsl.2008.06.034.

Wittlinger, G., and V. Farra (2007), Converted waves reveal a thick and layered tectosphere beneath the Kalahari super-craton, *Earth Planet. Sci. Lett.*, 254(3), 404–415, doi:10.1016/j.epsl.2006.11.048.

Wölbern, I., G. Rumpker, K. Link, and F. Sodoudi (2012), Melt infiltration of the lower lithosphere beneath the Tanzania craton and the Albertine rift inferred from S receiver functions, *Geochem. Geophys. Geosyst.*, 13, Q0AK08, doi:10.1029/2012GC004167.

Wong, I. G., and D. S. Chapman (1990), Deep intraplate earthquakes in the western United States and their relationship to lithospheric temperatures, *Bull. Seismol. Soc. Am.*, 80(3), 589–599.

Wooden, J. L., and P. A. Mueller (1988), Pb, Sr, and Nd isotopic compositions of a suite of Late Archean, igneous rocks, eastern Beartooth Mountains: Implications for crust-mantle evolution, *Earth Planet. Sci. Lett.*, 87(1), 59–72, doi:10.1016/0012-821X(88)90064-7.

Wyllie, P. J. (1995), Experimental petrology of upper mantle materials, processes and products, *J. Geodyn.*, 20(4), 429–468, doi:10.1016/0264-3707(95)00023-3.

Wyllie, P. J. (1987), Discussion of recent papers on carbonated peridotite, bearing on mantle metasomatism and magmatism, *Earth Planet. Sci. Lett.*, 82(3), 391–397, doi:10.1016/0012-821X(87)90213-5.

Yeck, W. L., A. F. Sheehan, M. L. Anderson, E. A. Erslev, K. C. Miller, and C. S. Siddoway (2014), Structure of the Bighorn Mountain region, Wyoming, from teleseismic receiver function analysis: Implications for the kinematics of Laramide shortening, *J. Geophys. Res. Solid Earth*, 119, 7028–7042, doi:10.1002/2013JB010769.

Yuan, H., and K. Dueker (2005a), Upper mantle tomographic V_p and V_s images of the Rocky Mountains in Wyoming, Colorado, and New Mexico: Evidence for a thick heterogeneous chemical lithosphere, in *The Rocky Mountain Region: An Evolving Lithosphere Tectonics*, Geophys. Monogr. Ser., vol. 154, pp. 329–345, AGU, Washington, D. C., doi:10.1029/154GM25.

Yuan, H., and K. Dueker (2005b), Teleseismic P-wave tomogram of the Yellowstone plume, *Geophys. Res. Lett.*, 32, L07304, doi:10.1029/2004GL022056.

Yuan, H., and B. Romanowicz (2010), Lithospheric layering in the North American craton, *Nature*, 466(7310), 1063–1068, doi:10.1038/nature09332.

Yuan, H., B. Romanowicz, K. M. Fischer, and D. Abt (2011), 3-D shear wave radially and azimuthally anisotropic velocity model of the North American upper mantle, *Geophys. J. Int.*, 184(3), 1237–1260, doi:10.1111/j.1365-246X.2010.04901.x.

Yuan, H., S. French, P. Cupillard, and B. Romanowicz (2014), Lithospheric expression of geological units in central and eastern North America from full waveform tomography, *Earth Planet. Sci. Lett.*, 402, 176–186, doi:10.1016/j.epsl.2013.11.057.

Zandt, G., and W. D. Richins (1979), An upper mantle earthquake beneath the middle Rocky Mountains in NE Utah, *Earthquake Notes*, 50(4), 69–70.

Zurek, B., and K. Dueker (2005), Lithospheric stratigraphy beneath the southern Rocky Mountains, USA, in *The Rocky Mountain Region: An Evolving Lithosphere*, Geophys. Monogr. Ser., vol. 154, pp. 317–328, AGU, Washington, D. C., doi:10.1029/154GM24.

Figures

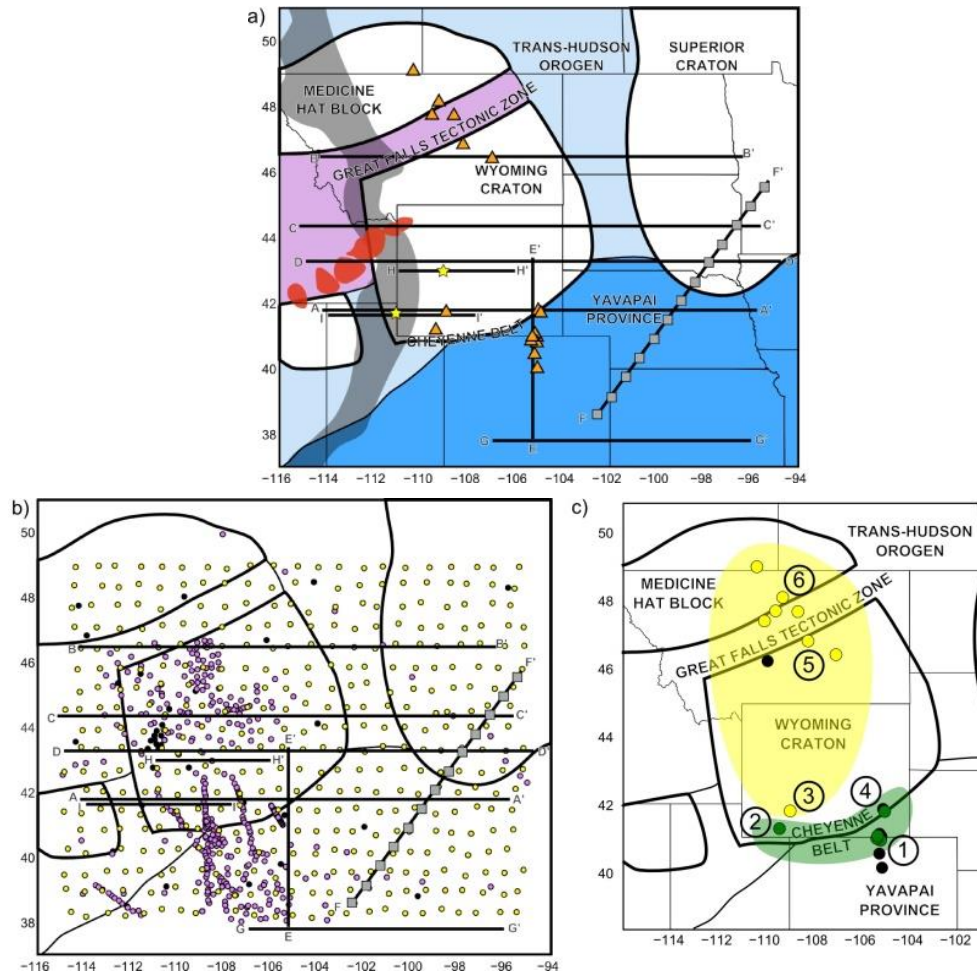


Figure 1: a) Map of the study area. Basement map after Whitmeyer and Karlstrom [2007]. White areas: Archean crust; light blue shading: Paleoproterozoic reworked Archean crust; lilac shading: 2.0–1.8 Ga juvenile arcs; dark blue shading: <1.8 Ga juvenile crust. Red shading: rhyolite calderas in the eastern Snake River Plane, after Smith et al. [2009]. Grey shading: Sevier Fold and thrust belt, after DeCelles and Coogan [2006]. Orange triangles: locations of xenolith and xenocrysts. Thick black lines: cross-section lines; grey squares mark location on Figure 8. Yellow stars are mantle earthquake hypocenters (Section 4.2.2). b) Map showing station locations. Filled circles: broadband stations that contributed data to this study. Purple circles are permanent stations; yellow circles are Transportable Array stations from EarthScope's USArray; pink circles are temporary stations from 13 arrays. Network information in Acknowledgments. c) Map showing xenolith and xenocryst localities, shown by filled circles: (1) State Line District, including the Sloan, Nix-Moen, and George Creek pipes; (2) Cedar Mountain; (3) Leucite Hills; (4) Iron Mountain District; (5) Grassrange intrusions, including the Homestead kimberlite; (6) Montana alkali province, including the Williams kimberlite and the Bearpaw Mountains. Green circles: significant eclogite present [McCallum et al., 1975; Ater et al., 1984; Egglar et al., 1987a; Kuehner and Irving, 1999; Schulze et al., 2008]. Yellow circles: significant phlogopite present [Hearn and Boyd, 1975; Hearn, 1989, 1999, 2004; Egglar et al., 1987b; Macdonald et al., 1992; Lester and Farmer, 1998; Buhlmann et al., 2000; Carlson et al., 2004; Downes et al., 2004].

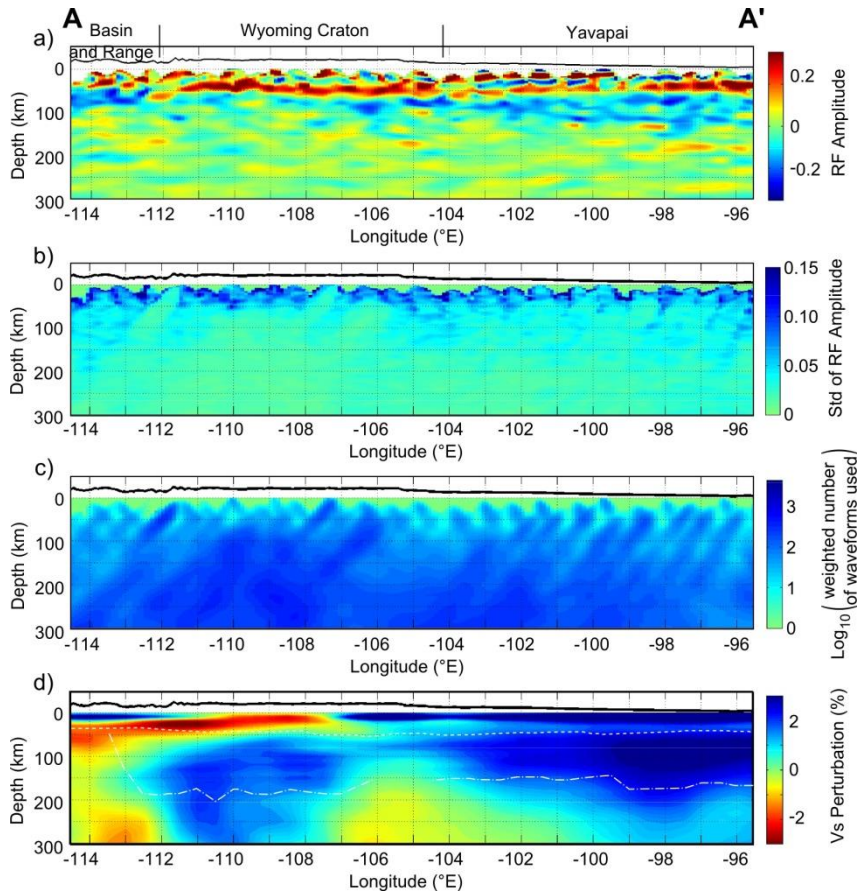


Figure 2: E-W cross-section A-A'. For all sections, thick black line: topography, at 10X vertical exaggeration. a) Mean of the bootstrapped 4–33 s Sp CCP stack. Labels correspond to approximate terrane boundaries. b) Standard deviation of the amplitude between the 50 calculated bootstrap stacks. c) Data density in CCP stack, calculated as number of whole waveforms at a point given the spline weighting used. (d) Shear velocity anomalies from the tomography model of Porritt et al. [2014]. Dashed white line: Moho (Lowry, personal communication, 2014). Dash-dotted white line: approximate LAB depth range from tomography. This depth is defined as the maximum negative gradient in absolute shear velocity between the peak velocity and the velocity minimum above 210 km; the gradient is taken over 30 km. If the average velocity between the Moho and the maximum velocity is slower than 4.24 km/s, all resolvable velocities are assumed to be asthenospheric, and the LAB is defined as directly beneath the Moho. A single NVG is observed west of 112°W and corresponds to the LAB. More complex or multiple NVGs are observed beneath cratonic regions (east of 112°W).

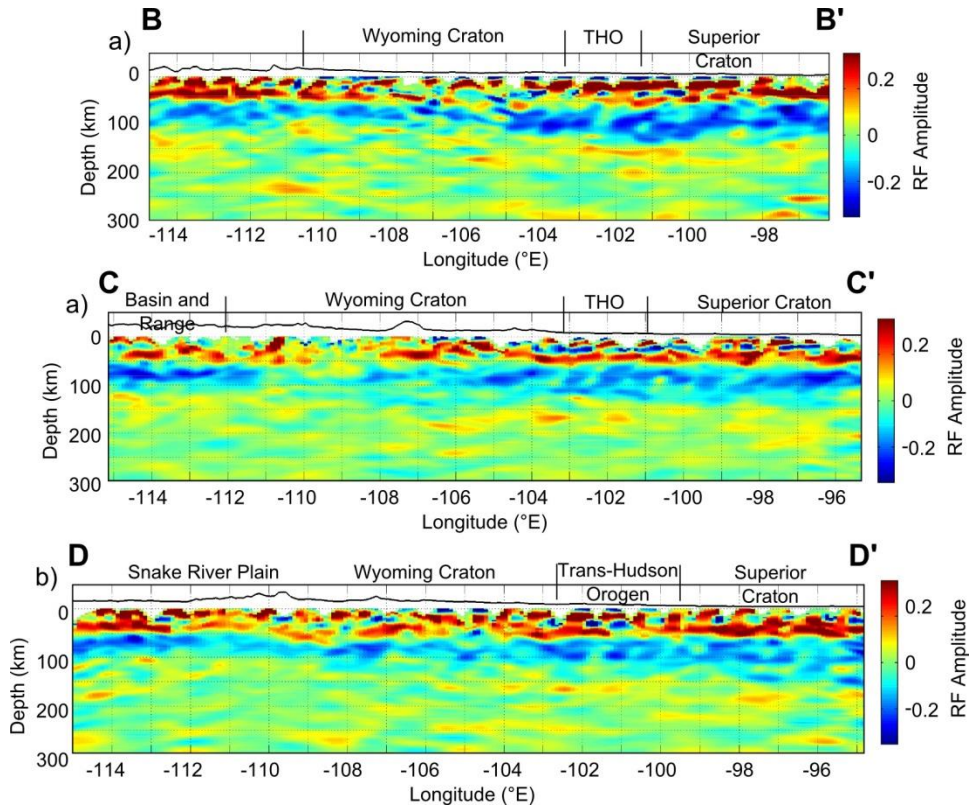


Figure 3: E-W cross sections through the mean of the bootstrapped Sp CCP stack (4–33 s). For all sections, thick black line: topography, at 10X vertical exaggeration; labels correspond to approximate terrane boundaries. A single NVG is observed west of 112°W and corresponds to the LAB. More complex or multiple NVGs are observed beneath cratonic regions (east of 112°W).

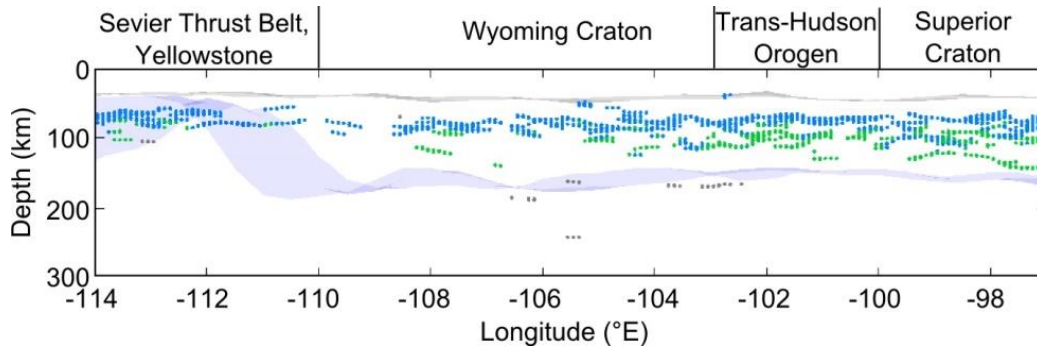


Figure 4: E-W cross section showing mantle discontinuity depths between 44°N and 46°N. Translucent grey surface: Moho from Lowry (personal communication, 2014). Translucent purple surface: approximate LAB depth range from regional tomography [Porritt et al., 2014], as described in Figure 2. Blue circles: automated pick of the shallowest negative peak amplitude beneath the Moho that has a amplitude of above 10% of the incident wave amplitude, and a standard deviation of less than 5% of the incident wave amplitude. Green circles: automated picks of deeper negative amplitude peaks, with the same quality requirements. If two peaks are identified within a 10 km depth range, the depth of the higher-amplitude peak is chosen. Grey circles: automated picks of positive amplitude peaks below the Moho, with the same quality requirements. In the craton, the two classes of NVGs from the Sp CCP stacks lie within the mantle lithosphere.

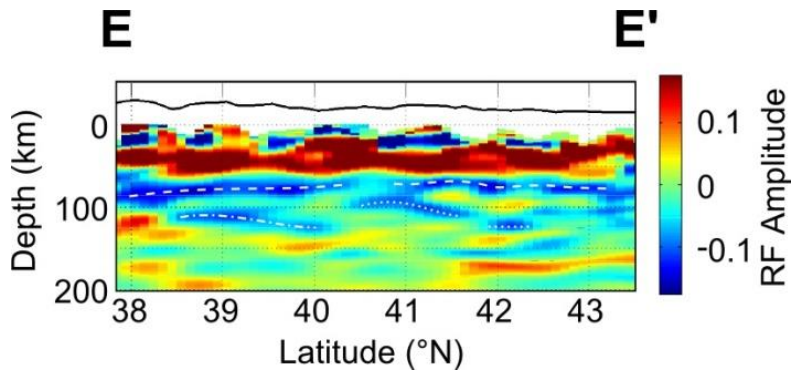


Figure 5: Cross section normal to the Cheyenne Belt of the mean of the bootstrapped Sp CCP stack (4–33 s). White dashed line: uppermost negative phase. White dotted line: upper dipping negative phase. Dash-dotted white line: secondary dipping negative phase. Black line: topography, at 10X vertical exaggeration. Corresponding tomography [Porritt et al., 2014] shown in supporting information Figure S2.

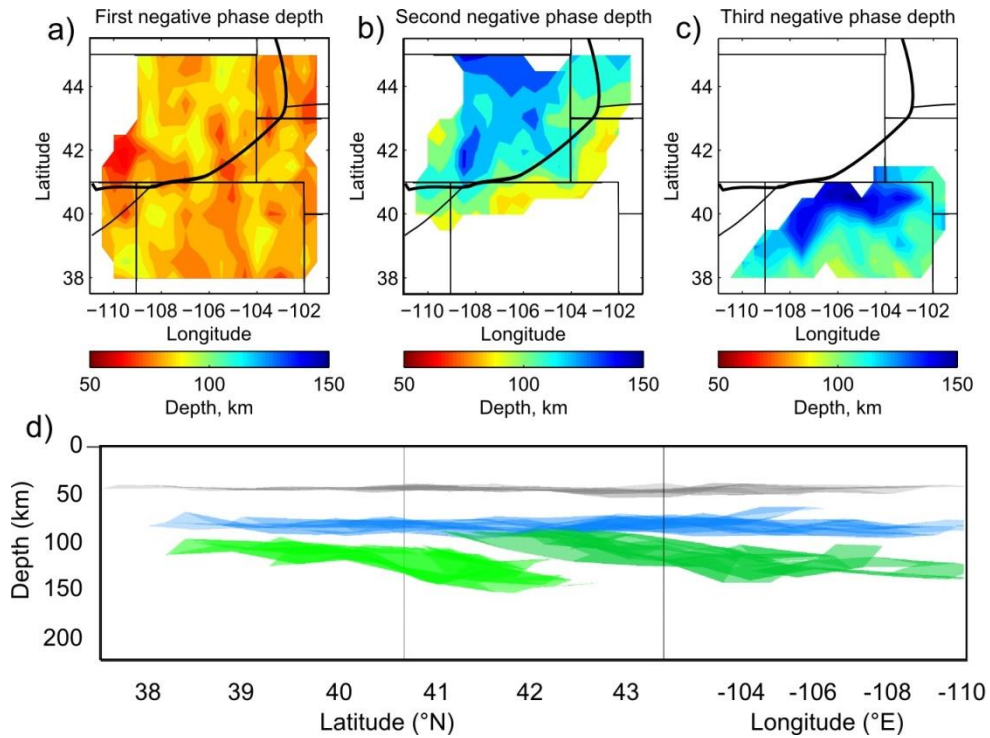


Figure 6: Contoured phase depth of NVGs beneath the Cheyenne Belt region. Plotted surfaces are calculated as an interpolation of hand picks of three separate surfaces. To be picked, phase had to be consistent over at least 100 km in cross section and clearly distinguishable as one of the three surfaces discussed in the text, and/or consistent in depth with picks made within 0.1° latitude or longitude on perpendicular cross sections. a) Uppermost NVG, as dashed line in Figure 6a. b) Upper dipping NVG, as dotted line in Figure 6a. c) Secondary dipping NVG, as dash-dotted line in Figure 6a. d) Three-dimensional plot of Cheyenne Belt phases, viewed approximately along strike looking from the NE to the SW (between 37.5°N , 110°W and 43.5°N , and 102°W). Grey surface: Moho (Lowry, personal communication, 2014). Light blue surface: uppermost NVG as in Figure 6a. Dark green surface: upper dipping NVG, as in Figure 6b. Light green surface: secondary dipping NVG, as in Figure 6c.

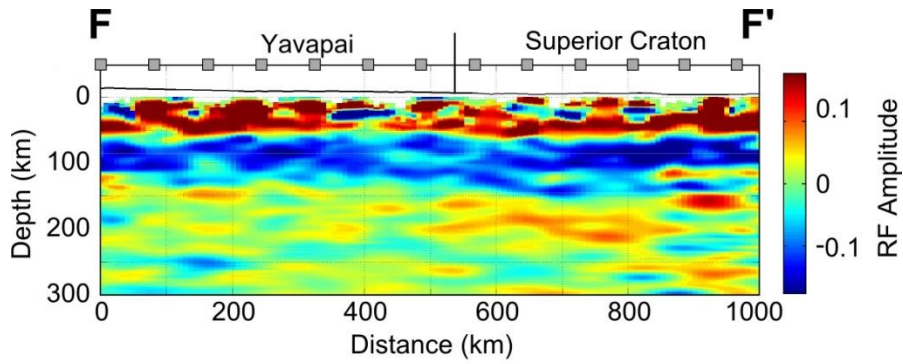


Figure 7: Cross section through the mean of the bootstrapped Sp CCP stack (4–33 s) showing the shallow NVG and a deeper NVG dipping beneath the Yavapai-Superior suture. Grey squares correspond to locations of grey squares in Figure 1. Corresponding tomography [Porrirt et al., 2014] shown in supporting information Figure S3.

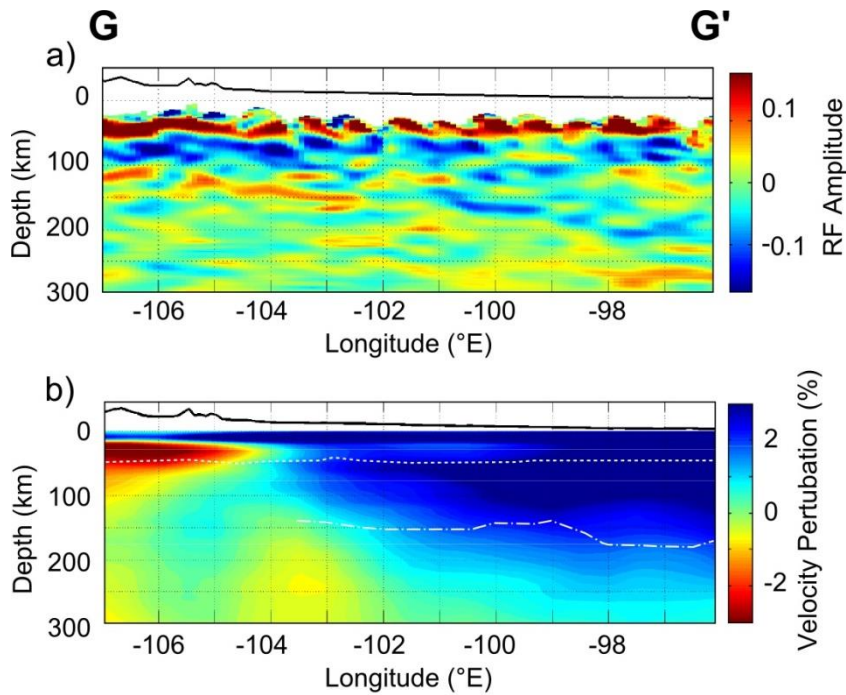


Figure 8: a) Cross-section G-G' through the mean of the bootstrapped Sp CCP stack (4–33 s) in the one region with a clear subcratonic NVG in the LAB depth range. b) Corresponding cross section through the shear velocity anomalies from the tomography model of Porritt et al. [2014]. Thick black line: topography, at 10X vertical exaggeration. Dashed white line: Moho (Lowry, personal communication, 2014). Dash-dotted line: approximate LAB from tomography, as Figure 2.

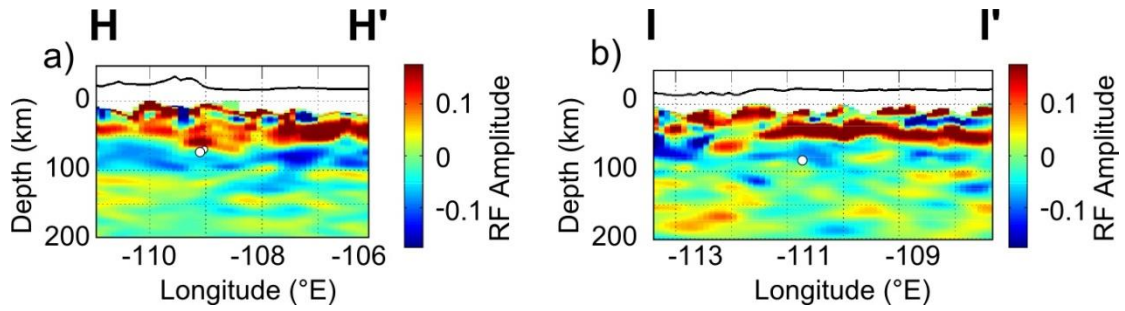


Figure 9: Cross sections through the mean of the bootstrapped Sp CCP stack (4–33 s) to show spatial correlation of mantle earthquake hypocenters (white circles) and the shallow NVG. a) Hypocenter of the Wyoming, September 2013 event (large white circle, size corresponds to uncertainty in depth - 75 ± 8 km [Craig and Heyburn, 2015]) and its aftershock on the same day (small white circle). b) Hypocenter of the Utah, February 1979 event [Zandt and Richins, 1979]. Corresponding tomography [Porrirt et al., 2014] shown in supporting information Figure S4.

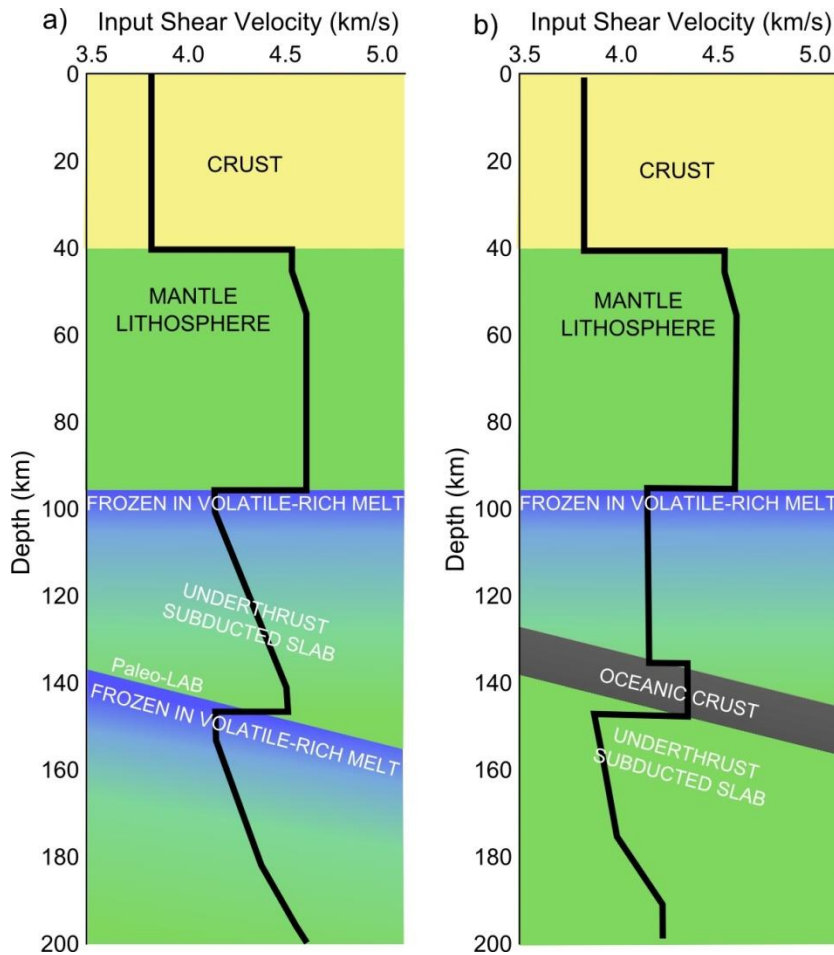


Figure 10: Schematic of the subcratonic lithosphere illustrating two possible velocity models. Both include a shallow frozen volatile-rich melt layer, our preferred model to produce the shallowmost NVG, as well as a 17% velocity increase at the Moho [Snelson et al., 1998]. Two alternative models are given for the deeper dipping NVG. a) A frozen volatile-rich melt layer from the base of underthrust oceanic lithosphere. This layer has a velocity structure similar to that for the upper NVG, although the amplitude is slightly smaller. The crust of the oceanic lithosphere is either invisible to Sp phases or has been removed. b) Eclogitized oceanic crust from the top of underthrust oceanic lithosphere. This layer is up to 4.5% faster than standard peridotite, whereas velocities in the underthrust oceanic mantle are reduced, as expected if the upper oceanic mantle is hydrated. In this case, the original base (paleo-LAB) of the oceanic lithosphere is invisible or has been removed. Yellow shading indicates crust; green shading is mantle lithosphere.

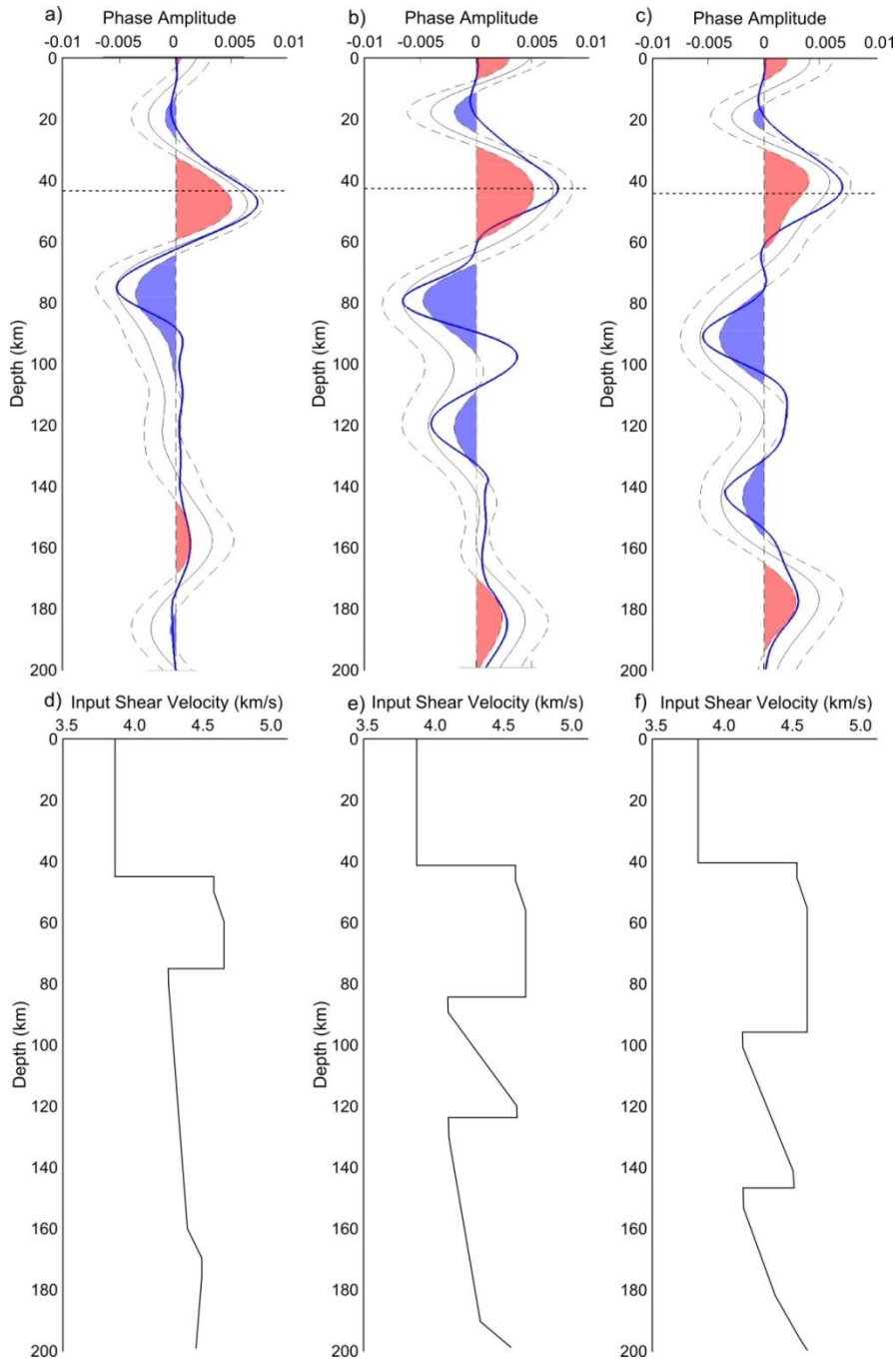


Figure 11: Comparison of observed receiver functions and synthetic receiver functions from models containing two frozen volatile-rich layers (e.g., Figure 10a). a–c) Single station stacks. Solid black line: mean of bootstrapped observations. Black dashed line: $\pm 1\sigma$ variation around the mean. Red and blue shading shows where positive and negative phases are statistically significant. Blue line: synthetic receiver function. d–f) Velocity models used to calculate synthetics. a and d) Transportable Array station R22A (38.2°N , 106.8°W). b and e) Transportable array station Q22A (38.9°N , 106.9°W). c and f) Transportable array station P22A (39.6°N , 106.8°W).

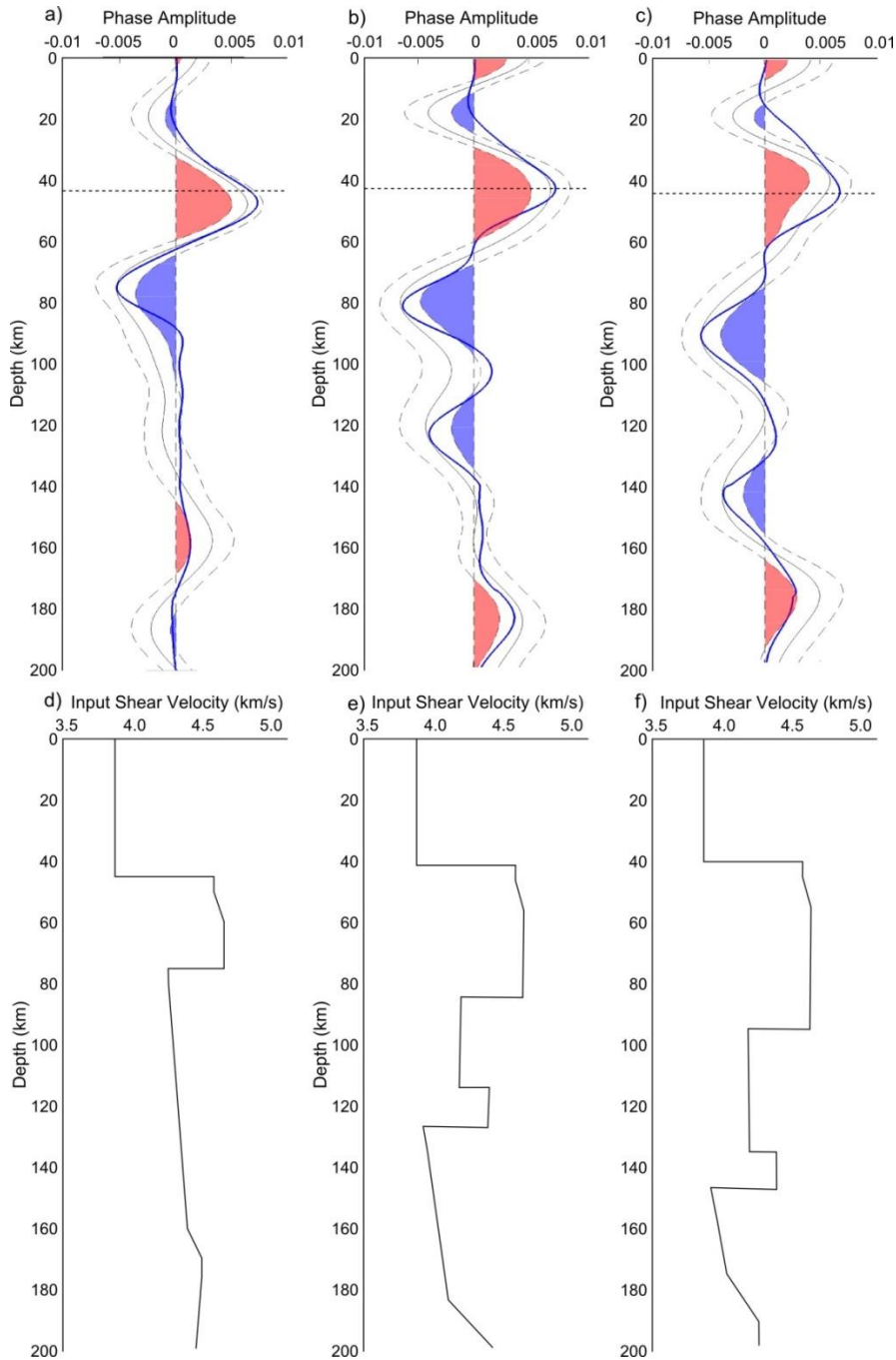


Figure 12: Comparison of observed receiver functions and synthetic receiver functions from models containing one shallow frozen volatile-rich layer and underthrust oceanic crust (e.g., Figure 10b). a–c) Single station stacks. Solid black line: mean of bootstrapped observations. Black dashed line: 61r variation around the mean. Red and blue shading shows where positive and negative phases are statistically significant. Blue line: synthetic receiver function. d–e) Velocity models used to calculate synthetics. a and d) Transportable Array station R22A (38.2°N, 106.8°W). b and e) Transportable array station Q22A (38.9°N, 106.9°W). c and f) Transportable array station P22A (39.6°N, 106.8°W).

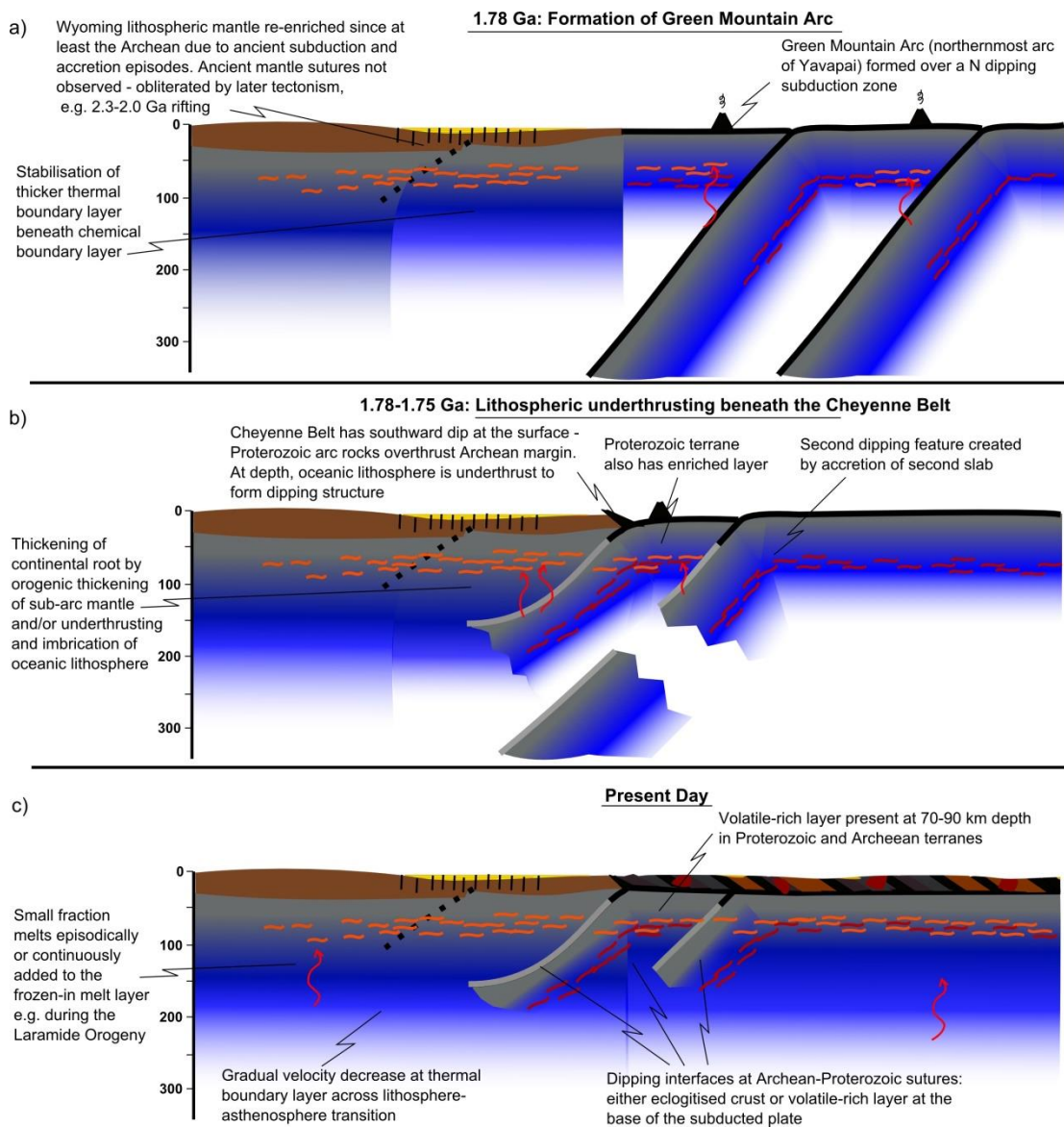


Figure 13: Schematic of Wyoming craton evolution as described in Section 4.8. Note that the idea of lithospheric replacement in the northern Wyoming craton [Humphreys et al., 2015] has not been included for simplicity.

Supplementary Materials

Introduction

This supporting information provides greater detail on 1) our criteria for interpreting the CCP stacks presented; 2) comparison of the CCP stacks in the main text with their corresponding tomography profiles, where not included in the main text; 3) backazimuthally restricted CCP stacks to look at potential signature of anisotropy; 4) more background information on the Wyoming lithospheric mantle earthquake; 5) more details on the forward modeling used to validate out proposed mechanisms.

S1. Example of criteria for interpreting CCP stack

As described in the text, three conditions must be met for a phase to be judged as significant. 1) Converted phase amplitude must be greater than 10% that of the parent phase. 2) The standard deviation of the bootstrapped stack must be less than 5% of the parent phase amplitude. 3) The phase must have a consistent depth or shape over at least 0.5° in latitude or longitude and be visible on perpendicularly oriented cross sections. These conditions are illustrated in Figure S1. This profile runs from north to south at 108.8°W . Marked in black (on the southern half of the figure) are phases that we judge to be interpretable, including the flat-lying shallow NVG at approximately 80-90 km depth between 41° - 45°N , and a dipping phase from 80-120 km south of 41°N . Also included is a portion of another dipping phase at 130 km depth between 42.5° - 43°N . If this phase appeared only on this cross section, it would not be judged to be interpretable, but because it extends more than 50 km in longitude (Figures 5 and 6) it is considered robust. In the northern part of this section, negative phases that are not considered interpretable are marked in white (Figure S6b). For the majority of these, the standard deviation of the stack exceeds 0.05. However, if a phase largely lies where standard deviation exceeds the 0.05 threshold but extends into a zone where standard deviation is lower than 0.05, it will also be excluded (e.g. cases between 45 - 45.5°N).

S2. Additional comparisons of CCP stack with tomography

As interpretation of these converted wave images is aided by comparison with velocity tomography, here we include side-by-side comparisons of Sp CCP stack cross-sections from the main text with equivalent cross-sections from the shear velocity tomography model of Porritt et al. (2014).

S3. Sp CCP stacks from different backazimuth ranges

Sp CCP stacks were calculated using data from the two dominant limited backazimuth ranges in our data (135°-175° and 300°-340°; Figure S5). Finer or more even sampling in back-azimuth was precluded by the distribution of waveforms. In the stacks, the same crust and mantle discontinuities appear. While the images from the two back-azimuth ranges vary, these variations can be explained by differences in the sampling provided by the waveforms for each case. Therefore, these images do not require the presence of azimuthal anisotropy. However, azimuthal anisotropy may exist, either in a form that does not produce variations between these back-azimuth ranges or with an amplitude that goes undetected given the uncertainties in these images. For example, many models containing azimuthal anisotropy produce an 180° period in Sp amplitude with back-azimuth, and because the two back-azimuth ranges are close to 180° apart (their mid-points are separated by 165°) similar discontinuities would be expected for the two sets of data.

S4. More background information on the Wyoming and Utah lithospheric mantle earthquakes

Although their depths are unusual for this type of tectonic environment, in other respects these Wyoming and Utah mantle events appear to be fairly typical double-couple earthquakes. Zandt and Richins [1979] located the 1979 Utah event at 80-90 km depth. Craig and Heyburn [2015] determined a depth of 75 ± 8 km for the 2013 Wyoming earthquake, and Frohlich et al. [2015] and Pechman et al. [2014] concur on a depth of ~ 75 km. The mechanism for this event can be characterized as largely strike-slip with a small reverse component and \sim N-S compression and \sim E-W extension axes [Froment et al., 2014; Pechmann et al., 2014; Frohlich et al., 2015; Craig and Heyburn, 2015]. These compression (P) and extension (T) axes are consistent with those of

crustal earthquakes along the western edge of the Wyoming craton where it intersects the Sevier Thrust Belt (with the exception of the anomalous Yellowstone region) (Figure 1a), suggesting that shallow and deep earthquakes are responding to a consistent regional deformation field [Frohlich et al., 2015; Craig and Heyburn, 2015].

The Wyoming and Utah mantle earthquakes are highly unusual in that most mantle earthquakes in continental settings are associated with subduction-like processes, or at least lithospheric underthrusting (e.g. the Hindu Kush, the Vrancea zone in Romania, and the Himalayas) [Frohlich, 2006; Sloan and Jackson, 2012]. The northern edge of the Australian cratonic mantle beneath the Arafura Sea is tectonic setting with a mantle earthquake [Sloan and Jackson, 2012] that is more analogous to our study region.

S5. Receiver function modeling

We used forward modeling to test our proposed mechanisms for velocity contrasts in the lithospheric mantle. Synthetic receiver functions were calculated using the RAYSUM package [Frederiksen and Boston, 2000]. We employed incident SV particle motion, under the assumption that SV incidence dominates the observed Sp receiver functions, despite the presence of incident SH motion. We used an input phase width of 2.5 s and applied a low-pass filter with a corner at 4 s, resulting in waveforms with an approximately 9 s period, which matches the dominant period of the bandpassed real waveforms.

To compare the synthetics with the data, we calculated single station stacks of observed receiver functions for a suite of stations in the Cheyenne Belt region. Individual receiver functions were calculated as for the CCP stack. These were then corrected to a reference ray parameter and migrated to depth assuming a velocity profile extracted from local tomography, as for the CCP stack. Each station stack includes at least 80 waveforms. The single station stacks are bootstrapped by randomly resampling the dataset 100 times. All plots in the main body of the paper show the mean of the 100 bootstraps, and the $\pm 1\sigma$ variation. The phases in the observed

single station stacks reflect the phases seen in the CCP stack. Where the CCP stack shows the upper NVG and a deeper dipping NVG, both of these phases appear in the single station stack (5 of 6 modeled stations).

The best-fitting velocity models were chosen to match the mean phase amplitudes. However, they are non-unique solutions. Many factors can impact predicted phase amplitudes, and so change the required amplitude of the velocity jump, including, but not limited to, the following.

- 1) Velocity gradient width in depth. In the models shown in the main text, all NVGs are assumed to occur instantaneously in depth. However, as the depth range of the velocity gradients increase, the amplitude of the phases from a given velocity drop decrease (Figures S6 and S7). Given the ~9 s dominant period in the data, changes in gradient depth range over <10 km have little impact on phase amplitudes. To match the breadth of the observed negative phases, a gradient over 20-25 km may be appropriate. This would require an increase in the velocity contrast of approximately 25%.
- 2) Dip of the velocity gradient. This is discussed in Section 4.4 of the main text
- 3) Adjacent velocity gradients. The velocity gradients adjacent to a given discontinuity/velocity gradient, have an impact on the magnitude of the velocity changes required to match a given amplitude in the observed single station stack. For example, in Figure S6 a step-wise drop in velocity of 7% with no other velocity changes (red model) produces the same phase amplitude as an 8.5% velocity drop in a model with a Moho and a gradual velocity increase below the velocity drop (black model). In general, we assume that velocities in the mantle gradually increase with depth (e.g. Figures 11d and 12d) except when perturbed by volatile-rich layers or subducted crust. The presence of a positive phase deep beneath some of our stations requires an increase in this positive velocity gradient beneath the second NVG.

Supplementary References

Craig, T. J., and R. Heyburn (2015), An enigmatic earthquake in the continental mantle lithosphere of stable North America, *Earth. Planet. Sci. Lett.*, 425, 12-23, doi:10.1016/j.epsl.2015.05.048.

Frederiksen, A. W., and M. G. Bostock (2000), Modelling teleseismic waves in dipping anisotropic structures, *Geophys. J. Int.*, 141 (2), 401-412, doi:10.1046/j.1365-246x2000.00090.x.

Frohlich, C. (2006), *Deep earthquakes*. Cambridge University Press, Cambridge, U.K.

Frohlich, C., Gan, W., and Hermann, R. B. (2015). Two deep earthquakes in Wyoming. *Seismol. Res. Lett.*, 86(3), 810-818, doi:10.1785/0220140197.

Froment, B., Prieto, G. A., and R. E. Abercrombie (2014). Source parameters of the upper-mantle September 21, 2013 M_w 4.8 Wyoming earthquake. Abstract S53B-4506 presented at 2014 Fall Meeting, AGU, San Francisco, Calif., 15-19 Dec.

Pechmann, J. C., Koper, K. D., Hermann, R. B., Whidden, K. M., Benz, H. M., Pankow, K. L., Lin, F., and D. S. Chapman (2014), An M 4.8 earthquake in the upper mantle beneath the Wind River Range, Wyoming, *Seimol. Res. Lett.*, 85, 507.

Porritt, R. W., Allen, R. M., and F. F. Pollitz (2014), Seismic imaging east of the Rocky Mountains with USArray, *Earth Planet. Sci. Lett.*, 402, 16-25, doi:10.1016/j.epsl.2013.10.034.

Sloan, R. A., and J. A. Jackson (2012), Upper-mantle earthquakes beneath the Arafura Sea and south Aru Trough: Implications for continental rheology, *J. Geophys. Res. Solid Earth*, 117 (B5), B05402, doi:10.1029/2011JB008992.

Zandt, G., and W. D. Richins (1979), An upper mantle earthquake beneath the middle Rocky Mountains in NE Utah, *Earthquake Notes*, 50 (4), 69-70.

Supplementary Figures

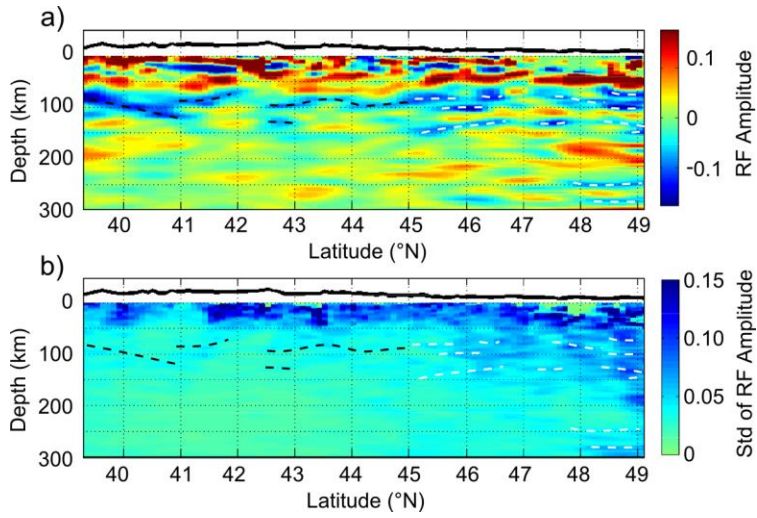


Figure S1: Cross section at 108.8°W. For all sections: thick black line: topography, at 10x vertical exaggeration. Dashed black line: negative phase pick deemed to be robust. Dashed white line: negative phase pick deemed to be not interpretable. a) 4-33 s Sp CCP mean stack. b) Standard deviation of the amplitude between the 50 calculated bootstrap stacks.

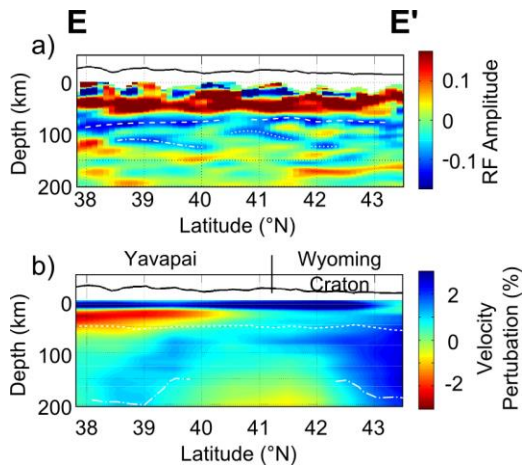


Figure S2: a) As Figure 5. b) Corresponding cross-section through the shear velocity anomalies from the tomography model of Porritt et al. [2014]. Thick black line: topography, at 10x vertical exaggeration. Dashed white line: Moho [Lowry, pers. comm., 2014]. Dash-dotted white line: approximate LAB from tomography, as Figure 2.

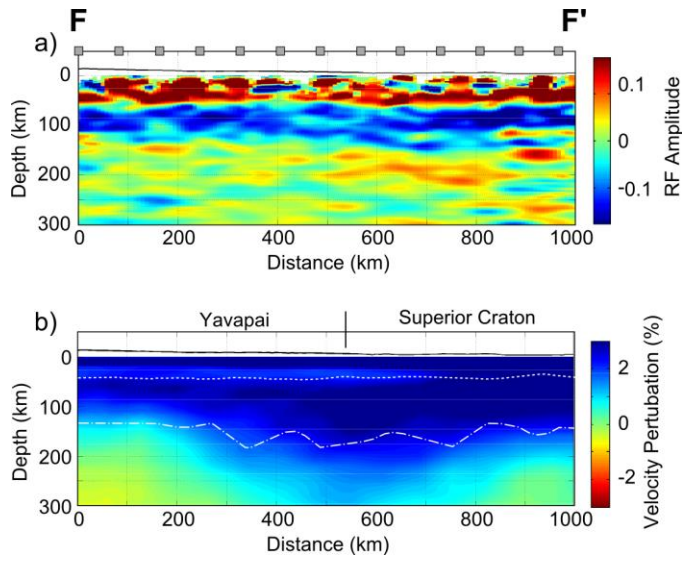


Figure S3: a) As Figure 7. b) Corresponding cross-section through the shear velocity anomalies from the tomography model of Porritt et al. [2014]. Thick black line: topography, at 10x vertical exaggeration. Dashed white line: Moho [Lowry, pers. comm., 2014]. Dash-dotted line: approximate LAB from tomography, as in Figure 2.

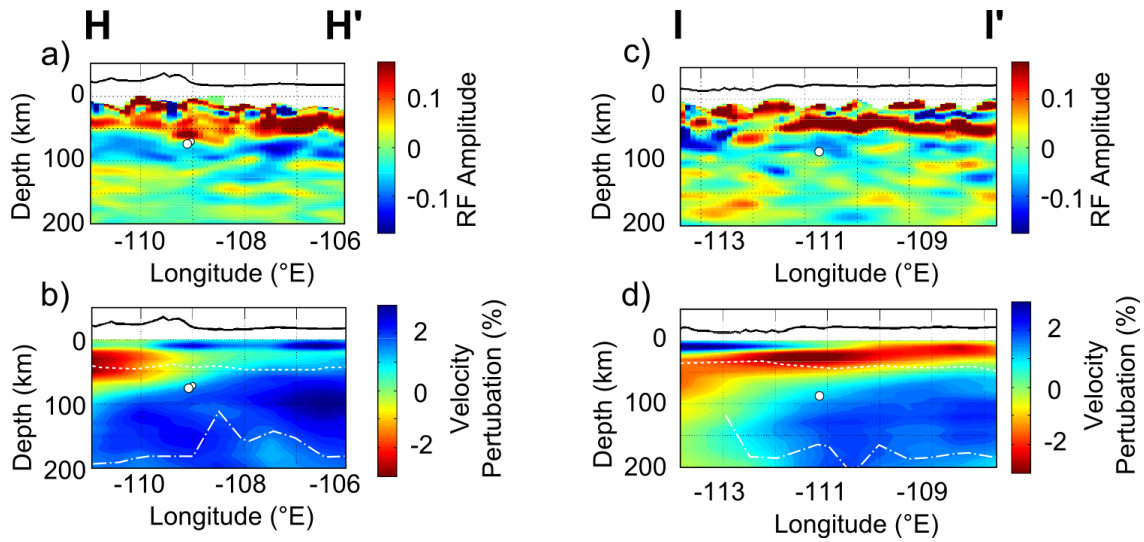


Figure S4: Cross sections to show relationship of mantle earthquake hypocenters (white circles) to mantle structure. Panels A and B show the hypocenter of the Wyoming, Sept. 2013 event (large white circle, size corresponds to uncertainty in depth – 75 ± 8 km [Craig and Heyburn, 2015]) and its aftershock on the same day (small white circle). Panels (c) and (d) show the hypocenter of the Utah, Feb. 1979 event [Zandt and Richins, 1979]. a and c) As Figure 9. b and d) Corresponding cross-section through the shear velocity anomalies from the tomography model of Porritt et al. [2014]. Thick black line: topography, at 10x vertical exaggeration. Dashed white line: Moho [Lowry, pers. comm., 2014]. Dash-dotted white line: approximate LAB from tomography, as Figure 2.

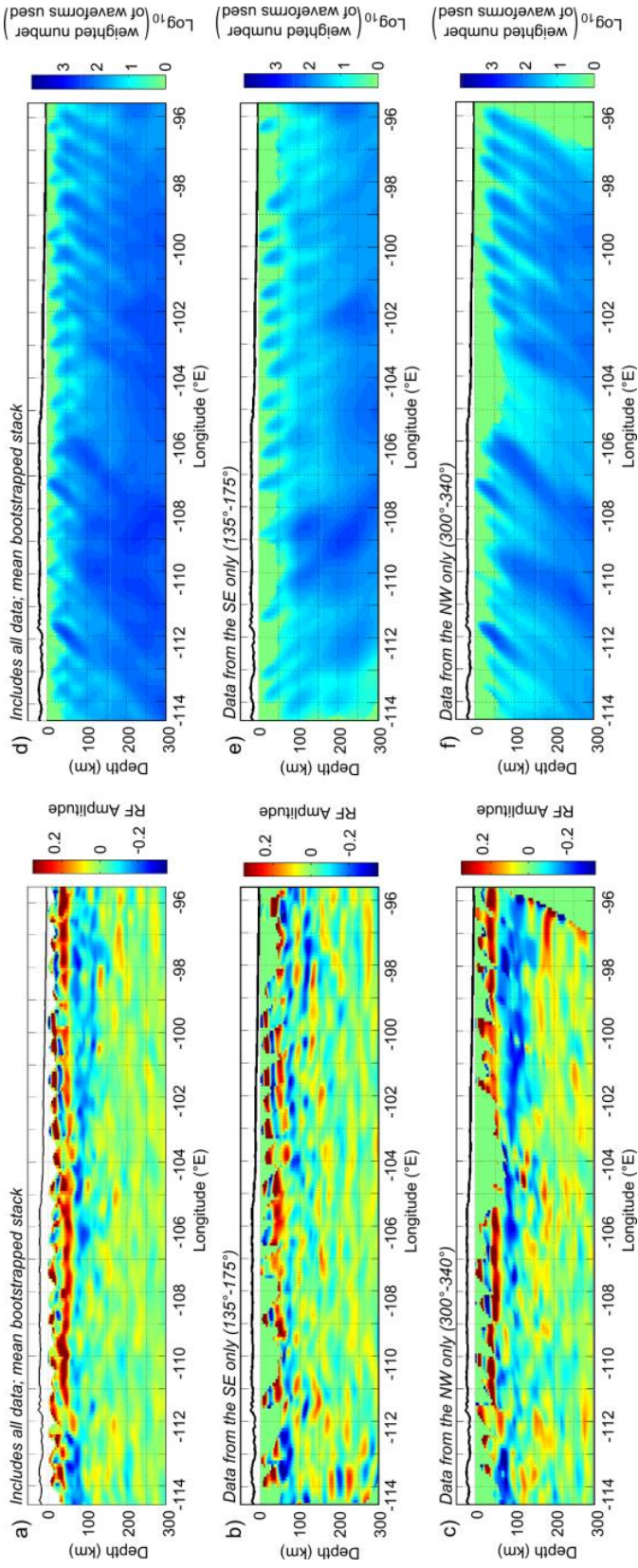


Figure S5: Cross section A-A'. For all sections: thick black line: topography, at 10x vertical exaggeration. a-c) 4-33 s Sp CCP mean stack. d-f) Data density in CCP stack, calculated as number of whole waveforms at a point given the spline weighting used. a and d) This stack includes all data, as Figure 2. b and e) This stack includes data from a backazimuthal range of 135°-175° only. c and f) This stack includes data from a backazimuthal range of 300°-340° only.

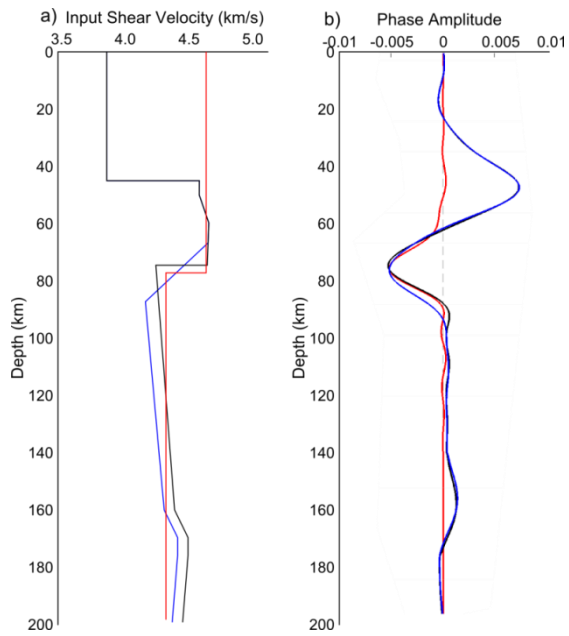


Figure S6: A sample of velocity models that can produce the same negative phase. Black: discontinuous velocity decrease (as Figure 11a,d and 12a,d) of 8.5%. Blue: velocity gradient distributed over 20 km depth with a decrease of 10.5%. Red: discontinuous velocity decrease of 7% with no other velocity changes in the input model

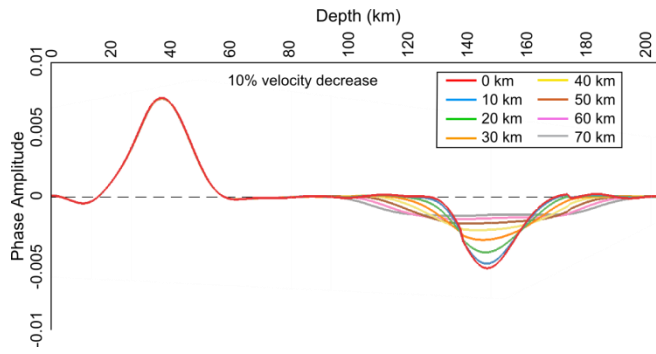


Figure S7: Dependence of amplitude of generated negative phase on the width of a velocity gradient